RESIDUAL CAPACITY OF CONCRETE SUBJECTED TO IMPULSIVE LOADS

A Dissertation
Presented to
The Academic Faculty

by

Rebecca Nylen

In Partial Fulfillment
of the Requirements for the Degree
Doctor of Philosophy in the
School of Civil and Environmental Engineering

Georgia Institute of Technology
August 2020

RESIDUAL CAPACITY OF CONCRETE SUBJECTED TO IMPULSIVE LOADS

Approved by:

Dr. Lauren Stewart, Advisor
School of Civil and Environmental Engineering
Georgia Institute of Technology

Dr. Min Zhou
School of Mechanical Engineering
Georgia Institute of Technology

Dr. Kimberly Kurtis
College of Engineering
Georgia Institute of Technology

Dr. Jim Cox
Engineering Sciences Center
Sandia National Laboratories

Dr. Laurence Jacobs
College of Engineering
Georgia Institute of Technology

Date Approved: July 15th, 2020

DEDICATION

Dedicated to the memory of Steve Attaway, who fueled my intellectual curiosity and gave me the strength of will to persevere.

ACKNOWLEDGEMENTS

I would like to extend my deepest gratitude to my advisor, Dr. Lauren Stewart. She provided me with the support, guidance, and encouragement I needed to succeed in pursuing research questions that truly interested me. Her technical proficiency and the care she extends to her students and mentees creates the environment needed for a research group to thrive. Thank you for shaping me into a confident researcher and for providing me with the necessary tools to pursue an enjoyable career. I would like to thank the other members of my committee, Dr. Kimberly Kurtis, Dr. Laurence Jacobs, Dr. Min Zhou, and Dr. James Cox, for their guidance and encouragement.

I would like to thank the following people at Sandia National Laboratories for their support: Russell Teeter, Kyran Mish, Peter Yeh, Samuel Bowie, and Craig Hamel. The beginning of my internship experience at Sandia three years ago sparked my interest in this research field and started me on the path that I am on today. The opportunity to work on a variety of interdisciplinary projects while learning from such talented engineers and scientists has been invaluable to my development as a researcher.

Of course, I could not have completed an experimental research program without the support of so many people. I would like to thank Andy

Udell, Victoria Novell, Blake Blakini, and Jeremy Stephens for their support and guidance during the design and fabrication process. Jeremy Mitchell provided exceptional support to the logistics of getting started and running an experimental program that required me to take over half of the structures lab at a time. Dr. Nan Gao provided invaluable mentorship and expertise to the technical aspects of conducting laboratory experiments. Thank you Nan, for patiently providing me with so much advice and guidance.

I would like to thank my fellow graduate students Maria Warren and Noel Flores for their constant support, friendship, and positive attitudes. I would also like to thank my undergraduate research assistants, Soniya Bhagat, Alex Nail, and Alexander Rice. Your enthusiasm to learn and unhesitating willingness to do arduous lab work was a source of inspiration for me.

I would like to extend my gratitude to my friends, who have been there for me through the ups and the downs of the past several years. Cynthia Lee, Samantha Corrado, Maya Goldman, Meron Wolde, Scotty Smith, and Erol Unal – thank you for your love and support, because of you I will forever cherish my time in graduate school.

Finally, I would like to thank my family. The support of parents, Jennifer and Peter Nylen, has been unwavering. The work ethic they instilled

in me provided me with the motivation and confidence I needed to succeed in my own goals. To my brother Japhet Nylen and sister-in-law Sarah Nylen, and to my brother James Nylen and sister-in-law Evelyn Ramírez – thank you for always being there for me.

TABLE OF CONTENTS

LIST OF TABLES

LIST OF FIGURES

SUMMARY

This research aims to achieve a better understanding of the behavior and residual capacity of concrete materials subjected to impulsive loading conditions such as blast and impact. Previous research efforts investigating the residual capacity of concrete subjected to these loading conditions have primarily focused on the response of full-scale structural components and frames. Existing test methods to investigate the strain rate dependent properties of concrete typically apply impulsive loads in such a magnitude that the concrete is fully damaged and has no residual capacity following the test. As such, little is known about how varying levels of damage imparted by impulsive loading affects the residual strength and stiffness of plain concrete. This information is vital to ensure that the damage formulations used in concrete constitutive models are accurately representing the material properties of concrete in the range of damaged states that are relevant to structural-scale residual capacity studies.

To address this issue, a dynamic compressive testing system and experimental protocol capable of damaging plain concrete cylinders under intermediate strain rates is developed. Following the impulsive loading, the residual capacity of the damaged specimen is assessed with a standard uniaxial compression test. The impulsive loading is achieved with the use of a high speed actuator, which accelerates a flyer mass to a desired velocity before the mass impacts the test fixture. The testing system is capable of producing impulsive loads in a controlled and repeatable manner to subject the specimen to single or repeated impacts.

Using the new experimental method, an experimental study was conducted on plain concrete cylinders to evaluate the residual strength and stiffness of concrete subjected to impulsive loads of varying intensity. The experiments were able to capture a clear decrease in the residual strength and stiffness for increasing levels of impulsive load. Most notably, the normalized loss of stiffness is much greater than the loss of strength at lower levels of damage. This differs from the behavior of concrete as it sustains damage through quasi-static mechanical loads, where the loss of strength versus stiffness is demonstrated to be nearly proportional. So, this trend in the impulsively damaged concrete is likely due to damage mechanisms that only are influential or present during impulsive loading. The existence of this trend is previously unknown and provides novel insight on the behavior of impulsively damaged concrete.

Finally, a numerical study was conducted to evaluate the suitability of plasticity-based concrete constitutive models for predicting the residual capacity of concrete subjected to impulsive loads. Three models commonly used for blast and impact applications were examined: the Karagozian and Case model, the Holmquist-Johnson-Cook concrete model, and the Johnson-Holmquist ceramic model. The concrete models show a more rapid loss of strength before the material experiences any significant reduction in stiffness, which does not match the trend observed in the experiments. This points to a potential shortcoming with the plasticity-based damage formulations used in these models, as the experimentally observed loss of stiffness is not captured. To improve the damage formulations, more experimental data is needed to fully characterize the relationship between the loss of modulus and loss of strength for impulsively damaged concrete and identify the damage mechanisms responsible.

CHAPTER 1. INTRODUCTION

1.1 Problem Statement

Mitigating the risk of structural collapse in the event of extreme loads such as blasts or impacts requires a thorough understanding of the response of structures to such environments. With concrete being the most commonly used building material in the world, it is especially important to fully characterize the response of reinforced concrete structures to dynamic loads. Once a building is damaged from an impulsive loading event, certain structural elements may be partially damaged and the integrity of the building and the safety of the building occupants depends on the residual capacity of these damaged structural elements.

Much of the motivation to understand the residual capacity of reinforced concrete subjected to impulsive loading is fueled from the progressive collapse of structures such as Ronan Point in 1968 and the Alfred P. Murrah Federal Building in 1995. Disasters such as these have historically pushed research efforts towards strengthening individual structural components and increasing the redundancy of the structure in the event that a structural element is effectively removed. These structural-level approaches have remained the primary focus for preventing the progressive collapse of structures and examining the residual capacity of damaged elements and buildings. However, in order to effectively predict the global response of reinforced concrete structures, it is essential to also isolate and characterize the response of the individual material constituents.

Numerical modeling is an increasingly common and attractive method for evaluating the response of structures to extreme events, as live blast and impact testing is often cost prohibitive. Thus, the research field has transitioned to conducting fewer experiments on full-scale structures and structural components, the results of which are used to calibrate numerical models. The successful calibration of these models to a chosen metric is often used as justification for using the methodology of the calibrated model to predict responses for additional scenarios. Common practice involves calibrating the model to match residual capacity metrics such as residual displacement in a column or exit velocity for a penetration problem. However, these structural-scale problems are highly complex, and the combination of reinforcing steel, concrete, and the bond between the two materials introduces many uncertainties. Matching a relatively simple residual capacity metric such as residual displacement or exit velocity does not necessarily ensure that the models are correctly capturing the damage mechanisms and the residual capacity of the individual material constituents. For example, Sanborn [1] found that commonly used finite element material models were unable to predict the residual capacity of shear damaged bolts without extensive calibration efforts.

There is currently no data that examines the residual capacity behavior of concrete subjected to impulsive loads at the material level. Instead, the behavior of concrete subjected to impulsive loads has been investigated through the use of test methods that apply impulsive loads so large in magnitude that the concrete becomes fully damaged with no residual capacity. This problem is the result of a lack of testing methods capable of applying impulsive loads in regimes that leave the concrete in a range of damaged states. Without fully characterizing the progression of damage at the material level and examining

how the level of damage influences the residual capacity of the material, it is not feasible to determine if constitutive material models are correctly predicting the residual capacity of concrete.

1.2 Research Objectives

The objective of this research is to develop a better understanding of the behavior and residual capacity of concrete materials subjected to impulsive loading conditions such as blast and impact. Previous research efforts have primarily focused on the response of full-scale structural components and frames. Existing test methods to investigate the material properties of concrete subjected to these loading conditions typically apply impulsive loads in such a magnitude that the concrete is fully damaged and has no residual capacity following the test. Thus, there is no experimental data on the residual capacity of impulsively damaged concrete at the material level.

To bridge this gap, the research focuses on the development of a new high-loading-rate compression testing system that is capable of testing plain concrete specimens under intermediate strain rates in a controlled and repeatable manner. The intention of the testing system is to evaluate the behavior of concrete during the dynamic loading and to impart varying levels of damage to the specimen. The impulsively damaged specimens can then be evaluated to determine changes in mechanical properties. This research also aims to investigate the suitability of commonly used plasticity-based concrete models for predicting the residual capacity of concrete damaged from impulsive loading. Three constitutive models are evaluated with the insight from the experimental program, and the sensitivity of the calibration process for the models is evaluated.

1.3 Research Contributions and Significance

The main contribution of this research is the novel experimental evaluation of the residual capacity of concrete damaged by impulsive loads. This experimental program successfully bridges the gap between materials-level high strain rate testing and structural level residual capacity testing to provide insight on the degradation of strength and stiffness of concrete for varying levels of impulsive damage. The experiments were able to capture and quantify a clear decrease in the residual strength and stiffness for increasing levels of impulsive load. Most notably, it was found that the normalized loss of stiffness is much greater than the loss of strength at lower levels of damage. In addition, a preliminary test demonstrated the capability of the test system to evaluate the dynamic residual capacity of damaged concrete with double hits. This test case provides a methodology for gaining insight on the behavior and degradation of concrete subjected to repeated impacts. Another important contribution of this research is the evaluation of plasticity-based concrete constitutive models based on the experimental data. The constitutive models were unable to sufficiently match the loss of stiffness that was observed in the experimental program, which is not surprising because they lack a damage mechanics framework that would result in stiffness degradation. However, with the novel trend shown in the experimental data, the lack of stiffness degradation in the models is even more problematic. This is concerning because these plasticity-based models are the most commonly used type of constitutive model in structural-scale residual capacity predictions. If the stiffness of the damaged concrete is not correctly represented, then the predicted stiffness and thus global response of the damaged structure is likely incorrect. Further characterization of the dynamic properties of concrete with the new experimental system will provide the insight needed to

further evaluate if plasticity-based models are appropriate for residual capacity calculations.

Finally, the new experimental system has great potential to perform various types of experiments because it can be easily adapted to accommodate specimens of different geometries and materials. The testing potential with plain concrete cylinders is significant alone. For example, the influence of concrete strength, curing conditions, aggregate type, or other mix design variables can be evaluated. This dissertation serves as a preliminary investigation into the behavior of concrete damaged by impulsive loads and provides the framework for future studies on the topic.

1.4 Outline of This Dissertation

Chapter 2 of this dissertation introduces the background of the mechanical behavior of concrete subjected to various stress states. An explanation for the strain rate sensitive material properties of concrete is provided, the dynamic fracture of brittle materials is reviewed, and the shock response of materials is discussed. Previous studies on the residual capacity of concrete at the structural and material level are summarized.

Chapter 3 presents the design of an impulsive concrete compression testing system as well as validation test results. The residual capacity test system is described and an in-development in-situ residual capacity testing capability is presented.

Chapter 4 presents the methodology and findings of an experimental program conducted to investigate the behavior of concrete subjected to impulsive loads. The performance and efficiency of the dynamic experimental setup is evaluated.

Chapter 5 presents the methodology and findings of an experimental program conducted to investigate the residual capacity of the concrete specimens damaged in the dynamic experimental program. The residual strength, stiffness, and work is compared to baseline undamaged concrete specimens.

Chapter 6 presents findings of a numerical investigation into the accuracy and validity of commonly used concrete constitutive models for the prediction of residual capacity of impulsively damaged concrete. The models are calibrated to the quasi-static baseline compression test data and the numerical residual capacity results are compared to the experimental findings.

CHAPTER 2. LITERATURE REVIEW

2.1 Fundamental Mechanical Behavior of Concrete

Concrete is the most widely used construction material in the world, with around 33 billion tons used annually [2]. It is a composite material that consists of a binding medium with embedded fine and coarse aggregates. The binding medium is comprised of Portland cement and water, which hydrates and forms a paste that binds the aggregates together, while crushed rock and sand are typically used as the coarse and fine aggregates, respectively. Although concrete is a composite material, most of its material characteristics do not follow the law of mixtures. The aggregates and hydrated cement paste fail elastically if tested separately, while the composite material shows inelastic behavior until failure and typically has much lower strength than the individual strength of the two components [2]. This behavior is primarily due to the interfacial transition zone (ITZ) between the aggregates and cement paste, which has higher porosity due to particle packing effects and a higher number of pre-existing microcracks due to differential shrinkage. The ITZ is the most critical phase of the concrete because it largely determines the constitutive behavior of the material.

2.1.1 Concrete in Compression

The compressive strength of concrete depends primarily on the porosity of the material, which is influenced by the characteristics and proportions of raw materials as well as the curing conditions. The primary factor determining the porosity of the material is the water to cement ratio. When this ratio increases, the porosity in the cement paste and the

interfacial transition zone increases. In addition, the testing parameters or loading conditions can affect the response of concrete to applied stress.

One of the most common test methods used to determine concrete strength is the uniaxial compressive test outlined by ASTM C39 [3]. In this test, a compressive axial load is applied to 6-inch by 12-inch concrete cylinders at a load rate of 35 ± 7 psi/s [0.25 ± 0.05 MPa/s]. These tests are commonly performed at 28 days of curing to obtain a standardized compressive strength value, f_c'. Below $0.3f_c'$, the stress strain response of the concrete is linear because the microcracks in the ITZ are nearly undisturbed. From $0.3f_c'$ to approximately $0.5f_c'$, the concrete no longer behaves linearly because the microcracks in the ITZ begin to extend. Between 0.5f'c and 0.75f'c, the microcracks begin extending into the cement paste matrix. In this range, the crack growth is considered to be stable because the cracks reach a terminal length when the load is held constant [4]. Beyond $0.75f'c$, the ITZ cracks grow and become unstable once the available internal energy exceeds the required crack-release energy [4]. $0.75f_c'$ is generally considered to be the critical stress value at which the volumetric strain begins to reverse [5]. After the maximum stress f_c', the specimen loses strength due the unstable propagation and coalescence of cracks and the stress strain curve descends. Figure 1 shows typical plots of normalized compressive stress versus axial strain as well as volumetric strain.

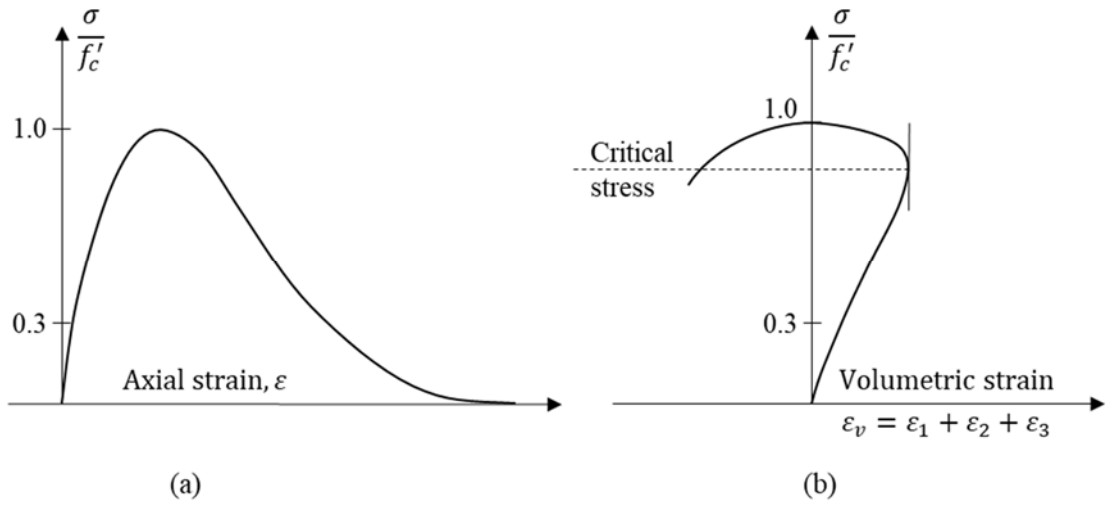

Figure 1: Typical plots of (a) compressive stress versus axial strain, and (b) volumetric strains during uniaxial compression, adapted from [4]

The post-peak branch of the stress strain curve is difficult to capture with standard testing machines because once the stress begins to decrease, the strain energy in the test machine is released and the severely damaged specimen is crushed [6, 7]. Only specialized testing machines that have high stiffness and displacement-controlled mechanisms to restrain the release of strain energy can capture the full descending branch. The volumetric strain response of concrete typically involves a decrease in volume as the material contracts up to the critical stress value, then an increase in volume due to shear-induced dilatation. Shear dilatation occurs when cracks that were once interlocked begin to slide past each other. Because the crack surfaces are very rough and include debonded aggregates, the sliding mechanism results in a bulk expansion of the material.

Figure 2 shows the response of concrete under uniaxial cyclical loading, where the specimen is initially unloaded between $0.50f_c'$ and $0.75f_c'$. Upon reloading, the specimen

exhibits nonlinearities and a significant degradation of stiffness due to the accumulation of microcracks and eventually macrocracks with each loading cycle.

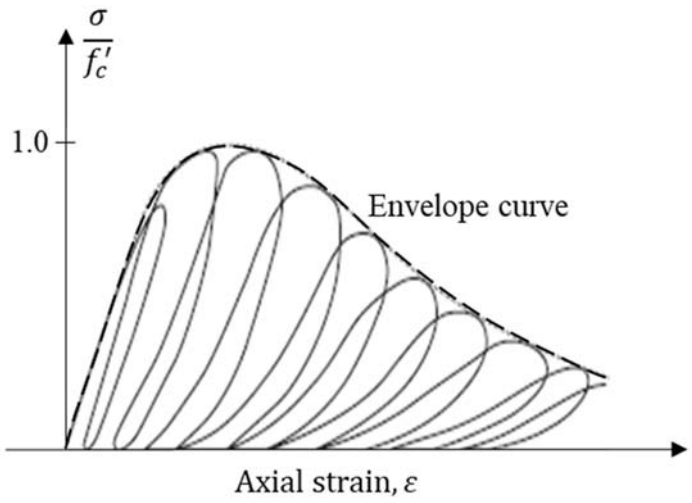

Figure 2: Response of concrete to cyclic uniaxial loading, adapted from [4]

For compressive tests performed on concrete cylinders, the macroscopic cracking pattern will vary depending on testing conditions and can serve as a useful indication of the end conditions and stress state of the cylinder during testing. The failure modes outlined in ASTM C 39 are show in Figure 3. The type 1 failure mode typically occurs when the friction between the cylinder surfaces and the bearing surface is high enough to impart lateral restraint on the ends of the cylinder, causing the ends of the cylinder to be in a state of compressive triaxial stress. Type 3 failure occurs when there is relatively little friction between the cylinder end surfaces and the bearing surfaces in the test machine, so the specimen is allowed to freely expand on either end resulting in tensile cracking due to the Poisson effect. Type 2 failure occurs due to a medium amount of friction between the specimen and the bearing plates, where the cylinder surfaces are partially restrained so that a cone may form on one end while the other end experiences more lateral expansion. Type

4 failure occurs for similar reasons to type 1 failure, but in this case the macroscopic cracking localizes in a shear plane across the specimen. Type 5 and 6 failure typically occur when the specimen is directly in contact with the bearing plates and a neoprene endcap is not used, or when the specimen end surfaces are not level and the corners of the specimen experience a locally higher stress.

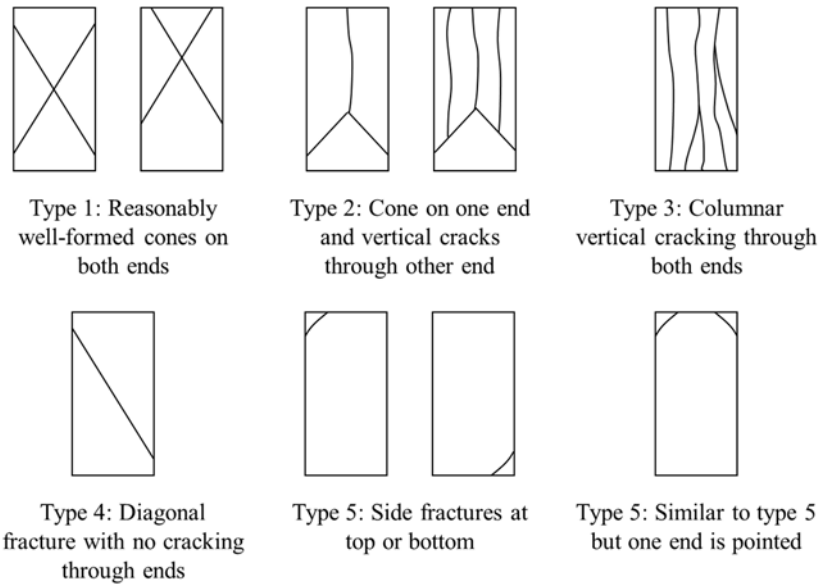

Figure 3: Typical failure modes during uniaxial compression testing, adapted from [3]

2.1.2 Concrete in Tension

The tensile strength of concrete is typically around 8 to 10 percent of the compressive strength. Similar to the behavior of concrete in compression, the stress-strain response of concrete in tension is characterized by an initial linear increase of stress with respect to strain, a period of softening before the maximum stress is reached, and then a decrease of stress with respect to strain. The descending portion of the stress-strain curve in tension is also difficult to capture experimentally, but several researchers have

demonstrated that it exists through the use of specialized displacement-controlled testing machines [8-10]. Figure 4 shows a stress-strain curve for normal strength concrete in direct tension obtained by Reichard et al. [10] with the use of a coupled hydraulic testing system.

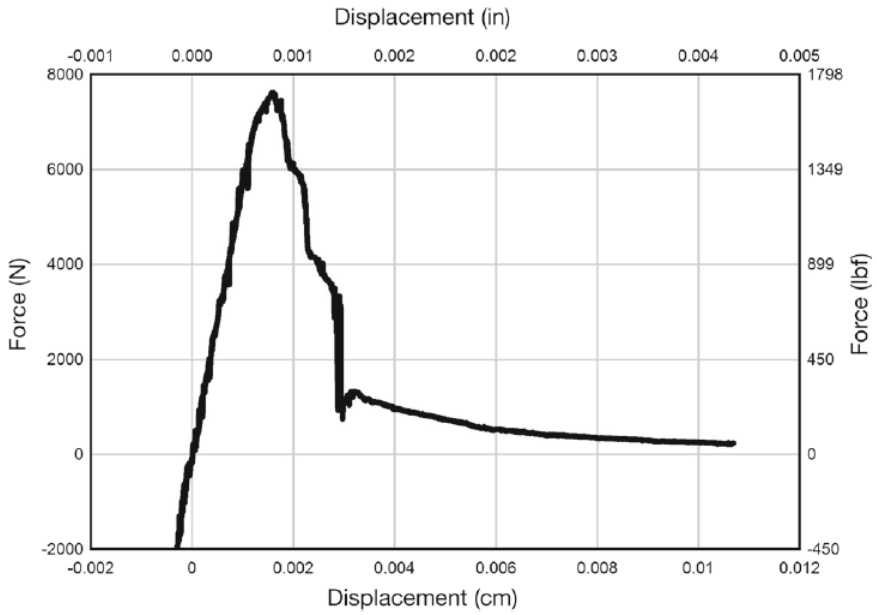

Figure 4: Stress-strain curve for concrete in direct tension, reprinted by permission from [10]

Direct tension tests are difficult to conduct experimentally, so tests that indirectly measure the tensile strength of concrete are often conducted. The most common test is the splitting tensile test, where a testing machine is used to diametrically compress a cylinder per ASTM standard C 496 [11]. The stress distribution is not tensile through the full diameter of the cylinder, as the outer edges are loaded in compression. However, the inner diameter of the cylinder has a quasi-uniform tensile stress distribution that is proportional to the applied compressive stress, so the maximum tensile stress can be determined based

on the maximum applied compressive stress. Figure 5 shows the test setup and the diametric distribution of compressive and tensile stresses.

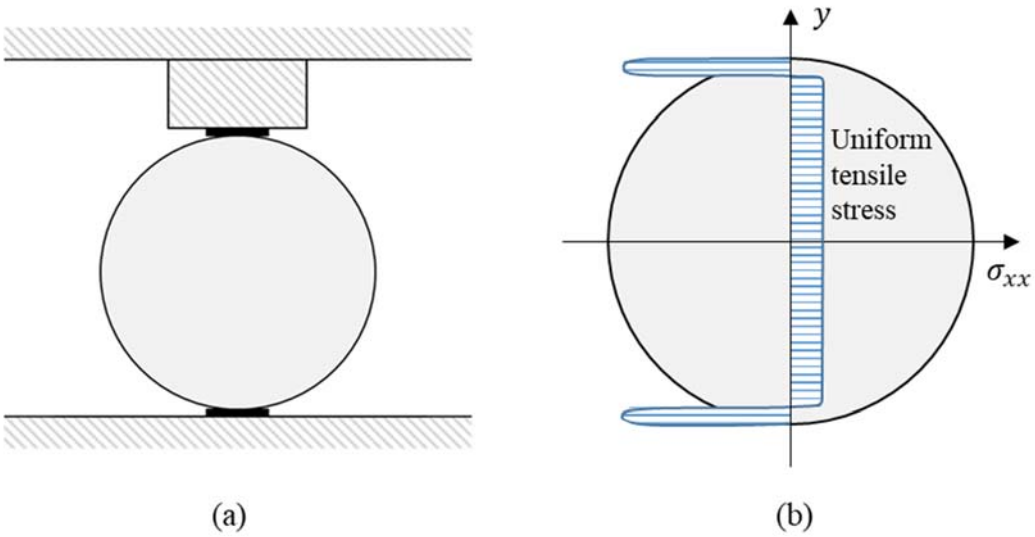

Figure 5: (a) ASTM C 496 test setup [11], (b) distribution of compressive and tensile stresses

Other test methods to indirectly determine the tensile strength of concrete include the three-point bending test and the four-point bending test. The basic procedure of these tests is to apply a load to the top of a beam to create tensile stress in the bottom fibers of the beam. The specimen may be notched to control the location of crack initiation so that deformation gauges can be placed obtain information about the crack propagation.

2.1.3 Concrete in Multiaxial Stress States

Concrete is rarely subjected to simple compression or tension during normal loading conditions. Even during testing procedures that target these specific stress states, the concrete specimen is generally in a combined state of stress due to end conditions and

due the heterogeneous internal nature of the material. So, utilizing compression and tension test results to represent the uniaxial behaviour of the material is an approximation of the true properties of the material, and it is important to consider the behaviour of the material in combined stress states.

Figure 5 shows the stress-strain behaviour of concrete under biaxial compression at varying stress ratios, and Figure 6 shows the stress-strain behaviour of concrete under biaxial tension-compression, as reported by Kupfer et al. [12]. For biaxial compression, the compressive strength of the concrete increases with increasing confining pressure. Under biaxial tension and compression, the compressive strength decreases at a rate proportional to the applied tensile stress. For biaxial tension, the tensile strength remains unchanged. Aside from the changes in compressive strength, the ductility of concrete in biaxial compression as well as biaxial tension and compression increases when a component of the compressive stress increases. Based on examination of failed test specimens, the orientation of maximum tensile strains are the primary failure mechanism of concrete subjected to biaxial stress states [4].

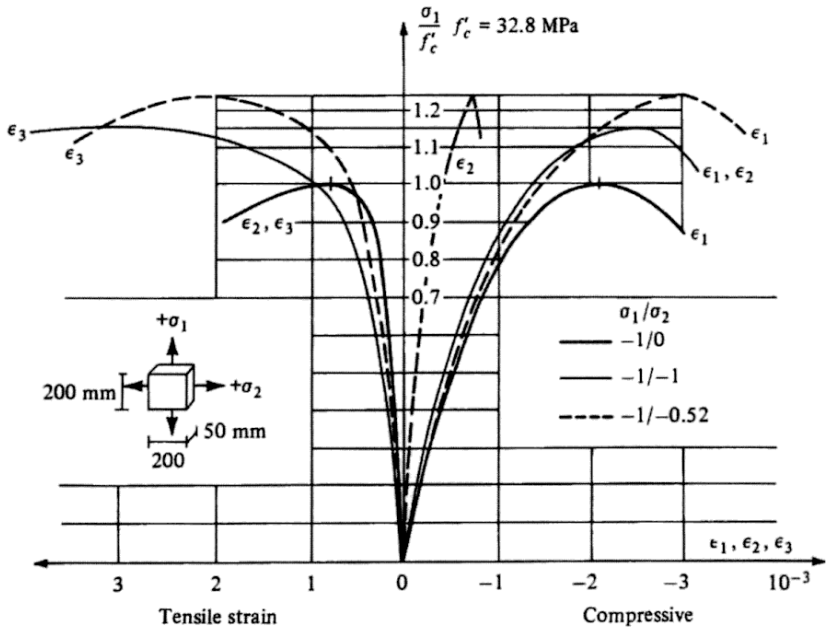

Figure 6: Stress-strain relationships of concrete under biaxial compression [12]

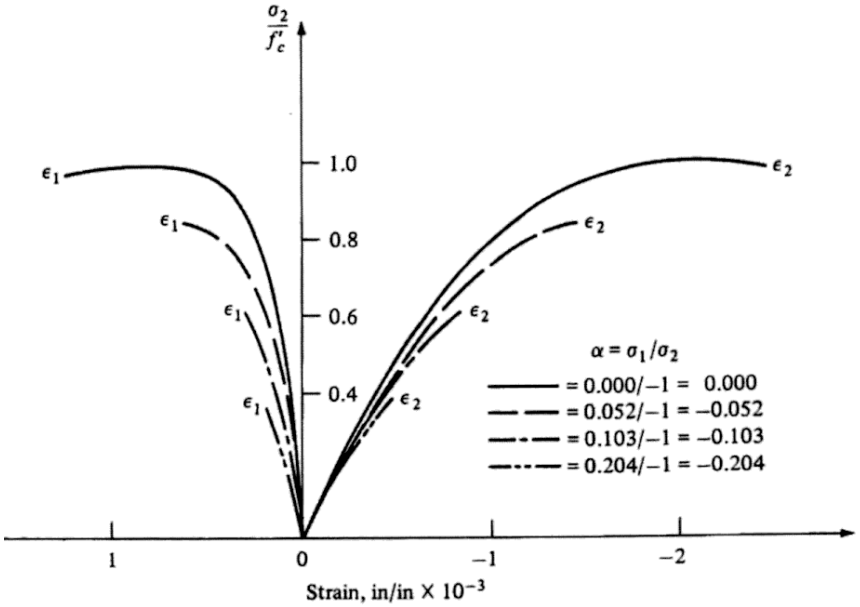

Figure 7: Stress-strain relationships of concrete under biaxial tension-compression [12]

The generalized stress-strain behaviour of concrete in triaxial compression is shown in Figure 8, where a cylinder is subjected to a confining pressure $p = \sigma_1 = \sigma_2$ and a compressive load is applied in the σ_3 direction. The σ_3 - ε_3 stress-strain relationship is initially linear up to the yield stress value, σ_{yield}, then the slope decreases until the maximum stress value, σ_{max}, is reached. Once σ_{max} is reached, the stress begins to decrease with increasing strain. Due to the presence of the confining pressure, p, the stress does not soften to a value of zero and it instead softens to a constant value, $\sigma_{residual}$. Although the descending portion of the curve and the residual stress value is difficult to obtain, Attard et al. [13] and Smith et al. [14] confirmed that the stress strain relationship does reduce to a constant residual stress value after reaching the maximum stress.

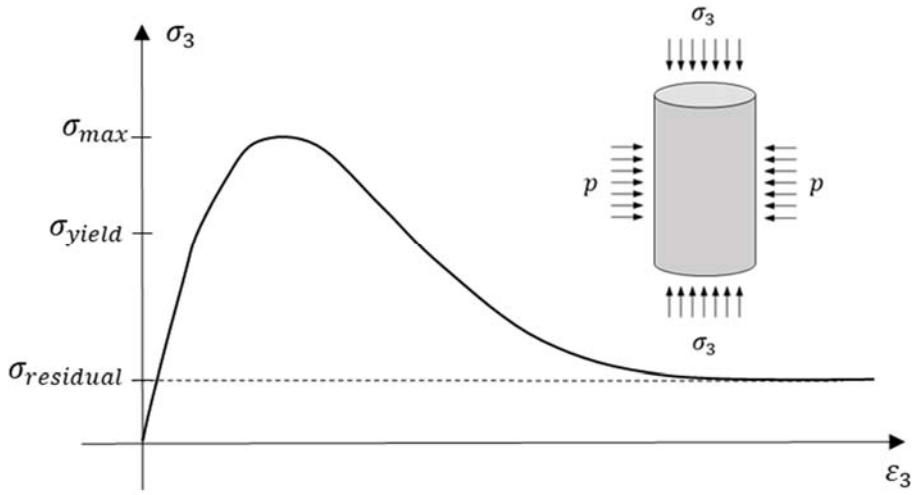

Figure 8: Stress-strain behaviour of concrete in triaxial compression under confining pressure p

2.2 Dynamic Properties of Concrete

The mechanical properties of concrete differ when subjected to dynamic loads due to inertial effects and material properties that change with increased strain rate. In general, there are three strain rate regions of interest for dynamic loading: intermediate strain rates ($10^{-1}\ s^{-1}$ to $10^{1}\ s^{-1}$), high strain rates ($10^{1}\ s^{-1}$ to $10^{4}\ s^{-1}$), and very high strain rates (beyond $10^{4}\ s^{-1}$) [15]. Figure 9 classifies the mechanical states and testing methods for strain rates ranging from creep strain rates to very high strain rates.

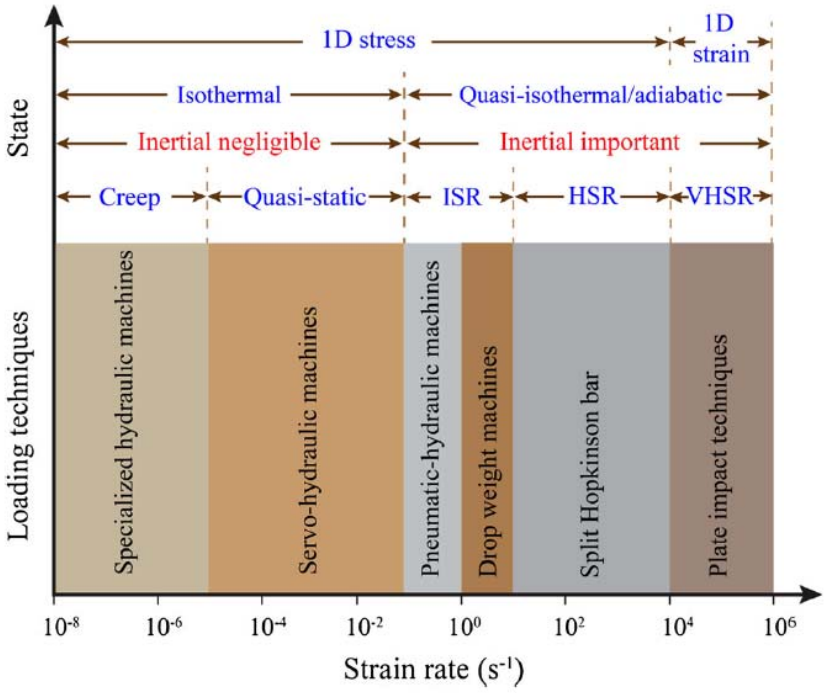

Figure 9: Classification of loading techniques over a wide range of strain rates, reprinted by permission from [15]

The most apparent changes in material properties of concrete subjected to increasing strain rates are summarized by Fu et al. [16], based on a review of data in the literature:

1. Compressive strength, tensile strength, and the modulus of elasticity increase with increasing strain rate.
2. Wet concrete is more sensitive than dry concrete to a change in loading rate, and lower strength concretes are more sensitive to strain rate increase than higher strength concretes.

3. The slope of the descending branch in the stress-strain diagram increases with increasing strain rate, and the ultimate strain appears to be independent of strain rate.
4. Concrete tends to fail explosively at high strains rates.

2.2.1 Dynamic Increase Factors for Concrete

One approach to account for the change in concrete material properties in the dynamic regime is to apply a dynamic increase factor (DIF), which is a ratio of the dynamic strength and the static strength as a function of strain rate. Many researchers have conducted experiments to quantify the relationship between strain rate and the apparent increase in strength. A comprehensive model of the strain rate effects relating to compressive and tensile strength is provided by the CEB model code [17], where the DIF relationship is given as a bilinear function of the strain in a log-log plot. In compression, the DIF relationship is given by:

$$f_c/f_{cs} = \begin{cases} \left(\frac{\dot{\varepsilon}}{\dot{\varepsilon}_s}\right)^{1.026\alpha_s} & for\ \dot{\varepsilon} \leq 30\ s^{-1} \\ \gamma_s \left(\frac{\dot{\varepsilon}}{\dot{\varepsilon}_s}\right)^{1/3} & for\ \dot{\varepsilon} > 30\ s^{-1} \end{cases} \tag{2.1}$$

where

f_c = dynamic compressive strength at $\dot{\varepsilon}$
f_{cs} = static compressive strength at $\dot{\varepsilon}_s$
$\frac{f_c}{f_{cs}}$ = compressive strength dynamic increase factor (DIF)
$\dot{\varepsilon}$ = strain rate in the range of 30 x 10^{-6} to 300 s^{-1}
$\dot{\varepsilon}_s$ = static strain rate, 30 x 10^{-6} s^{-1}
$\log \gamma = 6.156\alpha - 2$
$\alpha_s = 1/(5 + \frac{9f_{cs}}{f_{co}})$
f_{co} = 10 MPA [1450 psi]

The CEB model code recommends the following expression for the DIF in tension:

$$f_t/f_{ts} = \begin{cases} \left(\frac{\dot{\varepsilon}}{\dot{\varepsilon}_s}\right)^{1.016\delta} & for\ \dot{\varepsilon} \le 30\ s^{-1} \\ \beta \left(\frac{\dot{\varepsilon}}{\dot{\varepsilon}_s}\right)^{1/3} & for\ \dot{\varepsilon} > 30\ s^{-1} \end{cases} \quad (2.2)$$

where

f_t = dynamic tensile strength at $\dot{\varepsilon}$
f_{ts} = static tensile strength at $\dot{\varepsilon}_s$
$\frac{f_t}{f_{ts}}$ = tensile strength dynamic increase factor (DIF)
$\dot{\varepsilon}$ = strain rate in the range of 30 x 10^{-6} to 300 s^{-1}
$\dot{\varepsilon}_s$ = static strain rate, 30 x 10^{-6} s^{-1}
$\log \beta = 7.11\delta - 2.33$
$\delta = 1/(10 + \frac{6f_{cs}}{f_{co}})$
f_{co} = 10 MPA [1450 psi]

Bishchoff and Perry [18] compiled much of the data available in the literature to examine the relationship between compressive strength and strain rate, and summarized the data with the recommended CEB relationship shown in Figure 10.

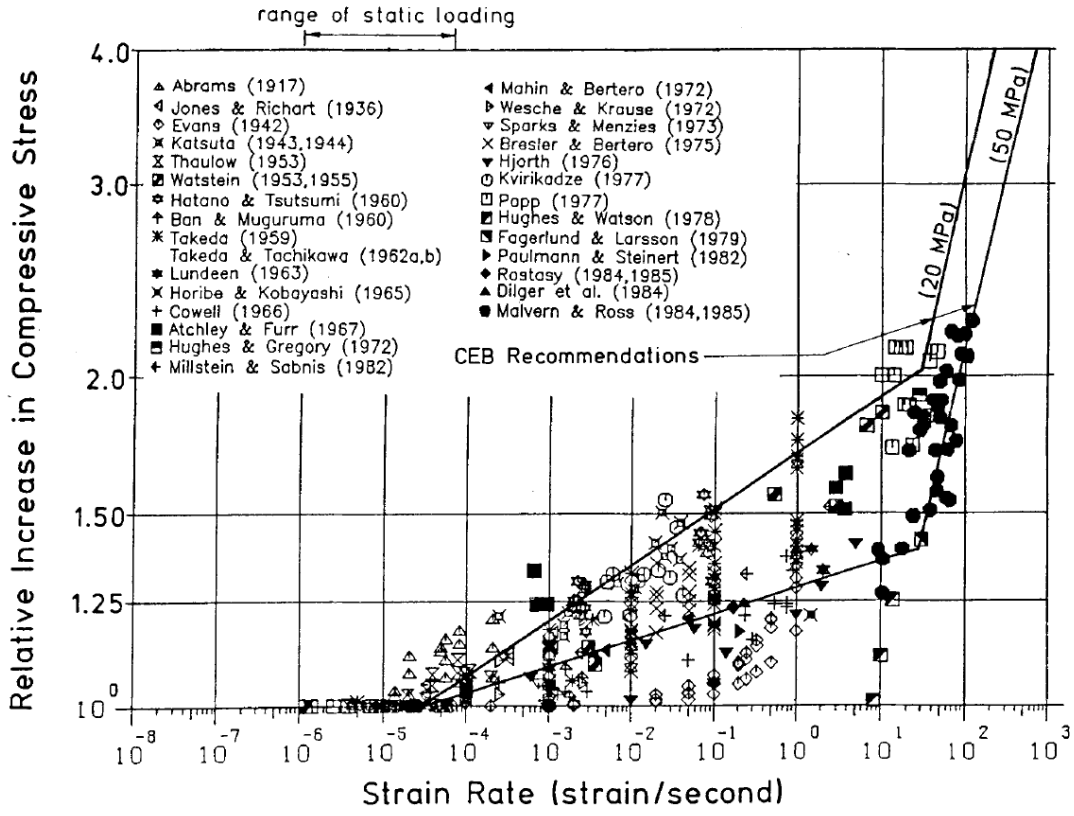

Figure 10: Strain Rate Influence on Compressive Strength, reprinted by permission from [18]

Bischoff and Perry found that the data in the literature generally fit the CEB recommendations, but a large amount of the scatter exists in the experimental results due to the wide variety of testing programs that were examined in this review. Minor modifications to recommended compression and tension CEB relationships were proposed by Malvar and Crawford [19] and Malvar and Ross [20], respectively, based on a review of data in the literature. Testing conducted by Ross et al. [21] found similar results to the CEB recommendations, and Ross et al. [22] proposed an exponential fit for the DIF expression instead of a bilinear fit. Despite discrepancies between different experimental programs and the recommendations of different researchers, it is clear that there exists an

initial gradual increase in strength with increasing strain rate followed by a sharp increase in strength with increasing strain rate.

The preceding data and recommended DIF relationships are a common method to account for the changing material properties of concrete at higher strain rates, but it is important to consider why these relationships exist before implementing them in design and analysis. Grote et al. [23] demonstrated with Hopkinson bar experiments that inertial effects are the primary reason for the steep secondary slope in the bilinear DIF relationship. Park et al. [24] further established this with numerical simulations that implicitly accounted for inertial effects, the results of which showed that only the initial slope of the bilinear DIF relationship is a material property. Because the inertial effects at high strain rates are generally accounted for in physics-based simulations, only the non-inertial strain rate effects should be considered in concrete constitutive models. For the initial slope of the bilinear DIF relationship, Rossi [25] proposed that the Stefan effect from the free water in concrete is the cause of the strain rate effects. This idea was confirmed by experimental results from Ross et al. [22] and several other research programs which are summarized by Fu et al. [16].

2.2.2 Dynamic Fracture of Brittle Materials

The response of quasi-brittle materials such as concrete to strain rates in the dynamic regime require an understanding of dynamic fracture and fragmentation. For a crack of width a subjected to tension or mode 1 opening, a stress concentration develops at the edge of the crack and a stress relaxation region exists adjacent the crack surfaces. A schematic of the crack and resulting stress distribution is shown in Figure 11.

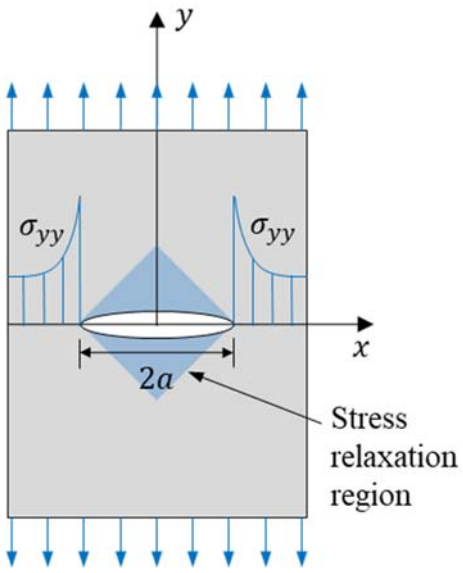

Figure 11: Stress distribution around a crack of width a

At a critical stress concentration, K_{IC}, the crack becomes unstable and the crack propagates. Equation 2.3 shows the expression for K_{IC} in terms of a geometric factor Y and the crack width a.

$$K_{IC} = Y\sigma\sqrt{\pi a} \tag{2.3}$$

The fracture response of a material can also be expressed in terms of energy release rate, G, as shown in Equation 2.4, where F is the external work and U is the internal strain energy resisting crack growth.

$$G = \frac{d}{da}(F - U) = {K_I}^2\left(\frac{1-\nu^2}{E}\right) \tag{2.4}$$

Dynamic fracture has significantly different behaviour from quasi-static fracture, with some distinguishing features including:

1) A limiting velocity of crack propagation exists.
2) Once a crack reaches the critical velocity, it will bifurcate.
3) The fracture toughness of materials can exhibit strain rate dependence.

The limiting velocity is generally accepted as the Rayleigh wave velocity of the material [26]. Broek [27] provides a simplified theoretical prediction of the maximum crack velocity, and Broek's derivation is shown here. The propagating crack shown in Figure 11 causes displacements u and v near the propagating crack. The displacements can be differentiated to result in the following expressions for the velocity field, where c_1 and c_2 are proportionality constants:

$$\dot{u} = c_1 \sigma \dot{a} / E \tag{2.5}$$

$$\dot{v} = c_2 \sigma \dot{a} / E \tag{2.6}$$

The total kinetic energy of the crack as it grows in size from a_c to a can be obtained by integrating the velocity field:

$$E_K = \frac{1}{2} \iint \rho (\dot{u}^2 + \dot{v}^2)\, dxdy = \frac{1}{2} k \rho a^2 \dot{a}^2 \sigma^2 / E^2 \tag{2.7}$$

The kinetic energy can also be expressed in terms of the energy release rate, G, and the crack resistance or energy level required for the crack to grow, R:

$$E_K = \int_{a_c}^{2a_c} (G - R)\, da = \frac{\pi\sigma^2}{E}(a - a_c)^2 \tag{2.8}$$

By equating the two kinetic energy expressions, the crack velocity, $\dot{a}$, is obtained with respect to the longitudinal wave velocity, C_1:

$$\dot{a} = \sqrt{\frac{2\pi}{k}}\sqrt{\frac{E}{\rho}}\left(1 - \frac{a_c}{a}\right) = 0.38C_1\left(1 - \frac{a_c}{a}\right) \tag{2.9}$$

Figure 12(a) shows the displacements u and v caused by the propagating crack, and Figure 12(b) plots the kinetic energy excess that occurs when G becomes larger than R. The normalized crack velocity obtained in Equation 2.9 is plotted against the normalized crack length in Figure 13. The crack velocity initially increases with increasing crack propagation before approaching the limiting crack velocity.

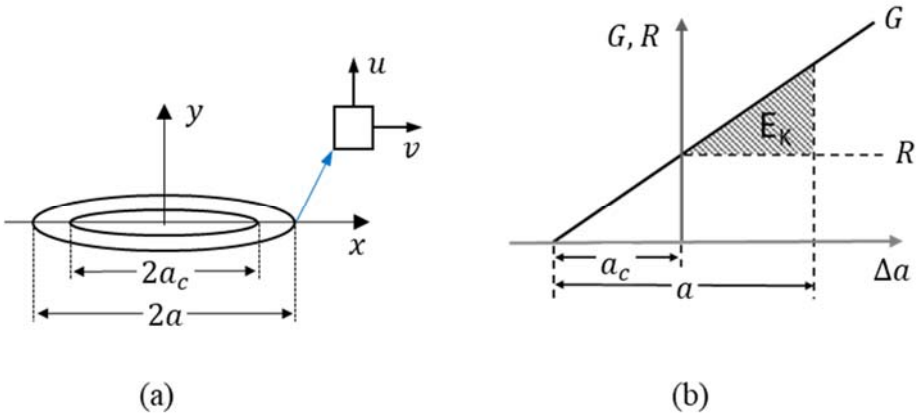

Figure 12: (a) Displacements u and v caused by propagating crack, (b) G, R plots showing kinetic energy excess E_K, during dynamic crack propagation, reproduced from [26]

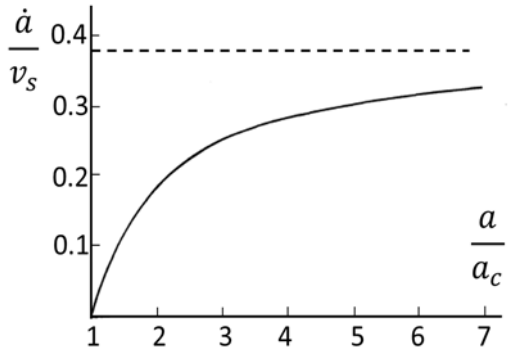

Figure 13: Normalized crack velocity versus normalized crack length, reproduced from [27]

More rigorous analytical solutions by Freund [28] show that the limiting crack velocity is close to the Rayleigh wave velocity. Zhang [15] summarized a large amount of data in the literature concerning the dynamic fragmentation of concrete and rock materials, and found that a constant limiting crack velocity does appear to exist. However, the actual

value for the limiting crack velocity for brittle and quasi-brittle materials is still a subject of ongoing research.

Once the energy release rate G in Equation 2.8 exceeds the crack resistance R, the crack will bifurcate due to the excess available energy. Figure 14**:** shows this mechanism of crack branching. When the crack length reaches a_c, there is sufficient energy for the crack to propagate until it reaches size $2a_c$. At this point, there is enough excess kinetic energy E_k to drive two cracks so the crack bifurcates. If there is sufficient energy in the material, the crack branching can continue indefinitely, leading to fragmentation. This phenomenon explains why concrete tends to fail explosively at high strain rates, as reported by Fu et al. [16].

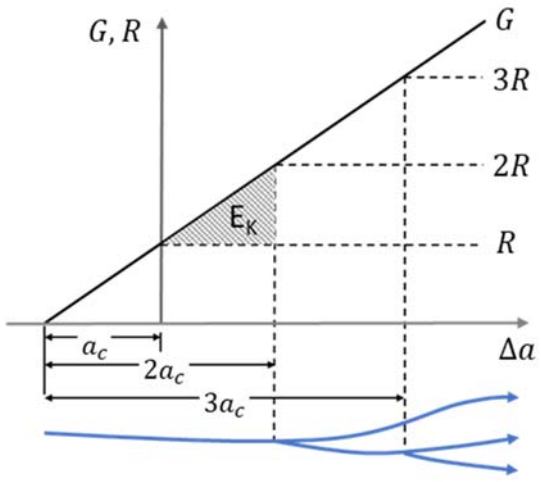

Figure 14: Mechanism of crack branching, reproduced from [26]

For some materials, the fracture toughness appears to be strain rate dependent and it can either increase or decrease with increasing strain rate [26]. The most important factor in determining the response of a material to dynamic fracture is the microstructural

response of the material. For heterogeneous materials such as concrete, the microstructure is quite complex and dynamic loading will interact pre-existing micro-cracks and voids. In addition, because concrete and rock-like materials exhibit quasi-brittle behaviour, the extent of plastic deformation during dynamic fracture may need to be considered to fully explain the strain rate dependence of fracture toughness. For any material that exhibits ductility, the toughness of the material is generally dependent on the shear flow of the material and the plastic deformation around growing voids. Experimental results from Zhang [15] and Grady and Kipp [29] demonstrate that there is a clear trend of strain rate dependence in the fracture stress of rock-like materials. Quantifying the specific mechanisms that cause this strain rate dependence in quasi-brittle materials is a subject of ongoing research.

2.2.3 Shock Response of Materials

Concrete can be subjected to shock waves as a result of blast or impact loading. A shock wave can be depicted as a sharp discontinuity of the material properties behind the shock wave and in front of it, while the shock wave is traveling at a velocity U_s. In the region ahead of the shock wave, the material density is ρ_o, the pressure is P_o, the energy is E_o, and the particle velocity is zero. For the region behind the shock front through which the shock wave has travelled, the material density is ρ, the pressure is P, the energy is E, and the particle velocity is U_p. A schematic of the shock front and the location of these material properties is shown in Figure 15.

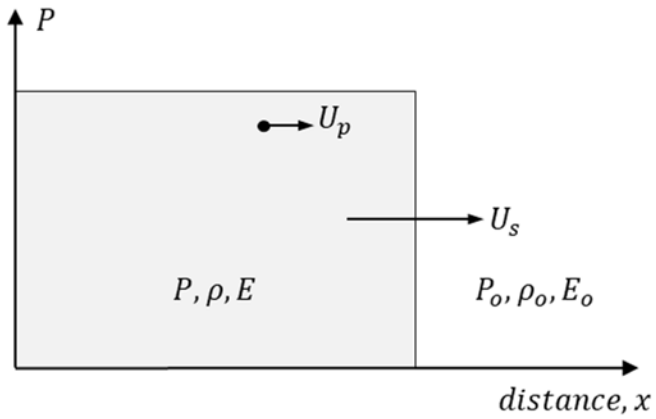

Figure 15: Schematic of a shock front propagating through a material, adapted from [26].

Shock waves require a state of uniaxial strain, which causes the hydrostatic stress to increase beyond the dynamic flow stress of the material. Because of this, the material essentially has no shear strength during shock loading. The shock wave parameters can be calculated from the Rankine-Hugoniot equations for the conservation of mass, momentum, and energy, which are depicted sequentially in the following equations [26]:

$$\rho_o U_s = \rho(U_s - U_p) \tag{2.10}$$

$$(P - P_o) = \rho_o U_s U_p \tag{2.11}$$

$$E - E_o = \frac{1}{2}(P - P_o)(V_o - V) \tag{2.12}$$

The Rankine-Hugoniot conservation equations contain five variables: pressure, particle velocity, shock velocity, specific volume, and density. To form an expression that depends on only two of these five variables, an additional equation is needed. This fourth

equation, which must be experimentally determined, is a polynomial expression that relates U_s and U_p by parameters $C_o,\ S_1,\ S_2,\ S_3$, etc.:

$$U_s = C_o + S_1 U_p + S_2 U_p^2 + S_3 U_p^3 + \cdots \tag{2.13}$$

This equation is known as the equation of state (EOS) for a material, where C_o is the sound speed of the material at zero pressure, and S_1, S_2, S_3, etc. are experimentally determined constants. For most metals, only S_1 is needed to characterize the shock response so the higher-ordered terms reduce to zero. However, for materials that are porous or that undergo phase transformations, higher ordered terms must be included. In this case, a pressure-volume relationship is derived from the conservation of energy. This relationship, which is referred to as the "Hugoniot," is experimentally determined as a locus of all shocked states for a material and is shown in Figure 16. When the pressure is increased in a material due to shock loading, the pressure changes discontinuously from P_o to P along the Rayleigh line instead of along the $P - V/V_o$ path.

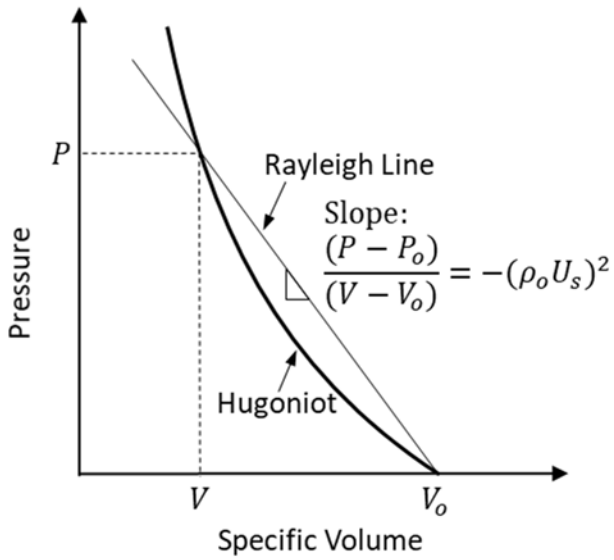

Figure 16: Pressure-volume Hugoniot relationship and Rayleigh line, adapted from [26]

2.3 Previous Studies on the Residual Capacity of Concrete

2.3.1 Full-Scale Structural Residual Capacity Studies

No studies exist in the literature concerning the residual capacity of concrete subjected to impulsive loading at the material level. Previous studies involving impulsive loading have instead focused on the behavior and residual capacity of full-scale reinforced concrete columns and buildings. Roller et al. [30] examined normal strength reinforced concrete columns subjected to close range detonations, and compared the results with concrete columns made of advanced concrete materials and columns with various retrofitting schemes. The residual capacity was determined based on the percentage of axial load carrying capacity of the damaged columns versus the axial compression strength of undamaged columns. Bao and Li [31] developed a finite element model based on experimental studies of reinforced concrete columns subjected to short standoff blast

conditions and performed a parametric study of columns based on various geometries, axial load conditions, and reinforcement ratios. The residual capacity was determined as the mid-height displacement to height ratio. Wu et al. [32] also utilized experimental results of columns subjected to short standoff blast conditions to build a finite element model and conduct a parametric study examining column detailing and blast conditions to determine a residual capacity index based on a normalized column dimension parameter. Kaewunruen et al. [33] conducted drop hammer experiments to investigated the impact strength and residual capacity of railway prestressed concrete sleepers.

Jayasooriya et al. [34] performed a residual capacity analysis of reinforced concrete framed buildings based on the experimental results of a near field explosion on a reinforced concrete frame. This study focused on the stability of the structure based on a finite element analysis, and the extent of damage was examined based on the principal stress time history of selected elements during the blast loading in addition to plastic strain contours in the column cross sections. These damage indicators were used to assess the residual capacity of key structural elements.

While full-scale studies are essential to understanding the behavior of structural elements subjected to impulsive loading, such studies do not necessarily isolate the response of the concrete due to the large-scale nature of the tests and the presence of reinforcing steel. When calibrating a numerical material model to match these tests, it is difficult to ensure that the damage mechanisms are being properly represented without data on the residual capacity of the material. Thus, there is a need to for experimental characterization of concrete at the material level to ensure that the material models are robust enough to correctly predict the residual capacity of full-scale structures.

2.3.2 Materials-Level Residual Capacity Studies

Although the literature lacks studies on the residual capacity of concrete subjected to impact loading, researchers have studied the residual capacity of concrete subjected to other loading conditions such as fire [35, 36], fatigue [37-39], and triaxial compression [40, 41]. While these studies involve non-impulsive load conditions, it is useful to examine the ways in which damage and residual capacity can be quantified. Xiao and Falkner [35] examined high-performance concrete subjected to elevated temperatures and quantified the residual strength with compressive tests and four-point bending tests to create a design curve relating the residual strength to temperature. Li and Franssen [36] tested the residual compressive strength of concrete subjected to heating and cooling phases and examined the effect of different initial compressive strengths and different aggregate types. Li and Franssen found that concrete containing siliceous aggregate had slightly lower residual capacity compared to calcareous aggregates, and that the normalized residual capacity of high strength concrete is much lower than that of normal strength concrete.

Fatigue studies provide some of the most thorough examinations of the degradation of concrete material properties due to applied mechanical loads. The damage that occurs to a concrete specimen during fatigue loading can be quantified through parameters such as total strain, residual strain, stiffness degradation, strength degradation, heat dissipation, crack growth, and through the use of various non-destructive evaluation methods [7]. Isojeh et al. [38] examined concrete cylinders subjected to fatigue in uniaxial compression to improve damage models based on strain evolution during fatigue loading. Damage was quantified at various levels of fatigue based on the degradation of secant modulus and the residual compressive strength. Zhang and Wu [42] studied the fatigue behaviour of

prismatic concrete specimens in bending and tested the post-fatigue residual bending strength. The accumulation of damage was additionally quantified with non-destructive testing via the striking method and resonance method to obtain the Young's modulus, Poisson's ratio, and shear modulus of the damaged specimens. Malek et al. [39] examined the residual capacity of unconfined and glass-fiber reinforced polymer-wrapped concrete cylinders subjected to various levels of low-cycle fatigue. The residual uniaxial compressive strength was quantified and the damage was assessed by measuring the oxygen permeability of damaged specimens to indirectly quantify the degradation occurring in the concrete microstructure.

Chinn and Zimmerman [41] examined the residual uniaxial compressive strength of concrete specimens subjected to hydrostatic triaxial compression. At higher levels of hydrostatic stress, the specimens showed a large amount of permanent axial deformation, decreased stiffness, and decreased residual strength. Roth et al. [40] subjected concrete specimens to triaxial compression stresses below the failure envelope and found a reduction in residual uniaxial compressive strength.

CHAPTER 3. DEVELOPMENT OF AN IMPULSIVE CONCRETE COMPRESSION TESTING SYSTEM

A novel concrete compression test system was designed to experimentally investigate the behavior and progression of damage of concrete materials subjected to impulsive loads. The experiment consists of two main components, (1) the dynamic compression test system, and (2) a system to quasi-statically determine the residual compressive strength of the damaged concrete specimens. The dynamic test system applies an impulsive compressive force to a plain concrete cylinder with the aim of damaging but not fully reducing the capacity of the specimen. The magnitude of the dynamic compressive force can be adjusted to impart varying levels of damage on the cylinder, and the residual capacity of the damaged, yet intact, specimen can be assessed. Two methods of determining the residual capacity of the damaged concrete were utilized in conjunction with the dynamic test system: (1) removing the damaged concrete specimen from the dynamic test setup and determining the residual strength in a servo-hydraulic compression testing machine, and (2) placing a quasi-static actuator in the dynamic testing area to determine the in-situ residual capacity of the damaged specimen. This chapter discusses the design procedure, test concepts, and validation and calibration of the experimental test system.

3.1 Dynamic Test System Concept

The dynamic test system is comprised of four components: a high-speed actuator mounted on a reaction wall, an impact mass, a specimen assembly, and a reaction wall to

anchor the specimen assembly. Figure 17 schematically illustrates the overall design of the testing system. The high-speed actuator, shown on the far left, accelerates an impact mass, or flyer plate, to a constant velocity before impacting the concrete specimen. The specimen assembly, shown on the far right, is designed to only impart compressive loading on the concrete cylinder.

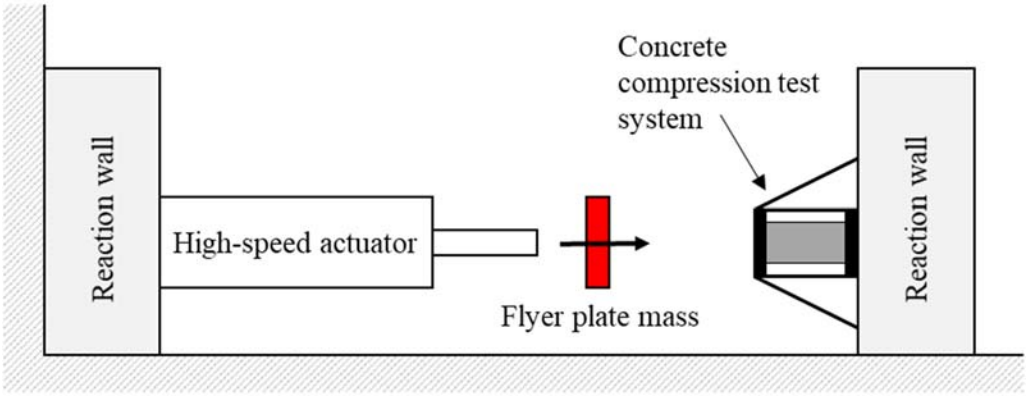

Figure 17: Test system concept for impulsive testing

3.2 Design of Dynamic Concrete Compression Test System

The compression test system was designed with the goal of imparting compression-only impulsive loading on a plain 6-inch by 12-inch concrete cylinder. The design process involved developing an initial design based on engineering judgement, developing a finite element model of the initial design to evaluate the overall performance of the test system, and refining the initial design based on the results of the finite element model.

3.2.1 Initial Design of Test System

Figure 18 shows the initial design of the test system. The concrete test rig is comprised of a frame that supports a 6-inch by 12-inch concrete cylinder secured between

steel endcap plates, which are connected by four high-strength steel rods. On the reaction side, the steel endcap is connected to a stiff reaction wall, and four load cells are located between the reaction endcap plate and the reaction wall. The endcap plate on the impact side moves on a rail system to impart compression loading, while the plate is restrained in the rebound direction by the steel rods. Four load cells are connected to the impact endcap plate to measure the impact forces, and a polycarbonate plate is in front of the load cells. Sanborn and Stewart [43] found polycarbonate to be a suitable loading medium for flyer plate impacts because it reduces the ringing caused by the impact event while providing high strength, stiffness, and impact resistance.

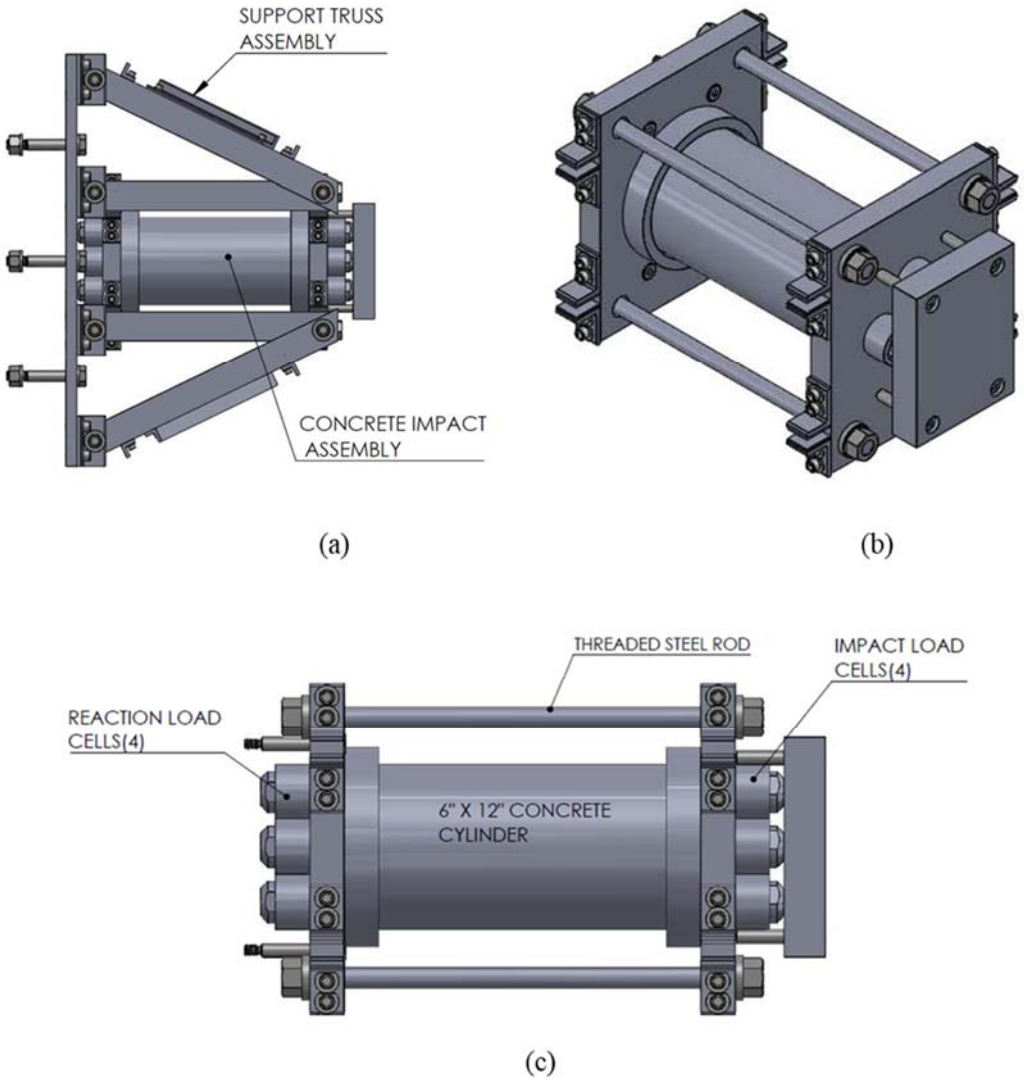

Figure 18: (a) Side view of concrete compression test frame initial design, (b) isometric and (c) side view of concrete cylinder assembly

3.2.2 Finite Element Model of Test System

A finite element model of the compression test setup was developed to evaluate the behavior of the initial design. The finite element analysis was conducted with Sandia National Laboratories computing software SIERRA Solid Mechanics with explicit time integration, and the mesh was generated with Sandia National Laboratories CUBIT

Geometry and Mesh Generation Toolkit [44]. The finite element model was simplified to only consider the concrete loading plate system in the test rig for the purpose of evaluating the overall response of the specimen. In addition, the bolted connections are not detailed, and gravity is not included in the model. The simplified mesh is shown in Figure 19.

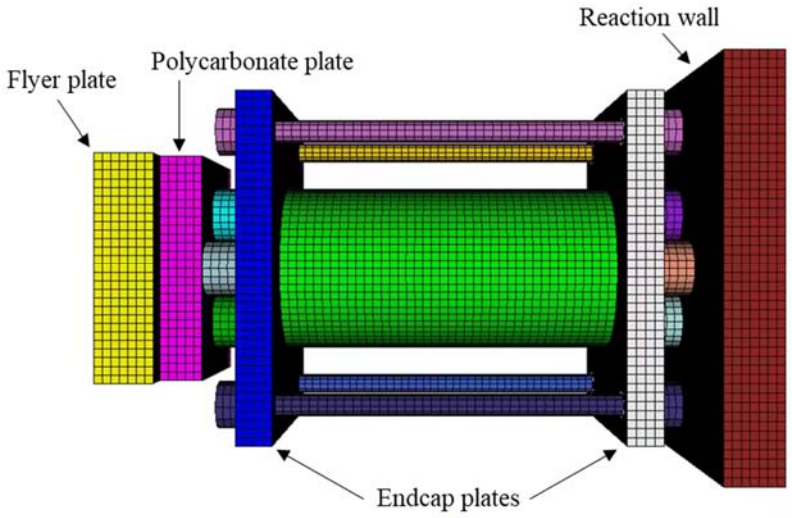

Figure 19: Simplified mesh of concrete compression assembly, initial design

All components are modeled with hexagonal single integration-point elements, with an average element size of 0.3 inches (0.76 cm). An elastic-plastic hardening model was used for all steel components, and the polycarbonate plate was modeled as an elastic-plastic material with parameters obtained from the manufacturer. The concrete is modeled with the Karagozian and Case concrete model, see Chapter 5 for a further description of this model with input parameters. The back surface of the reaction wall is fixed in space. The load cell surfaces are tied to the endcap plates, polycarbonate plate, and reaction wall. Frictionless contact is assumed between the rods and endcap plate surfaces and between

the flyer plate mass and polycarbonate plate. The coefficient of friction between the concrete and endcap surfaces is assumed to be 0.5.

Figure 20 shows a typical force-time history measured from the concrete specimen contact surfaces during a 49 ft/s (15 m/s) impact event. This force-time history shows that some ringing occurs between 2-4 milliseconds after the flyer plate impact due to the reverberations of the endcaps and the cylinder within the test frame. Figure 21 shows the force-time history measured from the load cell contact surfaces. Because the load cells in the simplified model use tied contact conditions, a large amount of ringing is artificially present in the force-time history after the flyer plate impact. However, it is clear from the impulse-time history that the load cells do not measure the reverberations of the specimen between 2-4 milliseconds due to their location on the outside of the endcap plates.

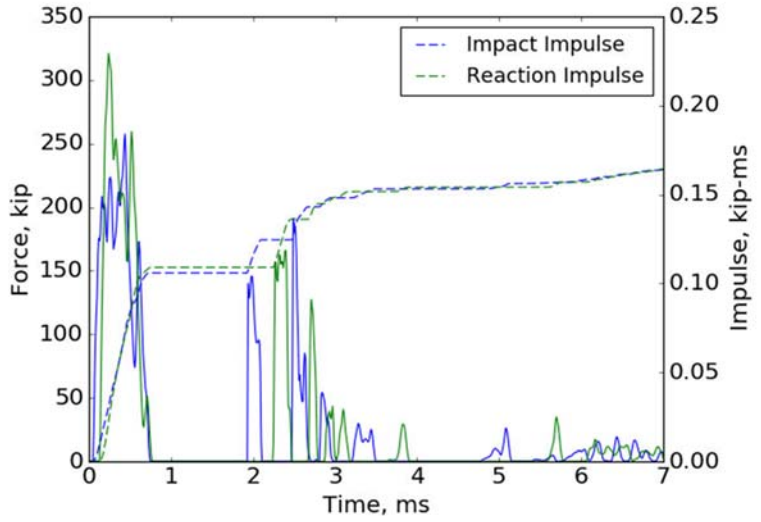

Figure 20: Force and impulse time history measured from concrete cylinder surfaces during a 49 ft/s (15 m/s) impact

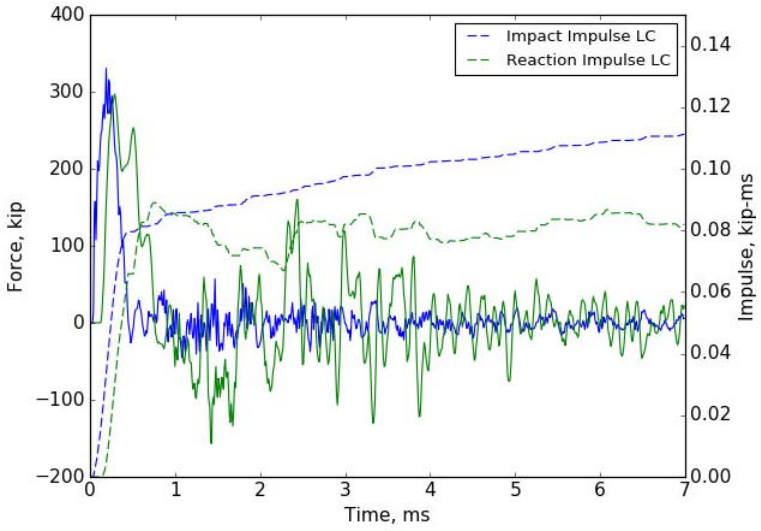

Figure 21: Force and impulse time history measured from load cell surfaces during a 49 ft/s (15 m/s) impact

3.2.3 Final Design of Concrete Compression Test Frame

An evaluation of the initial finite element model resulted in several design changes to the concrete compression test system. The load cells were repositioned to the inside of the endcap plates to ensure that any post-impact oscillations of the concrete specimen are measured during testing. An additional set of inner endcaps were added to the test frame between the load cells and the specimen. The polycarbonate plate and the flyer plate geometries were changed to increase the area over which the impulsive force is applied to the large endcap. In addition, the mass of the flyer plate was reduced from 38 lb. (17.2 kg) to 30 lb. (13.6 kg) to reduce the amount of force in the load cells. Finally, the diameter of the steel rods was increased from 0.75 inches (1.9 cm) to 1.25 inches (3.2 cm) to reduce the magnitude of the post-impact oscillations. Figure 22 shows the final design of the concrete compression test frame, and Figure 23 shows the simplified mesh for concrete compression assembly. Detailed drawings for the final design may be found in Appendix B.

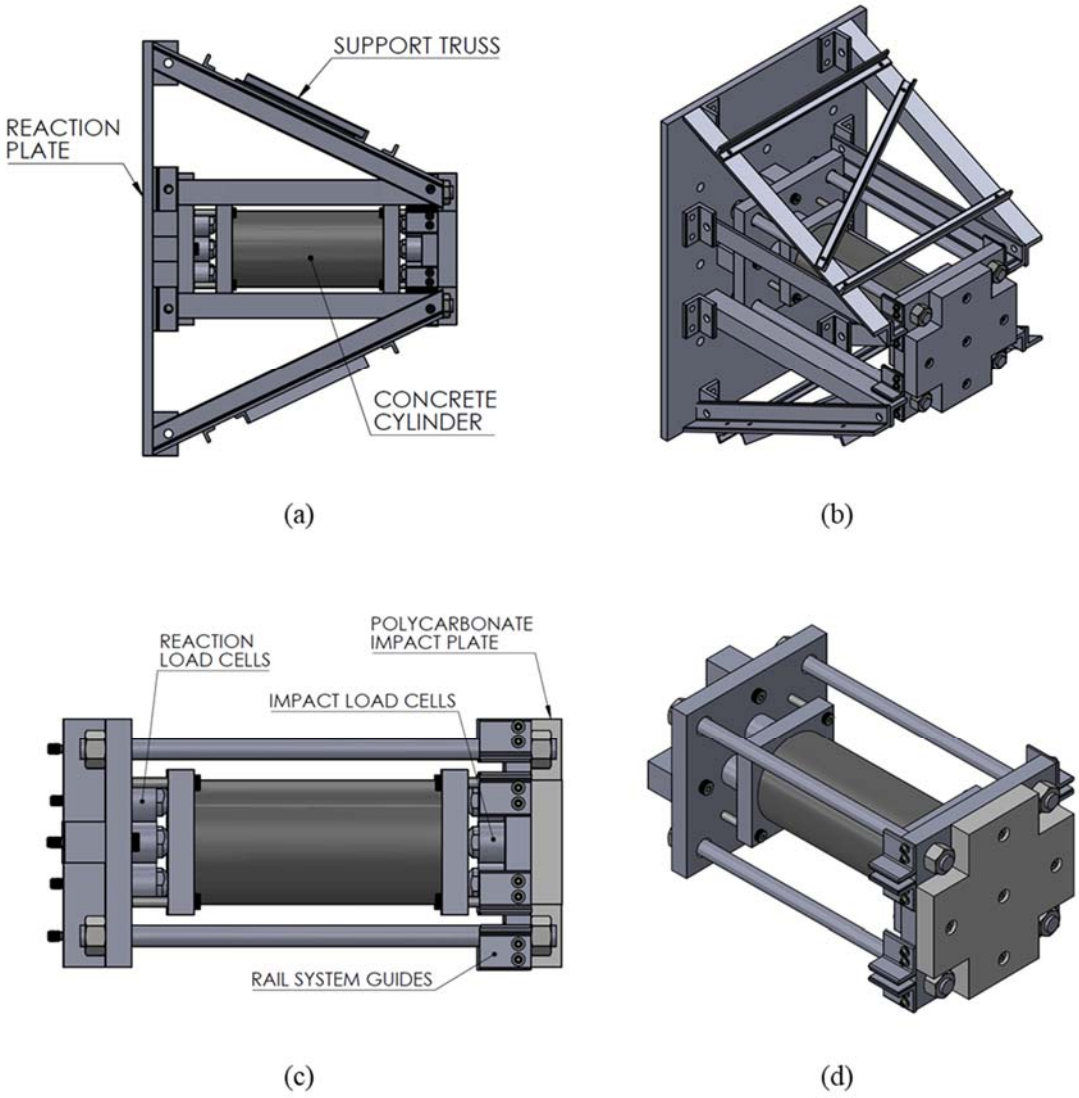

Figure 22: (a) Side view and (b) isometric view of compression test frame, (c) side view and (d) isometric view of concrete assembly

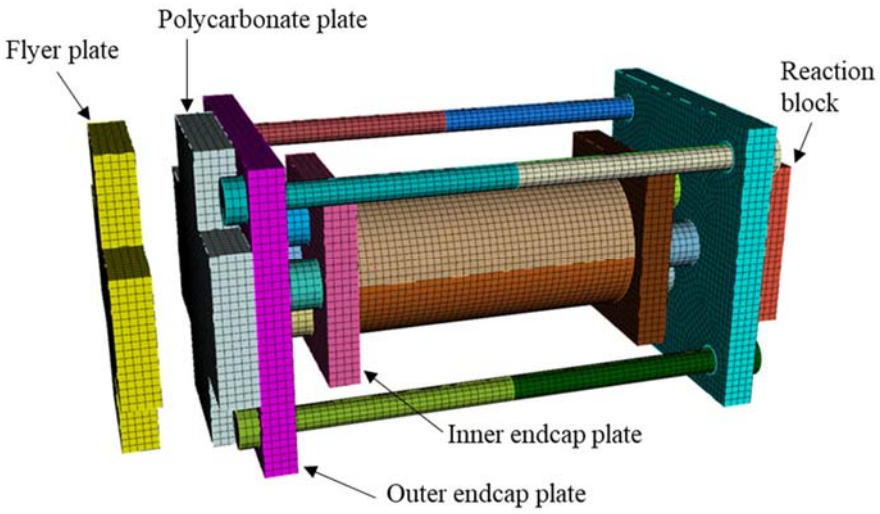

Figure 23: Simplified mesh of concrete compression assembly, final design

To evaluate the final design, the force and impulse time history measured on the cylinder surfaces and the load cell surfaces was evaluate for a 33 ft/s (15 m/s) impact. Figure 24 shows the force and impulse time history from the concrete surfaces, and Figure 25 shows the measured force and impact from the load cells. The load cells are now able to measure the post-impact reverberations of the specimen, as the impulse measured from the load cells now matches the impulse measured directly from the cylinder. The increased ringing in the load cell measurements is due to the fixed contact surfaces of the load cells in the simplified mesh, which is not representative of the real boundary conditions and will likely not be present in the experimental data.

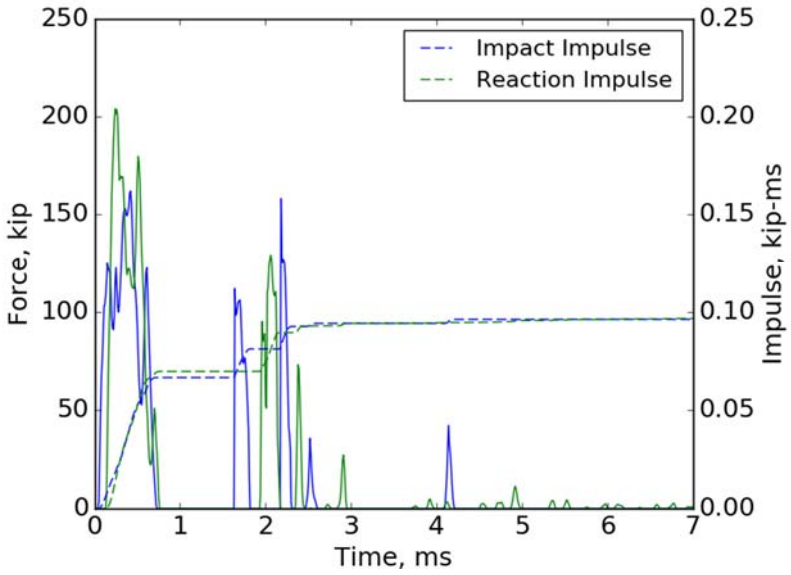

Figure 24: Force and impulse time history measured from concrete cylinder surfaces during a 33 ft/s (10 m/s) impact

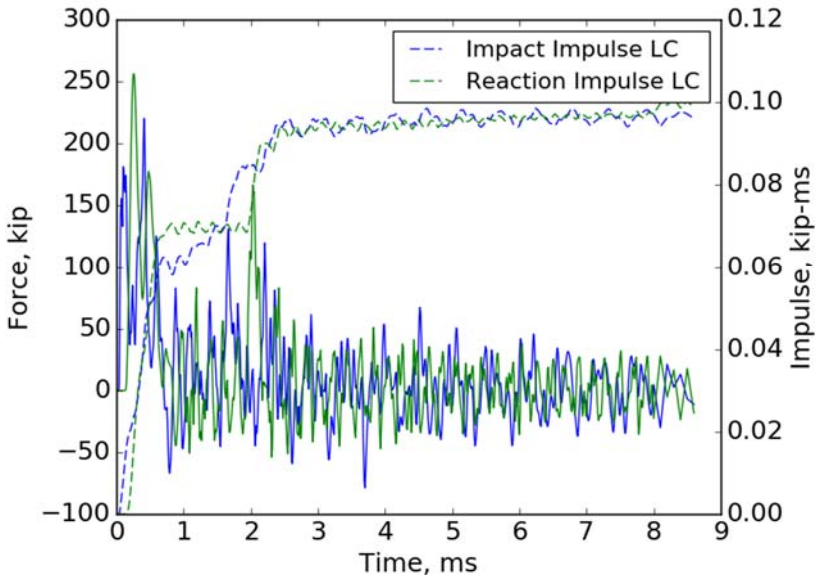

Figure 25: Force and impulse time history measured from load cell surfaces during a 33 ft/s (10 m/s) impact

3.2.4 Flyer Plate Mass Design

The flyer plate mass was designed based on previous research conducted by Sanborn and Stewart [43, 45], who also utilized the Georgia Tech blast generator system to launch an impact mass to impart impulsive loads on an experimental assembly. The flyer plate, shown in Figure 26, is supported by a rail system connected to the high speed actuator. The flyer plate was designed to weigh 33 lbm in total, based on the results of the finite element model of the test system. The mass is supported on the rail system by a set of steel hollow tube wings and c-channel connections. The c-channel connections keep the flyer plate level and prevent it from rotating as is it is pushed forward by the high speed actuator. A 1.25 inch (3.2 cm) thick neoprene bumper plate is located on the back of the flyer mass to ensure that the plate remains flush with the blast generator pusher plate. A programmer material is placed on front of the flyer plate to control the shape of the force-time history as the mass impacts the test system. The use of different programmer materials to achieve blast-like loading with the BG-25 system was explored by Stewart et al. [46] and Friedenberg et al. [47]. Sanborn and Stewart [43] conducted a study evaluating different programmer materials for flyer plates and found that a felt programmer provided the desired near-instantaneous rise in the force time history that is representative of a blast loading. Based on these results, a felt programmer was selected for the flyer mass for the dynamic concrete compressive test system.

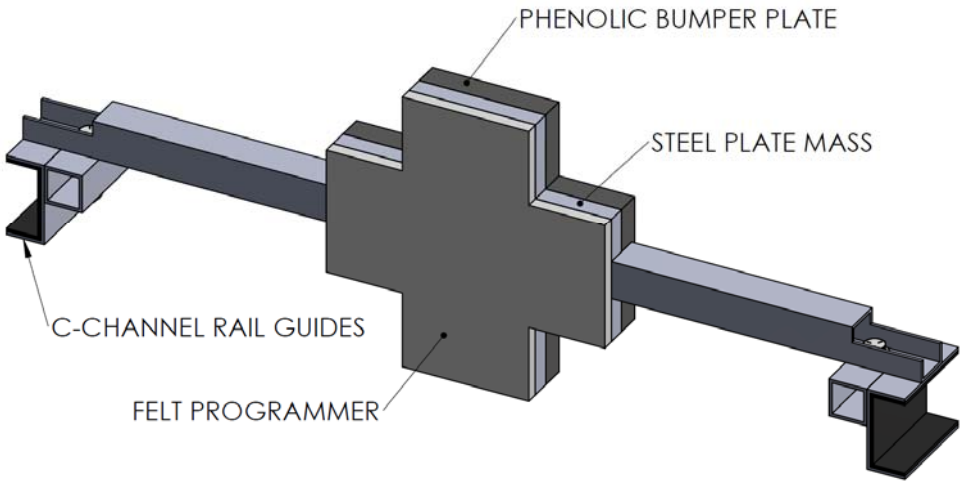

Figure 26: Flyer plate mass assembly

3.3 Dynamic Test System Experimental Setup

3.3.1 Configuration of Testing Area and High-Speed Actuator

The testing area and high-speed actuator used in this study is located in the Structural Engineering and Materials Laboratory at the Georgia Institute of Technology. Detailed information about the configuration of the high-speed actuator testing facilities in this laboratory can be found in [48]. The testing area, as shown in Figure 29, is surrounded by impact-resistant polycarbonate safety walls. Prior to every dynamic test, the laboratory area is cleared of personnel and the test operators control the hydraulic system remotely behind the polycarbonate safety walls. The lab is equipped with CCTV security cameras as well as an announcement system to alert lab personnel prior to a dynamic test. The laboratory has a 6-foot thick strong floor as well as reaction walls with an embedded grid of DYWIDAG bars, which permit the construction and anchoring of modular reaction walls used in this study.

The impulsive loading used in this experiment is generated by an ultra-fast hydraulic actuator manufactured by MTS, termed Blast Generator (BG). The BG model in the Georgia Tech Structural Engineering and Materials Laboratory is a BG-25 model, which can accelerate a 110 lbm (50 kg) impact mass up to 112 ft/s (34 m/s). A detailed description of the hydraulic system is provided in Gram et al. [49], and the use of the hydraulic system to replicate blast loading is demonstrated in Stewart et al. [50] and Friedenberg et al. [47].

For this study, the high speed actuator is used to accelerate a flyer plate mass towards the experimental assembly. The high speed actuator is mounted to a modular reaction wall and frame and rail system in the testing area, as shown in Figure 29. The frame and rail system supports the actuator and keeps the piston and impact mass level during linear motion. Prior to a dynamic test, the flyer plate mass is placed on the rail system and is pushed back to contact a pusher plate that is connected to the end of the actuator piston. Once the test begins, the hydraulic system drives the piston rod and thus the flyer plate mass forward. Once the mass has achieved a target velocity, the actuator decelerates the piston rod and pusher plate while the flyer plate continues to travel forward on the rail system at the target velocity. After impacting the experimental assembly, the flyer plate rebounds and falls to the laboratory floor, which is protected by a layer of sandbags. By controlling the inputs to the hydraulic system, the impact velocity of the flyer plate can be tailored to meet the test requirements.

3.3.2 Fabrication and Installation of Dynamic Compression Test System Frame

The components of the dynamic compression test system frame described in section 3.2 were fabricated at the machine shop of the School of Civil and Environmental

Engineering at Georgia Tech. The steel plates and the polycarbonate impact plate were cut and drilled by a water jet, and the bolt holes were drilled to the specified tolerance with a drill press, as shown in Figure 27 (a). The angle components were cut and drilled as specified, and the truss frame was then assembled prior to being installed in the testing area (Figure 27 (b) and (c)). The truss frame was then bolted to a 3-inch thick steel reaction wall which is anchored to a modular concrete reaction wall in the testing area. Figure 28 (a) shows the installed test rig with a concrete cylinder, and Figure 28 (b) shows the test rig with the flyer plate installed. The overall configuration of the testing area with the modular reaction walls, BG-25, BG-25 frame and rail system, and compression test system are shown in Figure 29.

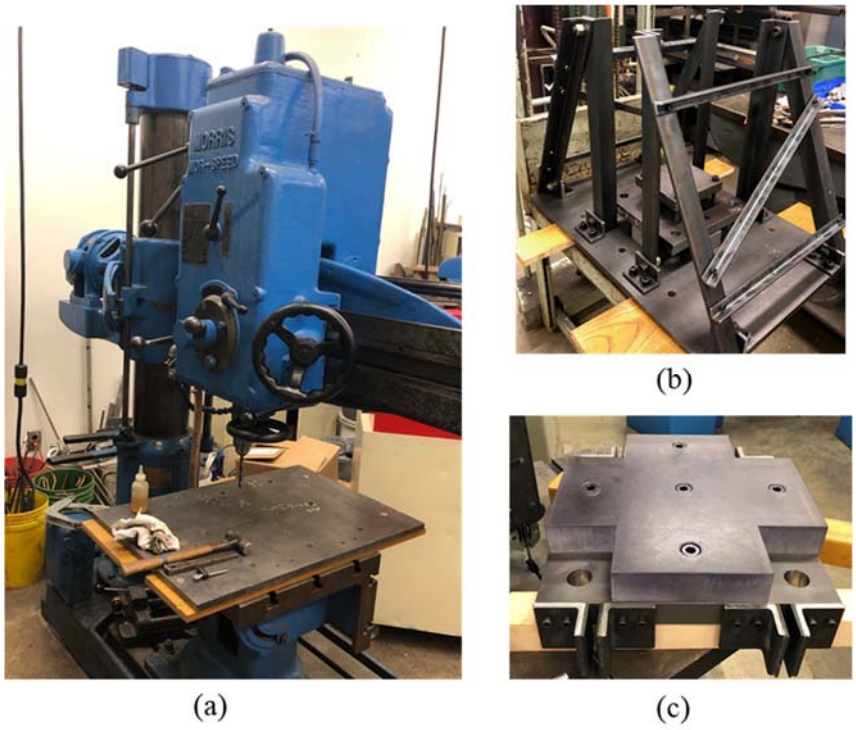

Figure 27: (a) Fabrication of the steel plates, (b) assembled truss frame and (c) front impact plate

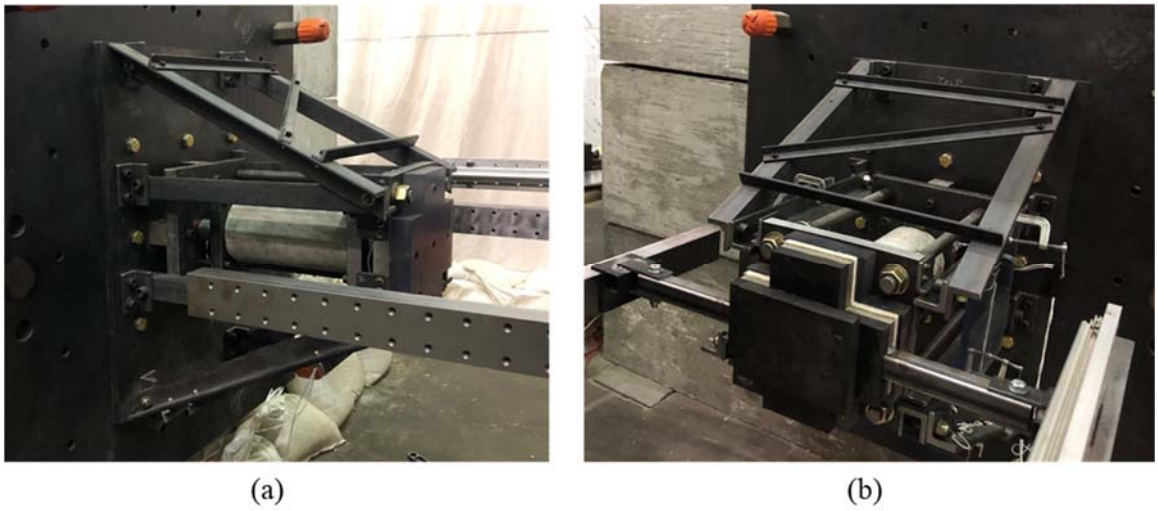

Figure 28: (a) Side view of concrete compression test rig installed in testing area, (b) front view with flyer plate

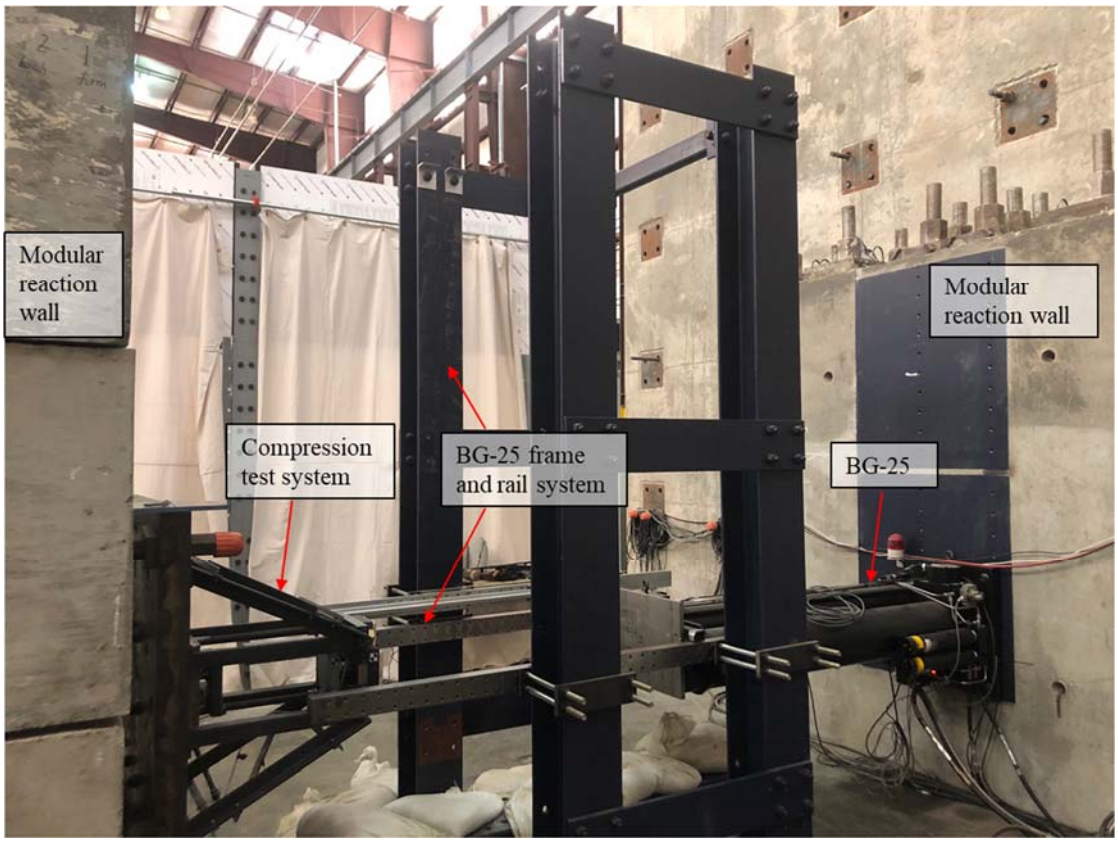

Figure 29: Overall configuration of test area

3.3.3 *Instrumentation of Dynamic Test System*

Displacement during the dynamic event is measured with two high speed camera systems. A Phantom Miro C110 high speed camera capable of recording at 1,200 frames per second at a resolution of 1280 x 800 is used to observe the movement of the test frame, concrete cylinder, and flyer plate. Custom targets are placed on the concrete cylinder to obtain axial strain measurements and on the impact and reaction plates to observe the global movement of the test system. The position time history of the flyer plate is also recorded with custom targets. The targets are analyzed with using Xcitex's ProAnalyst

software package [51]. The Phantom Miro M310 high speed camera is capable of recording up to 3,200 frames per second at a resolution of 1280 x 800. During the dynamic test, the cameras are controlled with the Phantom Camera Control v2.8 application [52].

The force-time history of the dynamic event is measured with eight Dytran 1061V6 piezoelectric force sensors. The force sensor is capable of measuring a maximum compressive force of 50 kips (222 kN) and a maximum tension force of 10 kips (44 kN). A Dytran 6217 impact cap is connected to each load cell to protect the load bearing surface from damage. Four of the load cells measure the force from the flyer plate impact, and the remaining four measure the reaction force on the other side of the concrete cylinder. The load cells are connected to the large endcap plates in the concrete test rig with threaded mounting studs, and the load bearing surface of each load cell are in contact with the inner endcaps that restrain the concrete cylinder. The signals from the load cells are recorded with a Synergy P Hi-Techniques data acquisition (DAQ) system, which supports up to 16 channels. Each channel can record up to 2 million sweeps per second and is equipped with a 200-kHz analogue filter.

3.3.4 *Dynamic Test Procedure*

The test procedure for conducting dynamic concrete compressive testing is as follows:

1. Place the prepared concrete specimen in the dynamic compressive test system; cover the specimen with moistened burlap. Ensure that the truss angles, rail guides, and impact endcap plate are level with the blast generator system. Apply synthetic grease to the appropriate contact surfaces.

2. Install the flyer plate mass, center it with respect to the concrete test frame, and tighten the C-channel bolts.
3. Conduct the blast generator safety protocols, inspections, and warmup sequence [53].
4. Move the flyer plate mass to contact the blast generator pusher plate; ensure that the bumper plate is flush with the plate. Loosen C-channel bolts and verify alignment with the blast generator rail system. Remove the burlap from the concrete specimen and adhere motion tracking targets.
5. Verify instrumentation settings and test trigger sequence.
6. Execute the blast generator firing sequence [53].

3.3.5 Validation of Dynamic Test System and Capability for Repeated Impacts

Validation tests were conducted to test the instrumentation of the test setup and ensure that consistent and repeatable impacts are possible. Initial validation testing was conducted with a 6 inch x 12 inch aluminum cylinder instead of concrete specimens to eliminate uncertainties that may arise in the test data due to the inelastic behavior of concrete. Figure 30 shows the force time history for two validation tests conducted with the same input parameters of at a test velocity of 16 ft/s (5 m/s) and a flyer plate mass of 33 lbm. Figure 31 shows the force time history recorded in the load cells.

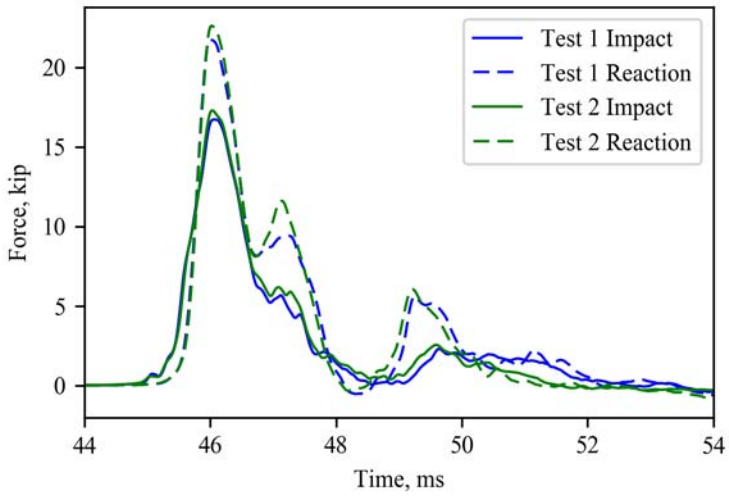

Figure 30: Force time history for 16 ft/s aluminum validation tests

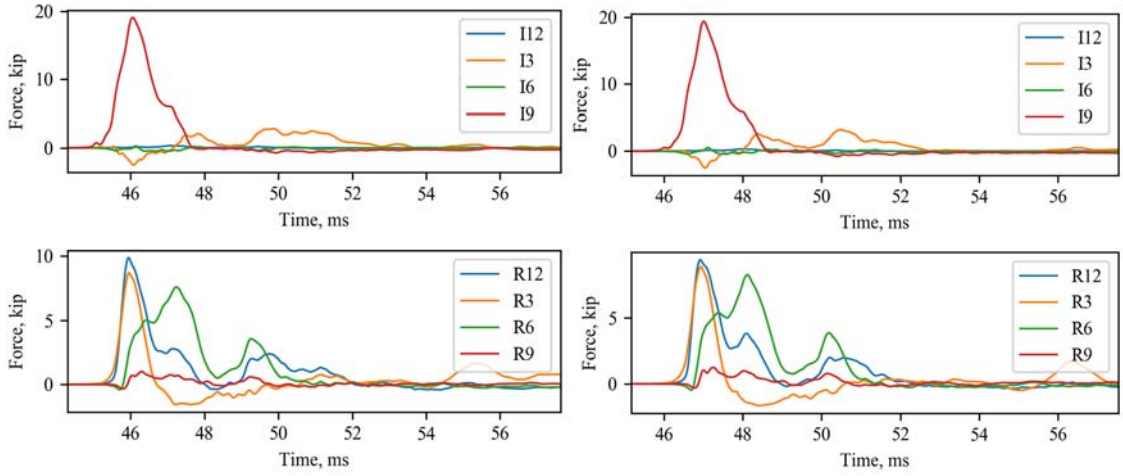

Figure 31: Force time history for 16 ft/s test 1 impact (top left) and reaction (bottom left) load cells, and test 2 impact (top right) and reaction (bottom right) load cells

These data demonstrate the repeatability of the test system, as both tests conducted with the same input parameters produced the same force-time history to the specimen. The force-time history in the impact side was largely collected from one load cell and showed

an overall smooth rise and fall in force. On the reaction side, the majority of the force-time history was collected by three load cells, which appeared to record the force at later times in the loading resulting in two force peaks on the reaction side. This behavior is likely due to the aluminum cylinder not being perfectly level with the reaction plate. However, due to the demonstrated repeatability of the test system, these results were deemed acceptable and testing was then conducted with concrete specimens.

Two tests were conducted at the same test parameters of an impact velocity of 33 ft/s (10m/s) with a flyer plate mass of 33 lbm, and are used to demonstrate the repeatability of the dynamic test system with concrete specimens. The force-time and impulse-time history for both test is shown in

Figure 32, and the load cell force-time history is show in Figure 33. The shape of the force-time history is representative of the test data resulting from tests conducted with concrete specimens, as the main pulse is much smoother than observed in the tests conducted on the aluminum specimen. This is likely due to improved leveling of the concrete specimens and due to the decreased stiffness of the concrete as compared to aluminum, which may help distribute the load across the load cells more evenly and reduce reverberations even if the specimen is not perfectly flush with the endcap plates. Figure 33 shows the force time history of the load cells for both tests. Compared to the aluminum tests, the load cell force-time history is much more smooth and the four load cells record the impact and reaction forces fairly evenly. This improved agreement in load cell time-history was observed as the test velocity increased. This is likely due to how the load cells are installed. The load cells are sandwiched between two A36 steel plates that and are not guaranteed to be perfectly flush to the plates, so any eccentricity in the installation is more

likely to result in varying load cell readings at lower test velocities. This behavior is deemed insignificant in the overall test system performance and the sum of the force-time history is considered to be the more important diagnostic.

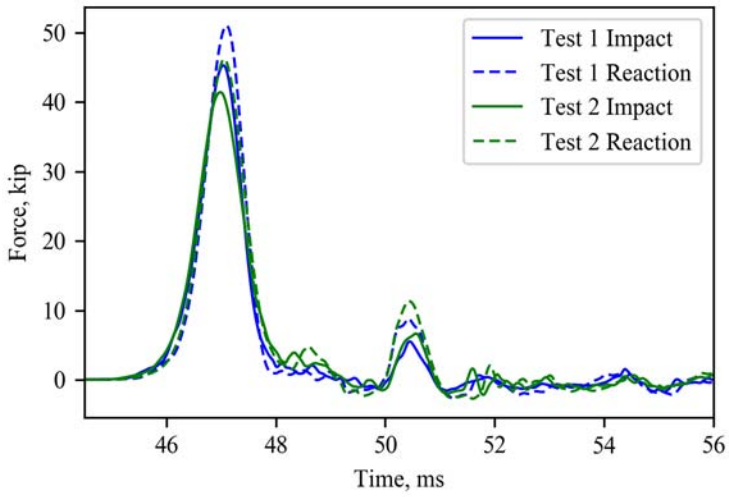

Figure 32: Force time history for 33 ft/s concrete validation tests

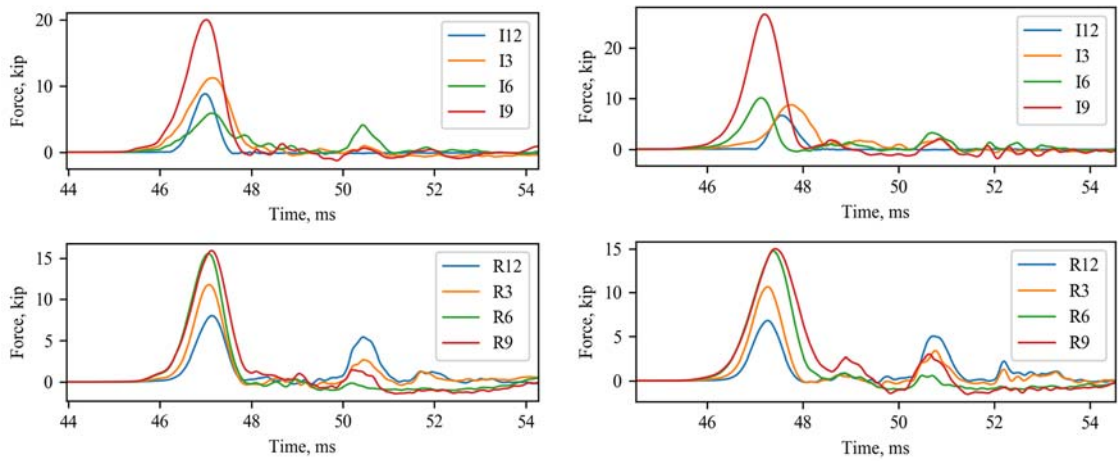

Figure 33: Force time history for 33 ft/s test 1 impact (top left) and reaction (bottom left) load cells, and test 2 impact (top right) and reaction (bottom right) load cells

Two additional concrete tests were conducted with repeated test parameters and can also be used to demonstrate the repeatability of the dynamic test system.

Figure 34 shows the force-time history of a test conducted on a concrete specimen at a test velocity of 56 ft/s (17 m/s) and a flyer plate mass of 44 lbm, and

Figure 35 shows the force-time history of the load cells for each test. For this test, the force-time histories match well, and the difference in shape for the force pulse is due to the concrete becoming damaged during this test, which affected the descending slope of the force-time history.

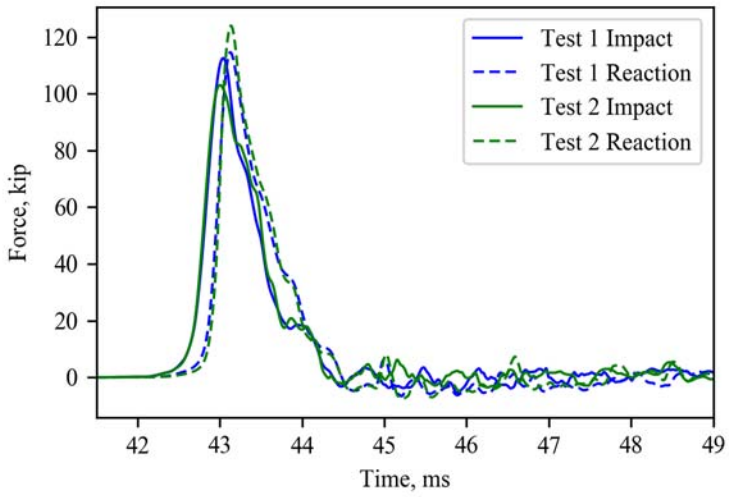

Figure 34: Force time history for 56 ft/s concrete validation tests

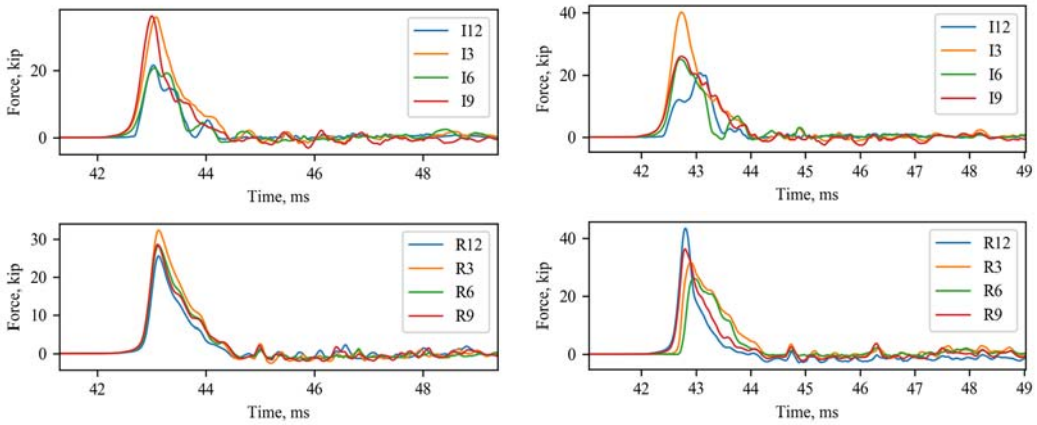

Figure 35: Force time history for 56 ft/s test 1 impact (top left) and reaction (bottom left) load cells, and test 2 impact (top right) and reaction (bottom right) load cells

One notable difference in the repeated tests with concrete specimens versus the aluminum specimen is that the second tests performed on the concrete specimens showed slightly lower impact and reaction forces, while this did not occur in the tests with the aluminum specimen. For the aluminum tests, the specimen did not have to be reset or

adjusted in any way between tests, so the actuator was fired twice in a short time period. After each concrete test, however, residual capacity testing is performed and a longer time period elapses between tests, so the hydraulic system must be warmed up again prior to performing the second test. Even though the exact same inputs are provided to the control system, the hydraulic pressure for the second concrete tests was slightly lower that the first test performed on the same day, which resulted in the flyer plate velocity to be slightly lower and thus the impact and reaction forces are slightly lower. This minor difference does not have a negative impact on the test system performance for this experimental test series because the parameter of interest is the actual impact and reaction forces for each test rather than the target velocity of the flyer plate. However, this points towards an additional capability in the developed test system for subjecting specimens to repeated impacts. If the specimen does not need to be reset, which could be the case for repeated impacts of concrete specimens or other materials, multiple and nearly identical impulses can be applied to the specimen in a short time period, with the only required step between each firing being to reset the flyer plate.

3.3.6 Selection of Programmer Material and Modified Flyer Plate Design

As the test velocity was incrementally increased, a second peak in the descending portion of the force time history was observed at a test velocity of 38 ft/s (11.5 m/s). Examination of the high speed camera footage of the experiment showed that the flyer plate was level upon impact of the experimental assembly and it did not interact with or rebound off of the actuator pusher plate to cause the second peak. Based on previous researchers investigations on programmer materials for flyer plates [43], it was believed that this second peak was due to the nonlinear behaviour of the felt programmer used in the test.

The felt programmer layer was then doubled from a thickness of 0.5 inches to 1.0 inches, which successfully eliminated the double peak in the force-time history for this test case and for all subsequent testing velocities. The results for these tests, all at a constant test velocity of 38 ft/s (11.5 m/s) are shown in Figure 36. The sensitivity of the force-time history to the choice in programmer points to the potential capability for pulse shaping in this experimental method, as different programmer configurations could be used to target a specific pulse shape.

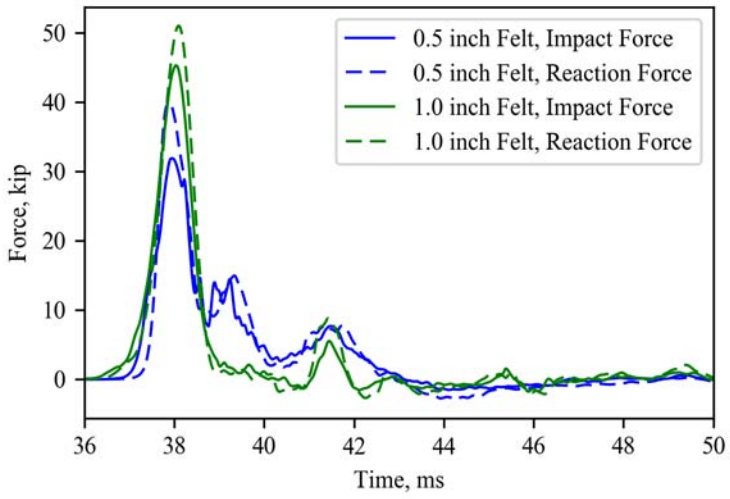

Figure 36: Force time history for 0.5-inch and 1.0-inch felt programmers

An additional issue with the original flyer plate design occurred as the testing velocity was incrementally increased during testing, as the rail guide wings on the flyer plate began to bend and fracture during tests at velocities higher than 38 ft/sec (11.5 m/s). The wings and c-channel guides shown previously in Figure 26 still have forward momentum after the mass impacts the experimental assembly, and the energy to stop their forward travel is absorbed by their connection to the mass plate. The welded connection

did not provide sufficient plasticity to absorb this energy as it proved too brittle to survive repeated testing. The damage sustained in the welds required the flyer plate to be repaired after every dynamic test and became the limiting factor in how quickly tests could be performed. To eliminate this problem, a new flyer plate was designed to incorporate a rail guide connector as a sacrificial connection that is allowed to deform plastically to stop the forward momentum of the rail guide wings. This design is shown in Figure 37. The cruciform shape used in the previous flyer plate design was changed to a rectangular shape so that the flyer plate mass thickness could be increased to allow space for a bolted connection to the flyer plate wings. The slight increase in mass of this flyer plate design, at 44 lbm, provides the added benefit of being able to test at slightly lower testing velocities to reduce the damage sustained by the sacrificial components of this flyer plate.

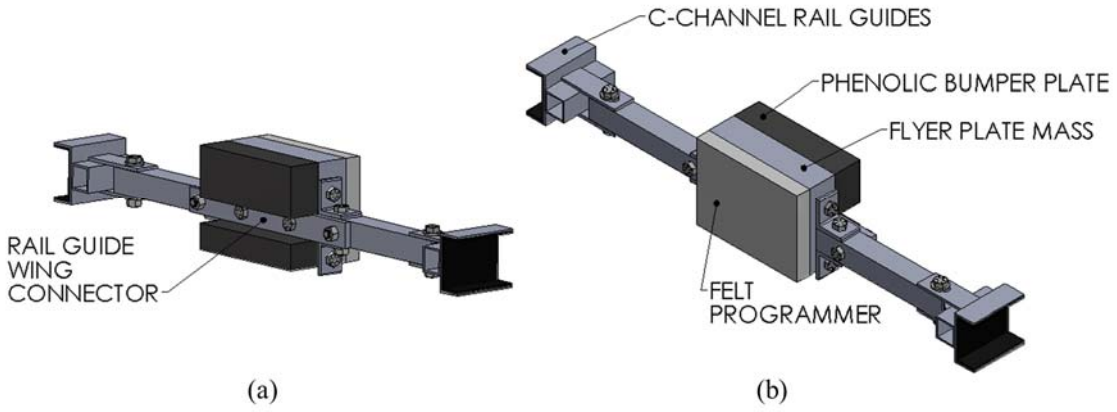

Figure 37: Final flyer plate design (a) back view and (b) front view

3.4 Residual Capacity Testing with a Compression Testing Machine

Two different methods were utilized to determine the quasi-static residual capacity of concrete specimens subjected to impulsive loads. The first method involves removing

the damaged concrete specimen from the dynamic compression test system and placing the specimen in a servo-hydraulic compression frame to determine the residual compressive strength in accordance with the ASTM C39 standard for determining the compressive strength of cylindrical concrete specimens [3]. The second method involves installing a quasi-static actuator in the dynamic testing area to determine the in-situ residual capacity of the damaged specimen. The use of a servo-hydraulic compression testing machine is discussed in this section.

3.4.1 Test Procedure for Determining Residual Capacity

The first method for determining the residual capacity consists of carefully removing the damaged concrete specimen from the dynamic compression test frame placing it in a static servo-hydraulic SATEC compression frame. Compression testing is conducted in accordance with the ASTM C39 standard compressive test method for determining the compressive strength of cylindrical concrete specimens [3]. The cylinder is placed between two steel endcap plates and is subjected to a load rate of 60 kips per minute. The testing is completed after the maximum load is recorded and as the load rate cannot be maintained due to the specimen failing. To compare the residual capacity result to an undamaged sample, a specimen from the same concrete batch is then immediately tested to determine the compressive strength for an undamaged representative sample.

3.4.2 Validation of Test Method

Figure 38 shows the force versus displacement curves for a specimen subjected to a 47 ft/s (14 m/s) impact with a 44 lbm flyer plate, as well as three undamaged specimens from the same concrete batch. Compared to the baseline tests, there is a slight reduction in

strength for the specimen subjected to the impulsive load. Three baseline tests were conducted for this test case to evaluate the overall precision of the compressive tests and acceptability of the mix design. According to ASTM C39, the acceptable range of individual cylinder strengths from a well-mixed sample of concrete made under laboratory conditions is 7.8% for tests performed by a single operator. The range of concrete strengths for the three baseline tests in this test case is 1.9%, so the concrete mix design and method for determining the compressive strength is deemed acceptable. Because the range in baseline strength test results is so low, only one baseline strength test is performed to accompany each future residual capacity test.

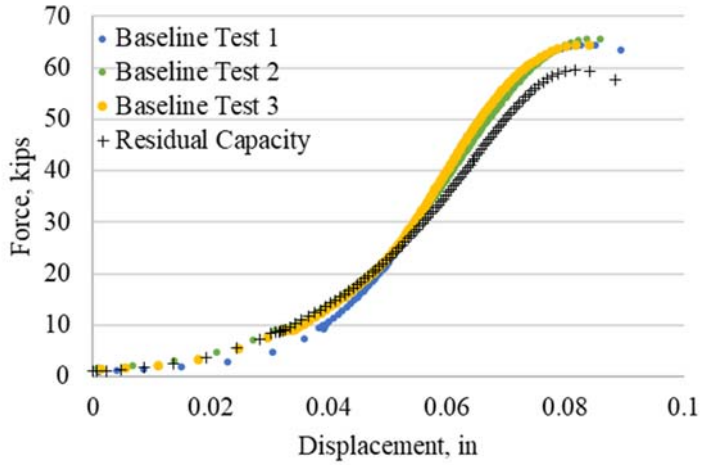

Figure 38: Force versus displacement curve for the residual capacity of a concrete specimen subjected to a 47 ft/s impact and three undamaged specimens

Figure 39 shows the force versus displacement curves for a specimen subjected to a 59 ft/s (18 m/s) impact with a 44 lbm flyer plate and one undamaged specimen from the same concrete batch. With the increase in test velocity there is a greater reduction in

strength compared to the previous 47 ft/s test. An initial concern with this test method was that with increasing levels of applied impulsive force, the removal of the damaged concrete specimen could affect the residual capacity result or the specimen could not be able to be tested for residual capacity once removed because it may not remain intact. However, this proved to not be a problem as careful removal of the specimen from the dynamic test setup was possible and the residual capacity test clearly captured the reduction in strength and stiffness in the damaged specimen.

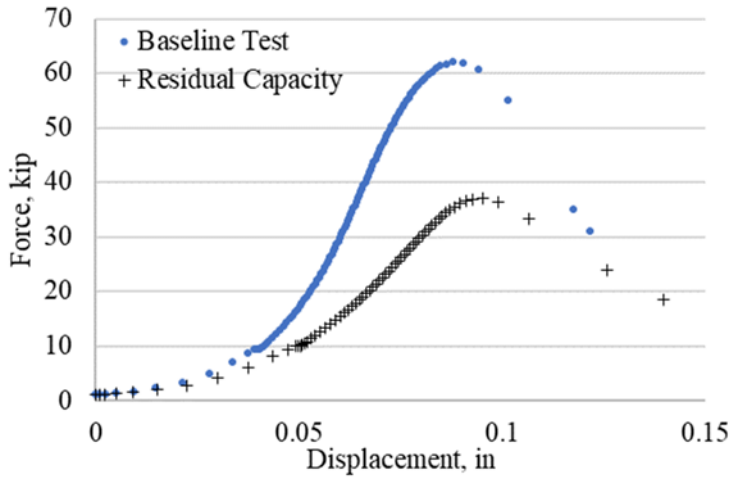

Figure 39: Force versus displacement curves for the residual capacity of a concrete specimen subjected to a 59 ft/s impact and one undamaged specimen

3.4.3 *Determination of Full Force-Displacement Curves*

In typical compression tests on concrete specimens, determining the descending branch of the force versus displacement curve is not possible. In most tests, the stored strain energy in the compression machine is released once the specimen reaches its maximum load and it fails very quickly under the applied load rate so very few data points can be collected to represent the descending branch. For this experimental program, determining

the descending branch is of interest to evaluate the strain energy density of the damaged versus undamaged specimens.

The quasi-static test procedure used with the SATEC compression machine involves stopping the test once the maximum load is achieved and when the applied load rate can no longer be sustained. At this time, the specimen is unloaded and the compression machine returns to its original position. As this occurs, several data points past the maximum load are collected, but because the hydraulic controls of the compression machine help restrain the release of its strain energy, the specimens prepared for this experimental study generally remained intact after unloading. Because of this, the damaged specimen could be reloaded by the compression machine to determine a new maximum force, and after the specimens fail a second time several data points past this second maximum load are collected. This process can be repeated as long as the specimen remains intact, and the descending branch of the force versus displacement curve can be determined by connecting the data points that are collected past the recorded maximum load.

Figure 40 shows the full force-displacement curves obtained for a specimen subjected to a 59 ft/s (18 m/s) impact with a 44 lbm flyer plate and one undamaged specimen from the same concrete batch. For this test case, each specimen remained intact enough to be loaded three times quasi-statically.

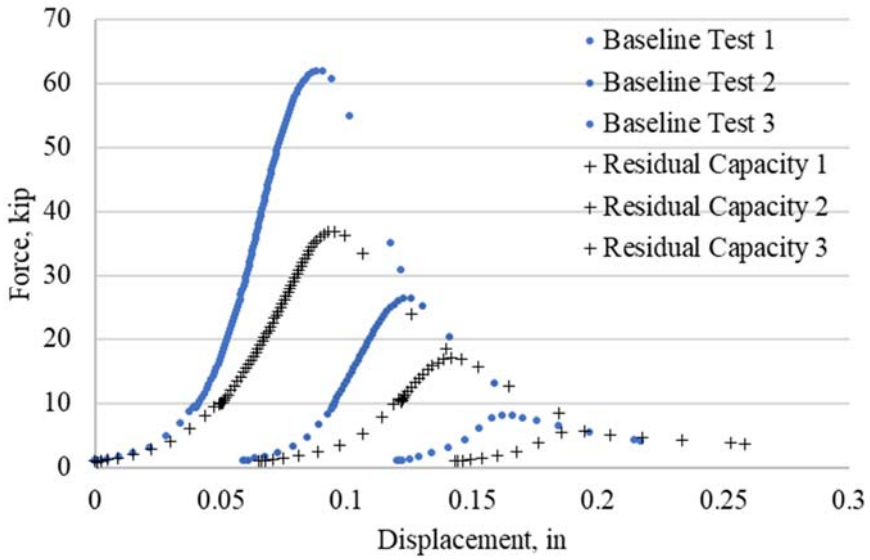

Figure 40: Full force versus displacement curves for the residual capacity of a concrete specimen subjected to a 59 ft/s impact and one undamaged specimen

3.5 Development of an In Situ Residual Capacity Testing Capability

The second method of determining the residual capacity of damaged specimens involved moving a quasi-static actuator into the testing area after the dynamic test is performed, as illustrated in Figure 41. The quasi-static actuator is then used to determine the in-situ residual strength of the damaged concrete by loading it in compression until failure. The actuator is mounted on a support fixture that can be maneuvered in and out of the testing area with an overhead crane.

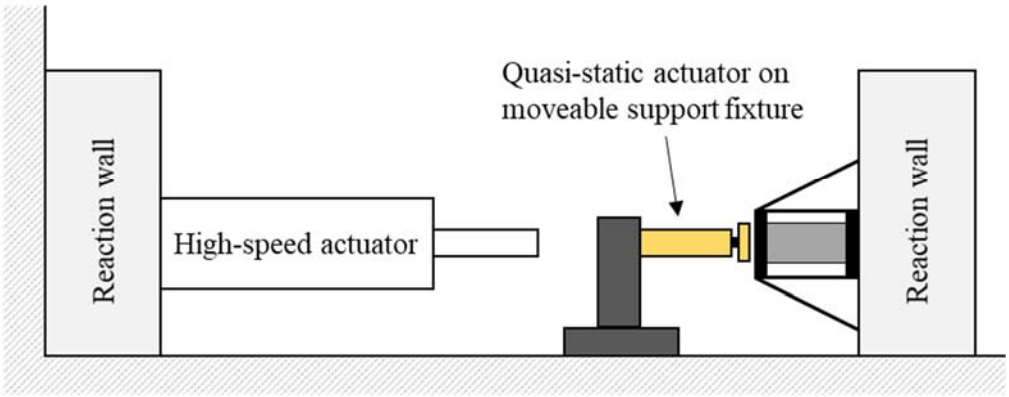

Figure 41: Test system concept for determining in situ residual capacity

3.5.1 In Situ Quasi-Static Test System Components

The in situ quasi-static test system uses the same concrete compression test rig used in the dynamic test system in order to obtain the in-situ residual capacity. Prior to quasi-static testing, the polycarbonate impact plate is removed and ASTM A36 steel blocks are inserted between the inner endcaps and large endplates of the test rig to protect the dynamic load cells.

The following elements of the quasi-static system adapted for this test program were designed by Sanborn and Stewart [43, 45] for testing the residual capacity of components damaged with the blast generator. In this system, a quasi-static actuator is bolted to a W14x145 column, which bolts to a W12x65 steel beam. The W12x65 steel beam is connected to the strong floor in the center of the blast generator's frame with DWYIDAG post-tensioning bars. The beam is installed prior to the dynamic test and remains in place to facilitate a quick transition between the dynamic and quasi-static test setups. The columns and quasi-static actuator, with a 100-kip load cell attached, are moved

into the testing area as a single unit after completion of a dynamic test with a 30 ton overhead crane. Figure 42 (a) shows the quasi-static loading assembly installed in the testing area. During the quasi-static test, the actuator position is controlled by a manual hand pump, shown in Figure 42 (b).

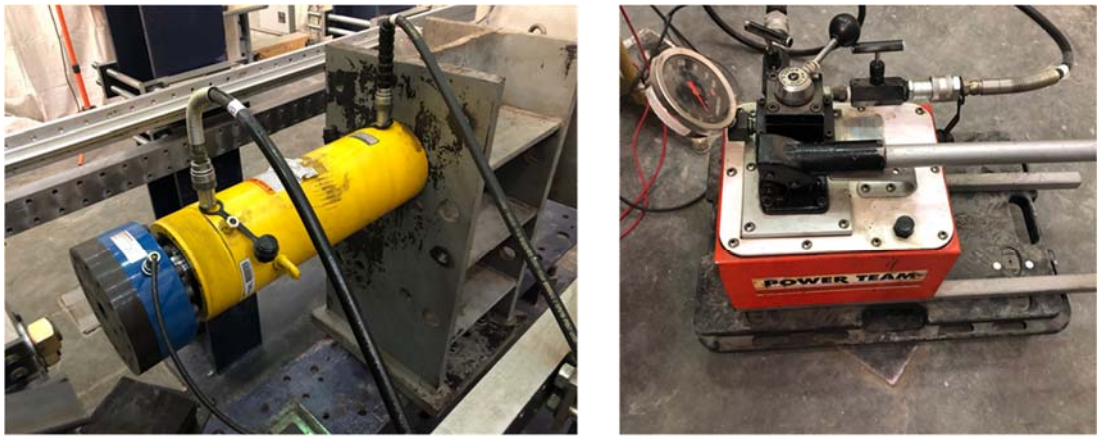

(a) (b)

Figure 42: (a) Quasi-static actuator loading assembly in the testing area with (b) manual hand pump

In order to evaluate a range of concrete strengths, the initial design of the quasi-static loading assembly was modified to replace the 100-kip load cell with a 200-kip load cell. A custom base plate was designed and fabricated to allow the installation of a load-profile ball joint, which protects the actuator piston from bending and directs the applied force uniformly on the test rig bearing plate if any eccentricities occur. Prior to the test, the ball joint is lifted into place and supported with a small hydraulic jack to ensure that it remains center before any force is applied to the cylinder. Once approximately 500 lbs. (2.2 kN) of force is applied to the test rig, the small hydraulic jack is lowered to allow the

ball joint to freely move as needed. Figure 43 shows the compression test rig prior to a quasi-static test.

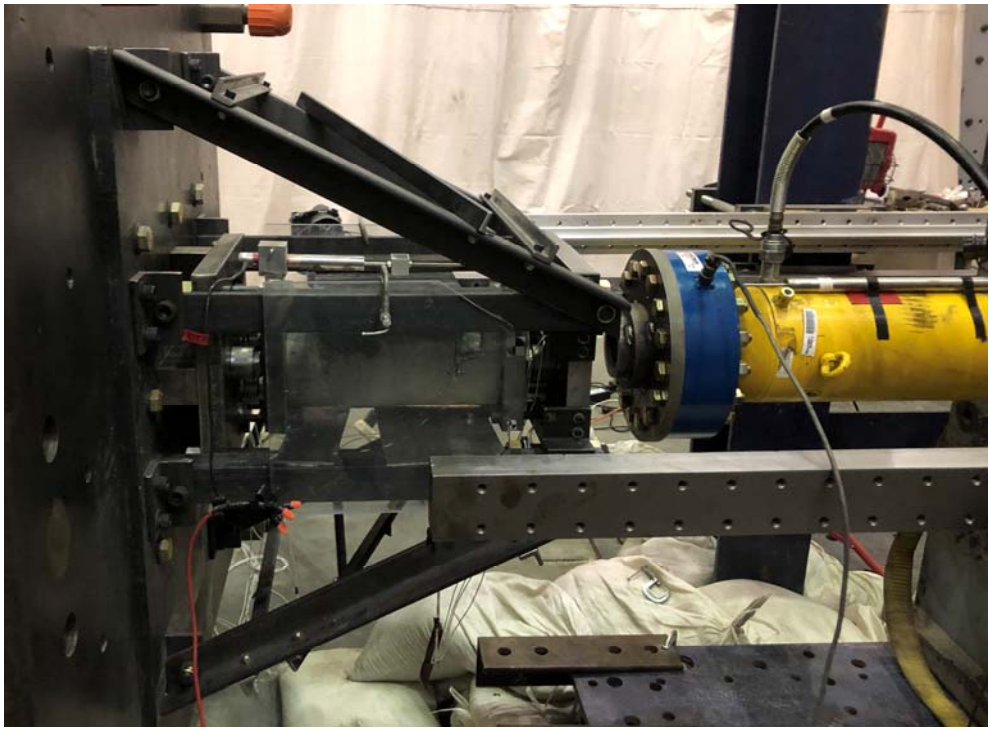

Figure 43: Quasi-static compression test system prior to testing

3.5.2 Instrumentation of In Situ Quasi-Static Test System

The applied force during the in situ quasi-static loading is measured from the load cell mounted on the actuator. The load cell is an Interface model 1232-AF load cell that is capable of measuring a maximum compressive force of 200 kips (890 kN). The load cell was calibrated with a universal testing machine to determine the slope of the linear load and voltage signal relationship. The displacement of the concrete cylinder is measured with two LVDTs that are affixed to the inner endcaps of the concrete test frame with custom fabricated metal clamps. One LVDT is positioned on top of the cylinder while the other is

placed under the cylinder. The LVDTs were calibrated with the use of precision gauge blocks, and the readings of each LVDT is verified prior to quasi-static testing. To protect the LVDTs from fragments when the concrete specimen fails, 1/8-in thick steel plates are clamped to the test frame between the specimen and the LVDTs. The installation location of the LVDTs is shown in Figure 44. An additional LVDT is installed on the hydraulic ram to monitor the position of the load cell.

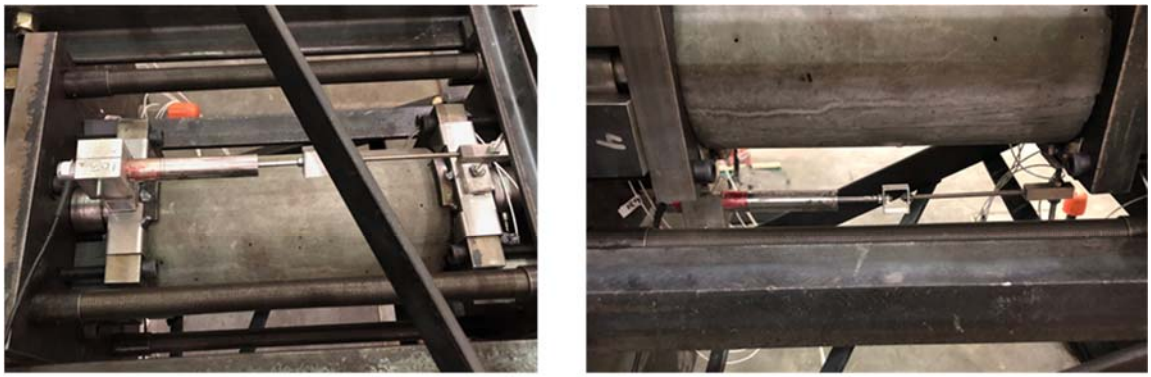

(a) (b)

Figure 44: Location of LVDTs (a) above cylinder and (b) below cylinder

The required excitation voltage of 10 volts for the load cell and 24 volts for the LVDTs is provided by a model 1711 BK Precision DC Power Supply. The voltage from the LVDTs and load cell is acquired with a National Instruments cDAQ-9178 compact data acquisition system and a NI 9219 universal module. A sample rate of 1,000 S/s was used for the quasi-static tests with the arithmetic mean taken of the samples. A baseline function was incorporated in the closed-loop DAQ system which subtracts the initial signal readings to provide a baseline zero reading.

3.5.3 In Situ Quasi-Static Test Procedure

The test procedure for conducting quasi-static residual capacity testing is as follows:

1. Prepare the concrete test rig for quasi-static testing by removing the polycarbonate impact plate and install the bearing blocks.
2. Install the W14x145 column, actuator, and load cell system with overhead crane. Bolt the column base to the floor beam with ten 7/8 in (22.2 mm) A325 bolts. Connect hydraulic pump to the actuator, and connect the load cell cabling to the DAQ and power supply.
3. Install the LVDTs and connect the cabling to the DAQ and power supply. Clamp 1/8 inch (0.32 cm) thick steel plates to the test frame between the LVDTs and concrete sample.
4. Move the ball joint into place with the small hydraulic jack.
5. Load the concrete test rig to approximately 500 pounds (2.2 kN). Confirm that the ball joint is secured between the load cell and test rig, and lower the small hydraulic jack.
6. Resume loading the concrete specimen by pumping the manual hydraulic pump while observing the readings from LVDTs and load cells. Continue at a steady load rate until the concrete specimen fails.

3.5.4 Validation of In Situ Quasi-Static Test System

Validation of the quasi-static test system involves achieving consistent test results and ensuring that the instrumentation captures the desired material properties. The stress strain curves for three validation tests are shown in Figure 45. Two of these tests were

conducted on 3-day old specimens, and one test was performed on a 4-day old specimen for a 4,000 psi design concrete mix. The ultimate strength in these tests matches the expected strength gain for the concrete mix. The difference in stress strain behavior between the two tests on 3-day old specimens is due to differences in the manual loading rate, as the first test (shown in blue) was stopped a few times to ensure the test setup remained level. In subsequent tests, the manual load rate was carefully monitored to be as consistent as possible.

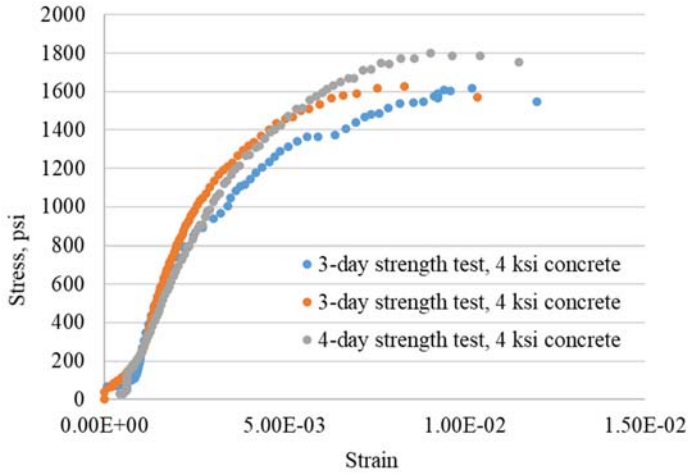

Figure 45: Stress versus strain curves for initial validation tests

Figure 46 (a) shows the failure mode for the 4-day specimen, which matches the Type 1 cone failure detailed in the ASTM C 39 test procedure. Figure 46 (b) shows the failure modes for the two 3-day tests, which also show a Type 1 failure mode.

(a) (b)

Figure 46: Type 1 failure modes for (a) 4-day old and (b) 3-day old concrete specimens

To evaluate the effect of end conditions on the observed failure modes, quasi-static compression tests were conducted in a standard servo-hydraulic compression machine. Figure 47 (a) shows the failure modes for cylinders tested with steel bearing plates representative of those used in the compression test setup in this experimental study. These tests showed Type 1 failure modes consistent with the failure modes observed in the quasi-static compression system. Figure 47 (b) shows failure modes for cylinders tested with an unbonded cap system. Because the friction on the ends of the cylinders is much lower in the unbonded cap system than it is with steel bearing plates, the cylinders showed columnar cracking typical of a Type 3 failure mode.

(a) (b)

Figure 47: ASTM C39 failure modes: (a) Type 1 from steel bearing plates, (b) Type 3 from unbonded cap system

Based on the initial validation results of the in-situ residual capacity test setup, the test was deemed suitable for determining the residual capacity of concrete subjected to impulsive loads. A series of tests was conducted on fully cured specimens from the same concrete mix. Two baseline tests were conducted to determine the undamaged concrete strength, and five specimens were tested for residual capacity after varying levels of applied impulsive loads. The results of this test series are shown in Figure 48. Although the two baseline tests showed close agreement in maximum force, the residual capacity results do not show any clear trends with relation to the test velocity and instead show a fair amount of scatter in both the shape of the force-displacement relationship and the residual strength.

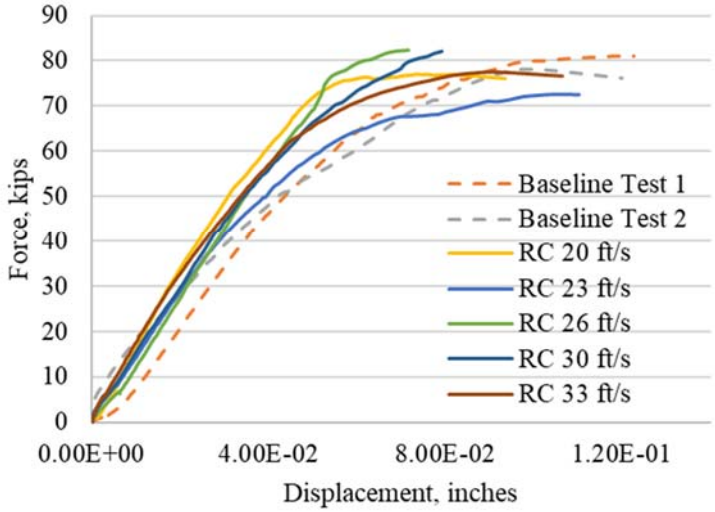

Figure 48: Force versus displacement for baseline and residual capacity concrete tests on fully cured specimens

To evaluate the behavior of the in-situ residual capacity tests, video footage of the tests was collected and the motion of the test setup was observed. Due to a lack of rigidity in the connections between the quasi-static actuator, support column, and beam anchoring the assembly to the floor, the compression test rig does not remain level during the test. This is shown in Figure 49, where the upward deflection in the front endcap plate between the beginning and end of a test is illustrated. This amount of deflection means that the cylinder is likely not in pure compression during the test, which explains the lack of consistency in the residual capacity results.

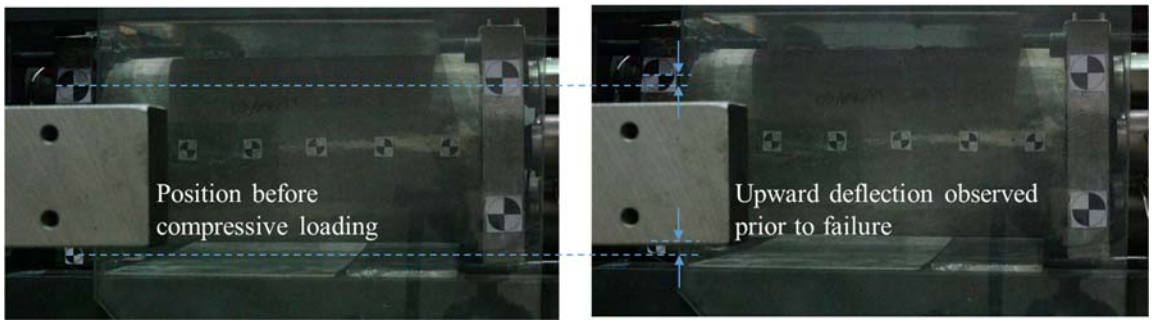

Figure 49: Upward deflection of front endcap plate observed during compressive loading

3.5.5 Future Improvements to In Situ Residual Capacity Test System

Due to the observed deflection in the front endcap plate during testing, improvements must be made to the in-situ residual capacity test setup to ensure the residual capacity tests are reliable and the cylinder remains in compression during loading. The primary improvement is that the rigidity of the connections between the actuator, support column, and laboratory floor should be increased as much as possible. Additional restraints should be attached to the end of the actuator to anchor it to the lab floor and further resist any upward motion during the test. Finally, a larger ball joint should be used to help eliminate eccentricities between the quasi-static actuator and the test setup.

CHAPTER 4. EXPERIMENTAL STUDY OF CONCRETE SUBJECTED TO IMPULSIVE LOADS

4.1 Introduction

An experimental test series was conducted to investigate the behavior of plain concrete subjected to impulsive loads. The objective of this series was to subject cylindrical concrete specimens to a variety of impulses and impact energies in order to evaluate the damage and residual capacity of the damaged specimens. Two test series were conducted with the dynamic experimental test system, with 27 tests completed in total. The first test series used fully cured concrete specimens which were then tested for residual capacity using the in-situ experimental setup described in section 3.5. The second test series used early age concrete specimens which were then tested for residual capacity with a hydraulic compression testing machine, as described in section 3.4. This chapter presents the materials and methods used in the impulsive loading experimental program, the theory and calculation methods used to examine the collected data, and key takeaways from the test program.

4.2 Materials and Methods

4.2.1 Materials

The concrete mix was designed based on the ACI Absolute Volume Method, with the materials and proportions shown in Table 1. Based on the results of initial finite element simulations, a concrete strength of 4,000 psi was selected so that a range of concrete damage states could be produced within the constraints of the test system. Specimens were

placed in a climate-controlled fog room 24 hours after placement, where they remained prior to testing.

Table 1: Typical batch weights for 4000 psi (28 MPa) concrete

Material	**Weight, lb / yd^3**
Water	320
Type I Cement	571.4
#67 Coarse Aggregate (SSD)	1669.5
Silica Sand (SSD)	1337.7
Total weight per cubic yard	3898.6
Unit weight, lb / ft^3	144.4

The experimental method was designed with consideration given to the requirements outlined in ASTM C39, the standard test method for determining the compressive strength of concrete specimens [3]. Prior to testing, the end surfaces of the cylinders were ground to meet the ASTM C39 planarity tolerance and to ensure that the cylinders were fully in contact with the endcap plates in the dynamic test system. Figure 50 shows the cylinder end preparation process. Because the dynamic test system used steel endcap bearing plates, all cylinders used to determine baseline strength are also ground on both ends. Baseline tests and residual capacity tests conducted with the hydraulic compression machine used steel bearing plates instead of unbonded endcaps to ensure that the friction conditions were consistent between the dynamic testing and quasi-static testing.

Figure 50: Cylinder end grinding process

After being placed in the dynamic test rig, the test specimen was covered in moistened burlap to avoid any drying while the warmup sequence of the high-speed actuator was conducted. Immediately prior to the dynamic test, the burlap was removed, and high-speed motion tracking targets were adhered to the specimen.

4.2.2 Experimental Method

The dynamic concrete compression tests system described in Chapter 3 was used to experimentally investigate the behavior of concrete subjected to impulsive loads. A preliminary test series was conducted with fully cured concrete specimens to evaluate the behavior of the test system. This test series, which consisted of 14 experiments in total, began at lower impact velocities and the velocity was incrementally increased while residual capacity testing was completed for each specimen with the in-situ test system described in Section 3.5. A few problems with the experimental approach occurred during

the first test series. First, the in situ residual capacity test system was not rigid enough to keep the fully cured specimens horizontal during compressive loading and these eccentricities resulted in unreliable residual capacity results. Second, the levels of impulsive compressive force did not appear to be high enough to damage the fully cured concrete. The theoretical maximum force that could be applied to the concrete specimens with this test system was 200 kips due to the capacity of the dynamic load cells. However, because the force was not always evenly distributed across the load cells, the maximum load that could realistically be applied without damaging the load cells was closer to 150 kips. The dynamic strength of the fully cured concrete specimens used in this test series is unknown, but it appeared to be high enough that the concrete did not sustain damage at the levels of impulsive loading possible with the dynamic test system. To diagnose if the fully cured specimens were sustaining any damage during this first test series, two tests were conducted with 28-day aged specimens where the residual capacity and baseline testing was conducted with a compression testing machine. No change in strength or stiffness was observed for the two 28-day specimens after the impulsive loading, which confirmed that the specimens in the first test series did not sustain any measurable damage.

Based on the results of the first test series, the focus of the experimental test program shifted from quantifying the behavior of fully cured 4,000 psi concrete specimens to illustrating proof of concept of the dynamic test system using early age, lower strength concrete. The first test series showed that concrete of normal to higher compressive strength would likely not sustain any meaningful levels of damage without modifications to the experimental setup. So, to provide proof of concept, a second test series was conducted on early age concrete specimens to ensure that they were low enough in strength

to sustain damage during dynamic loading. The residual capacity and baseline strength testing of these specimens was conducted with the use of a hydraulic compression machine to eliminate any potential problems with the in-situ testing setup. In addition, a heavier and more robust flyer plate was used for the second test series.

Table 2 shows the test matrix for the experimental study, which is comprised of two main test series. Fourteen tests were conducted in the first test series on concrete specimens aged for one year with the in-situ residual capacity test setup. Nine tests were conducted in the second test series on early age concrete specimens, where the residual capacity testing was conducted with the use of a hydraulic compression machine, or universal testing machine (UTM).

Table 2: Experimental Test Matrix

Test Series ID	Target Velocity, in/sec	Specimen Age	Concrete Design Strength, psi	Flyer Mass, lbm	Residual Capacity Method
1-1	236	1 year	4000	33	In-situ
1-2	276	1 year	4000	33	In-situ
1-3	315	1 year	4000	33	In-situ
1-4	354	1 year	4000	33	In-situ
1-5	394	1 year	4000	33	In-situ
1-6	394	1 year	4000	33	In-situ
1-7	394	1 year	4000	33	In-situ
1-8	394	1 year	4000	33	In-situ
1-9	453	1 year	4000	33	In-situ
1-10	492	1 year	4000	33	In-situ
1-11	531	1 year	4000	33	In-situ
1-12	571	1 year	4000	33	In-situ
1-13	630	1 year	4000	33	In-situ
1-14	669	1 year	4000	33	In-situ
Hybrid	591	28 day	4000	33	UTM
Hybrid	630	28 day	4000	33	UTM
2-1	394	3 day	3500	44	UTM
2-2	472	3 day	3500	44	UTM
2-3	512	4 day	3500	44	UTM
2-4	492	3 day	3500	44	UTM
2-5	531	3 day	3500	44	UTM
2-6	551	3 day	3500	44	UTM
2-7	591	4 day	3500	44	UTM
2-8	591	4 day	3500	44	UTM
2-9	630	4 day	3500	44	UTM

4.3 Theory and Calculation

4.3.1 Impulsive Loading

The instrumentation scheme used in the dynamic experiments focused on capturing the displacement-time history of the flyer plate and the specimen as well as the force-time

history on both ends of the specimen. As discussed in Section 3.3.3 the displacement-time history is captured with two high speed camera systems, while the force-time history of the dynamic event is measured with eight piezoelectric force sensors. Neglecting any changes in the system due to friction or external applied forces, the conservation of momentum dictates that the impulsive load generated by the flyer plate should be equal to the impulsive load measured on the impact side of the specimen, and the impact impulse should be equal to the impulsive load measured on the reaction side.

The impulse generated by the flyer plate, S_{flyer}, is calculated from Equation 4.1, where m_{flyer} is the mass of the flyer plate and v_{impact} and $v_{rebound}$ are the impact and rebound velocity, respectively. The impulse measured at the impact and reaction surfaces of the specimen is determined by Equation 4.2, where S_{LC} is the impulse and $F(t)$ is the force-time history of the load cells. The kinetic energy imparted on the system from the flyer plate impact can be calculated from Equation 4.3.

$$S_{flyer} = m_{flyer}\left(v_{impact} - v_{rebound}\right) \tag{4.1}$$

$$S_{LC} = \int F(t)dt \tag{4.3}$$

$$E_k = \frac{1}{2} m_{flyer} {v_{impact}}^2 \tag{4.3}$$

The displacement-time history of the flyer plate was determined from high speed camera footage of the test. Xcitex's ProAnalyst software package [51] was used to track the motion of targets on the flyer plate. A still image from the results of the tracking software is shown in Figure 51, and Figure 52 shows the displacement-time history from the tracked targets. The impact and rebound velocities were determined by taking a linear regression of the

displacement time history prior to impact and after impact, respectively. This method of determining the rebound velocity proved somewhat unreliable because the flyer plate tended to rebound at an angle, and in these cases the true rebound velocity could not be accurately determined.

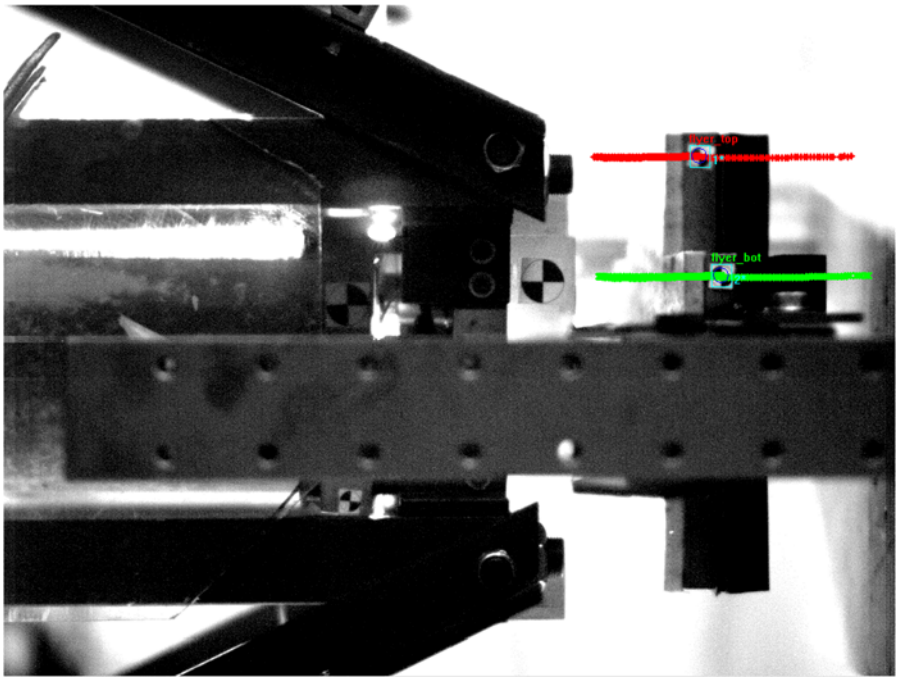

Figure 51: Flyer plate motion tracking results from Test 1-2

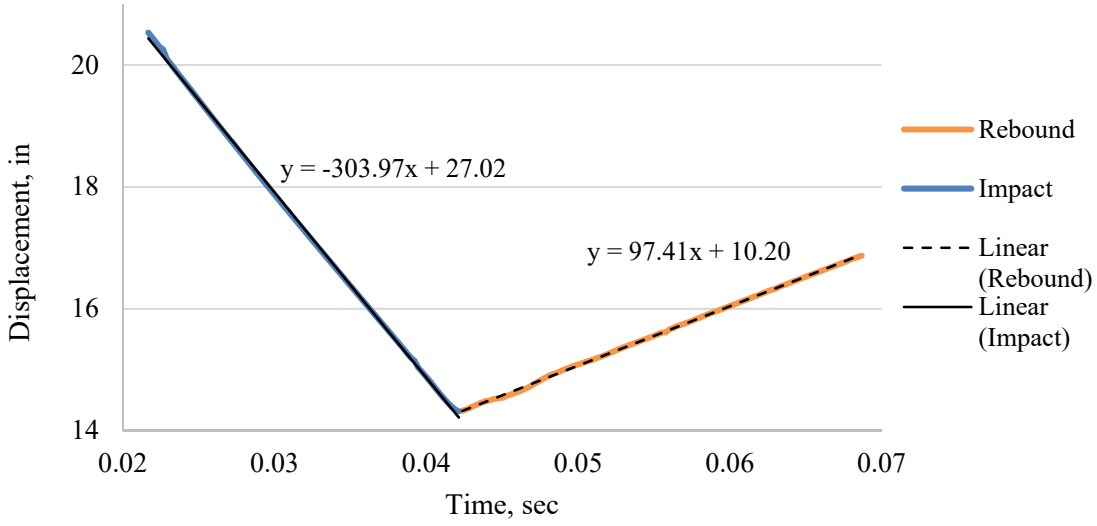

Figure 52: Typical flyer plate displacement-time history from Test 1-2

The force-time history for a typical test is shown in Figure 53, with the individual load cells shown in Figure 53 (a). Figure 53 (b) shows the overall impact and reaction

forces, which were calculated as the sum of the individual load cell measurements with time. The impact and reaction impulses were only calculated from the main pulse in the force-time history. Once the force values return to zero after the main pulse ends, the impulse is taken as a constant value. This method ensures that the impulse calculation is consistent between tests and does not include any reverberations in the plates that hold the load cells, which are not representative of the load on the specimen. Post-impact reverberations in the specimen appear to be minimal and these reverberations are low enough that they likely do not contribute to any additional damage to the specimen. So, this ringing in the load cells was neglected to ensure that the applied impulse was calculated in a consistent manner between tests.

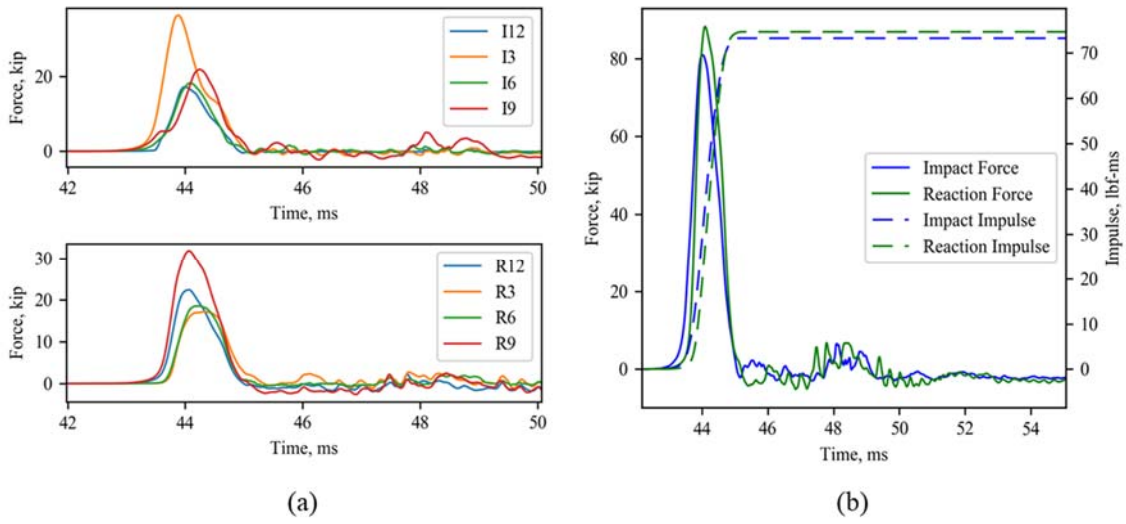

Figure 53: Displacement data from Test 2-5

4.3.2 Displacements During Impulsive Loading

A second high-speed camera was used to track the motion of the specimen. Targets were adhered to the top and bottom of the impact and reaction endcap plates, and five

targets were placed on the side of the specimen at 2-inch increments. Figure 54 shows a still image from the results of the tracking software. Tracking the motion of the targets on the side of cylinder proved more useful than tracking the motion of the endcap plates because they did not provide information on the movement of the specimen after the initial compression. Figure 55 shows the displacement of the first target on the cylinder (far left) and the last target on the cylinder (far right) during a typical test. Both targets moved forward during the impulsive load, which occurred approximately between 4.0E-2 and 5.0E-2 milliseconds. The reaction side of the test setup was not perfectly rigid, so the specimen experienced some rigid body motion as the assembly moved forward in response to the flyer plate impact. The test setup and the specimen then rebounded from the impact and moved backwards, and then forward again until the energy in the system dissipated. To eliminate the rigid body motion of the specimen and obtain the axial displacement time history, the motion of the fifth target was subtracted from the motion of first target, and the resulting displacement time history is shown in Figure 56.

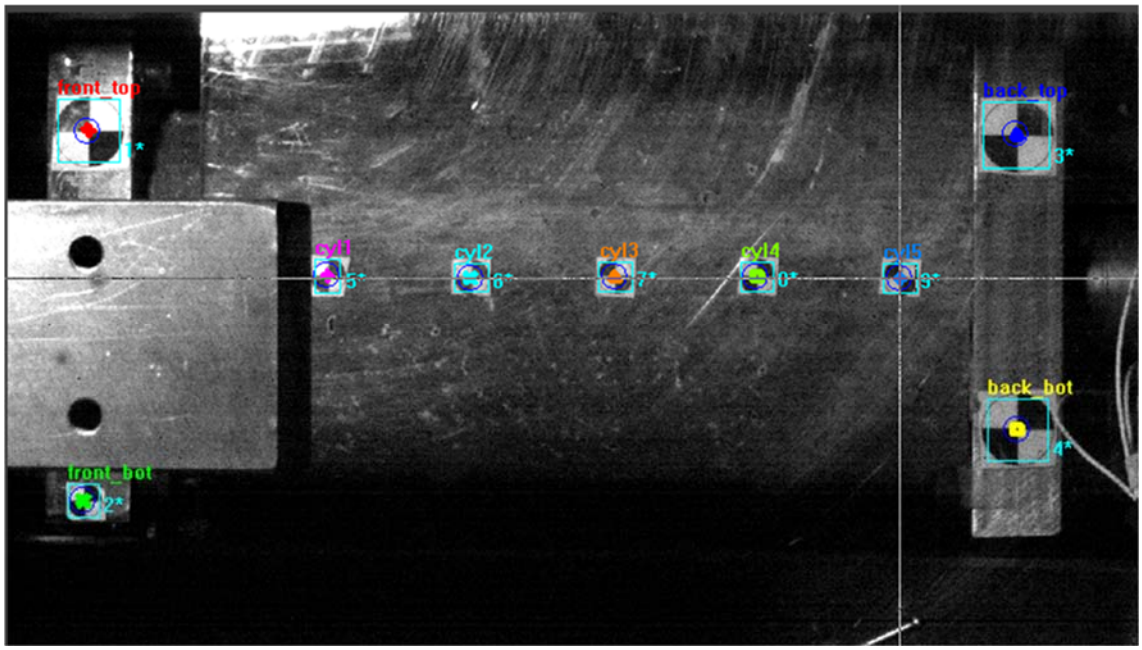

Figure 54: Specimen sideview target arrangement

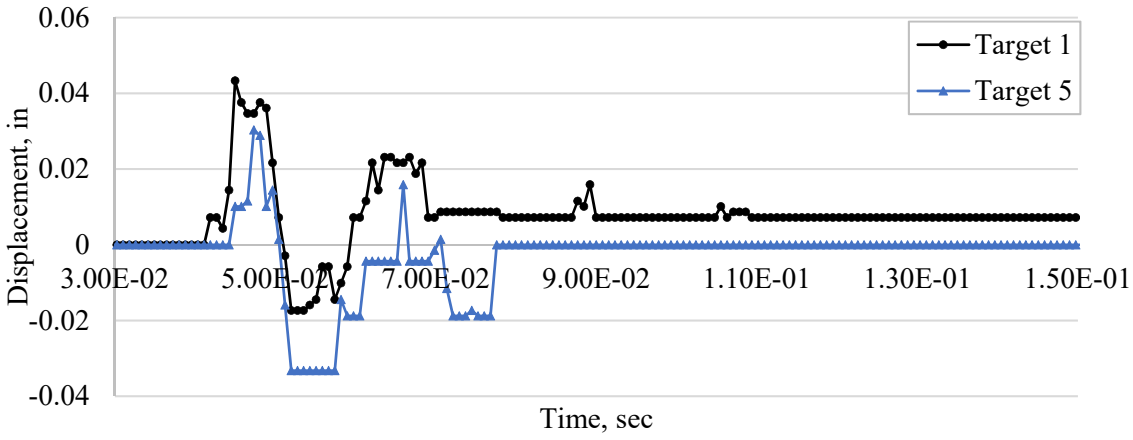

Figure 55: Displacement time history of targets 1 and 5

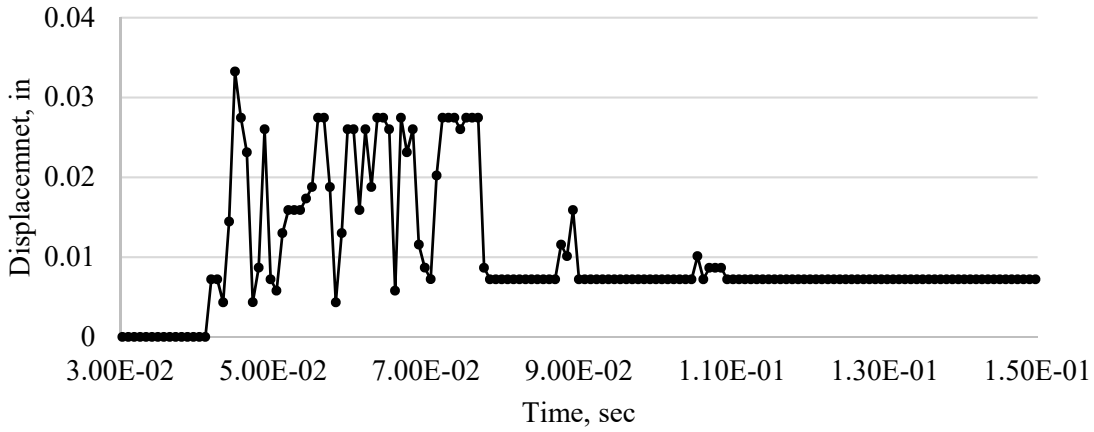

Figure 56: Net axial displacement time history between targets 1 and 5

The net displacement between the axial targets can be used to determine a value for the average axial strain in the specimen during the impulsive loading event. The engineering axial strain is simply given by:

$$\varepsilon_{axial} = \frac{\Delta l}{l} \tag{4.4}$$

where Δl is the change in distance between the two targets and l is the original distance between targets before the impulsive load. From this calculation, the maximum strain during the test can be determined as well as the residual strain in the specimen. The strain rate in the specimen can be determined from the slope of the initial increase in displacement, as this region corresponds to the application of the impulsive load. However, the displacement data lacks enough resolution in the time domain to ensure that the maximum strain is correct, as there are too few data points for the time scale of the impulsive load. The pixel resolution of the targets was low enough that the tracking software often had difficulty capturing the motion of the targets during and after the

impulsive load. So, there was often a substantial amount of noise in the displacement time history which contributed additional uncertainty to the strain calculations. In addition, in a few cases the targets detached from the specimen during the impulsive load. Although the displacement data did not always provide reliable measurements to provide insight on the behavior of the specimen, the displacement data and side camera view were useful to provide general information on the global movement of the test system and the specimen.

4.4 Results and Discussion

The major experimental results from the dynamic test series are presented in Table 3. The impact and rebound velocities, maximum impact and reaction forces, and impact and reaction impulses are shown, and no values are shown for tests in which problems occurred during data acquisition. Flyer plate camera data was not collected for tests 1-6, 1-11, and Hybrid-1 because the trigger sequence was executed incorrectly. Load cell data was not fully collected for tests 1-1, 1-9, 1-12, and 1-13 due to problems with the load cells or data acquisition during testing. These test are indicated by the hyphen symbol in the Table.

Table 3: Experimental results of the dynamic test program

Test Series ID	Impact Velocity, in/s	Rebound Velocity, in/s	Maximum Impact Force, kip	Maximum Reaction Force, kip	Impact Impulse, lbf-ms	Reaction Impulse, lbf-ms
1-1	304	97	-	-	-	-
1-2	342	139	29.2	46.1	31.3	36.0
1-3	391	177	28.7	42.4	31.2	38.6
1-4	423	150	42.6	68.9	32.7	42.4
1-5	461	189	38.7	43.4	42.9	42.7
1-6	-	-	31.9	39.9	53.6	56.4
1-7	443	143	45.3	51.0	44.9	45.6
1-8	436	228	41.4	46.2	46.6	47.7
1-9	510	265	-	62.3	-	50.0
1-10	564	176	42.1	46.8	56.7	57.6
1-11	-	-	84.7	99.1	60.4	63.1
1-12	603	176	-	-	64.7	67.4
1-13	680	174	-	-	-	-
1-14	756	82	133.8	166.7	81.2	85.5
Hybrid-1	-	-	91.6	105.0	68.1	70.4
Hybrid-2	680	200	78.5	94.3	70.7	74.5
2-1	421	167	60.4	64.0	59.3	57.4
2-2	527	196	83.7	85.7	68.2	70.3
2-3	565	109	88.0	98.2	72.3	74.3
2-4	512	144	75.7	87.2	67.0	70.0
2-5	564	148	80.9	88.2	73.2	74.6
2-6	641	210	98.5	100.4	76.9	77.5
2-7	679	143	112.5	114.6	79.1	79.7
2-8	674	165	103.0	124.0	80.2	79.8
2-9	705	70	127.7	133.0	86.0	84.4

4.4.1 Impulsive Loads

The impulse in the dynamic system can be determined from the flyer plate displacement time history as well as the impact and reaction force time history. Figure 57 shows the impulse calculated from the flyer plate displacement time history as a function of the impact velocity. Test Series 1 and 2 are plotted separately, as Test Series 1 used a 33

lbm flyer plate and Test Series 2 used the 44 lbm flyer plate. Determining the true rebound velocity was not possible in several test cases because the flyer plate tended to rotate laterally as it rebounded, which contributed to the scatter in the data and uncertainty in the calculated flyer plate impulse. However, the expected trend of increasing impulse with increasing impact velocity is present for both test series, with R-squared values of 0.93 for the first test series and 0.88 for the second test series.

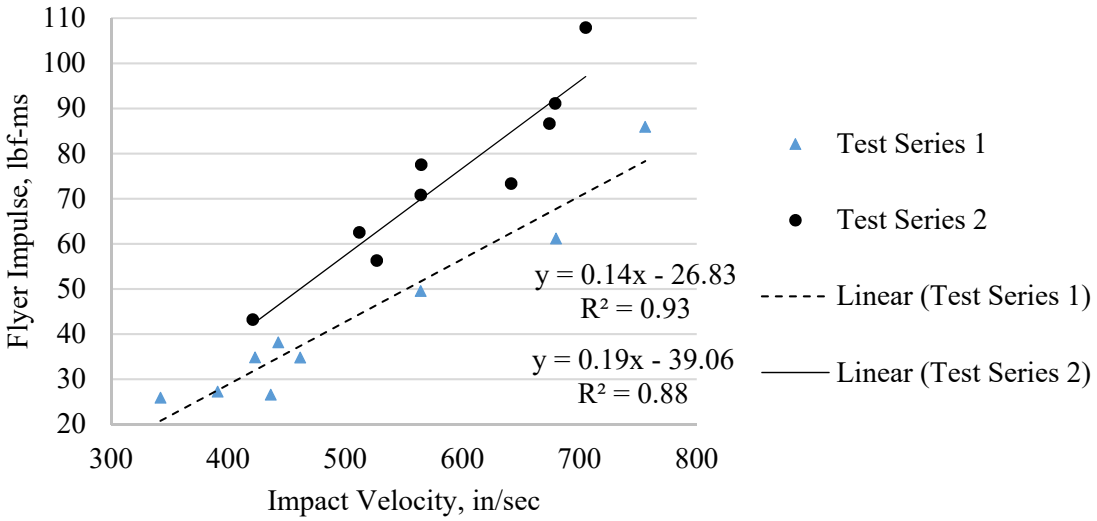

Figure 57: Flyer plate impulse versus impact velocity

The impulsive load calculated from the force-time history of the load cells is shown in Figure 58 as a function of the flyer plate impact velocity. The impact impulses display a linear trend with respect to the impact velocity for both test series in the range of velocities conducted in each test series. Closer examination of Figure 58 shows that for most test cases, the impact impulse is lower than the reaction impulse.

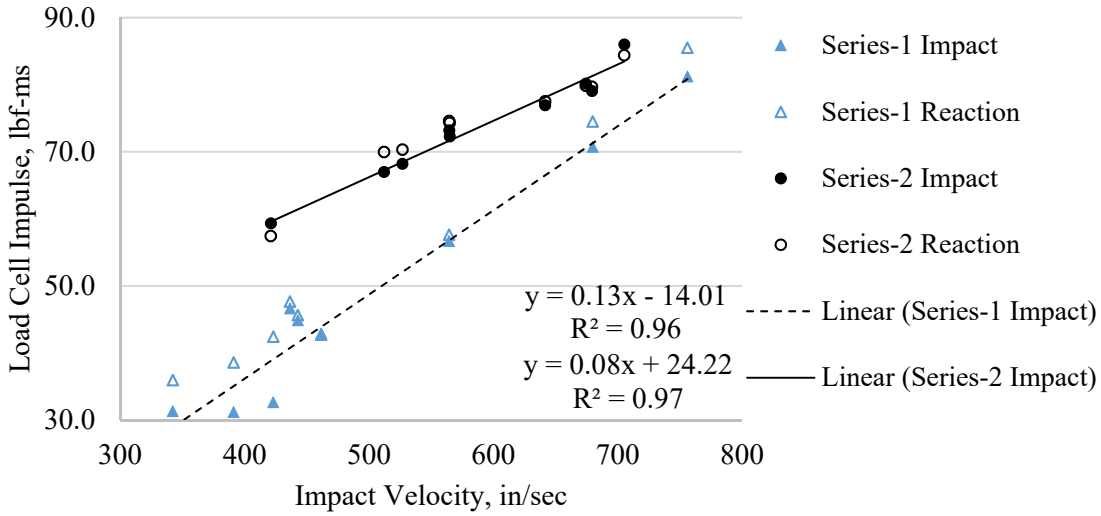

Figure 58: Load cell impulse versus impact velocity

Figure 59 shows load cell reaction impulse divided by the impact impulse plotted with respect to the impact velocity. For most tests, the reaction impulse was larger in magnitude than the impact impulse, as the reaction to impact impulse ratio is greater than 1.0 for most test cases. This caused by the inelastic collision of the flyer plate and the nonlinear behaviour of the programmer, which extends the duration of the impact. At the time that the impact impulse is measured, the flyer plate has not rebounded from the test system. Because the collision is not complete, there is still an applied external force acting on the test system. This causes the momentum in the system to increase and results in a higher measured impulse on the reaction side. The three lowest-velocity test cases in Test Series 1 had a significantly higher reaction impulse, which indicated that the test system was not efficient in this velocity range with the 33 lbm flyer plate. In addition, the force was not evenly distributed across the impact load cells for these three test cases. This issue was resolved as the test velocity increased and the test performance and efficiency

improved. For Test Series 2, the reaction impulse was generally larger than the impact impulse aside from the lowest velocity test case and a few of the highest velocity test cases. For the lowest velocity test, the impact impulse is higher because some ringing occurred in the force-time history before the impact force reduced to zero, and this ringing contributed to the higher impact impulse. Apart from this test, the ratio of reaction to impact impulse clearly decreased with increasing impact velocity. This trend corresponds to the increasing levels of damage and reduction in residual capacity observed in the specimens with increasing impact velocity. As the specimen becomes damaged, energy in the system is dissipated and the impulse measured on the reaction side reduces.

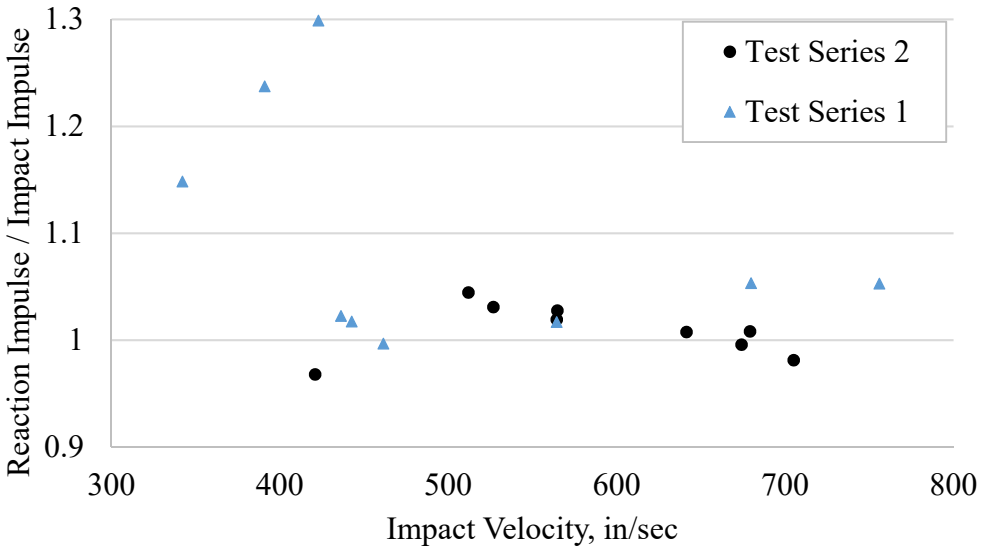

Figure 59: Reaction and impact impulse test efficiency versus impact velocity

4.4.2 Dynamic Behaviour of Concrete

Table 4 shows numerical results from Test Series 2 including kinetic energy, ratio of applied dynamic force to concrete strength, and estimations of the strain rate, maximum

strain and residual strain. The ratio of applied dynamic force to concrete strength, termed here as the apparent strength increase factor, SIF, is calculated as:

$$SIF = \frac{f_{dynamic}}{f_c} \tag{4.5}$$

where $f_{dynamic}$ is the maximum force during the dynamic test and f_c is the compressive strength determined from a quasi-static baseline compression test.

Table 4: Dynamic Test Series 2 results

Test Series ID	Kinetic Energy, ft-lb	Apparent SIF	Strain Rate, s^{-1}	Maximum Strain	Residual Strain
2-1	27064	1.08	2.00	0.0031	0.00103
2-2	42391	1.42	2.66	0.0047	0.00103
2-3	48722	1.36	4.11	0.0032	0.00145
2-4	40037	1.25	2.13	0.0017	0.00083
2-5	48664	1.35	4.04	0.0053	0.00145
2-6	62862	1.59	4.09	0.0023	0.00124
2-7	70462	1.67	4.48	0.0038	0.00145
2-8	69432	1.50	5.60	0.0043	0.00145
2-9	75958	1.80	5.60	0.0058	0.00145

Figure 60 shows the kinetic energy calculated from the flyer plate versus strain rate in the specimen during the impulsive load. For these calculations, a gauge length of 5 inches was used. There is some scatter in the data due to the uncertainties in the strain rate calculation, but the expected linear trend of increasing strain rate with increasing kinetic energy is present ($R^2 = 0.84$). With this established relationship of kinetic energy versus strain rate, a targeted strain rate can be achieved by simply adjusting the mass or impact velocity of the flyer plate. The Blast Generator (BG-25) system is capable of accelerating a 110 lbm impact mass up to 1,344 in/sec (112 ft/s) [49]. This is equivalent to a kinetic

energy of 21,316 ft-lb. Based on the established kinetic energy versus strain rate relationship from this test series, the theoretical maximum strain rate that the blast generator is capable of generating in a 6 inch by 12 inch a concrete specimen with this test setup is 60.0 s^{-1}. This higher strain rate regime can be targeted with two simple modifications to the test setup, (1) changing the load cell instrumentation scheme to accommodate higher levels of impulsive load, and (2) slightly increasing the mass of the flyer plate. The theoretical strain rates that this test setup is capable of achieving can be further adjusted by modifying the specimen geometry.

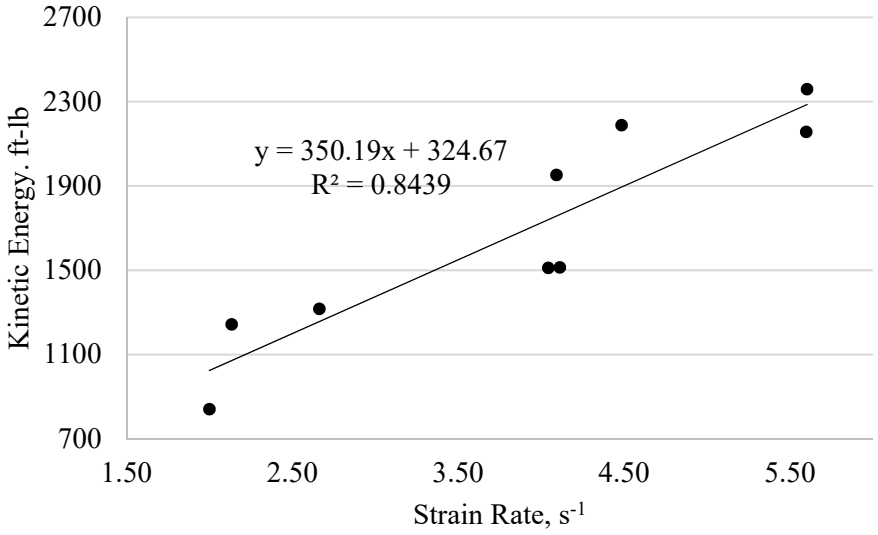

Figure 60: Kinetic energy versus strain rate for test series 2

It should be noted that the strain rate calculation performed for this test series provides an averaged value for the gauge length of 5 inches between targets. However, the strain in the specimen should ideally be measured at a gauge length that represents the length of the compressive pulse traveling through the specimen during the impact. The

elastic wave speed for a stress pulse traveling through a bar is given by $C = \sqrt{E/\rho}$. With E = 600 ksi and ρ = 0.08275 lbm/in^3, the one-dimensional elastic wave speed, C, is equal to 2,693 in/sec. The approximate rise time and pulse duration for the force versus time history in Figure 53 is approximately 0.5 ms and 1.5 ms, respectively. Assuming that this pulse is traveling at the elastic wave speed, the rise length and the pulse length is 1.35 inches and 4.04 inches, respectively. Based on this example calculation for a purely elastic stress wave traveling through a bar, the 5 inch gauge length used in this test series might be too large to accurately characterize the strain rate, and the true strain rate in the specimen might be slightly higher than the calculated averaged strain rate. To determine the appropriate gauge length for future tests, the length of the stress pulse could be estimated with the aid of numerical simulations to account for the geometry and the inelastic response of the specimen.

All the specimens in Test Series 2 remained intact during testing, so the dynamic increase factor for the uniaxial compressive strength of the concrete in this test series remains unknown. Figure 61 plots the apparent strength increase factor (SIF), or the maximum dynamic force divided by the compressive strength, with respect to the strain rate. The apparent SIF generally increases with increasing strain rate, with a maximum value of 1.8 at a strain rate of 5.6 s^{-1}. Because each specimen in this test series had residual compressive strength after the dynamic test, the dynamic increase factor (DIF) relationship for the concrete in this test series is larger in magnitude than this observed apparent SIF relationship.

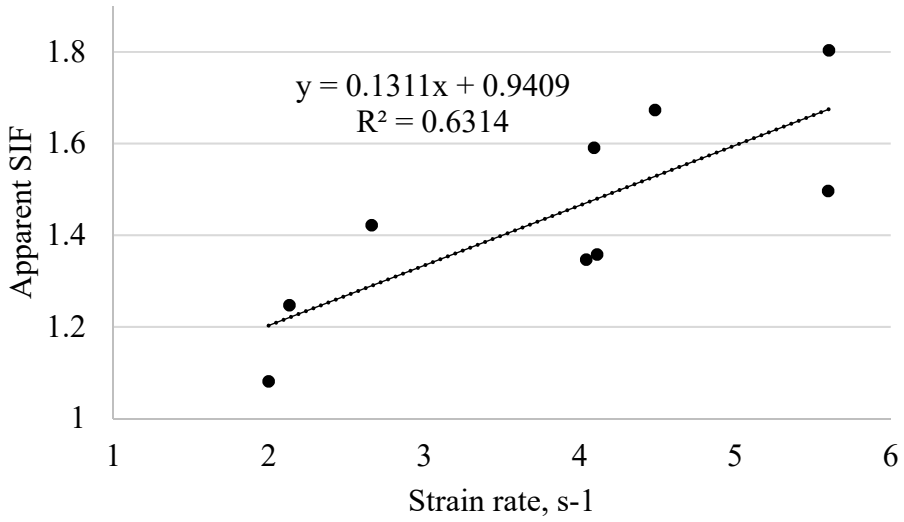

Figure 61: Apparent strength increase factor versus strain rate for Test Series 2

The apparent strength increase factor versus strain rate relationship established in this test series can be contextualized by comparing to the results of previous experimental programs. Bischoff and Perry [18] conducted a comprehensive review of experiments on the dynamic increase factor of concrete and plotted the experimentally determined dynamic increase factors versus the strain rate. Figure 62 shows this plot, with the apparent SIF values from Test Series 2 overlaid. The maximum SIF value of 1.8 from this test series is higher than most data points from other research programs in this strain rate regime as well as the CEB recommended dynamic increase factor curve. This is significant because the true dynamic increase factor for the concrete is higher than the SIF points plotted here, as the concrete did not fully break in any of these test cases. This is likely attributed to the low strength and early age of the concrete used in this test series.

Several researchers have postulated that the mode 1 DIF relationship is largely due to the Stefan effect, which is dependent on the water content of the specimen. Experimental

observations support the contribution of the Stefan effect on the dynamic strength, as wet concrete is more strain rate sensitive than dry [16]. Early age concrete is more porous and has more free water than fully cured concrete, which will enhance the Stefan effect. In addition, lower strength concrete is more sensitive to increasing strain rate [16]. The average compressive strength of the concrete used in this test series was 2.3 ksi, which is lower in strength than the CEB curve for concrete strengths of 20 Mpa (2.9ksi).

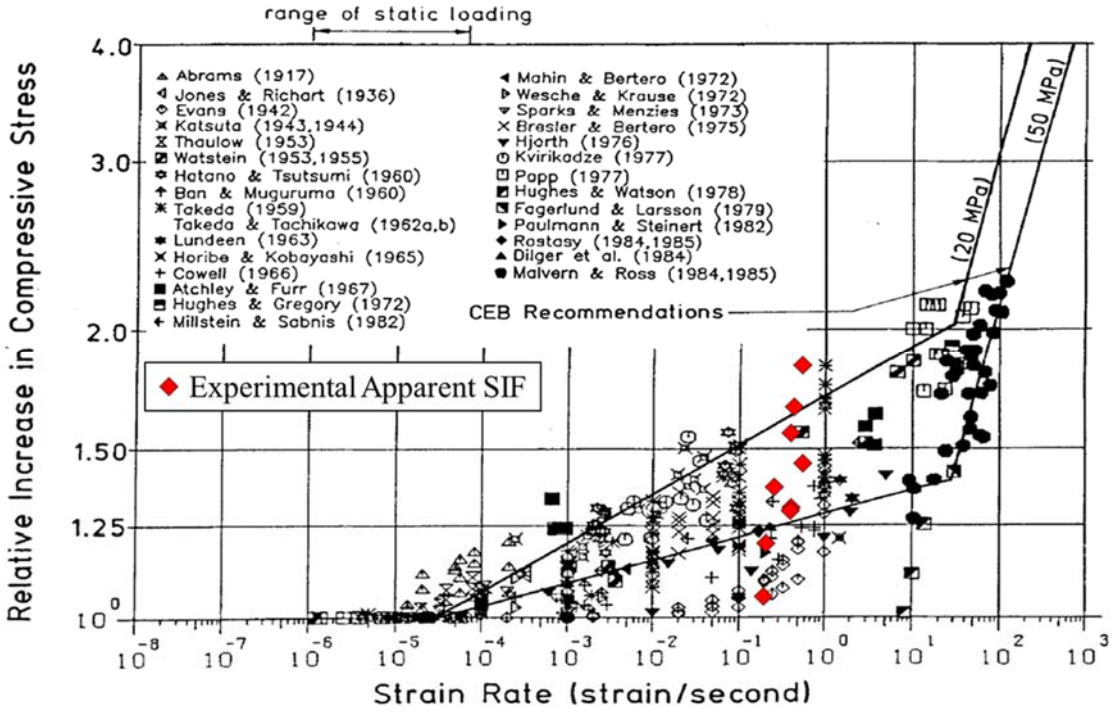

Figure 62: Strain rate influence on compressive strength with experimental data [18]

4.4.3 Quantification of Damage

Figure 63 shows the estimated maximum recorded strain in the specimen with respect to the impact velocity, and Figure 64 shows the residual strain of the specimen with respect to the impact velocity. Due to the lack of resolution and noise in the displacement

data, there is some uncertainty in these strain measurements. The actual maximum strain corresponding to the maximum value of applied impulsive load was likely not captured, and the residual strain measurement was difficult to quantify because the displacement data produced by the tracking software showed too much noise. However, it is expected that with increasing impact velocity and levels of impulsive load, the maximum strain and residual strain should increase.

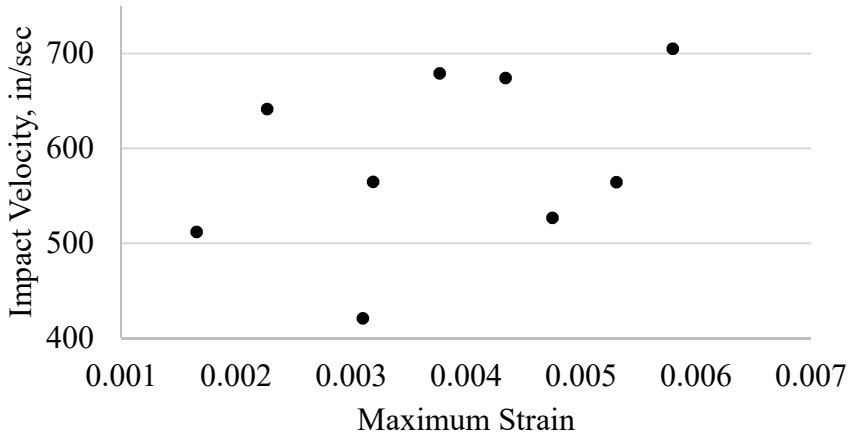

Figure 63: Impact velocity versus maximum strain for test series 2

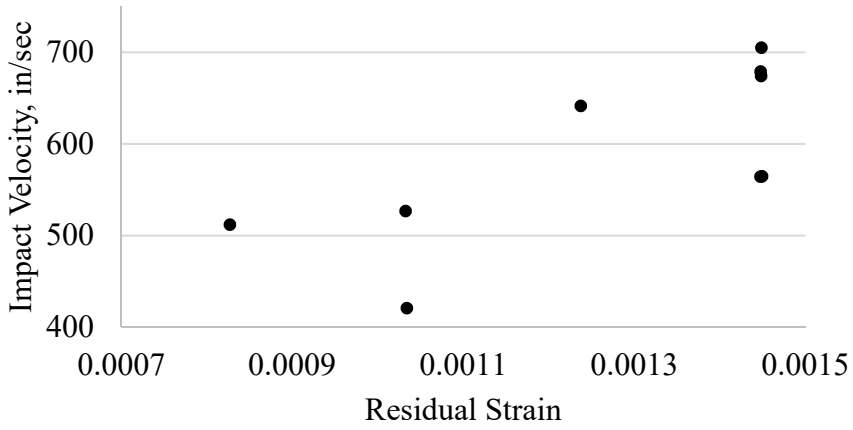

Figure 64: Impact velocity versus residual strain for test series 2

The specimens from Tests 2-6, 2-7, 2-8, and 2-9 all experienced damage from the impulsive loading in the form of visible macrocracks, as shown in the following figures. Tests 2-6, 2-7, and 2-8 showed a similar distribution and size of macrocracks, with the maximum crack size of approximately 0.04 inches. Test 2-9 showed much more extensive macrocracking with a larger maximum size of approximately 0.07 inches. The similar

crack sizes for the first three tests correspond to similar reductions in residual strength and stiffness, while Test 2-9 had a much greater loss of residual strength and stiffness.

Figure 65: Cracking observed on specimen from Test 2-6

Figure 66: Cracking observed on specimen from Test 2-7

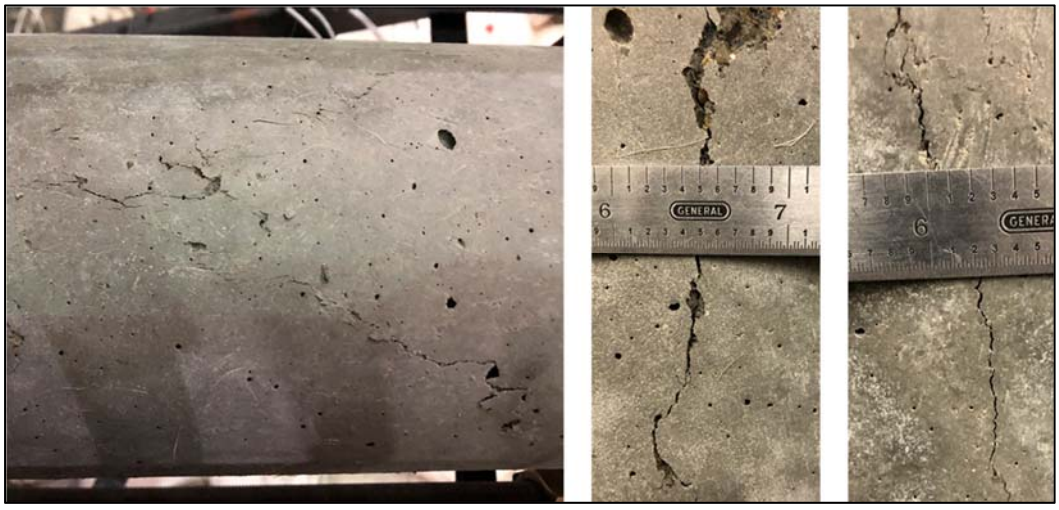

Figure 67: Cracking observed on specimen from Test 2-8

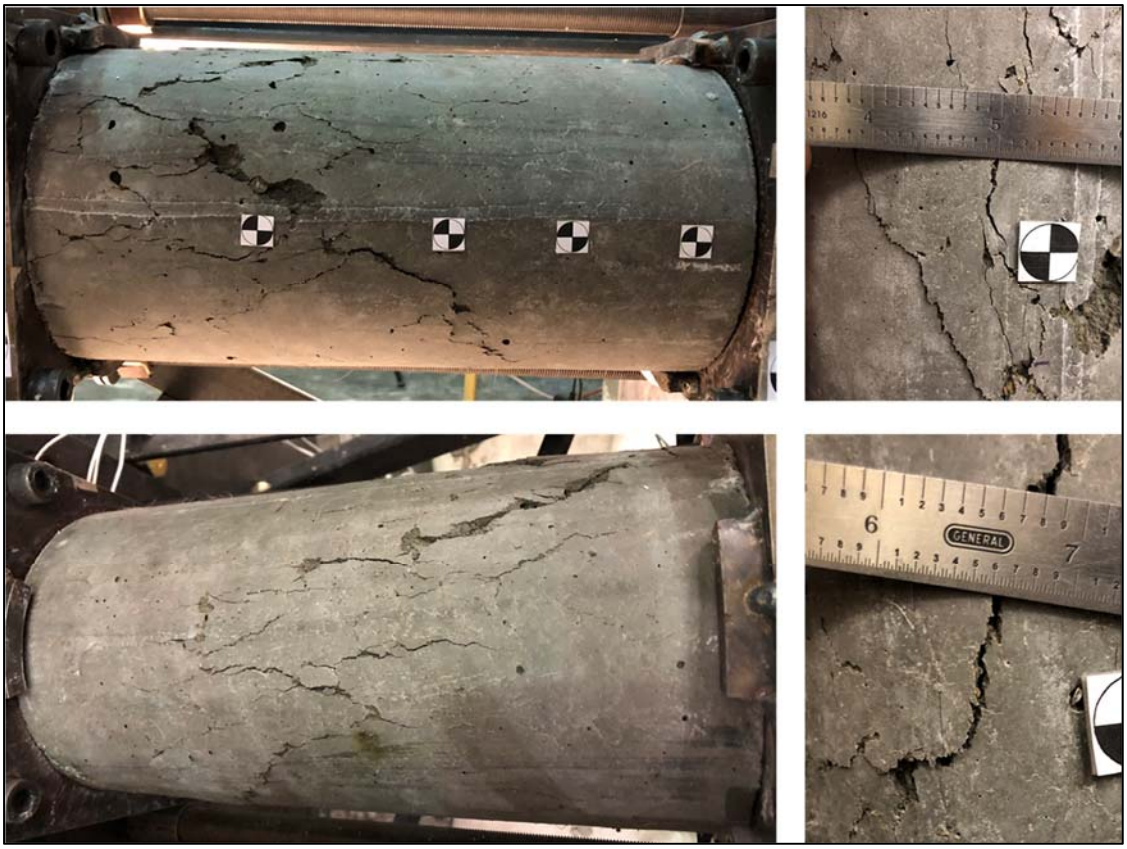

Figure 68: Cracking observed on specimen from Test 2-9

4.4.4 Double Hit Impulsive Test Case

During Test Series 2, one additional test was conducted at the same impact velocity as tests 2-7 and 2-8. During this test, flyer plate struck the blast generator pusher plate after rebounding from the experimental setup, which caused it to travel forwards again and impact the experimental setup a second time. This resulted in a double hit with two peaks in the force versus time history, as shown in Figure 69. In the subsequent tests 2-7 and 2-8, the double hit was eliminated by moving the starting position of the flyer plate and blast generator piston back several inches to increase the free flight distance of the flyer plate. Although this double hit was inadvertent, the results of this test case illustrate the potential

use of this test system to intentionally apply repeated impacts within a time span of a few milliseconds. The specimen was extremely damaged after the double hit but was still just barely balanced in the test rig, as shown in Figure 70. The specimen separated into pieces representative of a double cone failure mode upon removal from the test rig. The fracture surfaces primarily traveled through the cement paste matrix and along the interfacial transition zone instead of through the aggregate. This behavior is expected for early age concrete due to the high porosity in these regions.

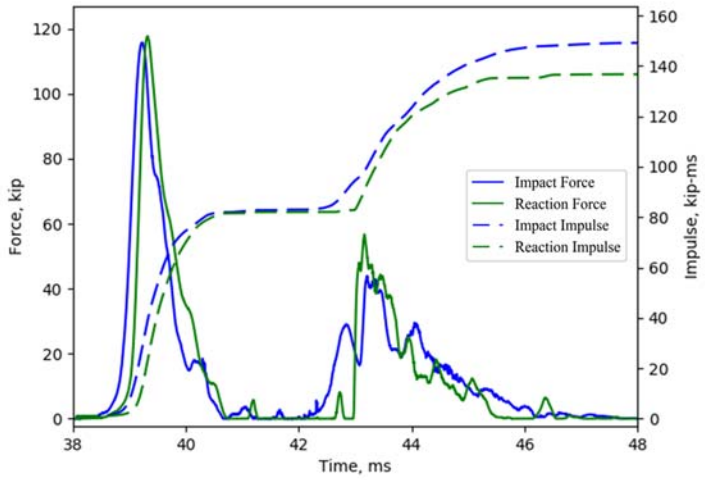

Figure 69: Force and impulse time history of double hit test case

Figure 70: Heavily damaged double hit specimen in test rig

Figure 71: Double cone failure mode of double hit specimen

4.5 Conclusions

An experimental test series was conducted to evaluate the performance of the dynamic test system and to investigate the behavior of plain concrete subjected to impulsive loads. The dynamic test setup was successful in applying impulsive loads on concrete specimens ranging from 31.2 lbf-ms to 86.0 lbf-ms in magnitude. The test system performance was evaluated to establish relationships between the system inputs and outputs and aid in the design of future test series. The test results showed a clear relationship between the kinetic energy of the flyer plate and the resulting impulse imparted on the specimen and the strain rate. Based on this established relationship between applied kinetic energy and strain rate, the theoretical upper limit of strain rates possible with this test system is 60 s^{-1}. Future test series can target higher strain rates by increasing the mass of the flyer plate and modifying the load cell instrumentation scheme to accommodate higher levels of impulsive loading.

The behavior of concrete subjected to dynamic loads was evaluated in Test Series 2 by examining the displacement time history, and visual indicators of damage in the form

of macrocracks were assessed. Improving the instrumentation scheme of the experiment to better capture the displacement time history during the impulsive load will provide improved metrics for quantifying the behavior of the concrete specimens. The rise time of the applied impulsive load through the specimen was approximately 0.4 milliseconds. To provide at least ten data points to characterize this time period, a frame rate of 25,000 fps is required. Achieving this frame rate at sufficient resolution with the high speed camera system used in this experimental program was not possible, so additional diagnostics should be incorporated.

Finally, the dynamic test setup has the additional capability of subjecting the same specimen to multiple repeated impulses. Two impulses can be generated within the timespan of a few milliseconds by intentionally rebounding the flyer plate off of the blast generator pusher plate. In this case, the second impulse is lower in magnitude due to a loss of momentum in the flyer plate. An alternative method to provide better control over the repeated impulsive loading is to simply reset the flyer plate and conduct the firing sequence of the blast generator. For this case, repeated impulses can be generated at approximately 10 minute intervals.

CHAPTER 5. RESIDUAL CAPACITY OF CONCRETE SUBJECTED TO IMPULSIVE LOADS

5.1 Introduction

An experimental study was devised and conducted to investigate the residual capacity of concrete subjected to impulsive loads. The reduction in strength, stiffness, and work of plain concrete cylinders was quantified for varying levels of applies impulsive loading. The observed trends of the reduction in strength versus stiffness for the impulsively damaged specimens were compared to experimental and analytical data for concrete damaged by quasi-static cyclic loading. This chapter describes the materials and methods used in the test series and discusses the significant results and observations.

5.2 Materials and Methods

5.2.1 Materials

This experimental series used the concrete cylinders that were damaged from impulsive loading in the dynamic test series. Table 5 summarizes the information for each test case along with relevant impulsive loading results from the dynamic test.

Table 5: Residual capacity test series information

Test Series ID	Specimen Age	Concrete Design Strength, psi	Maximum Impact Force, kip	Maximum Reaction Force, kip	Impact Impulse, lbf-ms	Reaction Impulse, lbf-ms
2-1	3 day	3500	60.4	64	59.3	57.4
2-2	3 day	3500	83.7	85.7	68.2	70.3
2-3	4 day	3500	88	98.2	72.3	74.3
2-4	3 day	3500	75.7	87.2	67	70
2-5	3 day	3500	80.9	88.2	73.2	74.6
2-6	3 day	3500	98.5	100.4	76.9	77.5
2-7	4 day	3500	112.5	114.6	79.1	79.7
2-8	4 day	3500	103	124	80.2	79.8
2-9	4 day	3500	127.7	133	86	84.4

5.2.2 Experimental Method

To perform residual capacity testing, the specimen is removed from the dynamic test setup immediately after the dynamic test and placed in a hydraulic compression machine. The test procedure outlined in section 3.4.1 is followed to determine the force-displacement behaviour of the damaged cylinder until failure, and cyclic loading is then performed to capture the descending branch of the force-displacement curve. After testing the damaged sample, the quasi-static test procedure is immediately repeated with a sample from the same concrete batch to determine the full force displacement curve of a representative undamaged sample.

5.3 Theory and Calculation

5.3.1 Calculation of Mechanical Properties

The mechanical properties considered in this study include the maximum compressive strength and the elastic modulus. The compressive strength is simply defined as the maximum force during compressive loading. Because the ascending portion of the force versus displacement curve is nonlinear, three types of elastic moduli are often computed [2]:

1) Tangent modulus: determined as the slope of a line drawn tangent to the force versus displacement curve at any point.
2) Secant modulus: determined from the slope of a line drawn between the origin of the curve to a point corresponding to 40 percent of the maximum compressive load.
3) Chord modulus: determined as the slope of a line connecting any two points on the curve.

For this experimental study, the elastic modulus was determined by quantifying the tangent modulus at a point corresponding to 40 percent of the maximum compressive load. The slope of this portion of force versus displacement curve was determined by performing a linear regression of the region of the curve corresponding to 35 to 45 percent of the maximum compressive load. The elastic modulus is then determined by converting the force and displacement to engineering stress and strain. Figure 72 shows an example of typical force versus displacement curves for residual capacity (RC) and baseline test specimens (QS). The portion of the curves used to compute the elastic moduli are highlighted in red, and the corresponding linear fits and R^2 values are listed.

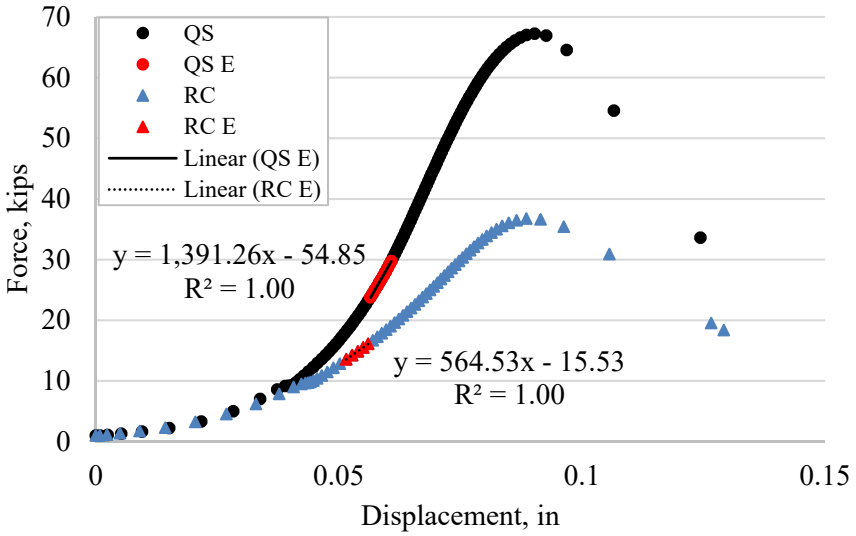

Figure 72: Force versus displacement curves and elastic moduli calculations for Test 2-7 residual capacity and baseline specimens

5.3.2 Cyclic Loading to Determine Envelope Curve

Determining the descending branch of the force versus displacement curve for concrete is typically difficult without the use of specialized testing machines and controlled hydraulics that limit the release of the stored strain energy in the machine as the specimen begins to fail. A direct determination of the envelope curve from a single compression test is generally not possible with the type of standard compression machine that was used in this test series. To circumvent this problem, cyclic loading was performed on the samples to determine the full force versus displacement curve. By performing the compression loading in cycles and controlling the unloading of the hydraulic compression machine, the release of the strain energy in machine is reduced and several data points corresponding to the descending branch of the curve can be collected with each cycle of loading. The

envelope curve formed by connecting these points is equivalent to the full force versus displacement curve of a monotonic uniaxial compression test [54].

Figure 73 shows typical force versus displacement curves resulting from the cyclic loading procedure for a residual capacity and undamaged baseline specimen. For most test case, the specimen was loaded three times to determine the full force displacement curve. After the first loading cycle, the specimen is still intact with some visible external macrocracking. After the second loading cycle, the macrocracks are larger in size and distribution. Finally, the specimen disintegrates during the third loading cycle. By not resetting the displacement from the initial zeroed valued at the start of the test during the subsequent cycles, the cyclical loading resulted in a smooth descending branch. However, for a few of the tests, the zeroed displacement was reset between loading cycles so the displacement was shifted in these cases to form a smooth descending branch. Attaching a compressometer to the specimen would be advantageous by directly measuring the displacements and moduli of cylinder with each cycle rather than relying on the displacement as measured from the compression machine platens.

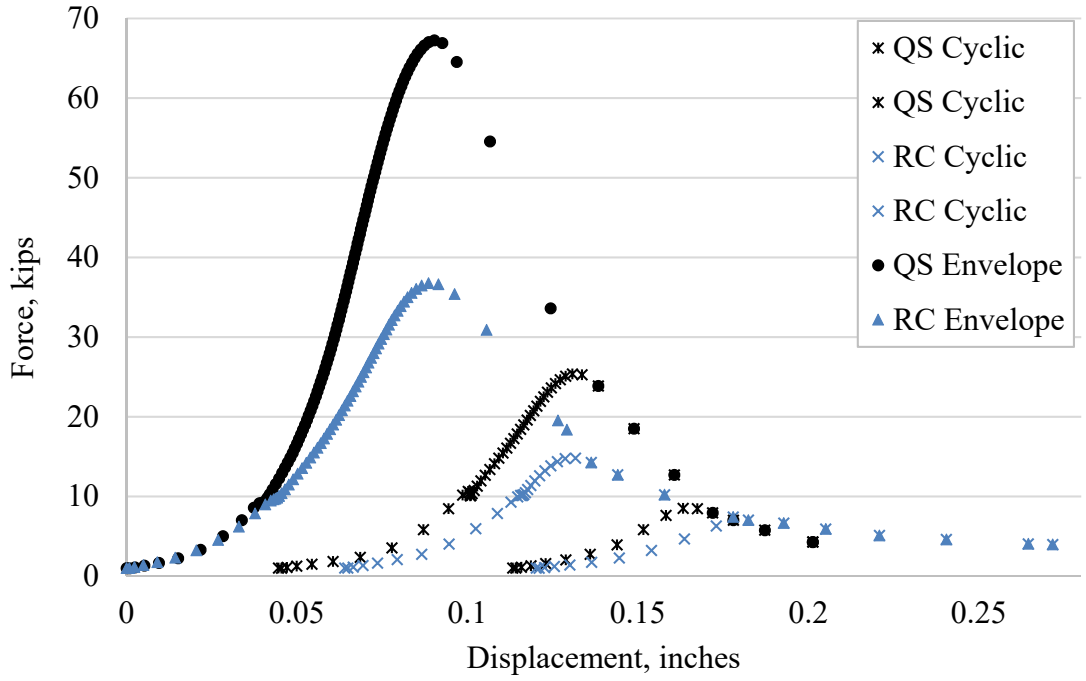

Figure 73: Cyclic loading conducted on Test 2-7 residual capacity and baseline specimens

The initial slopes of the force displacement curves in Figure 72 and Figure 73 are artificially low due to the slack in the compression machine before the sample becomes fully engaged under the applied load. To correct this, data points corresponding to this initial portion of the curve were removed and the elastic modulus was used to draw a linear fit of the data between 0 percent and 40 percent of the maximum force. Finally, the curve was shifted along the x-axis to begin at a point corresponding to zero force and displacement. Figure 74 shows the final envelope curves for a typical test with the corrected initial elastic regions.

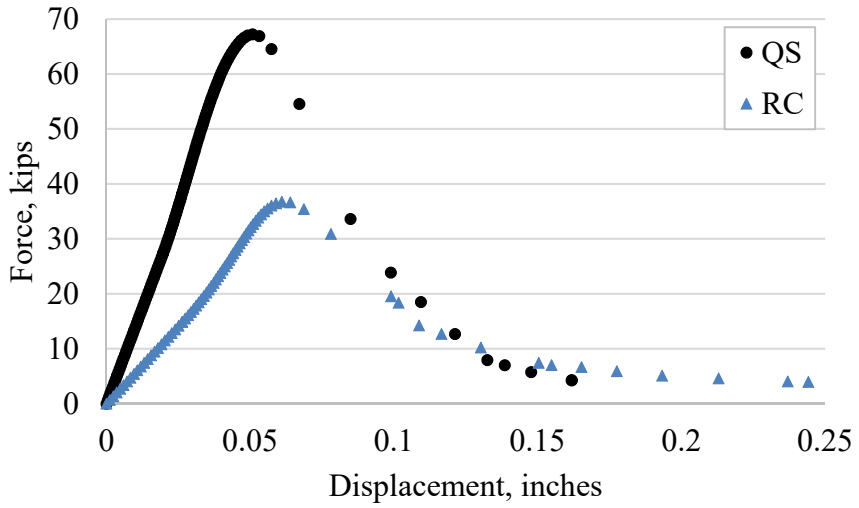

Figure 74: Envelope curves for Test 2-7 residual capacity and baseline specimens with corrected initial elastic regions

5.3.3 Quantification of Residual Capacity

The residual capacity of impulsively damaged specimens is quantified by evaluating three different metrics that define the mechanical behavior: the residual maximum compressive strength, the residual elastic modulus, and the residual work. The work is calculated by numerically integrating the force versus displacement envelope curve. These metrics for the damaged specimen are then compared to the compressive strength, elastic modulus, and work for an undamaged baseline specimen. The normalized residual strength, modulus, and work ratios are calculated by equations 5.1 – 5.3,

$$F_{r,norm} = \frac{f_{cr}}{f_{c,baseline}} \tag{5.1}$$

$$E_{r,norm} = \frac{E_r}{E_{baseline}} \tag{5.2}$$

$$w_{r,norm} = \frac{w_r}{w_{c,baseline}} \quad (5.3)$$

where f_r, E_r, and w_r, are the residual compressive strength, modulus and work of the damaged specimen, and $f_{c,baseline}$, $E_{baseline}$, and $w_{baseline}$ are the compressive strength, modulus, and work of the undamaged specimen. Determining the total work under the force verses displacement curves proved to be somewhat subjective, as the curves terminated at different levels of force and displacement for each test. To standardize this measurement for comparative purposes, the work corresponding to a maximum displacement of 0.15 inches was used.

5.3.4 Impulsive Loading Metrics: Impulse versus Force

Two primary metrics that are used to quantify the intensity of the impulsive loading event include the maximum force during the dynamic event and the impulse. Load cells are located on both sides of the cylinder to provide a measure of the force and impulse on the impact and reaction sides of the specimen. To characterize the severity of the dynamic loading event, the force and impulse measured on the impact side of the specimen is used instead of the reaction side because the behaviour of the specimen during the test influences the reaction impulse and force measurements. When the specimen does not accumulate damage during the impulsive loading, the impulse measured on the reaction side is slightly higher than the impact side, as discussed in Section 4.4.1. Once the impulsive loading is high enough to damage the specimen, the process of damage dissipates energy in the system and the reaction impulse and force decreases. Thus, the impact impulse and force should be used to characterize the inputs to the specimen.

It is unclear which metric has a greater influence on the damage of the specimen of this size: force or impulse. The impulse is more closely related to the kinetic energy imparted to the system by the flyer plate than the maximum force. Figure 75 (a) and (b) plot the relationship between the kinetic energy and the maximum impact force and the impact impulse, respectively. The impulse is more closely related to the kinetic energy input to the system than the maximum force ($R^2 = 0.96$ vs $R^2 = 0.93$). Results from Test Series 1 illustrated that the programmer has a significant influence on the shape of the force versus time history for the same levels of applied impulse, as explained in Section 3.3.6. Thus, the impulse more accurately characterizes the severity of the dynamic load because the maximum force is dependent on the behaviour of the programmer. For comparative purposes, the impact impulse is the primary metric that is used to characterize the dynamic loading event for this experimental program. To evaluate whether the magnitude of the impulse or the maximum force is more influential on imparting damage in concrete, the flyer plate programmer material can be changed to manipulate the pulse duration and magnitude of the dynamic load while the impulse remains constant.

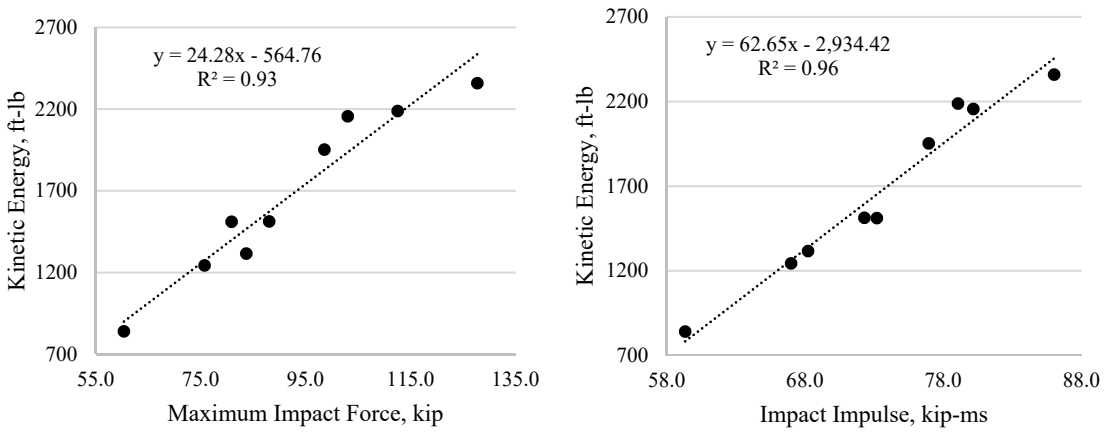

(a) (b)

Figure 75: Kinetic energy versus (a) maximum impact force and (b) impact impulse for Test Series 2

5.4 Experimental Results and Discussion

5.4.1 Test Data and Observations

The major numerical results for the residual capacity test series are shown in Table 6. Cyclic loading was not performed for Tests 2-1, 2-2, and 2-3, so baseline and residual work was not computed for these cases. For Test 2-9, the residual capacity work was not calculated because specimen disintegrated after the first loading cycle and the entirety of the force versus displacement envelope curve could not be determined. Figure 76 shows the force versus displacement envelope curves for the baseline and residual capacity specimens from Test 2 through Test 9. Figure 77 shows the corresponding work versus displacement computed from the envelope curves.

Table 6: Residual capacity test series results

Test Series ID	2-1	2-2	2-3	2-4	2-5	2-6	2-7	2-8	2-9
Impact Impulse, kip-ms	59.3	68.2	72.3	67.0	73.2	76.9	79.1	80.2	86.0
Maximum Impact Force, kip	60.4	83.7	88.0	75.7	80.9	98.5	112.5	103.0	127.7
Baseline Strength, kip	55.8	58.8	64.8	60.7	60.1	61.9	67.2	68.8	70.8
Residual Strength, kip	54.7	50.9	59.5	55.9	53.7	37.0	36.8	40.3	17.9
Residual Strength Ratio	**0.980**	**0.865**	**0.918**	**0.922**	**0.893**	**0.597**	**0.547**	**0.585**	**0.253**
Baseline Modulus, ksi	529	581	633	544	509	573	590	712	729
Residual Modulus, ksi	510	337	474	413	394	246	240	278	120
Residual Modulus Ratio	**0.965**	**0.579**	**0.748**	**0.760**	**0.773**	**0.429**	**0.406**	**0.391**	**0.165**
Baseline Work, ft-lb	-	-	-	398	392	368	392	448	463
Residual Work, ft-lb	-	-	-	309	341	251	237	229	-
Residual Work Ratio	-	-	-	**0.777**	**0.869**	**0.683**	**0.604**	**0.511**	-

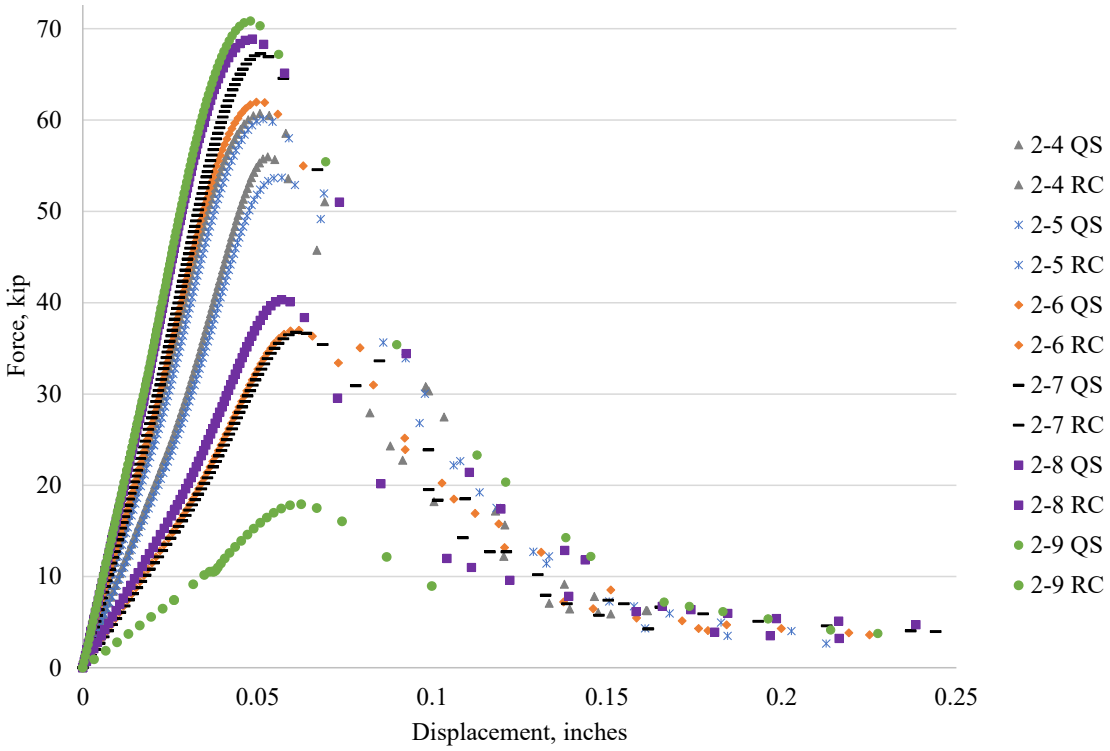

Figure 76: Force versus displacement envelope curves

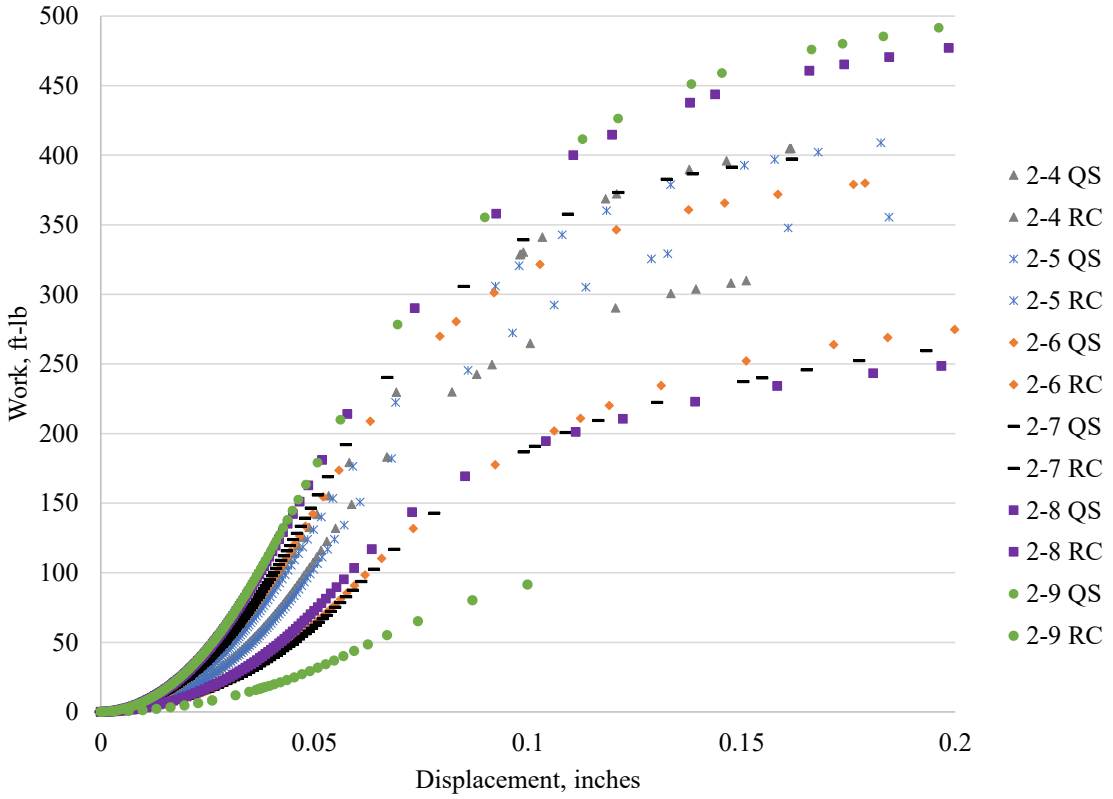

Figure 77: Work versus displacement curves

Table 7 lists the averages and standard deviations of the compressive strength, modulus, and work for the baseline specimens from the test series. The statistical measures are reported for the entire test series as well as for Test 2-4 through 2-9, for which the envelope curves were determined. There is some variability in the mechanical properties of the specimens used in this test series, with the elastic modulus having a higher percent standard deviation than the compressive strength.

The standard deviation in the baseline mechanical properties should not have a large influence on the normalized residual capacity ratios, because each residual capacity measurement is normalized by the baseline measurement specific to that specimen. So, as long as the differences in mechanical behavior are not large enough to result in changes to

how the material damages and responds to impulsive loading, there is theoretically less uncertainty in the residual capacity ratios.

Table 7: Normalized baseline metric averages and standard deviations

Normalized Residual Capacity Metric	Average	Standard Deviation	Percent Standard Deviation
Full Test Series 2: Tests 2-1 through 2-9			
Undamaged Compressive Strength, kip	63.2	4.71	7.44%
Undamaged Elastic Modulus, ksi	600	72.9	12.14%
Envelope Curve Tests: Test 2-4 through 2-9			
Undamaged Compressive Strength, kip	64.9	4.19	6.46%
Undamaged Elastic Modulus, ksi	610	82.3	13.51%
Undamaged Work at 0.15 inches, ft-lb	410	33.7	8.22%

To provide a better visual comparison between the baseline and residual capacity envelope curves, the incremental force values are normalized by the maximum compressive baseline strength for each test, as displayed in Figure 78. Displayed in this format, the overall shape of the envelope curves is clearer and the trends in the residual capacity tests can be observed more easily. The residual capacity envelope curves show a clear decrease in both the stiffness and the maximum force with increasing levels of impulsive load.

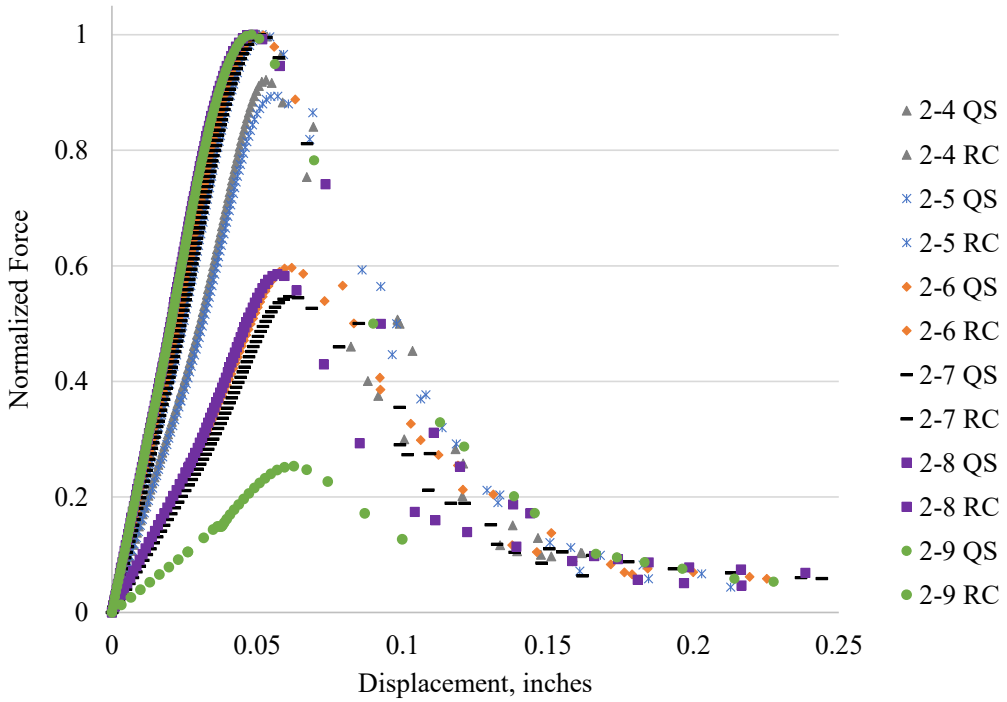

Figure 78: Normalized force versus displacement curves

As the data is portrayed in Figure 78, the envelope curves formed by the residual capacity specimens fall entirely below the baseline strength envelope and the residual descending branches do not align with the descending branch of the baseline specimens. In reality, the origin of the residual capacity curves should be shifted along to the x-axis to correspond to the amount of residual strain in the specimen. Because the exact amount of residual strain in the damaged specimens is unknown, the quasi-static residual envelope curves are presented as starting at zero strain. However, the amount of residual strain in the damaged specimens was qualitatively notable during the test series. Prior to the impulsive loading, the dynamic test rig restrained the specimen to provide a snug tight compressive fit with no observable gap between the specimen and the endcap plates. After the impulsive loading, the snug tight fit was significantly reduced, the fit of the specimen

was much looser, and a gap existed between the endcap plates and the specimen. Figure 79 illustrates the observed gap in the endcap plates.

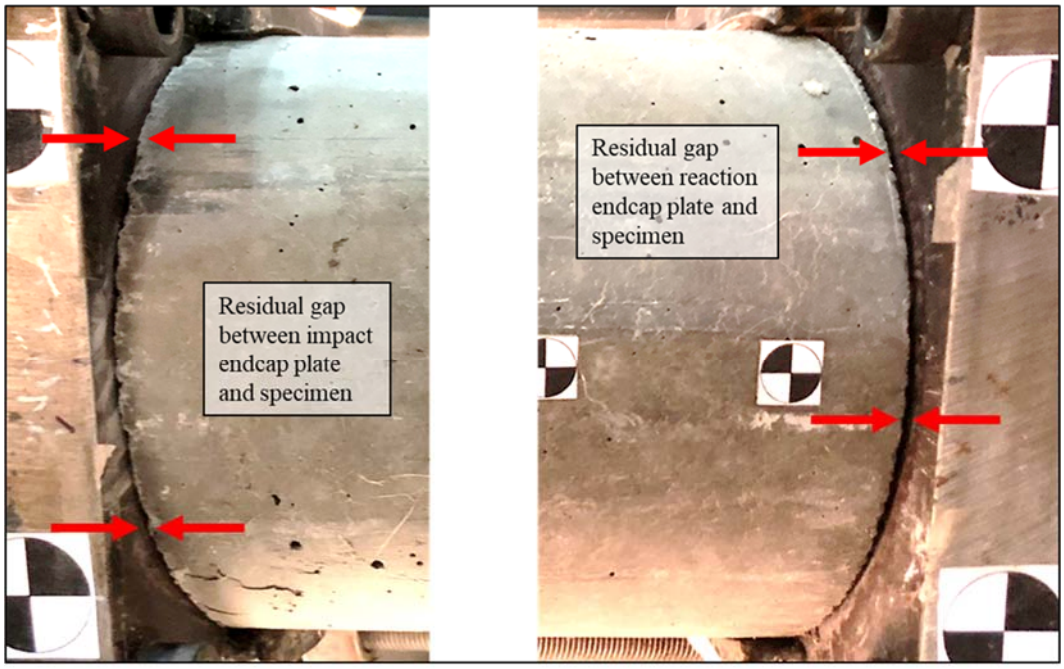

Figure 79: Observed residual gap between specimen and endcap plates for (a) Test 2- 8 and (b) Test 2-9

5.4.2 Residual Capacity Ratio Comparisons

Figure 80 shows the residual ratios of force, modulus, and work versus the maximum impact force during the dynamic test, and Figure 81 shows the residual ratios versus the impact impulse. Overall, there is a clear decreasing trend for all residual ratios with increasing impact force and impulse. For every test case, the residual modulus ratio is lower than the residual force ratio. The work ratio shows less of a clear trend in comparison to the other residual capacity metrics. This is likely because the termination of

the work calculation was fairly subjective for the residual capacity tests. In reality, the work calculation might be more consistent if extent of the work calculation was chosen as a function of the residual strain in the material. However, an overall decreasing trend appears to be present despite the scatter.

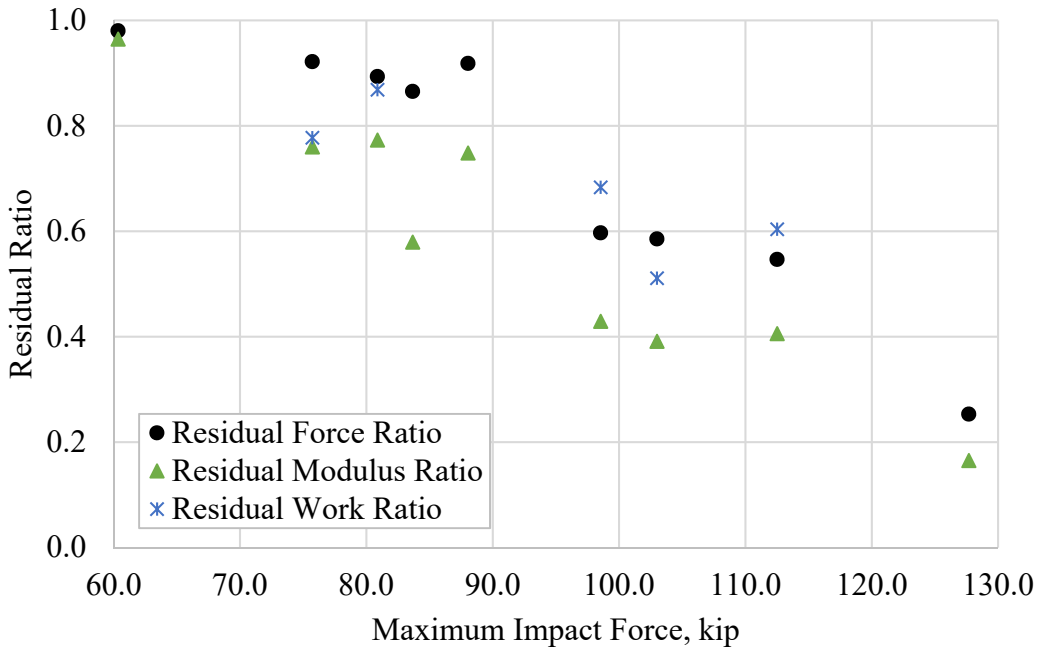

Figure 80: Residual capacity ratios versus maximum impact force

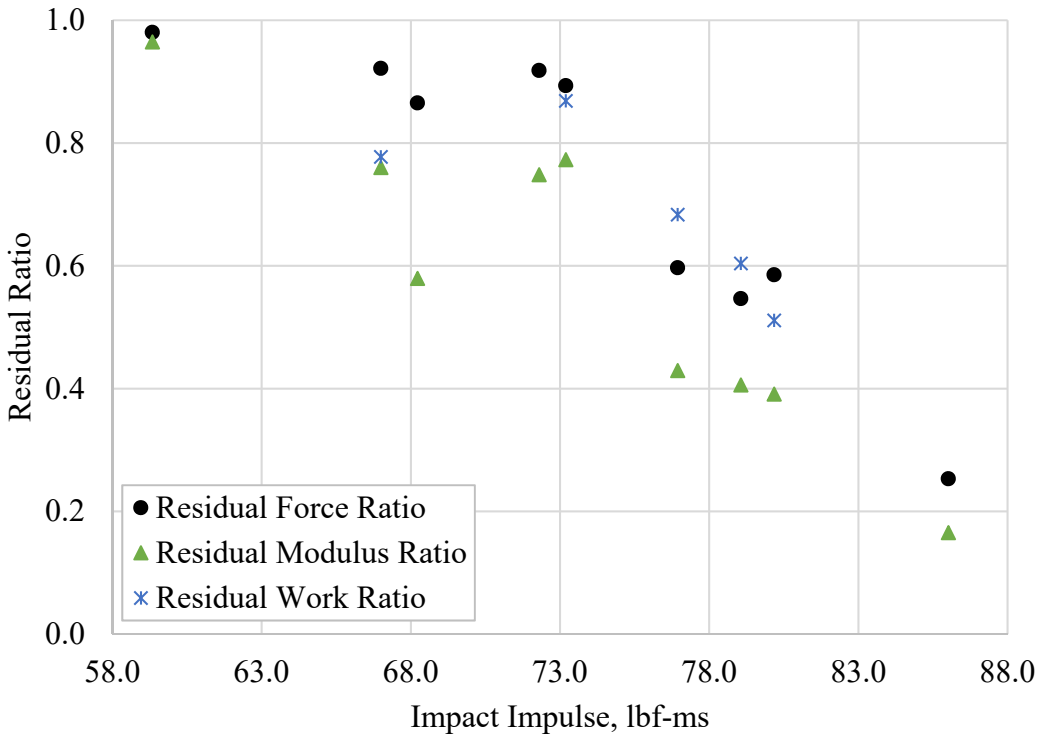

Figure 81: Residual capacity ratios versus impact impulse

Figure 82 plots the residual strength ratio versus the residual modulus ratio to provide a visual comparison of how they evolve with respect to each other. At the (1.0, 1.0) point on this figure, there is no reduction in residual strength and modulus. The plotted values decrease in magnitude as the level of applied impulsive force and impulse increase. However, their reduction is not linearly proportional as the residual modulus decreases much faster than the residual strength ratio. This trend shows that the material experiences a fairly significant loss of stiffness before a notable decrease in strength occurs.

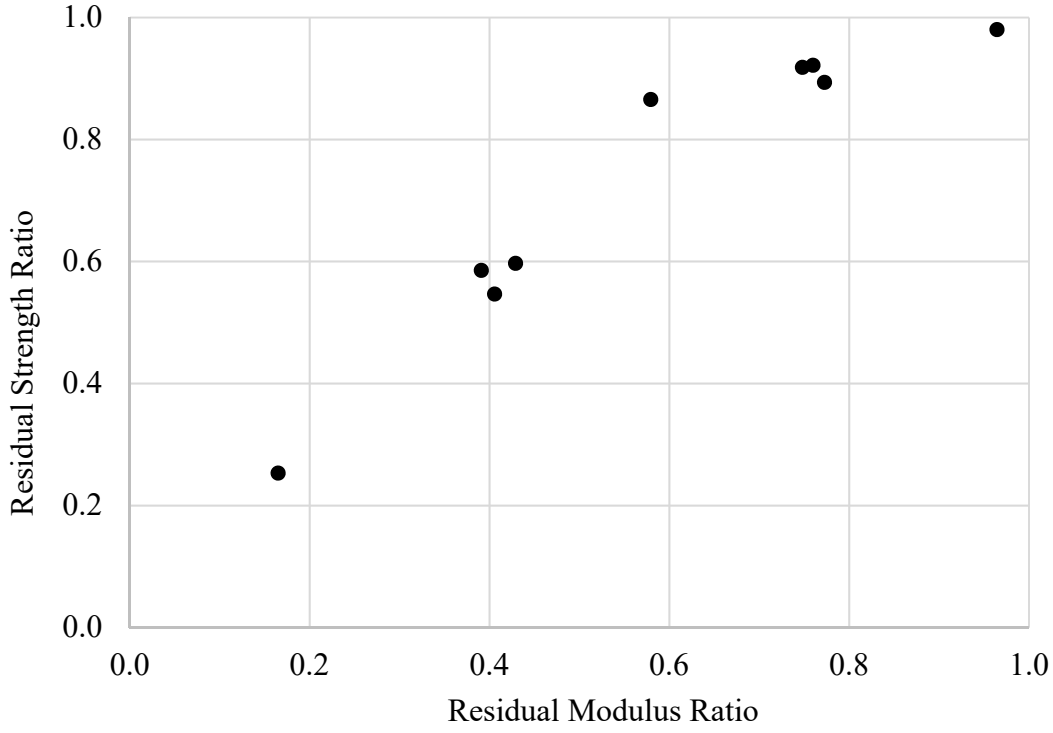

Figure 82: Residual strength ratio versus residual stiffness ratio

5.4.3 Comparing the Behaviour of Impulsively Damaged Concrete with Quasi-statically Damaged Concrete

The experimental residual capacity results show that for impulsively damaged concrete, there is a fairly significant loss of stiffness before a notable decrease in strength occurs with increasing levels of impulsive loading. To provide insight on whether this phenomenon is specific to impulsively damaged concrete or if it is typical behaviour for mechanically damaged concrete in general, the impulsive residual capacity results are compared to the residual capacity of quasi-statically damaged concrete. The experimental data obtained from the cyclical baseline specimen tests provide a measure of the post-peak

residual capacity of the concrete as it accumulates damage. A cyclic loading model is calibrated to the experimental data to provide additional comparisons on the degradation of strength and modulus that occurs with cyclic loading.

The cyclic tests conducted on the baseline specimens 2-4 through 2-9 are evaluated to determine the residual modulus and strength ratios of the specimen at the second loading cycle. The third loading cyclic was not used, as there were generally too few data points to obtain a meaningful measure of the modulus. Table 8 summarizes the residual modulus and strength for each test. The residual modulus is determined from the slope of the reloading curve at cycle two, and the residual force is the maximum force obtained during reloading.

Table 8: Baseline specimen residual capacity measurements at loading cycle 2

Test Series ID	Baseline Modulus, ksi	Baseline Force, kip	Cycle 2 Residual Modulus, ksi	Cycle 2 Residual Force, kip	Residual Modulus Ratio	Residual Strength Ratio
2-4	544	60.7	280	31.3	0.515	0.516
2-5	509	60.1	193	24.4	0.378	0.406
2-6	573	61.9	308	26.3	0.538	0.425
2-7	590	67.2	264	25.4	0.447	0.377
2-8	712	68.8	266	23.6	0.374	0.343
2-9	729	70.8	271	24.3	0.372	0.344

The residual ratios obtained from the baseline experiments range between values of approximately 0.3 – 0.5. To provide a better understanding of the typical evolution of concrete modulus and strength for a wider range of damage, the cyclic loading analytical

model developed by Darwin and Pecknold [55] was used to produce more data points for comparison. The model, as shown in Figure 83, is comprised of idealized and approximated loops that are based on the experimental findings of Karsan and Jirsa [56].

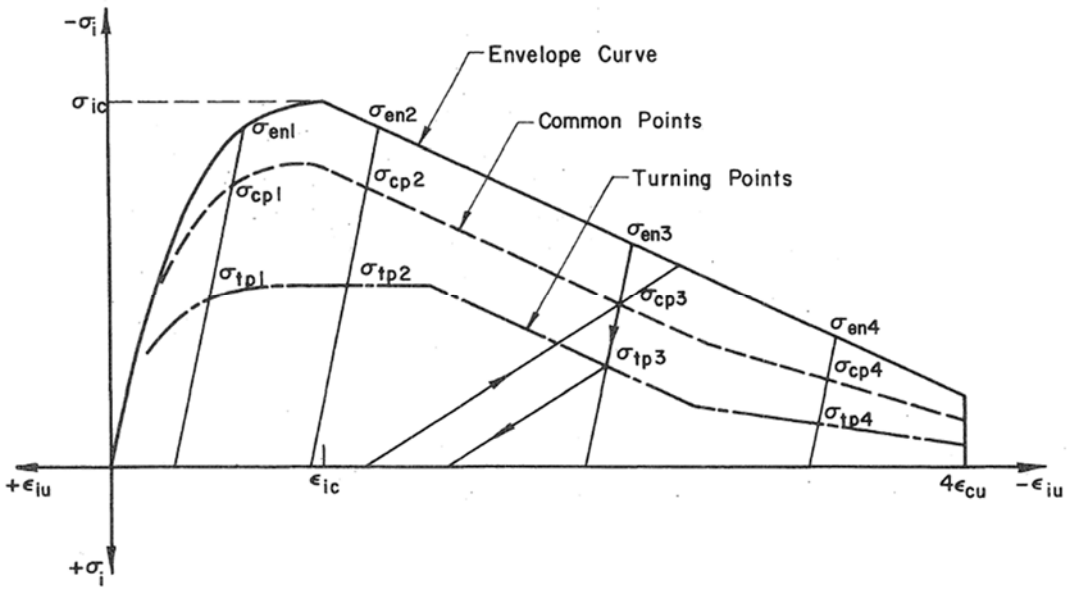

Figure 83: Analytical model for the compressive cyclical loading of concrete [55]

The response of the model is bound by the envelope stress versus strain curve. Equation 5.4 proposed by Saenz [57] describes the ascending branch of the envelope curve, and the descending branch is approximated as a straight line passing through two points (f_c', ε_c) and $(0.2f_c', 4\varepsilon_u)$:

$$\sigma = \frac{E_0 \varepsilon}{1 + [(E_0/E_s) - 2](\varepsilon/\varepsilon_c) + (\varepsilon/\varepsilon_c)^2} \tag{5.4}$$

where f_c' is the maximum compressive strength, ε_c is the strain at f_c', E_0 is the initial tangent modulus at zero stress, and $E_s = f_c'/\varepsilon_c$. An empirical relationship exists between the strain on the envelope curve at unloading and the residual plastic strain at zero stress:

$$\frac{\varepsilon_p}{\varepsilon_c} = 0.145\left(\frac{\varepsilon_{en}}{\varepsilon_c}\right)^2 + 0.13\left(\frac{\varepsilon_{en}}{\varepsilon_c}\right) \quad (5.5)$$

where ε_p is the residual plastic strain and ε_{en} is the strain on the envelope curve at unloading. The behaviour of the unloading and reloading cycles are defined by a locus of "common points" and "turning points," which are represented by curves. The common point curve relates to the degradation of concrete under continued cycles of load, and the turning point curve controls the energy dissipation in each cycle. Darwin and Pecknold provide expressions for these curves based on Karsan and Jirsna's experimental data [56] for standard concrete as given in Equations 5.6 – 5.13.

$$\sigma_{cp1} = \frac{5}{6}\sigma_{en1} \quad (5.6)$$

$$\sigma_{tp1} = \frac{1}{2}\sigma_{en1} \quad (5.7)$$

$$\sigma_{cp2} = \sigma_{en2} - Min(\frac{1}{6}\sigma_{en2}, \frac{1}{6}f_c') \quad (5.8)$$

$$\sigma_{tp2} = Min(\frac{1}{2}\sigma_{en2}, \frac{1}{2}f_c') \quad (5.9)$$

$$\sigma_{cp3} = \sigma_{en3} - \frac{1}{6}f_c' \quad (5.10)$$

$$\sigma_{tp3} = \sigma_{en3} - \frac{1}{3}f_c' \quad (5.11)$$

$$\sigma_{cp4} = \frac{2}{3}\sigma_{en4} \quad (5.12)$$

$$\sigma_{tp4} = \frac{1}{3}\sigma_{en4} \quad (5.13)$$

At low values of strain, the unloading path follows a slope of E_0. For higher values of strain, the reloading path is approximated by a straight line from (ε_p,0) through the common point. The unloading curve is represented with three lines, the first at a slope of E_0 down to the turning point, then from the turning point down to zero stress at a slope equal to the reloading line, and the third with zero slope. The slope of the reloading curve represents the updated elastic modulus of the material at each cycle.

Because the envelope curve was experimentally determined for the quasi-static baseline tests in this experimental program, the envelope curve from Test 2-7 was used instead of the expressions recommended by Darwin and Pecknold. The incorporation of this known data improves the accuracy of the model and the common point and turning point curves were determined based on the experimental envelope stress values. Four loading cycles were performed with the model to determine the predicted loss of modulus and strength at different points along the ascending branch of the envelope curve. The curves and the unloading and reloading paths for each cycle are shown in Figure 84, and the residual modulus and strength values and ratios from each cycle are listed in Table 9.

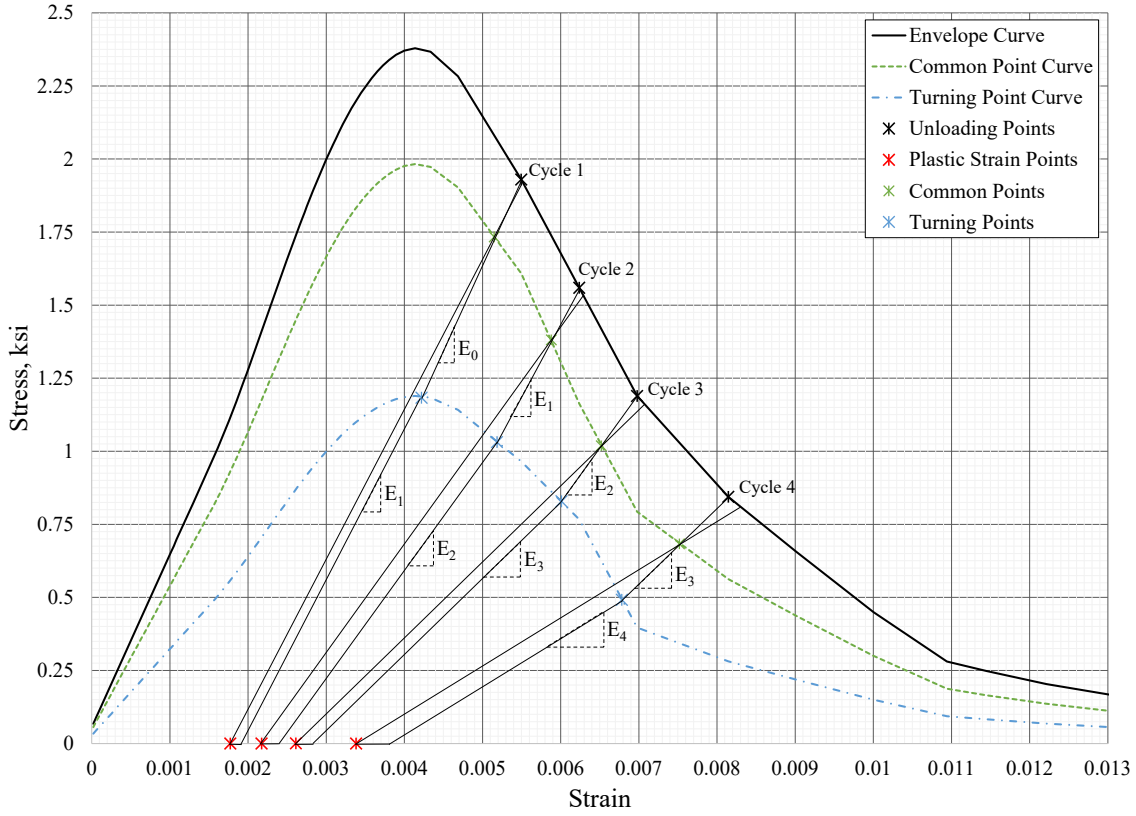

Figure 84: Darwin and Pecknold cyclic model [55] adapted to Test 2-7 envelope curve with four loading cycles

Table 9: Predicted residual modulus and strength values for Darwin and Pecknold model loading cycles on Test 2-7 envelope curve

Loading Cycle	Residual Modulus	Residual Strength	Residual Strength Ratio	Residual Modulus Ratio
Cycle 1	513	1.92	0.807	0.869
Cycle 2	373	1.53	0.645	0.631
Cycle 3	261	1.16	0.488	0.442
Cycle 4	165	0.81	0.341	0.280

Figure 85 plots the residual strength versus residual modulus ratios for the impulsively damaged specimens, the quasi-static cyclic specimens, and the Darwin and Pecknold cyclic model predictions. The accuracy of the analytical model predictions can be evaluated by comparing the predictions to the experimentally determined values. Due to simplifying assumptions in the model behaviour, the predicted residual strength should be artificially higher than the experimental behaviour because the model assumes that no softening occurs in the material as the new maximum stress is approached during reloading cycles. So, the analytical values provide an upper bound on the residual strength predictions. Considering this, the analytical model provides an excellent fit to the experimental trends in residual strength versus modulus.

The quasi-static cyclic results display a different trend from the impulsively damaged specimens in that the loss of strength versus modulus is nearly proportional. This indicates that the residual capacity trend of the impulsively damaged specimens is likely caused by a phenomenon unique to the impulsive loading. For lower levels of impulsive loading, the damage manifests in some way that mainly affects the stiffness of the material while having little effect on the strength. It is possible that this is caused by dynamic fracture, where the high strain rate cause cracking to occur in the form of non-localized finely distributed microcracks that reduce the stiffness of the material while having relatively little effect on the strength. The use of advanced diagnostics such as micro computed tomography is needed to further investigate the damage mechanisms involved.

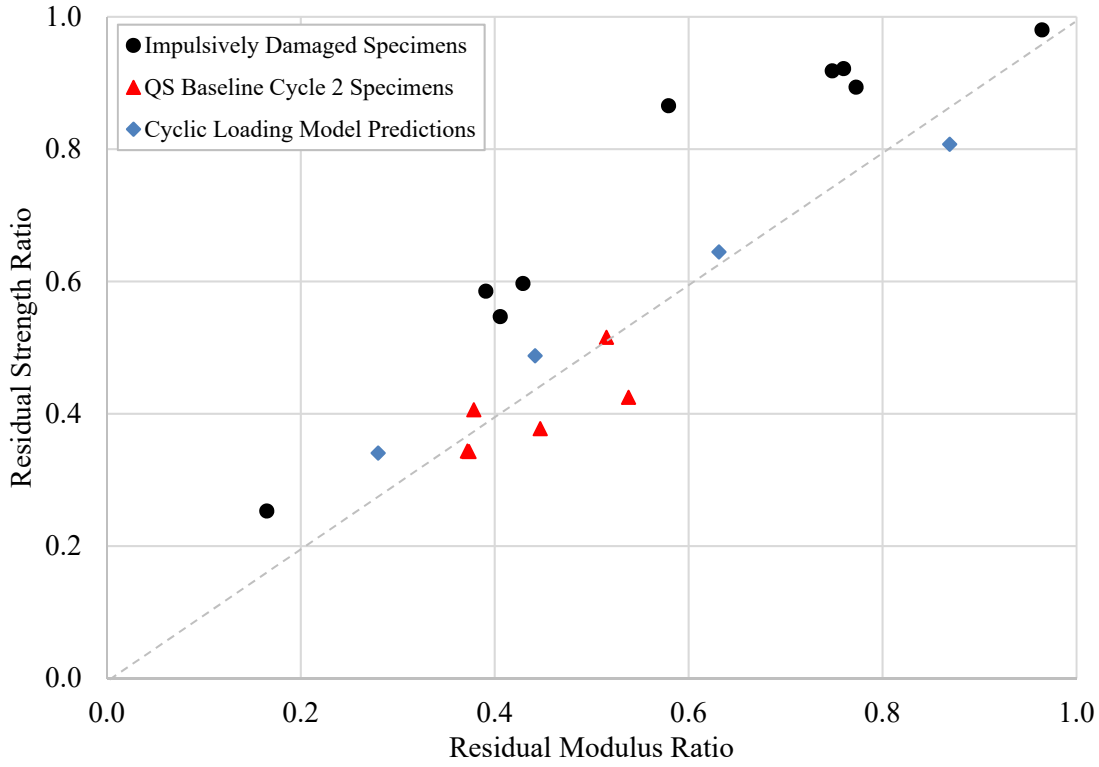

Figure 85: Residual strength versus residual modulus ratios for impulsively damaged specimens, quasi-static cyclic specimens, and cyclic loading model predictions

5.4.4 Dynamic Residual Capacity: Double Hit Impulsive Test Case

The double hit test case described in section 4.4.4 provides a measure of the dynamic residual capacity of the concrete in Test Series 2. This test was performed on a 4-day old specimen at the same impact velocity as tests 2-7 and 2-8. After the second hit, the specimen was extremely damaged and had zero residual capacity. Because the specimen was just barely balanced in the test rig as disintegrated upon removal, it can be assumed that the second peak in the force time history was equivalent to the residual capacity of the material. Figure 86 shows the damaged specimen after the double hit, and Figure 87 shows the force and impulse time history.

Figure 86: Specimen from double hit impulsive test case

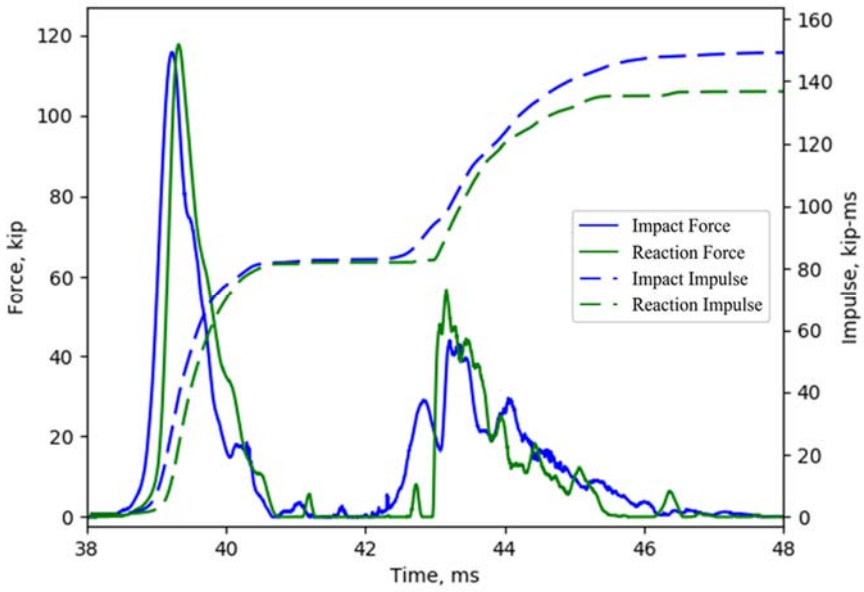

Figure 87: Force versus time history of dynamic residual capacity specimen

The first impulsive hit showed the characteristics of a typical dynamic test. The reaction force was slightly higher than the impact force, but the impact impulse was higher than the reaction impulse. Because the reaction impulse is lower, this indicates that the specimen accumulated damage during the first impact causing the energy in the system to reduce. The second impact is characterized by a longer pulse duration and lower magnitude

force, with the reaction force higher than the impact force but the impact impulse again higher than the reaction impulse. The dynamic residual capacity of the specimen can be determined as the magnitude of the second impulse divided by the baseline strength of the specimen. The true force in the specimen is likely somewhere between the impact and reaction values, so both are considered. Table 10 lists the numerical results for the two impulsive hits as well as the baseline strength and the impulsive residual force ratios.

Table 10: Double hit test results

First Hit Impact Impulse, kip-ms	81.97
First Hit Reaction Impulse, kip-ms	81.54
Second Hit Impact Impulse, kip-ms	65.63
Second Hit Reaction Impulse, kip-ms	54.60
Impact Residual Force, kip	43.21
Reaction Residual Force, kip	56.69
Baseline Strength, kip	69.18
Impact Residual Force Ratio	**0.625**
Reaction Residual Force Ratio	**0.820**

Figure 88 shows the impact and reaction impulsive residual force ratios plotted with the quasi static residual capacity ratios from Test Series 2. The impulsive residual capacity is clearly higher than the quasi-static residual capacity trend, which is expected due to the strain rate effects that are likely caused by the impulsive loading.

The average force in the specimen is likely somewhere between these two values. Dynamic residual capacity would be affected by strain rate, and that is probably why these data points are higher than the trend of quasi-statically determined residual force. The strain rate dependence of damaged concrete is unknown. Further testing on concrete with repeated impacts should be conducted to determine the strain rate dependent behavior of damaged concrete.

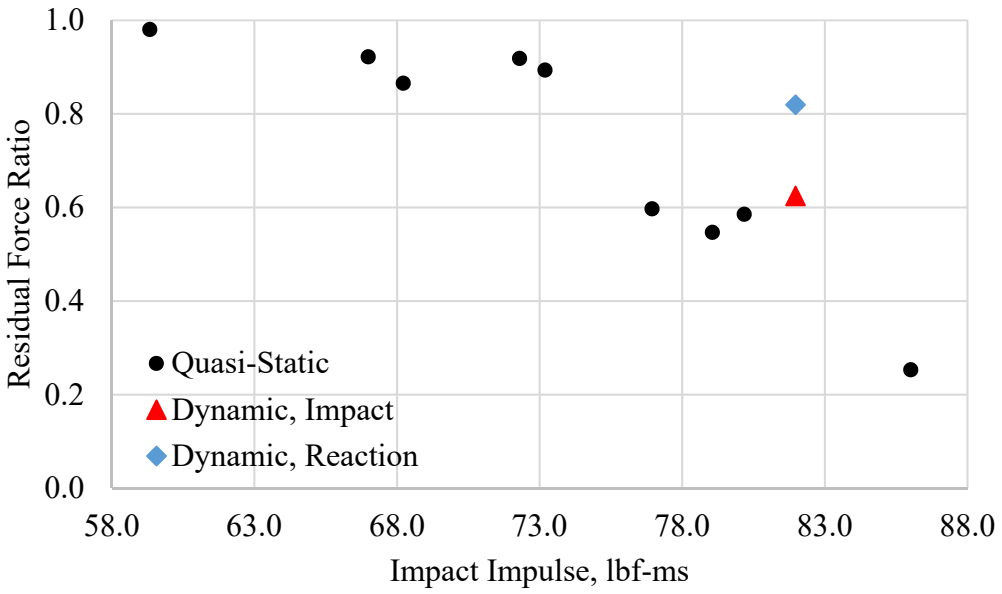

Figure 88: Dynamic residual capacity force ratios and quasi-statically determined residual force ratios versus impulse

5.5 Conclusions

The experimental program successfully characterized the residual capacity of concrete materials subjected to a range of impulsive loads. Quasi-static baseline measurements were used to determine normalized measures of the residual force, modulus,

and work of the impulsively damaged specimens. Cyclic loading was performed on the baseline and residual capacity specimens to determine the descending branch of the force versus displacement curve. The residual capacity trends of the impulsively damaged concrete were compared to equivalent quasi-static residual capacity measurements and model results. It was found that the stiffness degradation of the impulsively damaged concrete was unique to those specimens. Finally, a double hit impulsive test case illustrates a novel method for determining the dynamic residual capacity of impulsively damaged concrete. The experimental methodology demonstrated in this test series can be extended to a test a wide range of concrete mix designs or various materials for a wide range of applied impulsive loads. The major conclusions of the experimental series are as follows:

1) There is a clear decrease in residual strength, modulus, and work with increasing applied impulsive load. Most notably, the residual modulus decreases much faster than the residual strength. This may have large implications for the successful prediction of residual capacity and should be carefully considered for applications in which the material stiffness is influential.
2) The trend of a larger reduction of residual modulus versus strength for the impulsively damaged specimens differs from the behavior of quasi-statically damaged specimens. This trend is likely caused by some damage mechanism that only occurs to an influential degree in the concrete during impulsive loading. The existence of this trend is previously unknown and provides novel insight on the behavior of impulsively damaged concrete. It is possible that the high strain rate causes damage to occur in the form of distributed microcracking, which could reduce the stiffness of the material while having a lesser effect on the strength. The

use of advanced diagnostics is necessary to further investigate the damage mechanisms involved.

3) Preliminary test results show that the dynamic residual force capacity is larger in magnitude than the quasi-static residual force. This is an expected result due to strain rate effects, but very little is known specifically about the strain rate effects of damaged concrete and further testing could provide novel insight on the degradation of concrete subjected to repeated impacts.

CHAPTER 6. EVALUATION OF CONCRETE CONSTITUTIVE MODELS

6.1 Introduction

The use of constitutive models for predicting the response of concrete to impulsive loads requires an accurate representation of the dynamic and other properties of concrete. The novel data from the experiments are used to investigate the suitability of commonly used concrete models for predicting the damage and residual capacity of concrete damaged from impulsive loading and to provide recommendations for improvement, if necessary. Three models are investigated: (1) Karagozian and Case (K&C) model [58], (2) the Holmquist-Johnson-Cook (HJC) model [59], and the Johnson-Holmquist (JH-2) ceramic model [60]. Each is suited to modeling the phenomenological behavior of brittle and quasi-brittle materials for dynamic loading and incorporates strain rate effects, pressure versus strength dependence, and dilatation induced by damage.

This chapter reviews the basic elements of the K&C, HJC, and JH-2 models. A preliminary residual capacity study was conducted prior to the experimental series to compare the residual capacity predictions of the K&C and HJC models. Then, following the experimental test series, the three models were calibrated to the quasi-static force versus displacement envelope curves from Test Series 2 and a second residual capacity study was conducted on the calibrated models. A representative impulsive loading force versus time history from the experimental test series was used to impart varying levels of impulsive

load on the models. The residual capacity quantities with respect to impact impulse are compared for each model against the experimental data, and the major trends and conclusions of the study are presented.

6.1.1 Karagozian and Case Concrete Model

The K&C model formulation is based on three failure surfaces, which are defined as the yield, maximum, and residual surfaces as shown in Figure 89. Figure 90 shows a triaxial compression test curve with the location of points that correspond to the three failure surfaces. The yield surface represents the end of the linear stress-strain relationship and thus the onset of plasticity, the maximum surface corresponds to the maximum strength, and the residual surface is defined by the remaining strength due to confinement.

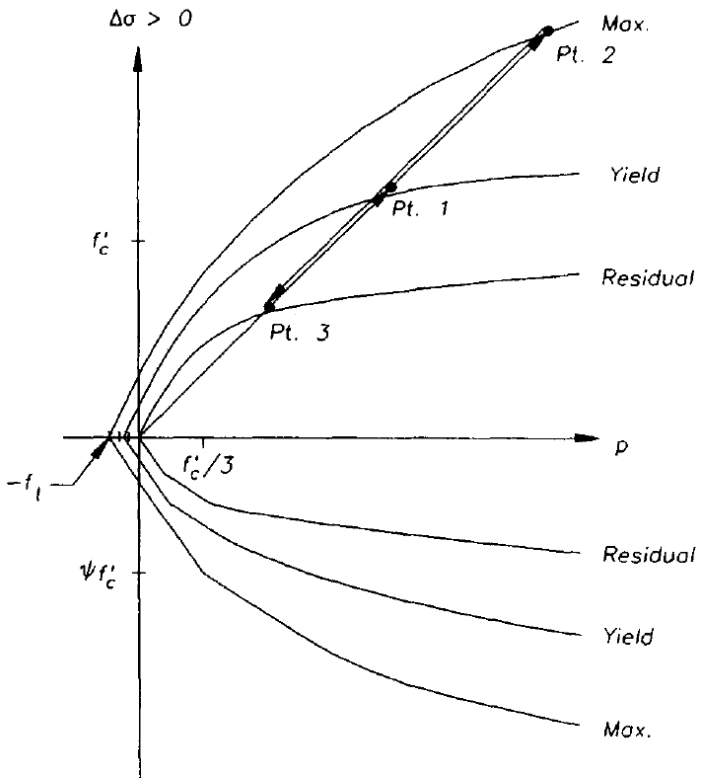

Figure 89: Failure surfaces in K&C model [58]

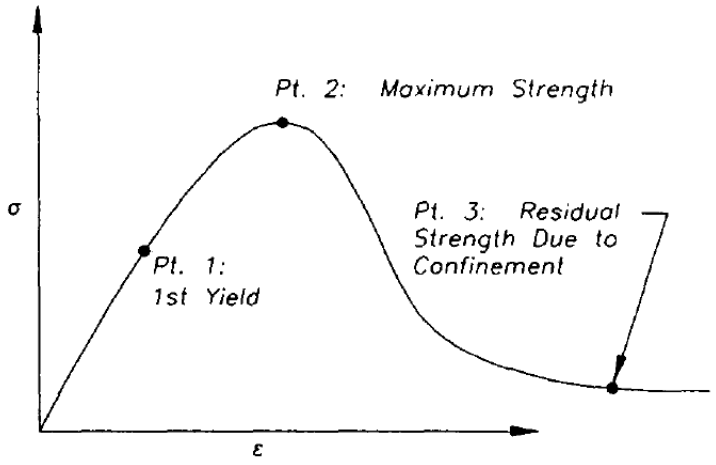

Figure 90: Triaxial compression test with points that correspond to K&C failure surfaces [58]

The surfaces are defined with three parameters with the functional form as follows:

$$\Delta\sigma = a_0 + \frac{p}{a_1 + a_2 p} \tag{6.1}$$

where $\Delta\sigma$ is the deviatoric stress invariant, p is the pressure invariant, and a_0, a_1, a_2 are the constants used to fit the surface. The three failure surfaces define the dynamically changing plasticity surface at each step in the model. The plastic surface location is defined based on the interpolation of η, which is determined from a functional that is based on the amount of damage, λ, in the material. The accumulation of damage is defined as a function of several state variables:

$$d\lambda = h(\sigma)\sqrt{1 + 2\left(\frac{\omega\gamma_{,p}}{3}\right)^2}\, d\tilde{\mu} \tag{6.2}$$

$$\lambda^{n+1} = \lambda^n + d\lambda \tag{6.3}$$

$$h(\sigma) = \begin{cases} \dfrac{1}{r_f\left(1 + \frac{p}{r_f f_t}\right)^{b_1}} & p < 0 \\ \dfrac{1}{r_f\left(1 + \frac{p}{r_f f_t}\right)^{b_2}} & p \geq 0 \end{cases} \tag{6.4}$$

where b_1 and b_2 are input parameters determined from test data for compression and tension softening, respectively, and r_f is the radial strain rate enhancement factor. The failure surface is then computed by interpolating between the fixed failure surfaces with η, where $r' = r/r_c$:

$$\Delta\sigma = \begin{cases} r'\left[\eta\left(\Delta\sigma_m - \Delta\sigma_y\right) + \Delta\sigma_y\right] & \lambda \leq \lambda_m \\ r'\left[\eta\left(\Delta\sigma_m - \Delta\sigma_r\right) + \Delta\sigma_r\right] & \lambda > \lambda_m \end{cases} \tag{6.5}$$

6.1.2 Holmquist-Johnson Cook Concrete Model

Similar to the K&C model, the HJC model formulation is also based on a pressure dependent yield surface that represents the deviatoric strength of the material. However, the HJC model has two, rather than three, surfaces that represent the strength of the material in an undamaged and damaged state. These surfaces are plotted in Figure 91 with respect to the normalized equivalent stress versus the normalized pressure.

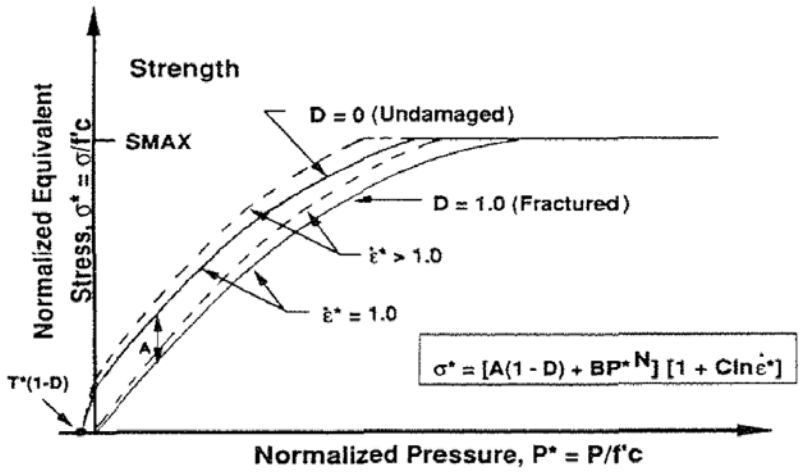

Figure 91: Yield surfaces of the HJC model [59]

The expression for normalized equivalent stress is as follows:

$$\sigma^* = [A(1-D) + BP^{*N}][1 + C ln\dot{\varepsilon}^*] \qquad (6.6)$$

where A is the normalized cohesive strength, B is the normalized pressure hardening coefficient, N is the pressure hardening coefficient, C is the strain rate coefficient, and

$SMAX$ is the normalized maximum possible strength. The accumulation of damage, D, is shown in Figure 92. Damage accumulates from both equivalent plastic strain and plastic volumetric strain.

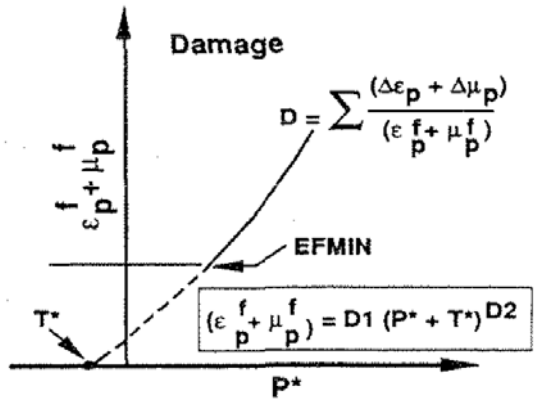

Figure 92: Damage versus normalized pressure [59]

The equation for damage is expressed as:

$$D = \sum \frac{\Delta\varepsilon_p + \Delta\mu_p}{\varepsilon_p^f + \mu_p^f} \tag{6.7}$$

where $\Delta\varepsilon_p$ is the equivalent plastic strain and $\Delta\mu_p$ is the plastic volumetric strain during a cycle of integration, while $\varepsilon_p^f + \mu_p^f = f(P)$ is the plastic strain to fracture under a constant pressure, P. The specific expression is:

$$\varepsilon_p^f + \mu_p^f = D1(P^* + T^*)^{D2} \tag{6.8}$$

where $D1$ and $D2$ are constants to fit the expression. The pressure and volumetric strain relationship for the model is shown in Figure 93.

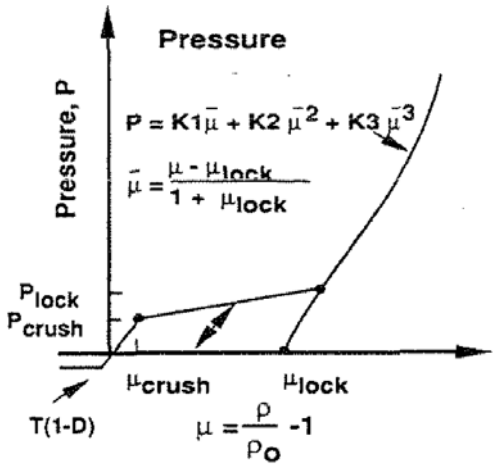

Figure 93: Pressure versus volumetric strain relationship [59]

The first region of the relationship is linear elastic and occurs at $P \leq P_{crush}$, where P_{crush} and μ_{crush} are the pressure and volumetric strain that occur in a uniaxial compression test. The second region, or transition region, occurs at $P_{crush} \leq P \leq P_{lock}$. This region corresponds to the air void being gradually compressed out of the concrete as plastic strain occurs. The third region corresponds to a fully compacted material with all air voids being crushed. This region begins when the pressure equals P_{lock} and the relationship is given as:

$$P = K1\bar{\mu} + K2\bar{\mu}^2 + K3\bar{\mu}^3 \qquad (6.9)$$

where

$$\bar{\mu} = \frac{\mu - \mu_{lock}}{1 + \mu_{lock}} \tag{6.10}$$

6.1.3 Johnson-Holmquist-2 Ceramic Model

The JH-2 ceramic model is suited to modelling quasi-brittle materials such as ceramic or concrete that are subjected to impact conditions that produce large strains, high strain rates, and high pressures. Two yield surfaces are used to represent the material in the undamaged and damaged states, which are shown in Figure 94. The material softens gradually from the intact surface to the fractured surface as damage begins to accumulate.

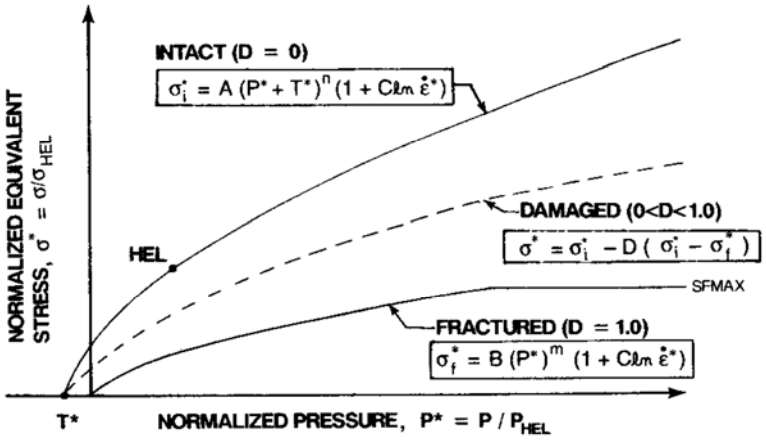

Figure 94: Yield surfaces of the JH-2 model [60]

The normalized strength of the intact, damaged, and fractured surfaces are given by equations 5.11, 5.12, and 5.13, respectively:

$$\sigma_i^* = \mathrm{A}(P^* + T^*)^N(1 + C ln\dot{\varepsilon}^*) \tag{6.11}$$

$$\sigma^* = \sigma_i^* - D(\sigma_i^* - \sigma_f^*) \tag{6.12}$$

$$\sigma_f^* = BP^{*N}(1 + C ln\dot{\varepsilon}^*) \tag{6.13}$$

where the material constants are A, B, C, M, N, and $SFMAX$. The normalized pressure is $P^* = P/P_{HEL}$, where P is the pressure and P_{HEL} is the pressure at the Hugoniot elastic limit. The normalized tensile pressure is $T^* = T/P_{HEL}$, where T is the maximum possible tensile hydrostatic pressure of the material. The dimensionless strain rate, $\dot{\varepsilon}^*$, is calculated as the current strain rate divided by the reference strain rate of 1.0 s^{-1}.

The accumulation of damage in the material is illustrated by the relationship between the equivalent plastic fracture strain, versus the normalized pressure. This relationship is plotted in Figure 95.

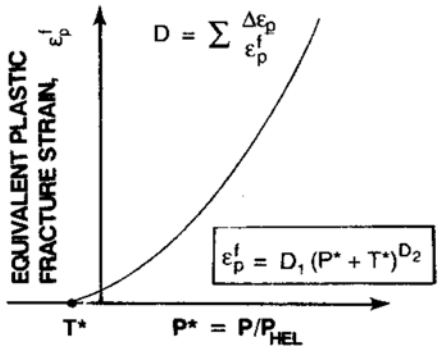

Figure 95: Equivalent plastic fracture strain versus pressure [60]

The equation for damage is expressed as:

$$D = \sum \frac{\Delta \varepsilon_p}{\varepsilon_p^f} \tag{6.14}$$

where $\Delta \varepsilon_p$ is the increment of equivalent plastic strain during a cycle of integration and ε_p^f is the equivalent plastic strain to fracture under a constant pressure, P, given by:

$$\varepsilon_p^f = D_1 (P^* + T^*)^{D_2} \tag{6.15}$$

where D_1 and D_2 are constants. The pressure versus volumetric strain relationship for the intact, damaged, and failed material is shown in Figure 96.

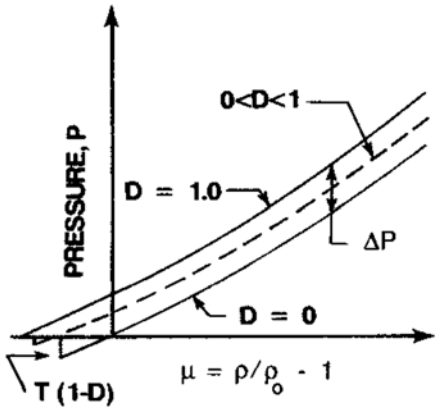

Figure 96: Pressure versus volumetric strain relationship [60]

The hydrostatic pressure before damage begins, indicated by D = 0, is given by:

$$P = K1\bar{\mu} + K2\bar{\mu}^2 + K3\bar{\mu}^3 \tag{6.16}$$

where $K1$, $K2$, and $K3$ are constants. As damage accumulates, the hydrostatic pressure is given by:

$$P = K1\bar{\mu} + K2\bar{\mu}^2 + K3\bar{\mu}^3 + \Delta P \tag{6.17}$$

where ΔP is the pressure increment calculated from the incremental internal elastic and potential internal energy of the material.

6.2 Preliminary Residual Capacity Study

Prior to the experimental series, a preliminary residual capacity study was conducted to compare the response of the K&C and HJC concrete models. The process of this preliminary study involved calibrating the uniaxial compressive response of the models to match the desired compressive strength, simulating dynamic tests with varying flyer plate impact velocities, and determining the residual strength and modulus of the damaged models.

6.2.1 Model Calibration Process

The most common parameter used to calibrate the constitutive behavior of concrete models is the uniaxial compressive strength of the concrete. Often, only the design or tested compressive strength is known to calibrate a model, and most other mechanical properties are estimated from this quantity. Additional data, such as triaxial compression test data, can aid in the calibration of model parameters to more accurately characterize the compressive behavior under confining pressures. For this preliminary study, it is assumed that only the compressive strength of the concrete is known.

The calibration procedure for this study involved simulating a uniaxial compression test and adjusting the K&C and HJC model parameters until the compressive strength matched the desired value and the shape of the force versus displacement curves were similar. The simulation was performed with Sierra Solid Mechanics finite element software

[61], and the mesh was generated with CUBIT meshing software [44]. In this test, a 6-inch by 12-inch concrete cylinder is compressed between two steel plates at a constant displacement rate. A friction coefficient of 0.5 was used between the concrete and steel surfaces. Figure 97 shows the mesh used in the test problem, with an average element size of 0.3 inches.

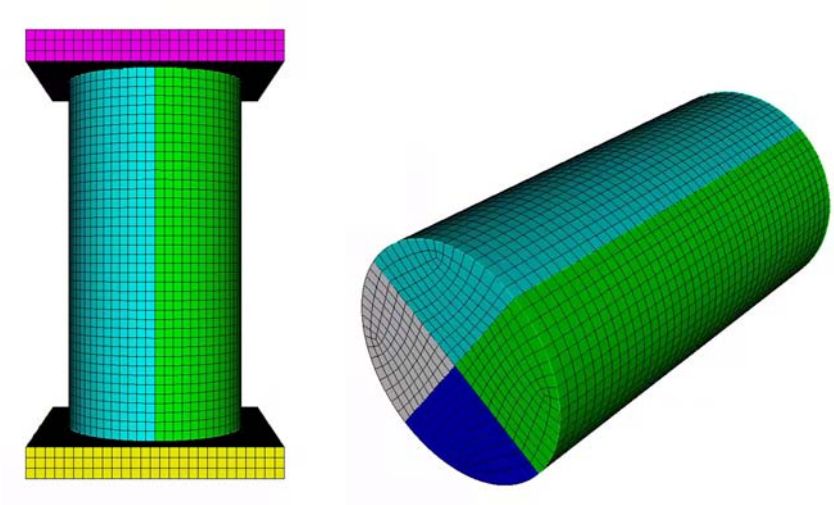

Figure 97: Mesh for uniaxial compression test simulation

The bottom surface of the lower steel plate provides the fixed boundary condition for the problem, while the top surface of the top plate is displaced at a rate of 4 inches per minute. The test was simulated with explicit time integration. To isolate the quasi-static response of the model, the strain rate sensitivity of the models was disabled, and the displacement rate of 4 inches per minute was chosen to be low enough to avoid inertial effects. The input parameters for the HJC and K&C models were primarily selected based on known material properties, while some of HJC parameters were iterated until the desired uniaxial compressive strength was achieved in the test problem. Table 11 shows the basic material

properties used in the K&C model, and Table 12 shows the material properties used in the HJC model.

Table 11: Material properties for 4,000 psi K&C concrete model

Material Property	Value
Compressive Strength, psi	4,000
Tensile Strength, psi	400
Young's Modulus, psi	3,605,000
Poisson's Ratio	0.19
Fractional Dilatancy	0.5
Maximum Aggregate Size, inches	0.75

Table 12: Material properties for 4,000 psi HJC concrete model

Material Property	Value
Compressive Strength, psi	4,000
Tensile Strength, psi	300
Poisson's Ratio	0.19
Shear Modulus, psi	1,624,000
Bulk Modulus, psi	1,784,000

The stress-strain response of the two models is shown in Figure 98. For the HJC model, the displacement rate was increased to 40 inches per minute to obtain stable results in the post-peak descending branch. For this increased load rate in the HJC model, no differences in the overall stress-strain curve were observed and the displacement rate is

well below the start of inertial strain rate effects. However, the increased load rate did result in some oscillations in the linear stress versus strain regime. The overall shape of the stress versus strain curve is similar for the two models.

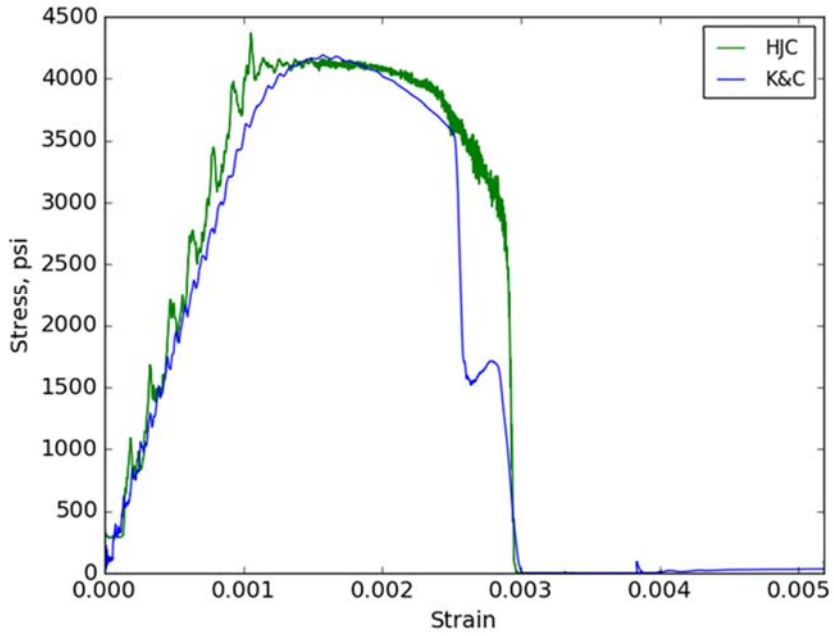

Figure 98: Stress-strain response of HJC and K&C concrete models in uniaxial compression

A mesh convergence study was conducted for the test problem to ensure that the results are independent of element size. Several simulations of different mesh densities were conducted with the K&C model, with the results summarized in Table 13. The maximum stress in the test problem showed little mesh sensitivity, with all results within 0.3% of each other. So, the element size of 0.30 inches was selected for computational efficiency. Figure 99 shows the convergence of maximum stress in the test problem with respect to number of elements in the model.

Table 13: Mesh convergence of uniaxial compression test

Element Size, inches	Number of Elements	Maximum Stress, psi	Iterative Percent Difference
0.5	4,672	4,165.9	
0.4	8,160	4,177.5	0.28%
0.3	19,734	4,189.7	0.29%
0.2	67,840	4,196.3	0.16%
0.18	96,369	4,196.7	0.01%
0.15	165,726	4,197.6	0.02%

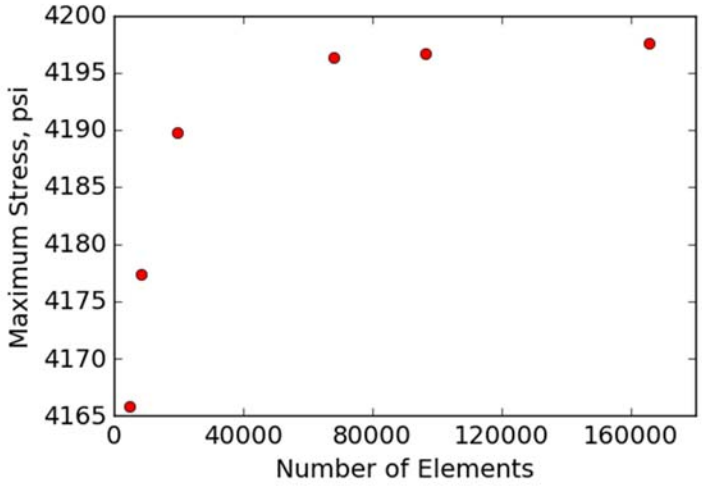

Figure 99: Maximum stress versus number of elements in uniaxial compression test

The damage for each model was examined with Kitware's ParaView post-processing software [62]. Figure 100 shows the post-failure damage in the concrete cylinder from uniaxial compression testing for the K&C model, and Figure 101 shows the damage for HJC model. For the K&C model, a damage value of 2 indicates that the element has no remaining unconfined strength, while in the HJC model this corresponds to a damage value of 1. For both models, the failure pattern resembles the Type 1 cone failure

mode that is typically seen in ASTM C39 tests for concrete cylinders with steel bearing plates.

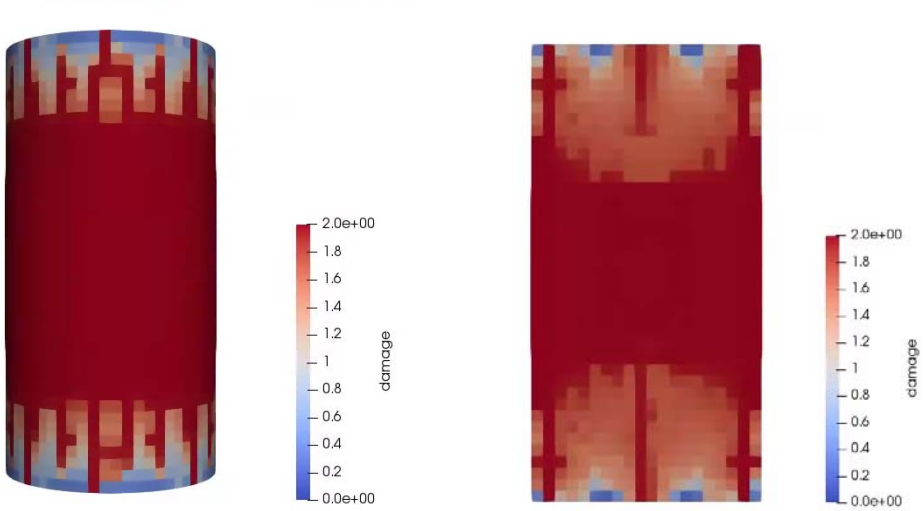

(a) (b)

Figure 100: Failure modes for K&C model, (a) side view and (b) cross-section view

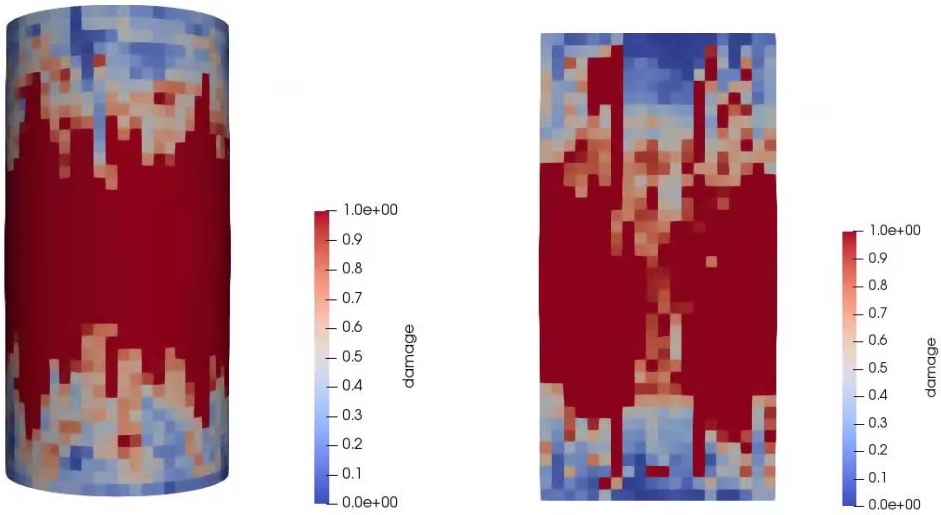

(a) (b)

Figure 101: Failure modes for HJC model, (a) side view and (b) cross-section view

6.2.2 Dynamic Concrete Compression with Residual Capacity Simulations

Dynamic concrete compression simulations were conducted using the simplified mesh for the dynamic concrete compression setup, which was described in Section 3.2.2. The mesh is shown in Figure 102.

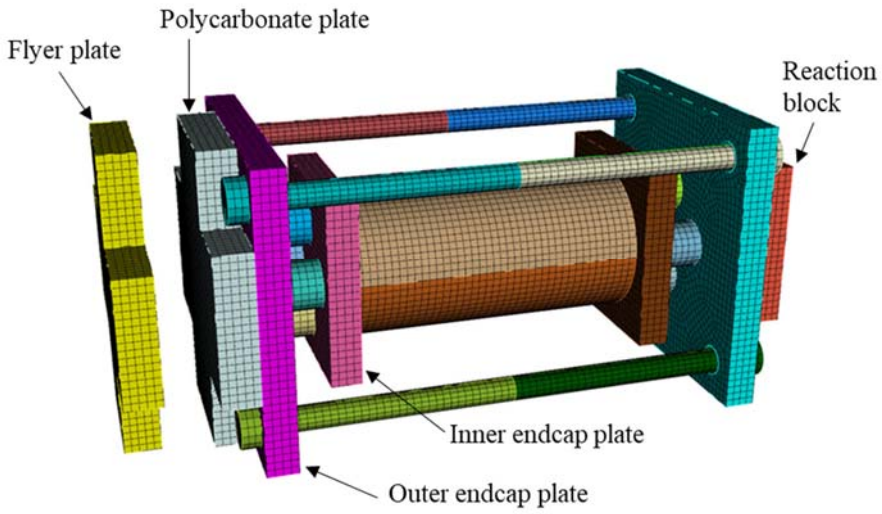

Figure 102: Simplified mesh of dynamic concrete compression setup

Simulations were conducted with a 33 lbm flyer plate for a range of different impact velocities. Figure 103 shows the force and impulse time history for a 10 m/s impact for the K&C model (left) and the HJC model (right). Figure 104 shows the corresponding progression of damaged elements in the cylinder cross section for each model.

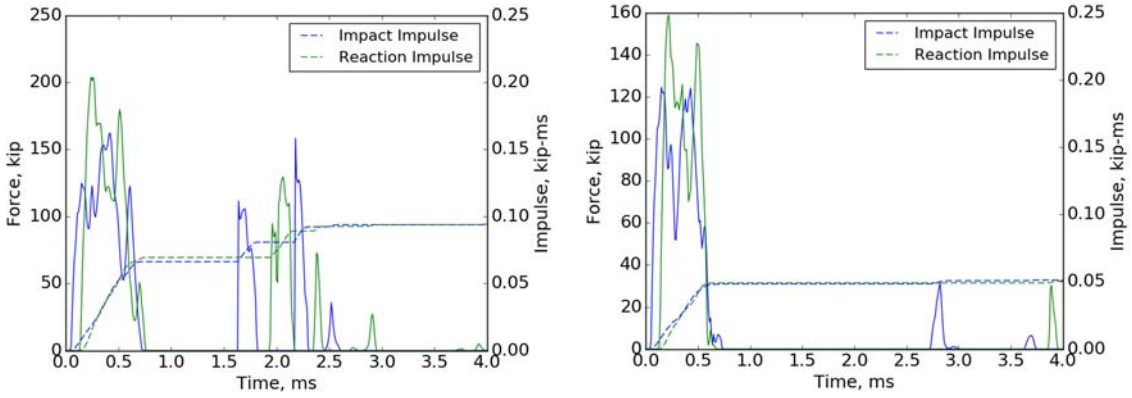

(a) (b)

Figure 103: Force and impulse time history of the (a) K&C model and (b) HJC model for a 10 m/s impact

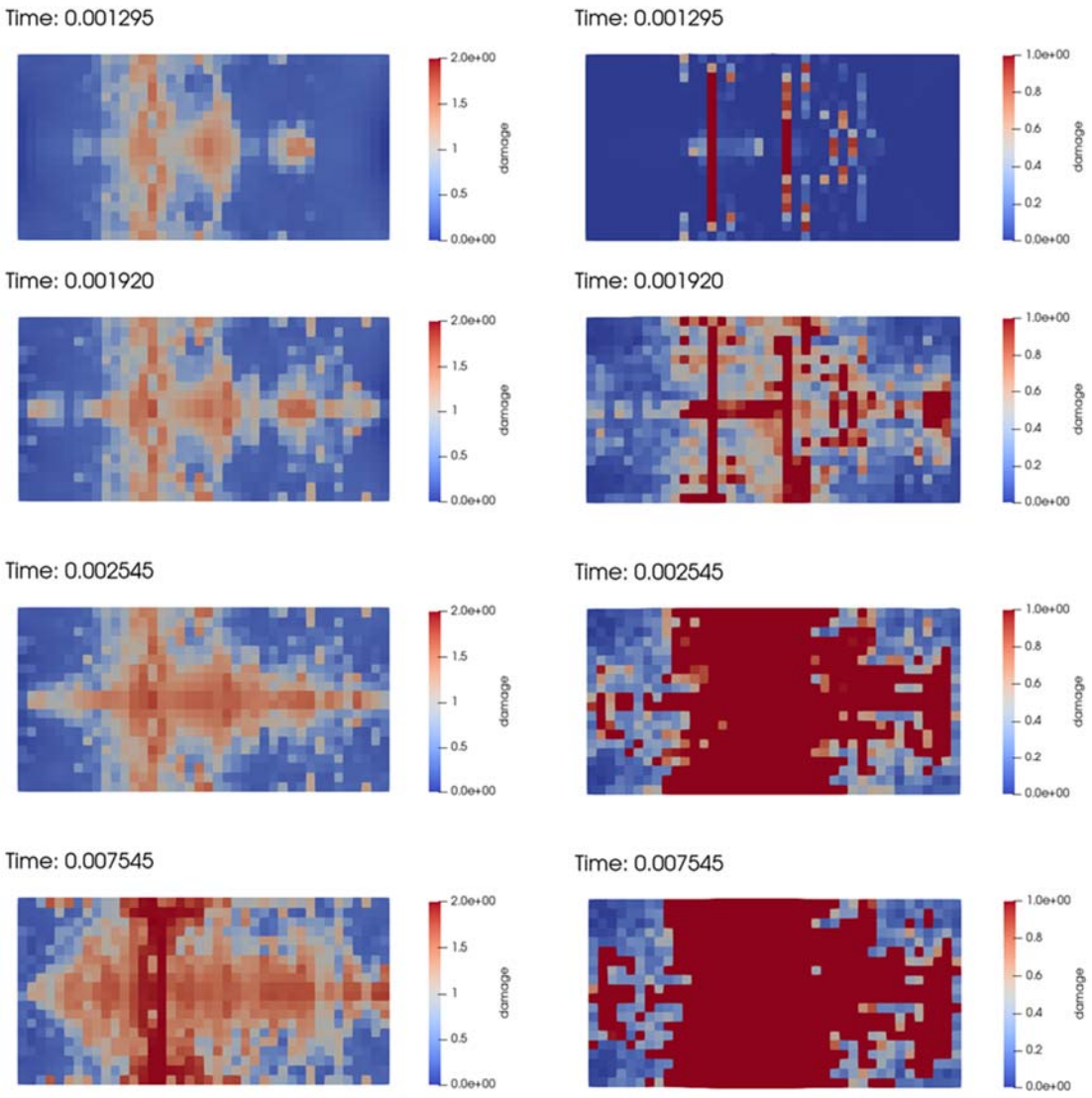

Figure 104: Cross section view of the progression of damage in seconds in K&C model (left) and HJC model (right)

The damage progression in both models appears similar for the first two milliseconds, after that point the HJC model quickly accumulates damage to failure while the K&C model experiences much less damage overall. This rapid damage accumulation

in the HJC model explains some of the differences in the force-time history of the specimen, because once the concrete has failed it will no longer support any applied force.

The 4,000 psi concrete specimens sustained a large amount of damage during the 10 m/s dynamic simulation, so the compressive strength was increased to 5,700 psi to conduct combined dynamic and quasi-static residual capacity simulations. After the flyer plate impact, a pressure load was applied to the front surface of the concrete compression assembly to simulate quasi-static loading at a load rate of 50 psi per second. The normalized residual capacity was determined as the ratio of the compressive strength of the damaged cylinder divide by the undamaged compressive strength. In addition to residual strength, the residual modulus is measured for the damaged specimen. Both models displayed a linear stress-strain relationship until failure during the residual capacity loading, so the modulus is determined by performing a linear regression of this regime. An example residual capacity stress-strain curve for the K&C model after a 15 m/s (49 ft/s) flyer plate impact is shown in Figure 105. In this test case, the cylinder sustained a large amount of damage and has very little residual strength.

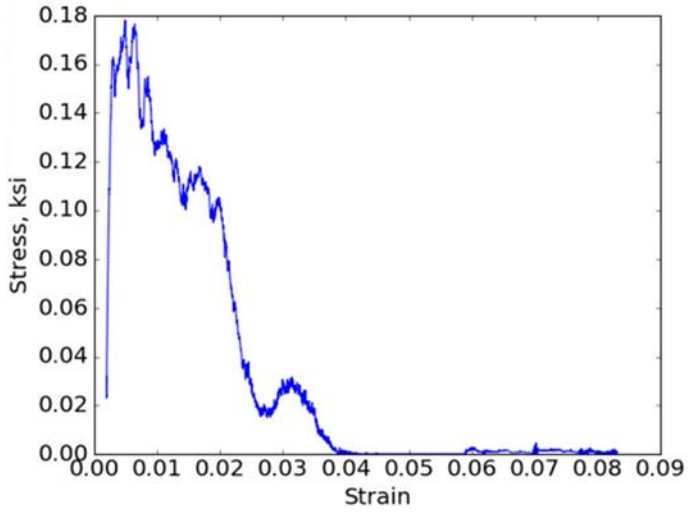

Figure 105: Residual capacity stress strain relationship for the K&C model after a 15 m/s impact

Simulations were conducted for flyer plate impact velocities ranging from approximately 200 in/sec to 600 in/sec. Table 14 summarizes the normalized residual compressive strength and the normalized residual modulus for each test case. The normalized residual strength and modulus are plotted against the impact velocity in Figure 106 and Figure 107.

Table 14: Residual compressive strength and modulus for 5,700 psi concrete

	Impact Velocity, in/sec	Normalized Residual Compressive Strength	Normalized Residual Modulus
HJC Model	197	1.00	0.82
	295	0.62	0.53
	394	0.25	0.09
	591	-	-
K&C Model	197	0.97	0.90
	295	0.88	0.89
	394	0.38	0.54
	591	0.03	0.06

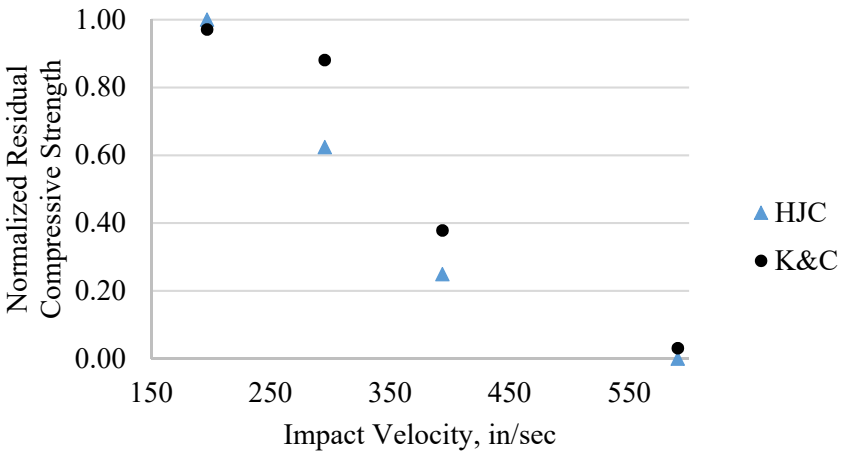

Figure 106: Normalized residual compressive strength versus impact velocity

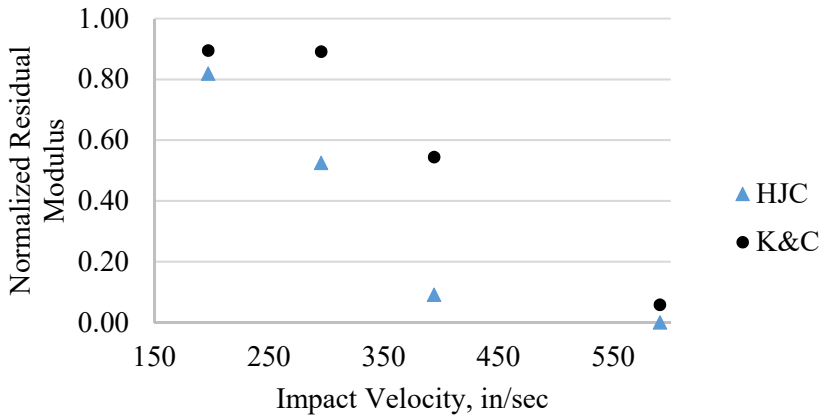

Figure 107: Normalized residual modulus versus impact velocity

Both models display the expected trend of decreasing residual strength and modulus with increasing impact velocity. However, the HJC model shows a more rapid decrease in residual strength and modulus than the K&C model. This trend is consistent with the increased number of damaged elements observed in the concrete cylinders for the HJC

model. These results show that the HJC model generally accumulates more damage than the K&C model for the same loading scenario.

These preliminary modeling results indicate the need to further investigate the suitability of these material models to predicting damage and residual capacity of concrete materials. For the case of a 7.5 m/s impact velocity, there is a 34% difference in the K&C and HJC residual compressive strength predictions. This discrepancy contributes a significant amount of uncertainty in the use of these models to predict the response of concrete materials and structures to impulsive loads, as the true reduction in strength and stiffness is unknown.

6.3 Simulation of Impulsive Experiments with Residual Capacity

Experimental results from the second experimental test series were used to evaluate the behavior of the K&C, HJC, and JH-2 concrete constitutive models and their ability to predict the residual capacity of concrete cylinders when subjected to impulsive loads. This section details the design of the computational study, the calibration process for each constitutive model, and the results of the residual capacity study.

6.3.1 Simplified Model and Problem Setup

A simplified finite element model is used in this computational study to avoid uncertainties associated with modeling the dynamic experimental setup in detail. The response of the concrete can be isolated to just the cylinder and the impact and reaction endcap plates, as shown in Figure 108 (a). The mesh is comprised of just these elements,

shown in Figure 108 (b). The force time history from the impact load cells is used as the input to the model, and the reaction endcap plate is restrained in the loading direction.

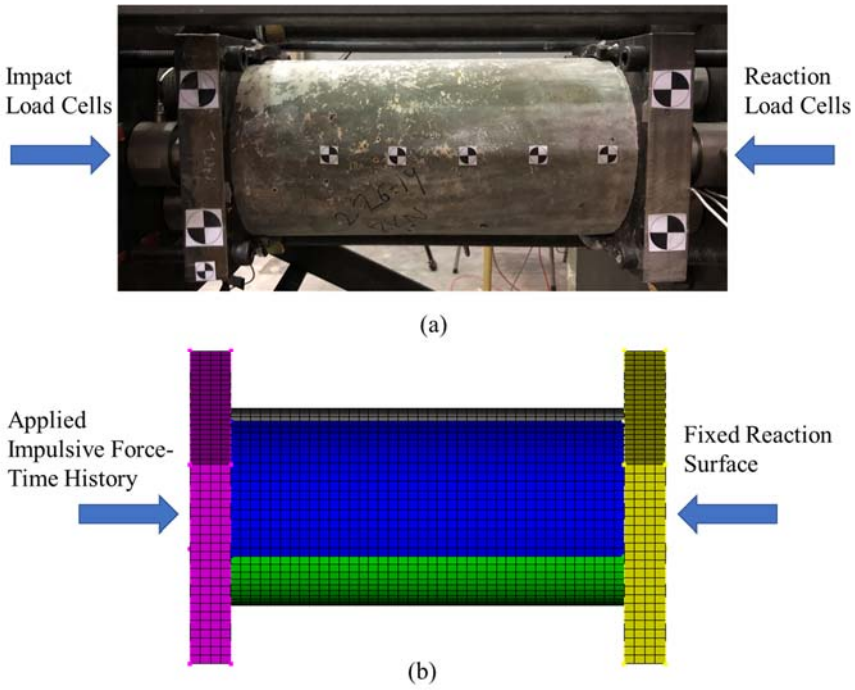

Figure 108: (a) Experimental setup and (b) simplified finite element model

A single force time history from the experimental test program was used to represent different levels of impulsive loading in this study. The force versus time history from Test 2-4, which is a typical representation of the impulse loadings in Test Series 2, is shown in Figure 109 (a). The impulsive force time history of the impact load cells during the flyer plate impact is extracted from the full experimental data and is shown in Figure 109 (b). This force versus time history is applied directly to the impact endcap plate in the finite element model, where it is represented as an applied pressure that is equal in magnitude to the desired applied force. To study different magnitudes of applied force and impulse, this force time history is linearly scaled by a constant scale factor.

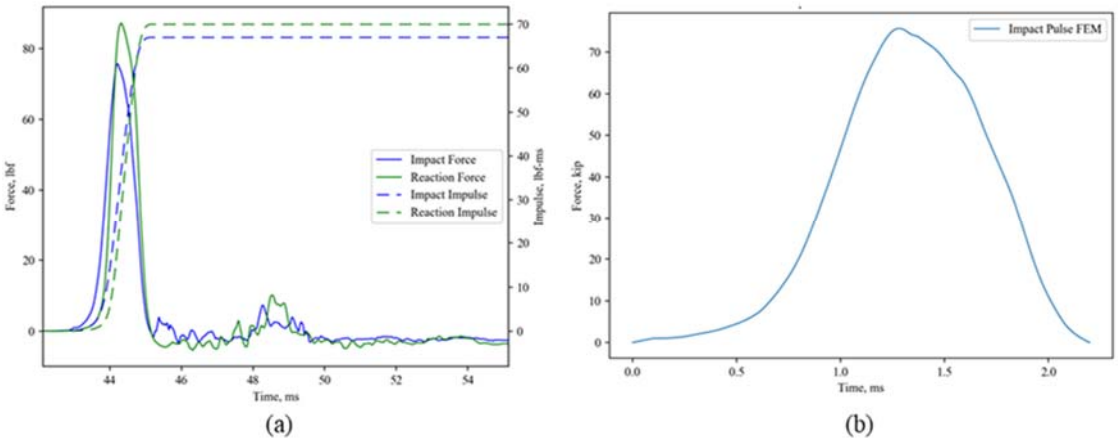

Figure 109: (a) Experimental force and impulse time history and (b) abbreviated impact force time history from Test 2-4

Example simulation results from applying the force time history with scale factors between 0.75 and 1.50 are shown in Figure 110 (a). These example simulations were conducted with the K&C model. The impact and reaction force time histories are measured as the contact force on the impact and reaction sides of the concrete cylinder. The impulse time history, shown in Figure 110 (b), is determined by numerically integrating the force time history of the impact and reaction surfaces. As observed in the experimental test series and discussed in Section 4.4.1, the reaction impulse is initially higher for lower levels of impulsive load. However, as the impulsive load increases and the concrete begins accumulating damage, energy is dissipated causing the reaction force and impulse to decrease.

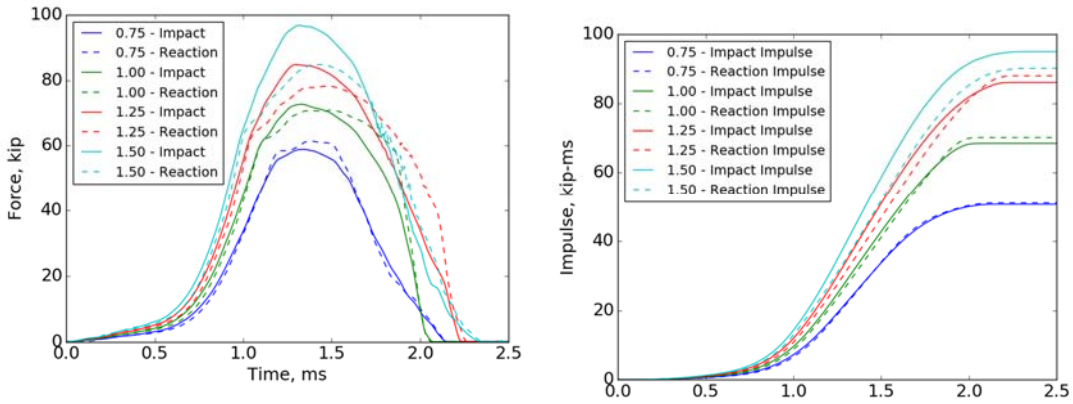

Figure 110: Example simulated (a) force and (b) impulse time history results for varying levels of applied impulsive loading with K&C model

After the impulsive load is applied, a prescribed velocity is applied to the impact endcap plate to test the damaged specimen at a strain rate of 0.05 s^{-1}. This strain rate is high enough that the simulation can be performed with explicit dynamics, but low enough that the strain rate effects in the specimen are negligible. The residual capacity results are evaluated to determine the residual modulus and maximum compressive strength, and the work is calculated by numerically integrating the area under the force displacement curve. The residual modulus is determined from one dimensional least squares polynomial fit of the residual force versus displacement curve. The linear regression was performed on a section of the residual curve corresponding to 30% and 50% of the maximum residual force.

6.3.2 Calibration Procedure for Concrete Constitutive Models

The full force versus displacement curves obtained during the second experimental test series were used to calibrate the concrete material models. To simplify the

computational study, each experimental curve was normalized to the maximum force for each specimen. The normalized curves, which are plotted in Figure 111 (a), can be used to calibrate the descending branch of the simulated uniaxial compression test. The work versus displacement, which is calculated by numerically integrating the force versus displacement curve, is shown in Figure 111 (b) for each specimen. The work for the simulated compression test can also be evaluated against the experimental curves to provide a comparison of how closely each the constitutive model matches the experimental behaviour.

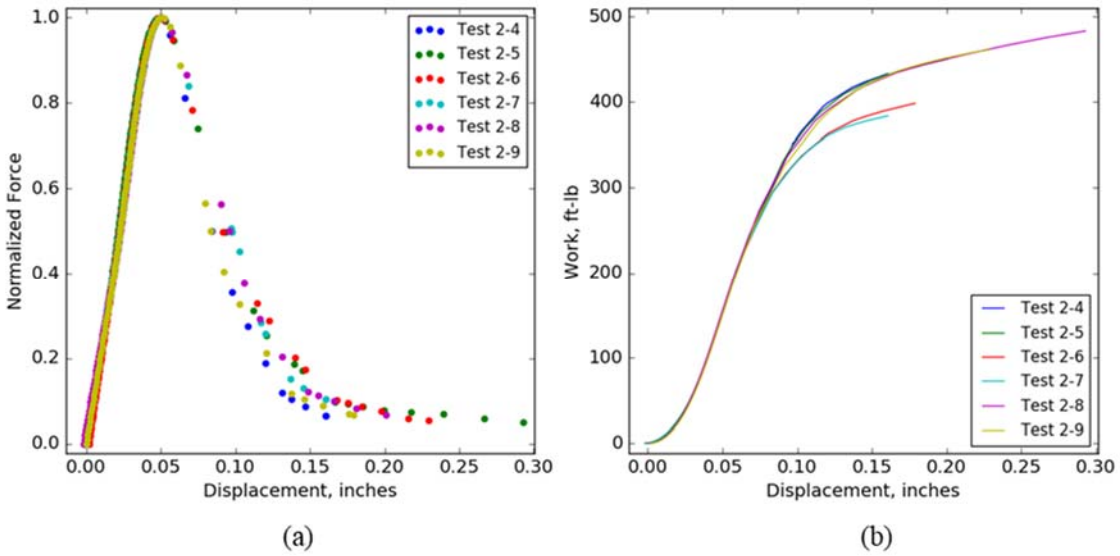

Figure 111: Normalized experimental (a) force versus displacement and (b) work versus displacement data

6.3.2.1 K&C Model Calibration

The K&C model is capable of auto-generating many of the constitutive material model parameters based on relatively few user inputs. Table 15 lists the input parameters

for the calibrated uniaxial compression simulation used in this study. Based on these parameters, the K&C model auto-generates functions to define the relationships between strength enhancement and strain rate, pressure and volume strain, unloading bulk modulus and volumetric strain, and hardening and softening. These functions can also be manually defined or modified by the user. For this study, the auto-generated functions were used.

The two main parameters that were used to calibrate the K&C model in this study include the compressive strength, $f'c$, and the maximum aggregate size, *MSA*. The compressive strength increases the maximum force and the height of force versus displacement curve. Changing the maximum aggregate size modifies the shear-induced dilatation behavior of the material, which results in changes to the softening characteristics of the force versus displacement curve. With larger *MSA*, the model exhibits a more rapid reduction in strength. The effects of changing the compressive strength and aggregate size are illustrated in Figure 112 (a) and (b), respectively.

Table 15: K&C model input parameters

K&C Model Input Parameter		**Value**
Compressive Strength, psi	$f'c$	2,100
Tensile Strength, psi	T	200
Young's Modulus	E	2,732,973
Poisson's Ratio	ν	0.19
Fractional Dilatancy		0.5
Maximum Aggregate Size, inches	*MSA*	0.25

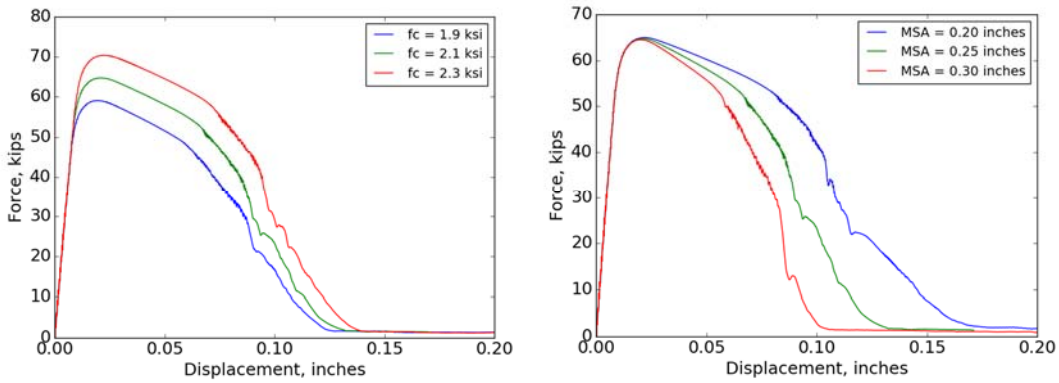

Figure 112: K&C uniaxial compression test results for varying values of (a) compressive strength and (b) aggregate size

6.3.2.2 HJC Model Calibration

Table 16 lists the HJC input parameters for the calibrated uniaxial compression simulation used in this study. The HJC model requires more input parameters than the K&C model. Many of these parameters are not directly based on known material properties. Holmquist and Johnson [59] provided values for several of the constants for a normal strength concrete. These constants are based on experimental data, although their derivation from what data is not explicitly clear. These values, combined with the known behavior of the concrete from the experimental study, served as the starting point for calibrating this model.

The two main parameters that were used to calibrate the HJC model include the strength constants *A* and *B*. The effect of varying the strength constant *A* is show in

Figure 113 (a). Changing *A* results in changes to the maximum compressive strength, but it does not have a large effect on the latter region of the softening portion of the curve. Similarly, varying *B* changes the maximum compressive strength while also extending the descending branch of the curve. Adjusting these two parameters simultaneously changes the maximum force and provides some control over the shape of the descending branch of the curve.

Table 16: HJC model input parameters

HJC Model Input Parameter		**Value**
Initial Density, lbm/in^3	ρ_0	0.08275
Initial Shear Modulus, psi	G	1,624,000
Strength Constant	A	0.4661
Strength Constant	B	0.725
Strength Exponent	N	0.610
Strain Rate Constant	C	0.007
Compressive Strength, psi	$f'c$	3,000
Normalized Maximum Strength	σ_{max}	7
Pressure Constant, psi	P_{crush}	2,000
Pressure Constant	U_{crush}	0.001
Pressure Constant, psi	K_1	1,442,286
Pressure Constant, psi	K_2	3,215,429
Pressure Constant, psi	K_3	2,469,714
Pressure Constant	μ_{lock}	0.1
Maximum Tensile Pressure, psi	T	300
Pressure Constant	μ_{plock}	152,300
Damage Constant	D_1	0.07
Damage Exponent	D_2	1
Minimum Failure Strain	ε^f_{min}	0.01

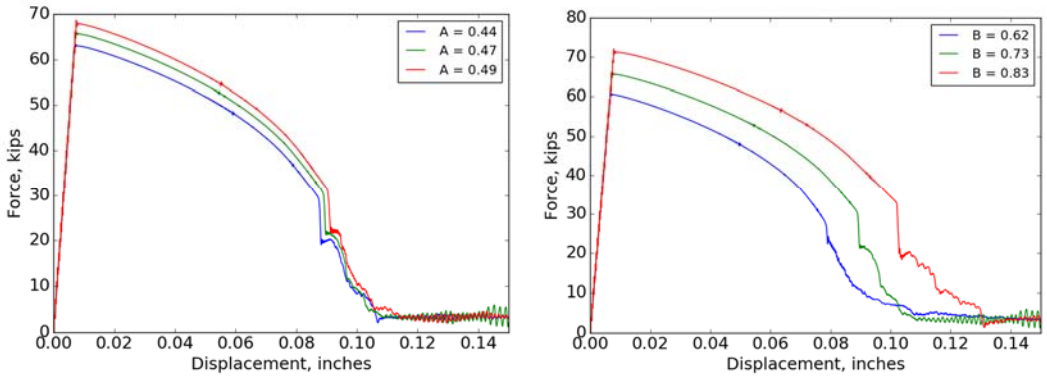

Figure 113: HJC uniaxial compression test results for varying values of (a) strength factor *A* and (b) strength constant *B*

6.3.2.3 JH-2 Model Calibration

Table 17 lists the JH-2 input parameters for the calibrated uniaxial compression simulation used in this study. The JH-2 model formulation is similar to the HJC model, therefore the parameters that are shared between the two models served as a starting point for calibration purposes. The three main parameters that were adjusted to calibrate the JH-2 model include the strength constant, A, the failed strength exponent, M, and the failed strength constant, B. Modifying the strength constant changes the maximum compressive force, and modifying M and B changes the softening behavior of the force versus displacement curve. The effects of changing these parameters are illustrated in Figure 114.

Table 17: JH-2 model input parameters

JH2 Model Input Parameter		Value
Initial Density, lbm/in3	ρ_0	0.08275
Maximum Tensile Pressure, psi	T	300
Strength Constant	A	0.79
Strength Exponent	n	0.61
Strain Rate Constant	C	0.007
Failed Strength Constant	B	0.525
Failed Strength Exponent	M	0.4209
Normalized Maximum Failure Strength	σ^f_{max}	1
HEL Pressure, psi	P_{HEL}	13053
Pressure Constant, psi	K_2	3215429
Pressure Constant, psi	K_3	2469714
Bulking Constant	$BULK$	1
Damage Constant	D_1	0.05
Damage Exponent	D_2	1
Minimum Failure Strain	ε^f_{min}	0.01

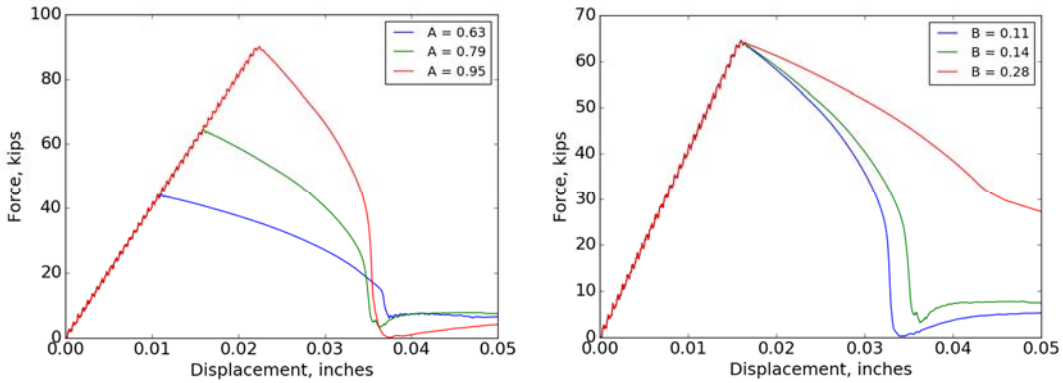

Figure 114: JH-2 uniaxial compression test results for varying values of (a) strength constant *A* and (b) failed strength exponent *B*

While the maximum strength could be adjusted easily by changing *A*, the descending branch of the curve tended to either be unstable and instantaneously drop to zero strength instead of softening gradually down to zero, or it tended to not soften down to zero and instead remain at a constant force level despite increasing displacement. These scenarios are not realistic for a uniaxial compression test, so the material parameters must be chosen carefully to avoid this behavior.

6.3.2.4 Summary and Comparison to Quasi-Static Experimental Data

The numerical results from each simulation are summarized in Table 18. Figure 115 (a) shows the force versus displacement for the simulated uniaxial compression test for each concrete model with the experimental data. Figure 115 (b) shows the work versus displacement for each model as well as the experimental data. The elastic modulus differs significantly between the experimental data and the simulated uniaxial compression tests. The early age concrete used in the experimental series had a much lower elastic modulus

than is typical for fully cured normal strength concrete. Changing the behavior of the constitutive model parameters to match this low elastic modulus proved difficult and may not be possible without an in-depth parameter study. Changing the K&C model elastic modulus input parameter did not result in changes to the stiffness of the material. Instead, the K&C model implementation in Sierra Solid Mechanics appears to auto-compute the elastic modulus based on the specified poisons ratio. This would not a problem for fully-cured normal strength concrete, as the elastic modulus can generally be estimated from the compressive strength and other elastic constants. However, this was not the case for the early age concrete used in this study. So, to simplify the computational study, a higher elastic modulus typical of fully cured concrete was used for all three models. This study assumes that the relative comparisons between applied impulsive load and residual capacity are not drastically altered by this choice. In fact, it is expected that this assumption results in a more accurate representation of the behavior of the material during the impulsive portion of the simulation. It has been observed in previous experimental research programs that the elastic modulus of concrete increases with increasing strain rate. However, the constitutive models only account for strain rate effects by scaling the compressive strength of the concrete, and the elastic modulus is not scaled as a function of strain rate. So by specifying a higher elastic modulus in the model, the behavior of the concrete during the impulsive loading might be more accurately represented.

Aside from the elastic modulus, the K&C and HJC models match the overall shape of the descending branch of the force versus displacement curve, while the JH-2 model has a much steeper descending branch. The work calculated from K&C and HJC force displacement curves is close to the experiment values at the end of the simulation, while

the JH-2 model work is much lower than the experimental data. The work corresponding to a displacement 0.15 inches was used for comparisons to the experimental data for the K&C and HJC models, while the work at 0.10 inches was used for the JH-2 model.

Table 18: Numerical and experimental uniaxial compression test results

	Compressive Strength, kip	**Elastic Modulus, ksi**	**Work at 0.15 inches Displacement, ft-lb**
Experimental Average	64.9	609.6	410.2
K&C Model	64.7	3,544.4	444.4
HJC Model	66.1	3,721.5	412.8
JH-2 Model	64.5	1,687.0	157.0*

*Work at 0.10 inches displacement

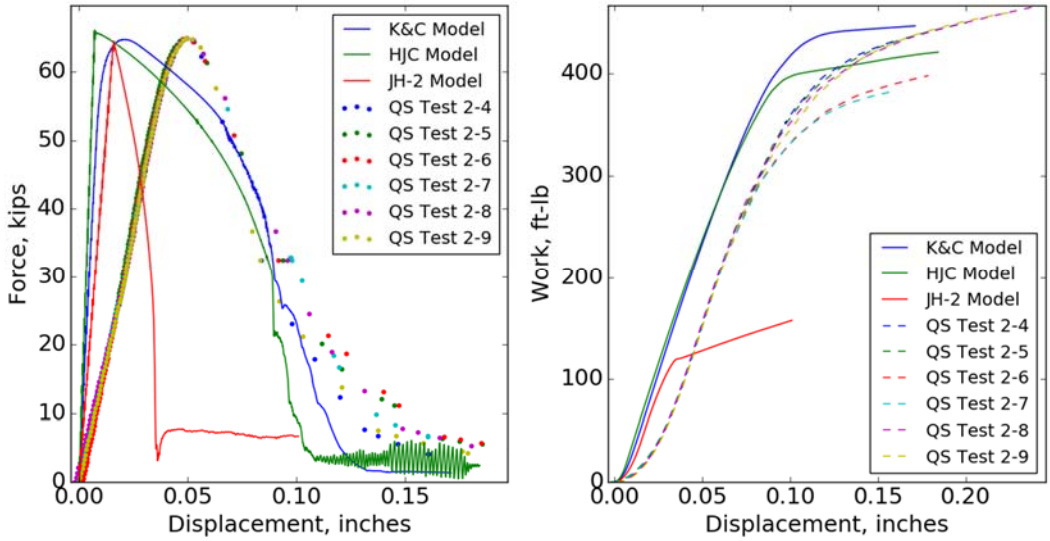

Figure 115: (a) Force and (b) work versus displacement for experimental and simulated uniaxial compression tests

Figure 116 shows the pattern of damage accumulated in the cylinder during the uniaxial compression test. The K&C model accumulates damaged elements without much localization, while the HJC and JH-2 models experience localized damage in the middle of the cylinder. The JH-2 model shows radial cracking along the length of the cylinder, and the HJC model experiences some localized radial cracking at the ends of the cylinder. The K&C damage parameter is distributed across more of the cylinder and is less localized because plasticity begins at the onset of yield for the K&C model, while plasticity does not begin in the HJC and JH-2 models until the maximum stress surface is reached. It is important to note that while the same term "damage" is used in all three models, the formulations for this parameter are different for each model. For the K&C model, a damage value of 0 indicates that the material is below the yield strength surface. Between the damage values of 0 and 1, the current stress surface is expanding to represent the strain

hardening that occurs after yield. At a value of 1, the maximum strength surface is reached. From this point, the material softens and the stress surface gradually collapses down to the residual surface, which corresponds to the maximum damage value of 2. For the HJC and JH-2 models, the damage parameter is 0 until the maximum strength surface is reached. From this point, the damage parameter begins increasing and the stress surface collapses down to the residual surface, which corresponds to a damage value of 1 in both models.

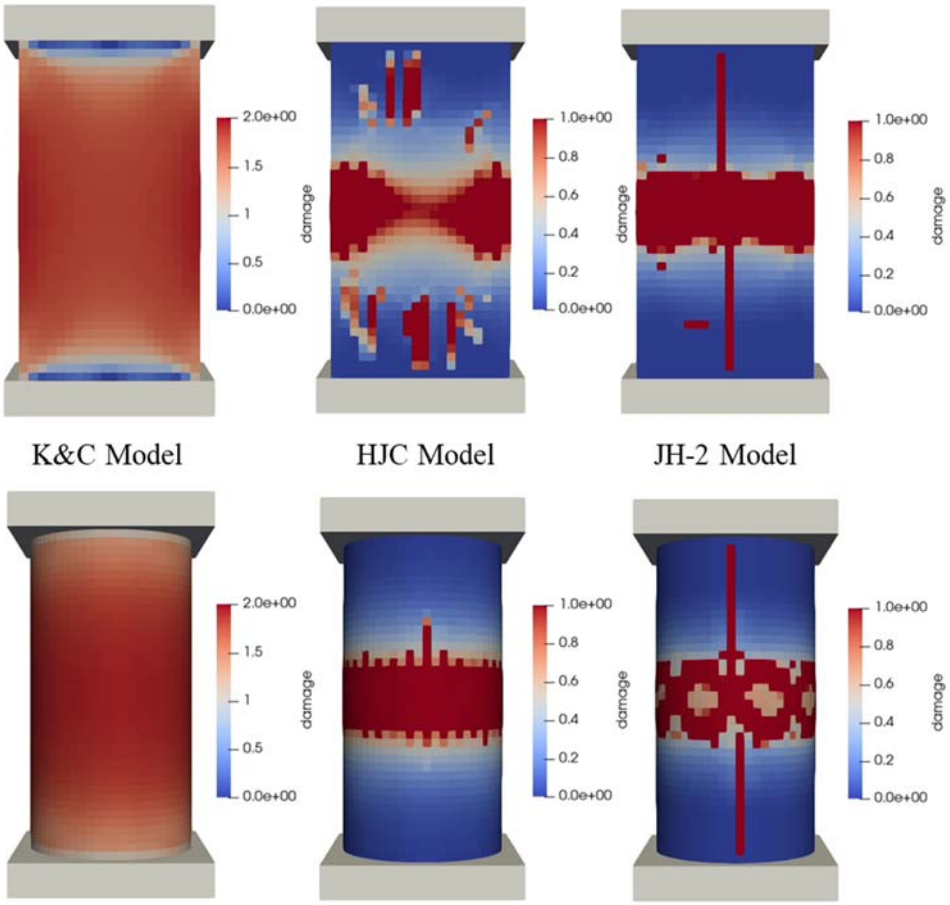

Figure 116: Cross-sectional view (top) and outside view (bottom) of damage patterns in concrete models

6.3.3 Residual Capacity Simulation Results and Discussion

A residual capacity study was conducted with the K&C, HJC, and JH-2 material models using the input parameters calibrated to the uniaxial compression test data. The experimental impact force versus time history from Test 2-4 was used to simulate the impulsive loading. The force versus time history was linearly scaled by a constant scale factor to apply a range of impulses to each model. Each model accumulated damage for different ranges of impulsive loading, so the scale factors levels of impulse were adjusted accordingly to observe the evolution of residual strength and stiffness.

6.3.3.1 Residual Capacity Results for K&C Model

Table 19 summarizes the inputs and major results from the K&C model residual capacity study. Figure 117 shows the force versus displacement curves for the combined dynamic and residual capacity loading. With increasing levels of impulsive load, there is a clear decrease in residual strength. The residual capacity curves all lie below the envelope formed by the quasi-static curve for the undamaged baseline simulation. Figure 118 shows the force versus displacement curves for residual capacity portion of the simulation, and the portion of each curve used to determine the residual modulus is indicated with black dashed lines. The behavior of the model can be qualitatively compared to the behavior of concrete subjected to cyclic loading, which was described in Section 2.1.1 and illustrated in Figure 2. Figure 2 illustrates that for repeated cycles of loading, the stiffness of the concrete degrades and plastic strain is accumulated. Figure 117 shows that for increasing levels of impulsive load, plastic strain accumulates but the stiffness does not appear to degrade as much as it should when qualitatively comparing Figure 117 to Figure 2. This is

unsurprising because the plasticity based models do not degrade the elastic response of the material, and instead represent the nonlinear behavior of concrete purely through the accumulation of plastic strain. However, at higher levels of impulse, the elastic modulus does appear to degrade in the modeled cylinder. This is caused by the accumulation of damage in failed elements. Once an element reaches the maximum stress surface and softening begins to occur, the stress surface will shrink and eventually degrade down to the residual surface as damage continues to accumulate. While the elastic modulus of the individual failed element does not change, once it reloads up to the softened surface it will deform plastically and result in an apparent reduction of elastic modulus for the global response of the damaged cylinder.

Table 19: K&C Residual capacity study inputs and results

K&C Simulation #	Impulsive Scale Factor	Impact Force, kip	Impact Impulse, kip-ms	Residual Strength, kip	Residual Modulus, ksi	Residual Work, ft-lb
1	0.700	66.04	47.35	64.96	3,611	452.78
2	0.750	65.90	50.56	64.83	3,601	445.03
3	0.800	64.27	53.75	63.19	3,579	412.45
4	0.850	64.71	56.95	62.09	3,655	386.23
5	0.900	67.40	60.69	61.61	3,647	368.37
6	0.950	70.06	64.52	57.55	3,647	306.07
7	1.000	72.70	68.42	50.68	3,563	210.03
8	1.050	75.29	72.23	42.57	3,235	157.33
9	1.100	77.78	75.90	37.36	2,731	117.57
10	1.150	80.23	79.44	37.81	2,968	105.33
11	1.200	82.57	82.84	32.74	2,746	86.48
12	1.250	84.80	86.04	26.62	1,897	65.65
13	1.200	87.08	89.06	21.69	1,203	50.28
14	1.350	89.48	91.87	13.04	1,509	41.23
15	1.400	91.90	94.24	11.20		
16	1.450	94.37	94.36	1.82		

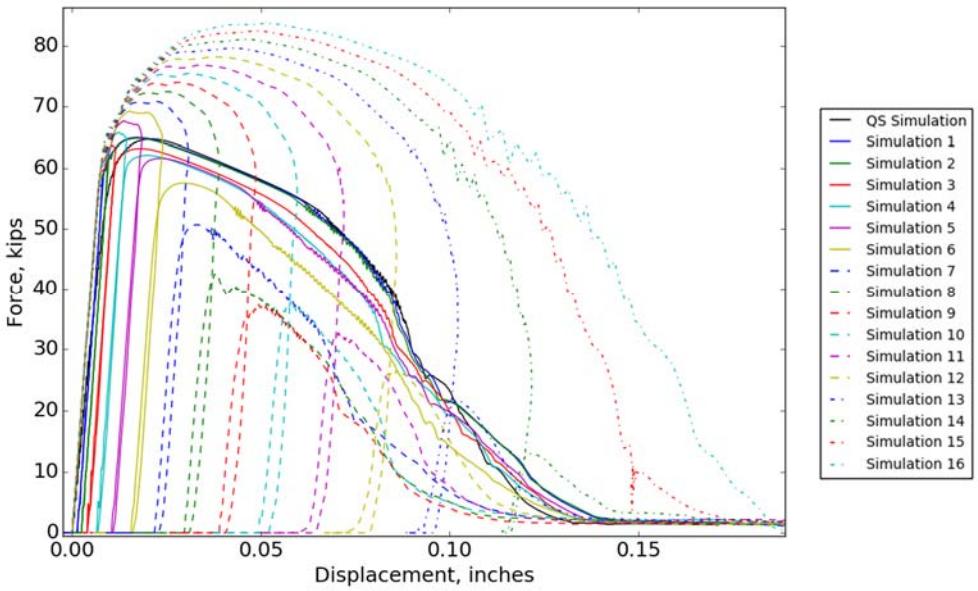

Figure 117: K&C model force versus displacement curves for combined dynamic and residual capacity loading

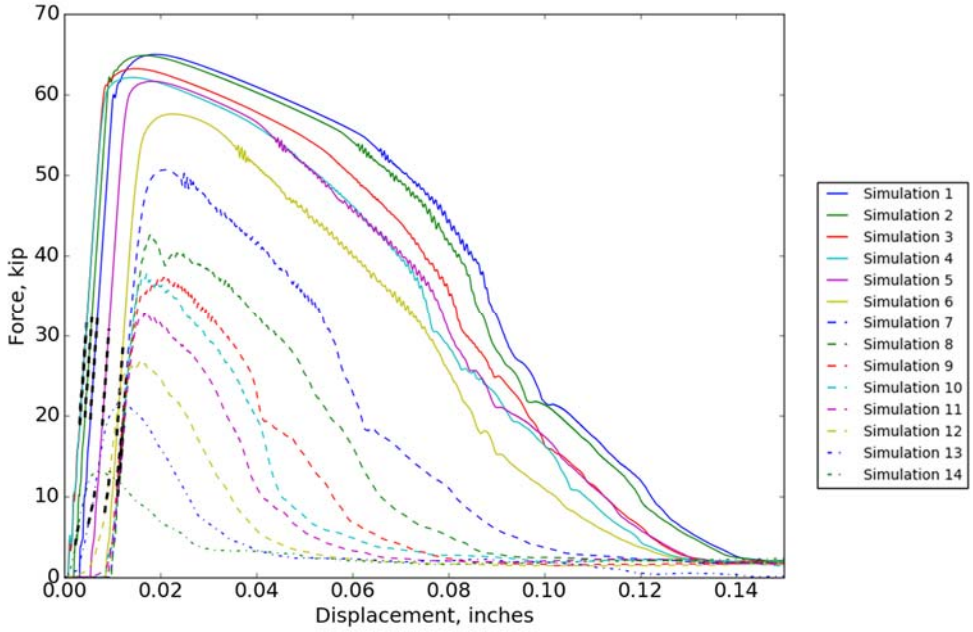

Figure 118: K&C model residual capacity force versus displacement curves

6.3.3.2 Residual Capacity Results for HJC Model

Table 20 summarizes the inputs and major results from the HJC model residual capacity study. Figure 119 shows the force versus displacement curves for the combined dynamic and residual capacity loading. With increasing levels of impulsive load, there is a clear decrease in residual strength, but the maximum forces during the dynamic loading are much lower than seen in the K&C model. The residual capacity curves all lie below the envelope formed by the quasi-static curve for the undamaged baseline simulation. Figure 120 shows the force versus displacement curves for residual capacity portion of the simulation. As discussed for the K&C model, the reloading curves show very little reduction in stiffness.

Table 20: HJC Residual capacity study inputs and results

HJC Simulation #	Impulsive Scale Factor	Impact Force, kip	Impact Impulse, kip-ms	Residual Strength, kip	Residual Modulus, ksi	Residual Work, ft-lb
1	0.850	66.84	57.14	66.41	3,809	434.97
2	0.900	67.52	60.33	65.87	3,918	420.96
3	0.925	68.35	62.41	65.28	3,856	405.46
4	0.950	69.06	64.43	63.24	3,829	372.01
5	0.975	69.71	66.41	60.30	3,783	328.17
6	1.000	70.28	68.63	56.48	3,681	280.29
7	1.025	70.81	70.74	52.51	3,562	237.56
8	1.050	71.41	72.68	49.04	3,459	212.97
9	1.075	72.09	74.44	43.01	3,169	170.13
10	1.100	72.74	75.90	33.87	2,897	112.41
11	1.110	72.99	76.39	32.24	2,905	120.38
12	1.115	73.13	76.52	23.25	2,302	121.61
13	1.120	73.26	76.40	16.31	1,652	102.01
14	1.125	73.39	76.03	12.76		75.15
15	1.150	73.98	73.14	6.17		

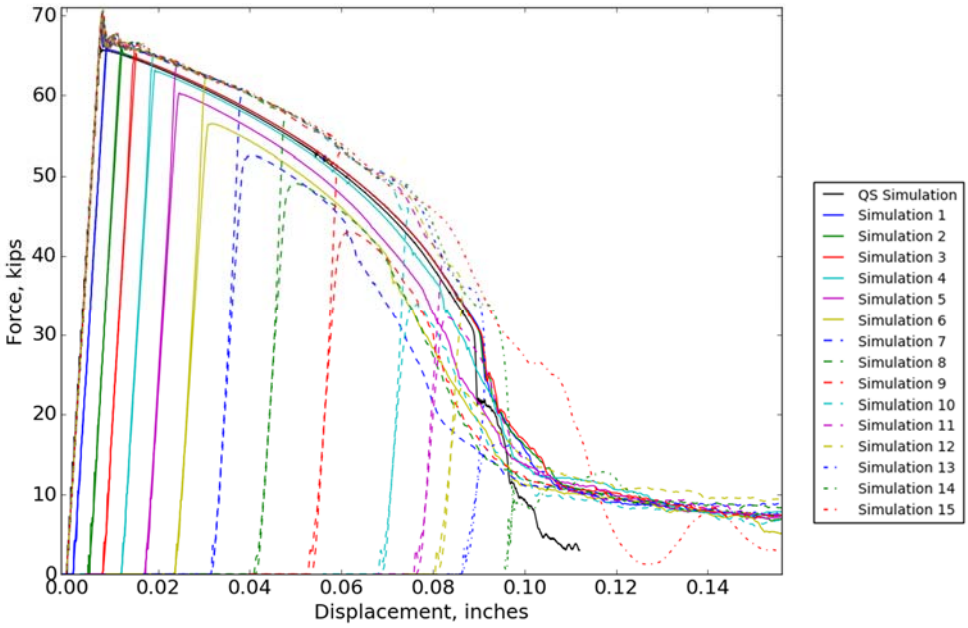

Figure 119: HJC model force versus displacement curves for combined dynamic and residual capacity loading

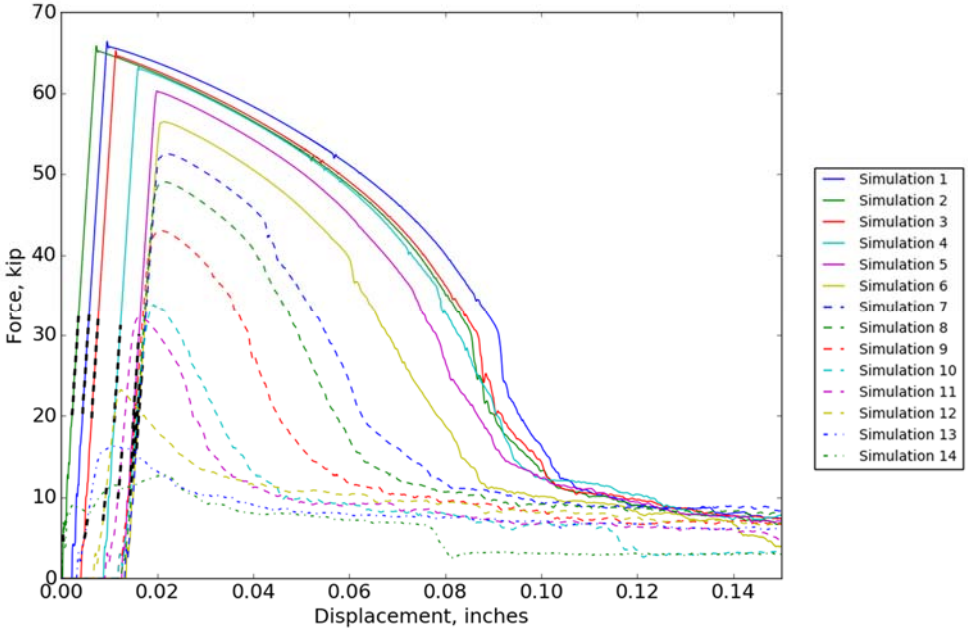

Figure 120: HJC model residual capacity force versus displacement curves

6.3.3.3 Residual Capacity Results for JH-2 Model

Table 21 summarizes the inputs and major results from the JH-2 model residual capacity study. Figure 121 shows the force versus displacement curves for the combined dynamic and residual capacity loading. Similar to the HJC model, the maximum forces during the dynamic loading are much lower than seen in the K&C model. Figure 122 shows the force versus displacement curves for residual capacity portion of the simulation. Compared to the K&C and HJC models, the JH-2 model began accumulating damage for at much lower levels of applied impulsive load. As discussed for the K&C model, the reloading curves show very little reduction in stiffness

Table 21: JH-2 Residual capacity study inputs and results

JH-2 Simulation #	Impulsive Scale Factor	Impact Force, kip	Impact Impulse, kip-ms	Residual Strength, kip	Residual Modulus, ksi	Residual Work, ft-lb
1	0.500	65.63	33.70	64.69	1,721	188.29
2	0.550	65.63	37.07	64.69	1,721	187.80
3	0.600	65.64	40.44	64.70	1,721	188.22
4	0.650	64.37	43.65	63.56	1,721	181.53
5	0.700	63.14	47.47	60.76	1,723	170.87
6	0.725	64.58	49.53	59.20	1,725	157.60
7	0.760	66.15	52.62	43.18	1,555	123.26
8	0.770	66.56	53.55	37.40	1,505	118.93
9	0.780	66.87	54.54	37.25	1,529	106.93
10	0.790	67.29	55.46	33.91	1,398	98.19
11	0.750	65.74	51.72	46.11	1,597	130.30
12	0.800	67.52	55.07	8.86	481	74.75
13	0.825	68.33	51.42	5.47	0	0

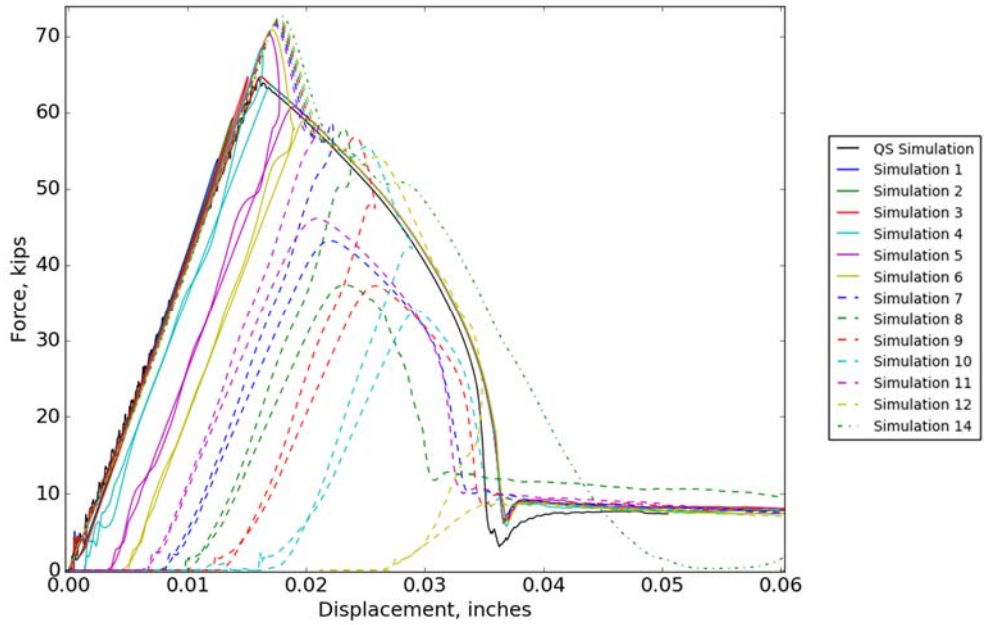

Figure 121: JH-2 model force versus displacement curves for combined dynamic and residual capacity loading

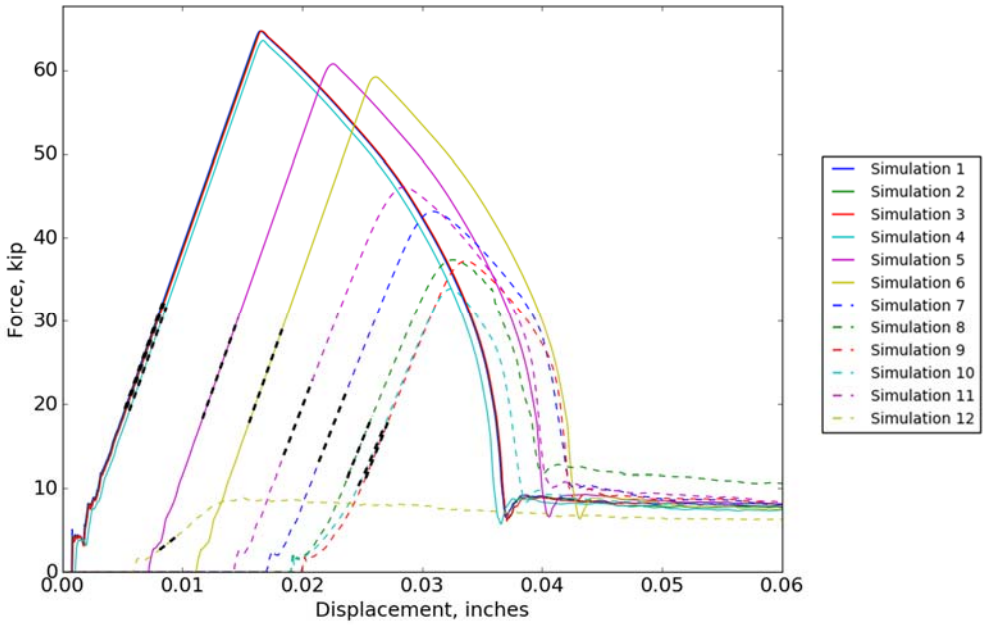

Figure 122: JH-2 model residual capacity force versus displacement curves

6.3.3.4 Model Comparison to Experimental Results

The residual strength, modulus, and work ratios are plotted with respect to the applied impulse in Figure 123, Figure 123, and Figure 125, respectively. The experimental data from Test Series 2 is plotted with the simulation results from each model. For each metric, the JH-2 model drastically under-predicts the residual capacity as compared to the HJC and K&C models, as well as the experimental data. This is likely a result of the model not accurately representing the descending branch of the force displacement curve.

The K&C and HJC models closely match each other for impulsive loads below 72 kip-ms. However, their predictions begin to differ around an applied impulse of approximately 72 kip-ms, where the HJC model quickly reduces in residual strength and stiffness with increased impulse. The predictions for residual strength are generally lower than the experimental results, with the HJC providing the closest fit for impulses up to 72 kip-ms. For impulses larger than 72 kip-ms, the K&C model closely matches the experimental data. The residual modulus predictions for the K&C and HJC models do not match the experimental trend, with both models generally over-predicting.

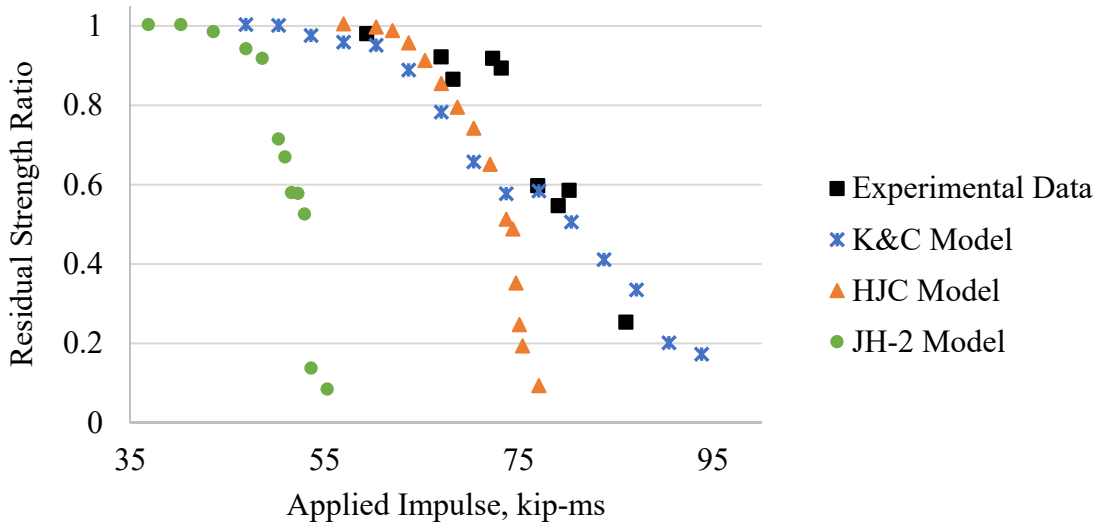

Figure 123: Residual strength ratio versus applied impulse

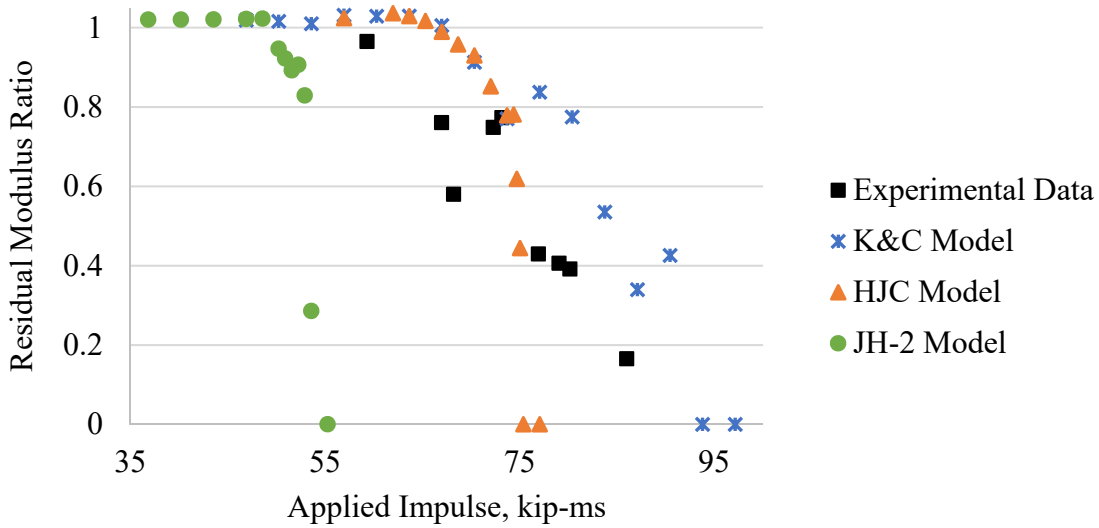

Figure 124: Residual modulus ratio versus applied impulse

Figure 125 shows the residual work ratio versus applied impulse. In this case, the experimental results are significantly higher than the model predictions. This may be

caused by the difference in shape of the descending branch of the curve between the models and the experiments.

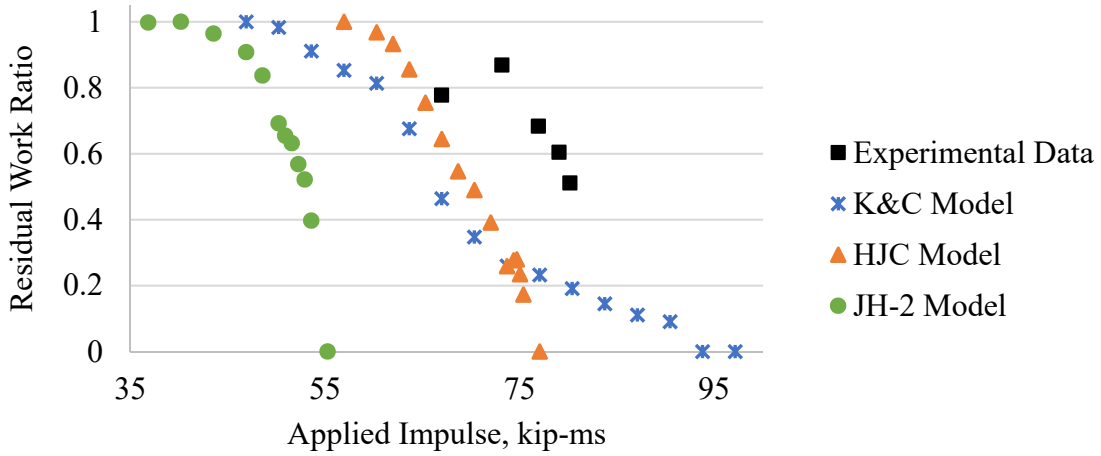

Figure 125: Residual work ratio versus applied impulse

Figure 126 plots the relationship between the residual strength and residual modulus. The behavior of the models differs significantly from the experimental results, as the models show a loss of strength much more rapidly than a loss stiffness, while the experimental results display the opposite trend. This indicates that the plasticity-based damage formulation in the models does not adequately capture the loss in stiffness that occurs as damage is accumulated. This is potentially concerning because correctly representing changes in stiffness is important when computing the global response of a damaged structure. To improve these models, it may be necessary to incorporate a damage mechanics formulation to appropriately degrade the elastic stiffness of damaged elements.

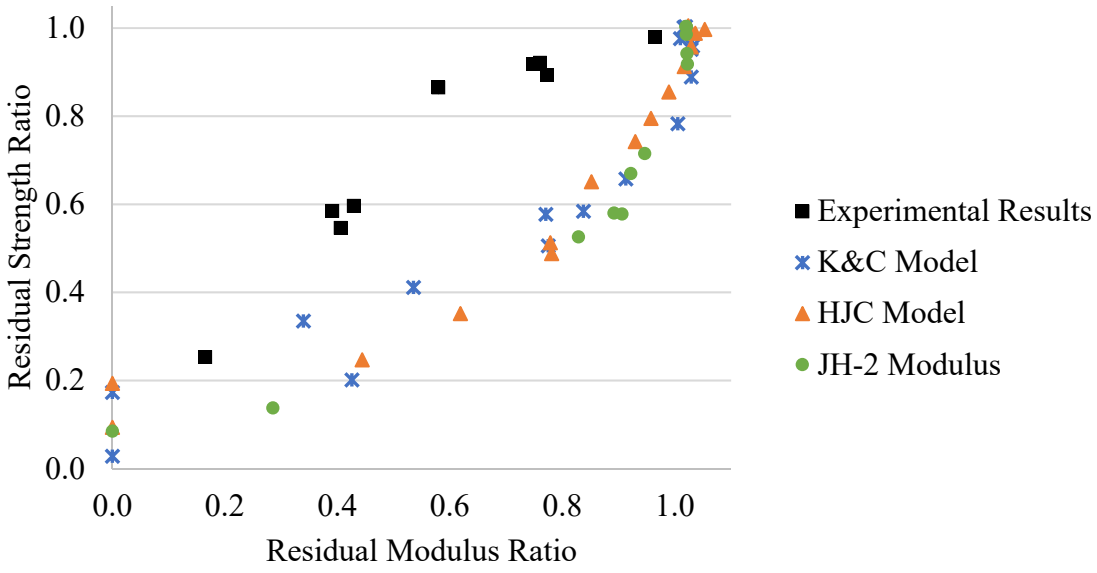

Figure 126: Residual strength ratio versus residual modulus ratio

6.3.3.5 Influence of Post-Peak Softening on Residual Capacity Predictions

To examine the importance of fully characterizing the descending branch of the force versus displacement curve, a series of simulations was conducted with the K&C model for different values of maximum aggregate size (MSA). This parameter, which is used in the model to estimate the shear inducted dilatation of the material, directly influences the slope of the descending branch. A series of combined dynamic and residual capacity simulations were conducted for aggregate sizes of 0.25 inches, 0.40 inches, and 0.50 inches. The quasi-static uniaxial compression curves for the varying MSA are shown in Figure 127. Increasing the MSA reduces amount of post-peak softening.

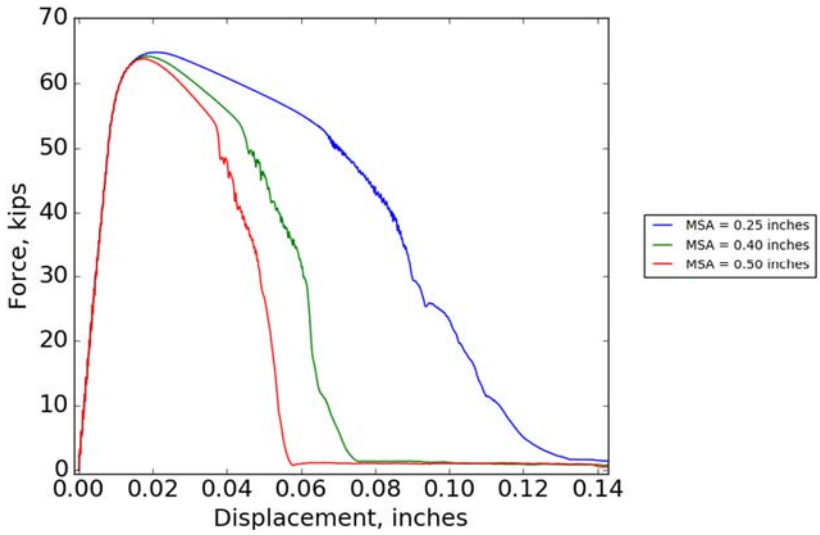

Figure 127: K&C uniaxial compression force versus displacement results for varying MSA

Table 22 and Table 23 list the input parameters and results for the simulations with MSA = 0.40 inches and 0.50 inches, respectively. Figure 128 and Figure 129 show the force versus displacement curves for the combined dynamic and residual capacity loading for each case. The 0.50 MSA case clearly shows a more rapid decrease in strength with increasing levels of applied impulsive load.

Table 22: K&C residual capacity study inputs and results for MSA = 0.40 inches

0.40-inch MSA	Impulsive Scale Factor	Impact Impulse, kip-ms	Residual Strength. kip	Residual Modulus, ksi	Residual Work, ft-lb
1	0.70	46.90	64.53	3,612	292.77
2	0.75	50.25	64.24	3,617	283.57
3	0.80	53.60	61.89	3,565	248.45
4	0.85	56.95	58.11	3,678	209.94
5	0.90	60.30	46.67	3,476	159.96
6	0.95	63.65	41.80	3,105	113.98
7	1.00	67.00	36.41	2,887	72.44
8	1.05	70.35	28.97	2,440	50.84
9	1.10	73.70	21.01	2,004	40.56
10	1.15	77.05	11.43	1,187	27.48
11	1.20	80.39	1.25	32	12.35

Table 23: K&C residual capacity study inputs and results for MSA = 0.50 inches

0.50-inch MSA	Impulsive Scale Factor	Impact Impulse, kip-ms	Residual Strength. kip	Residual Modulus, ksi	Residual Work, ft-lb
1	0.70	46.90	64.27	3612	232.39
2	0.75	50.25	63.82	3617	223.27
3	0.80	53.60	61.45	3562	193.88
4	0.85	56.95	54.04	3644	154.96
5	0.90	60.30	40.94	3395	104.93
6	0.95	63.65	38.19	2889	68.37
7	1.00	67.00	31.28	2372	45.25
8	1.05	70.35	15.56	1697	32.34
9	1.10	73.70	2.83	0	15.45

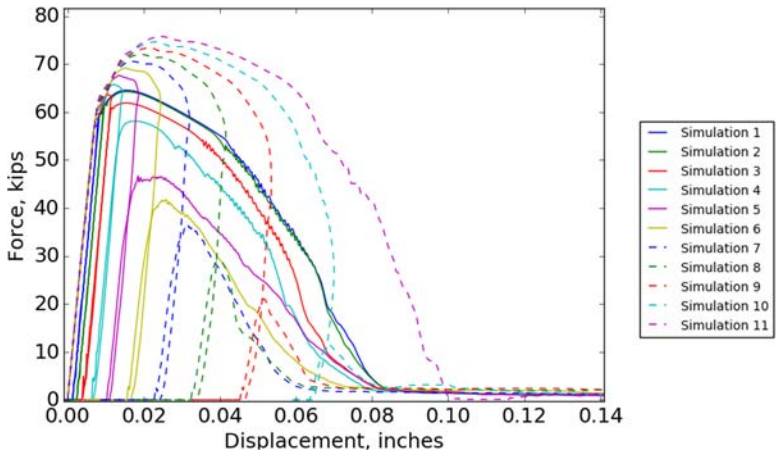

Figure 128: K&C model force versus displacement curves for combined dynamic and residual capacity loading with MSA = 0.40 inches

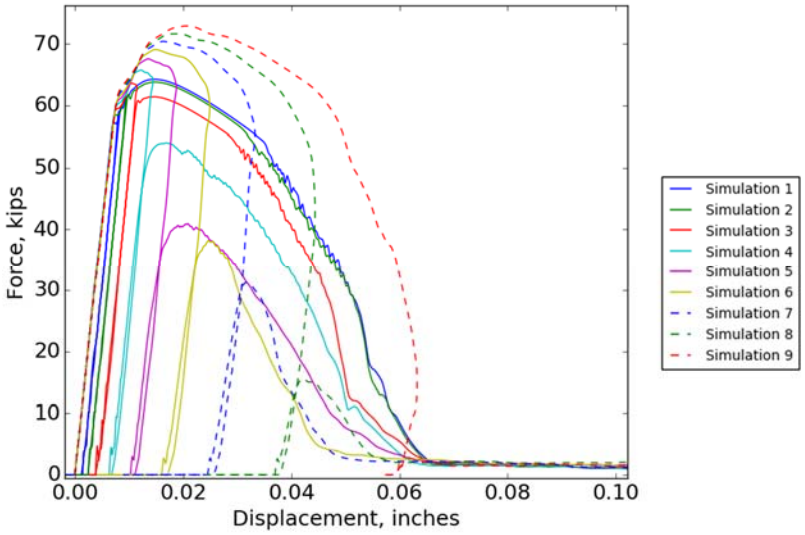

Figure 129: K&C model force versus displacement curves for combined dynamic and residual capacity loading with MSA = 0.40 inches

The residual strength ratio, residual modulus ratio, and residual work ratios are plotted with respect to the applied impulse in Figure 130, Figure 131, and Figure 132. With increasing MSA, and thus loss of post-peak softening, there is a clear reduction in residual strength, modulus, and work. These results indicate that to accurately predict the behavior of concrete as it sustains damage, it is critical to correctly represent this characteristic of the material.

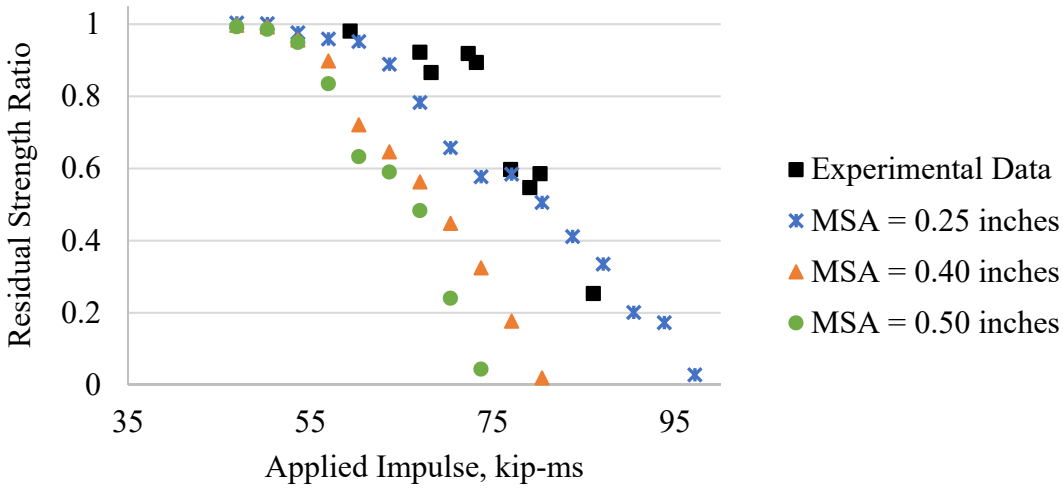

Figure 130: Residual strength ratio versus applied impulse

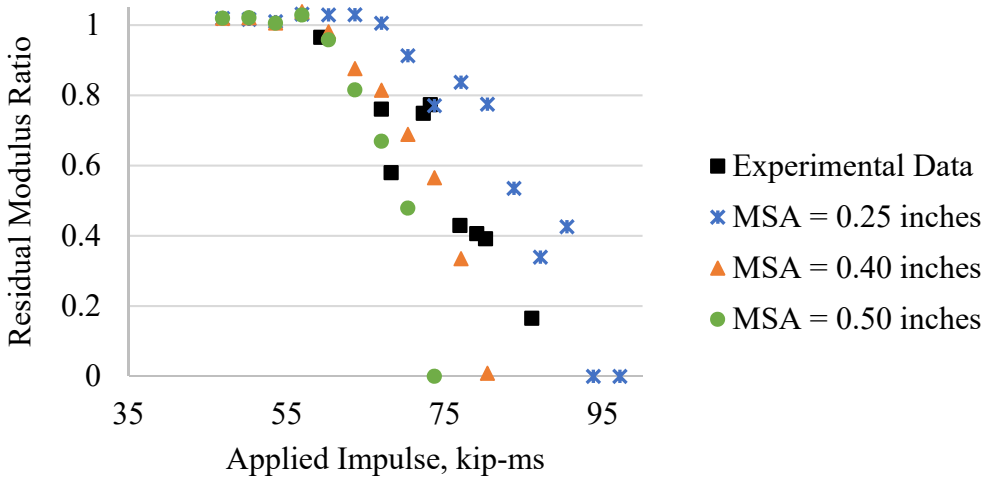

Figure 131: Residual modulus ratio versus applied impulse

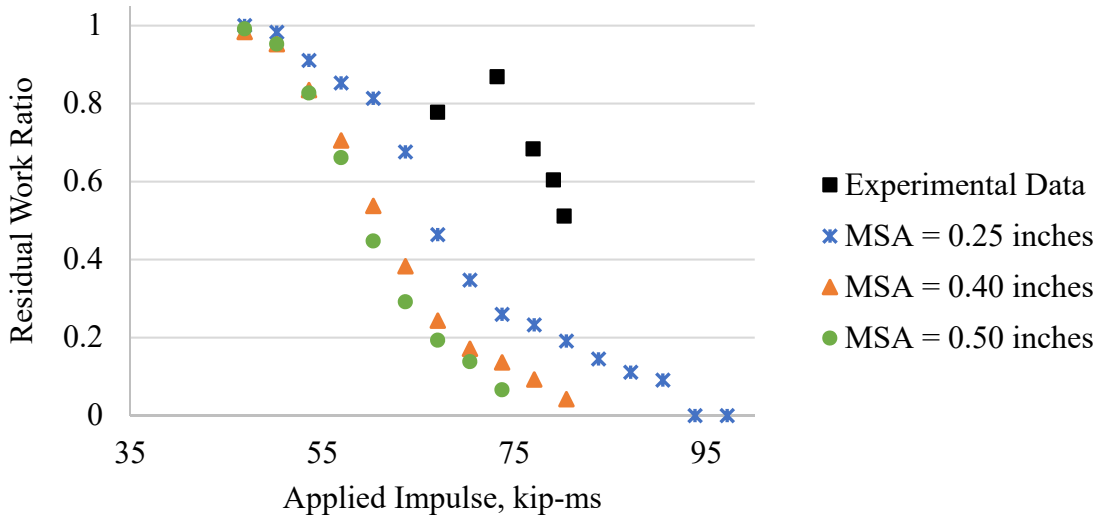

Figure 132: Residual work ratio versus applied impulse

6.4 Conclusions

A computational study was conducted to evaluate the response of concrete constitutive models to varying levels of impulsive load. The predicted residual strength, modulus, and work of the damaged concrete cylinder was determined and compared to the results of the Test Series 2. The JH-2 model provided a poor fit to the experimental data as it became fully damaged for relatively low levels of impulse. For impulses levels lower than 72 kip-ms, the HJC provided the closest match to the experimental data for residual force. Above 72 kip-ms, the K&C model provided a close fit to the experimental data. The K&C and HJC models both over predicted the residual modulus and under predicted the residual work. The significance of correctly characterizing the post-peak softening behavior was illustrated with the K&C model. The major insights from of the computational study are as follows:

1) Experimentally characterizing and calibrating concrete constitutive models to match the post-failure softening behavior is critical for accurately predicting residual capacity. There is a need for a thorough experimental characterization of the post-peak response to concrete in compression, as there is little relevant experimental data in the literature.
2) The residual capacity of damaged concrete lies under the envelope curve that corresponds to the full force versus displacement behavior of the undamaged material. Thus, the residual capacity predictions of concrete constitutive models can be improved by providing more control over the shape of the full force displacement curve.
3) The experimental data indicate that a loss of stiffness occurs more rapidly than a loss of strength for increasing levels of applied impulsive load. However, the concrete models examined in this study exhibit the opposite behavior, with a more rapid loss of strength before the material experiences any significant reduction in stiffness. This points to a potential shortcoming with the use of these models, as their plasticity-based damage formulations do not degrade the elastic modulus as damage is accumulated. This is concerning because these plasticity-based models are the most commonly used type of constitutive model in structural-scale residual capacity predictions. If the stiffness of the damaged concrete is not correctly represented, then the predicted stiffness and thus global response of a full-scale damaged structure is likely incorrect. Thus, there is a need to incorporate a damage mechanics competent to these models to account for the experimentally-observed loss of stiffness.

CHAPTER 7. CONCLUSIONS AND RECOMMENDED FUTURE RESEARCH

7.1 Conclusions

7.1.1 Development of an Impulsive Concrete Compression Testing System

One of the primary outcomes of this research is the development of an impulsive compression testing system and protocol that is capable of subjecting concrete cylinders to compression-only forces and impulses. This system is designed to be adaptable and versatile to test concrete with single or repeated impulsive hits of controlled magnitude. The basic methodology can be applied to test a variety of specimens with different shapes, sizes, and material properties. The conclusions from the impulsive experimental program are as follows:

- The testing program conducted testing up to strain rates of 5.6 s^{-1}. In the rate ranges tested, there is a linear relationship between the applied kinetic energy to the system and the resulting strain rate in the specimen. Based on this relationship and the maximum kinetic energy that can be achieved with the blast generator system, a maximum strain rate of 60 s^{-1} can be theoretically achieved with the current experimental setup.
- The test environment was capable of producing repeatable impulses given the same input parameters to the hydraulic system. The test setup is capable of subjecting separate specimens to nearly identical impulses, or subjecting the same specimen to repeated hits. In addition, a special test case demonstrates the ability of the test

system to generate double hits within a timespan of several milliseconds. This testing capability provides a methodology for gaining insight on the behavior and degradation of concrete subjected to repeated impacts

- The test system design is conducive for conducting finite element simulations that isolate the response of the material without needing to account for uncertainties involved with modeling the full response of the test system frame or the flyer plate programmer material. The load cells directly measure the compressive forces on the impact and reaction sides of the specimen to isolate the material response without the influence of other variables. This allows the behavior of the specimen to be fully isolated from the rest of the system, and the experimental impact force can provide the input to the finite element simulation to directly compare the model with the observed experimental response.

7.1.2 Experimental Investigation of the Residual Capacity of Concrete Subjected to Impulsive Loads

One of the most important contributions of this research is the novel experimental evaluation of the residual capacity of concrete damaged by impulsive loads. This research successfully bridges the gap between materials-level high strain rate testing and structural level residual capacity studies to provide insight on the degradation of strength and stiffness at the material level for varying levels of impulsive damage. The following conclusions result from the experimental study:

- There is a clear decrease in the quasi-static residual strength and stiffness for specimens subjected to increasing levels of impulsive load. Most

notably, the proportional loss of stiffness is much greater than the loss of strength at lower levels of damage. This differs from the behavior of concrete as it sustains damage through quasi-static mechanical loads, where the loss of strength versus stiffness is nearly proportional. So, this trend in the impulsively damaged concrete is likely due to damage mechanisms that only occur during impulsive loading. The existence of this trend is previously unknown and provides novel insight on the behaviour of impulsively damaged concrete. It is possible that the high strain rate causes damage to occur in the form of distributed microcracking, which may reduce the stiffness of the material while having a lesser effect on the strength.

- A preliminary test shows that the dynamic residual strength capacity is larger in magnitude than the quasi-static residual strength. This is an expected result due to strain rate effects, but very little is known specifically about the strain rate effects of damaged concrete. This test case provides a methodology for gaining novel insight on the degradation of concrete subjected to repeated impacts.

7.1.3 Evaluation of Concrete Constitutive Models

A numerical study was conducted to evaluate the suitability of concrete constitutive models for predicting the residual capacity of concrete subjected to impulsive loads. Three models commonly used for blast and impact applications were examined: the Karagozian and Case (K&C) model [58], the Holmquist-Johnson-Cook (HJC) concrete model [59],

and the Johnson-Holmquist (JH-2) ceramic model [60]. The major conclusions from the numerical study are as follows:

- Experimentally characterizing and calibrating concrete constitutive models to match the post-failure softening behaviour is critical for accurately predicting residual capacity. There is a need for a thorough experimental characterization of the post-peak response to concrete in compression, as there is little relevant experimental data in the literature.
- The experimental data indicate that a loss of stiffness occurs more rapidly than a loss of strength for increasing levels of applied impulsive load. However, the concrete models examined in this study exhibit the opposite behaviour, with a more rapid loss of strength before the material experiences any significant reduction in stiffness. This points to a potential shortcoming with the plasticity-based damage formulation in these models, as their current form does not account for the experimentally-observed loss of stiffness. Model advancements are needed to represent the degradation of stiffness in addition to the currently represented accumulation of plastic strain. This could potentially be achieved by incorporating a damage mechanics component to penalize the elastic modulus as damage is accumulated. To assist this effort, more experimental data is needed to characterize the full extent of the relationship between the loss of modulus and the loss of strength for impulsively damaged concrete.

7.1.4 Summary of Experimental and Numerical Investigations

A summary of the major findings of the experimental and numerical study is presented in Figure 133, which plots the residual strength ratio versus residual modulus ratio for the impulsive and quasi-static data sets. There is a proportional reduction in strength versus modulus for quasi-statically damaged concrete, while impulsively damaged concrete experiences a much larger reduction in stiffness than strength. The computational models display the opposite trend from the experiments.

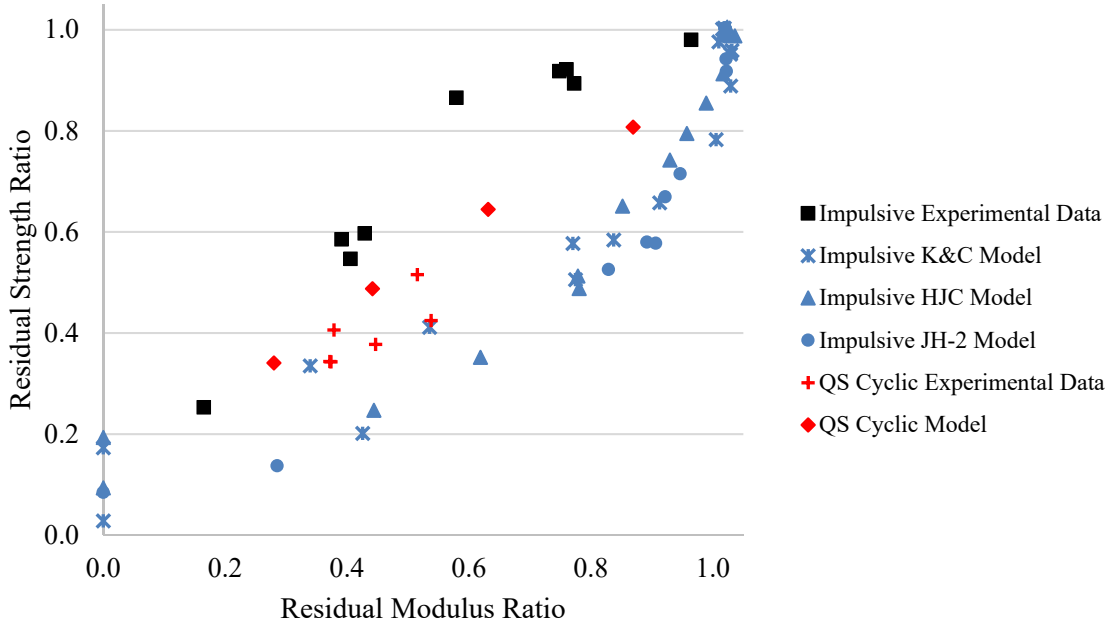

Figure 133: Residual strength versus modulus ratio for impulsive and quasi-static experiments and models

Based on the major findings of this research, the current modeling methods evaluated are not sufficiently characterizing the damage and residual capacity of concrete subjected to impulsive loads. Purely accounting for strain rate effects by scaling the

compressive strength of the material is likely not enough to account for the changes in mechanical behavior that occur during impulsive loading. In addition, the current literature on the dynamic behavior of concrete does little explain these observed experimental trends in residual capacity. All previous experimental efforts to characterize the residual capacity of concrete have focused on structural scale problems. However, if the residual capacity behavior and damage mechanisms of concrete subjected to impulsive loads is not well characterized at the material level, as these results indicate, then the use of constitutive models for complex residual capacity calculations should be approached with caution.

7.2 Recommendations for Future Work

7.2.1 Recommended Improvements to the Dynamic and Residual Capacity Test Systems

This work served as the proof of concept stage to develop the framework needed to study concrete damaged by impulsive loads. As such, many improvements were noted throughout the process of designing, fabricating, and executing the experimental program. The improvements that are recommended for future experimental programs are included in the following sections.

7.2.1.1 Improvements to the Dynamic Test System

Improving the diagnostic system to better monitor the displacement during the impulsive loading event would provide additional insight on concrete behaviour. The camera system and settings used in this experimental program was not sufficient in frame rate or resolution to capture the displacement in a reliable manner. Better displacement data would be helpful to determine the force versus displacement time history during dynamic

loading and to quantify the residual strain of the damaged specimen. Knowledge of the displacement and residual strain of the specimen subjected to impulsive loading will permit a characterization of the response and residual capacity with respect to the quasi-static envelope curve.

The use of higher capacity load cells will permit testing to be conducted at much higher strain rates, and will permit testing to be conducted on fully cured normal strength concretes. In addition, the ability to test for a wider range of applied impulse will provide better characterization of normal strength concrete, ranging from little damage to fully damaged. With this capability and with improved displacement diagnostics, dynamic strength and modulus increase factors can be determined and a wide range of damaged states can be evaluated

7.2.1.2 Improvements to the Residual Capacity Test System

To improve the residual capacity method utilized in this research program, the concrete specimen can be outfitted with a compressometer to directly measure the axial and radial strains of the specimen. This would eliminate the uncertainties involved in the interpretation of the displacement data, such as with the large amount of slack observed in the test system.

7.2.1.3 Improvements to the Prototype In Situ Residual Capacity Test System

The prototype in situ residual capacity test setup can be improved by supplying a more rigid connection between the floor, beam, column, and hydraulic ram to eliminate eccentricities at high compressive loads. A vertical restraint can be added to the ram to

limit upward motion during compressive loading. If this eccentricity is eliminated, then the in situ residual capacity test system can be applied to obtain data in cases where the removal of the specimen will prohibit obtaining reliable residual capacity measurements.

7.2.2 Recommended Future Research

This dissertation research served as the proof of concept phase to develop the testing capability needed to study concrete damaged by impulsive loads. As such, a limited number of tests was conducted. Now that the basic framework and experimental methodology has been established, future research programs can focus on generating more data to better characterize the response of concrete to impulsive loading. One of the most important research findings was the observation that as concrete sustains damage from impulsive loading, the damage first manifests in the form of a loss of material stiffness before there is a notable loss of strength. Testing should be conducted to diagnose the damage mechanisms responsible for this trend and to provide insight on how constitutive models can better represent this material behavior.

In addition, the strain rate dependent properties of concrete can be studied in depth. The strength and stiffness can be evaluated under various strain rates to provide insight on suitability of using dynamic increase factors to account for such effects. Additional diagnostics such as axial and radial strain gauges can be used to evaluate the bulk response of the material. In addition, novel insight on the strain rate dependent properties of damaged concrete could be studied by subjecting specimens to repeated impacts.

The parameters to fully characterize concrete are nearly endless, with potential variables in both material properties and loading conditions. For example, the effect of

changing concrete strength and aggregate type can be evaluated with regard to the residual capacity and dynamic response of the material. High performance concretes and the inclusion of admixtures or fibers can be studied to evaluate their resistance to impulsive loads. During the development of the dynamic test, it was observed that changing the programmer material on the flyer plate changed the pulse shape and magnitude of the applied dynamic force. Thus, the loading conditions on the specimen can likely be manipulated in magnitude and duration to study how these parameter influence the resulting damage. In summary, the experimental methodology presented in this research, with the combined further development of the in situ residual capacity test capability, can be applied for many types of studies. The basic concept illustrated here can be extended to not only evaluate the residual capacity of materials such as concrete, but also structural components such as beams and columns subjected to flexural impulsive loads.

APPENDIX A: EXPERIMENTAL DATA

Test 1-1

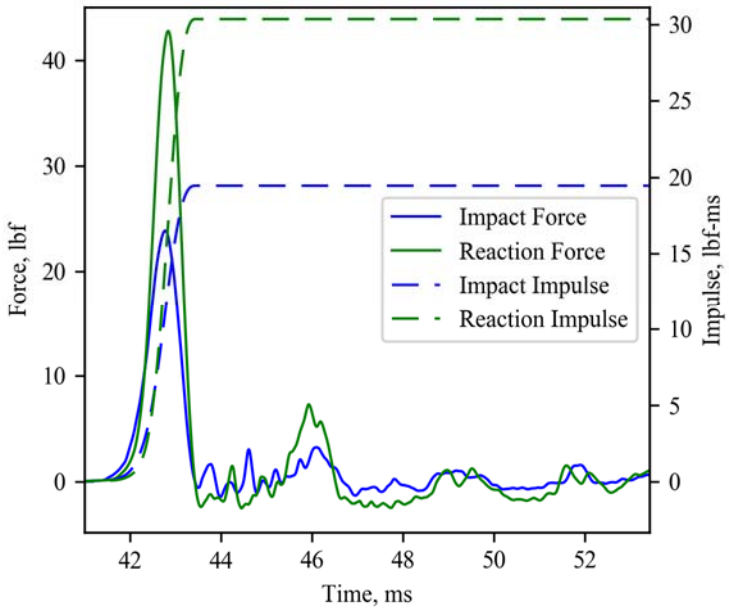

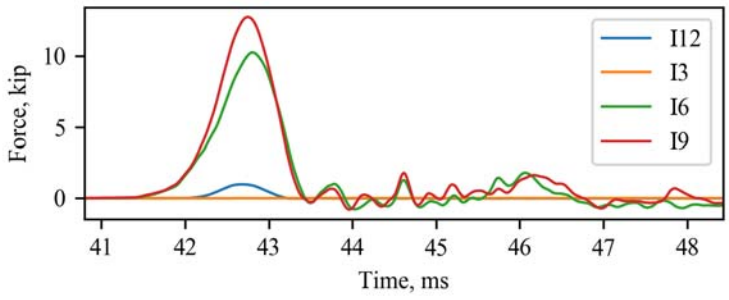

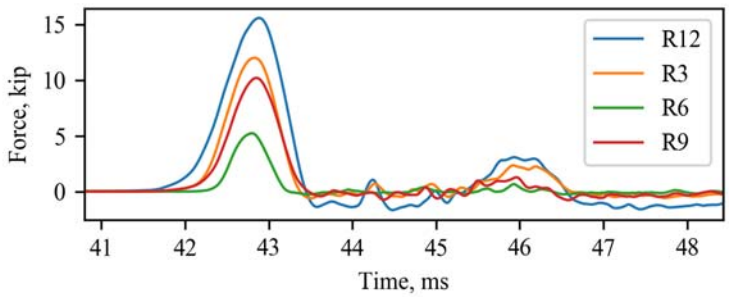

Test 1-2

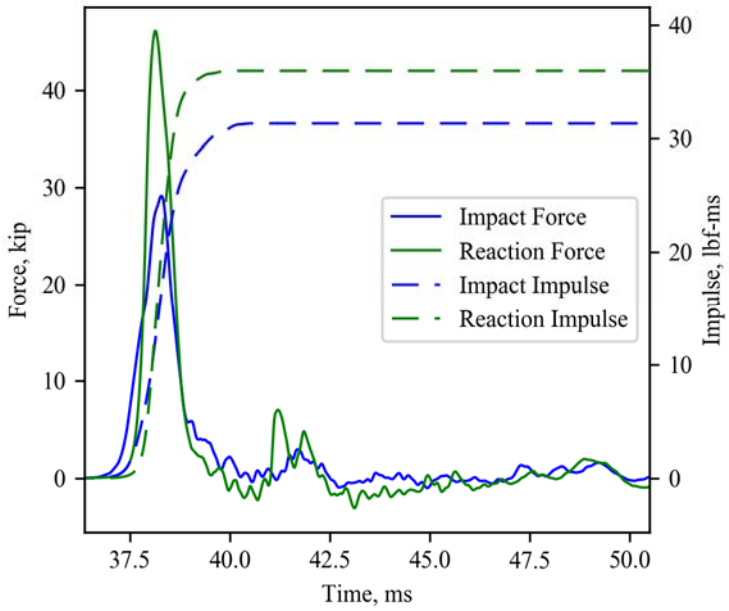
Force, kip
Impulse, lbf-ms
Time, ms
Impact Force
Reaction Force
Impact Impulse
Reaction Impulse

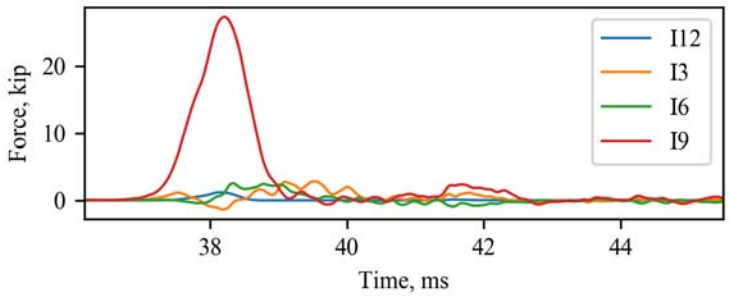
Force, kip
Time, ms
I12
I3
I6
I9

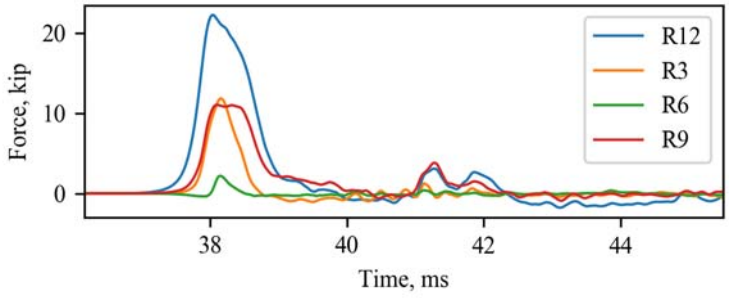
Force, kip
Time, ms
R12
R3
R6
R9

Test 1-3

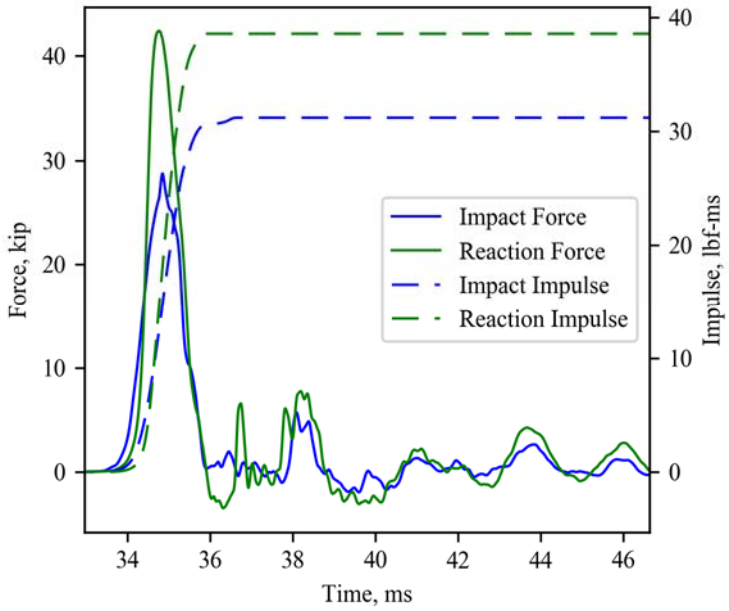
Force, kip
Impulse, lbf-ms
Time, ms
Impact Force
Reaction Force
Impact Impulse
Reaction Impulse

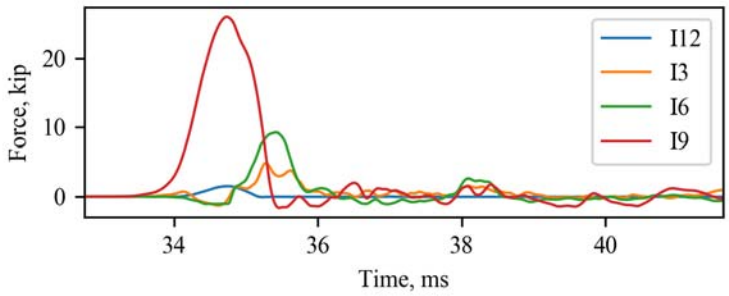
Force, kip
Time, ms
I12
I3
I6
I9

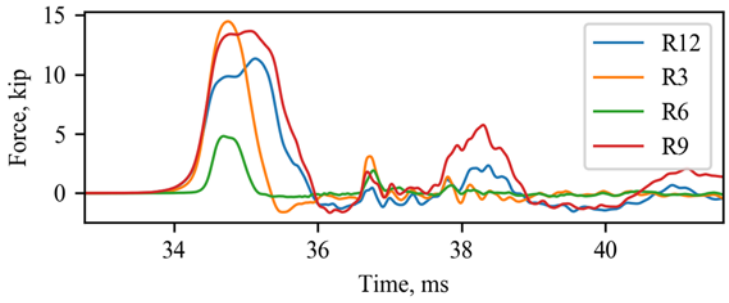
Force, kip
Time, ms
R12
R3
R6
R9

Test 1-4

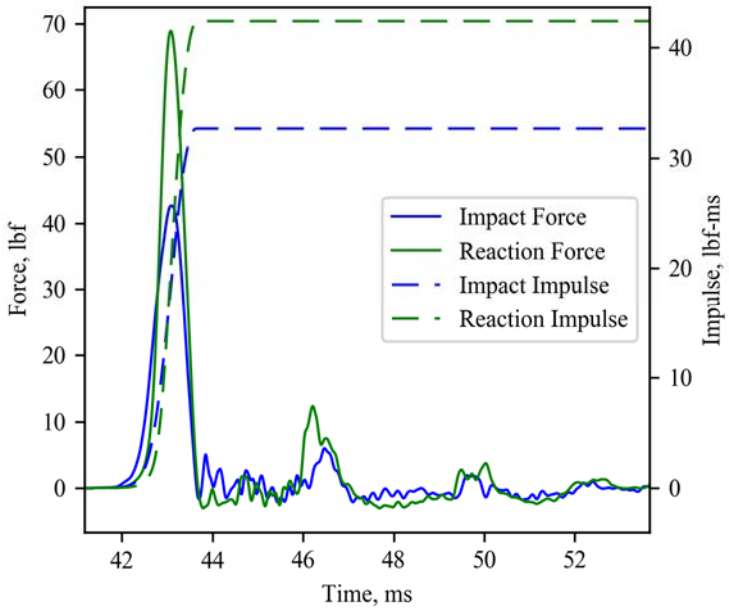
Force, lbf
Impulse, lbf-ms
Time, ms
Impact Force
Reaction Force
Impact Impulse
Reaction Impulse

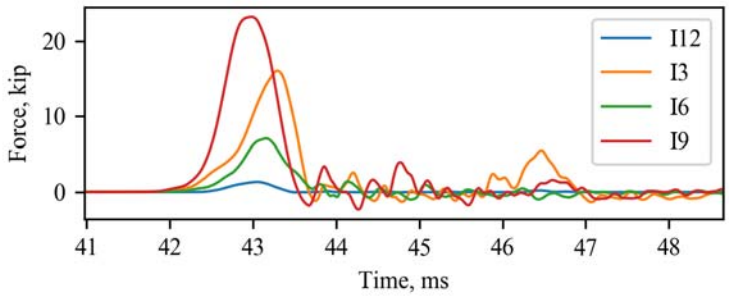
Force, kip
Time, ms
I12
I3
I6
I9

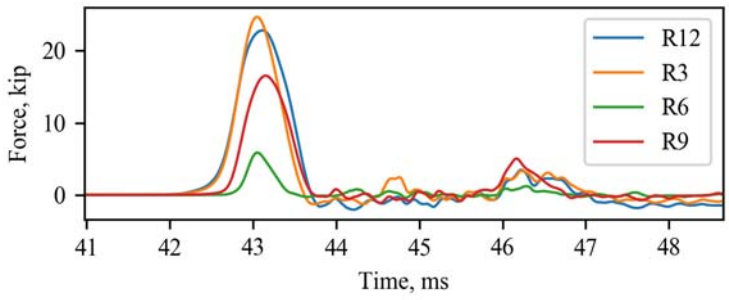
Force, kip
Time, ms
R12
R3
R6
R9

Test 1-5

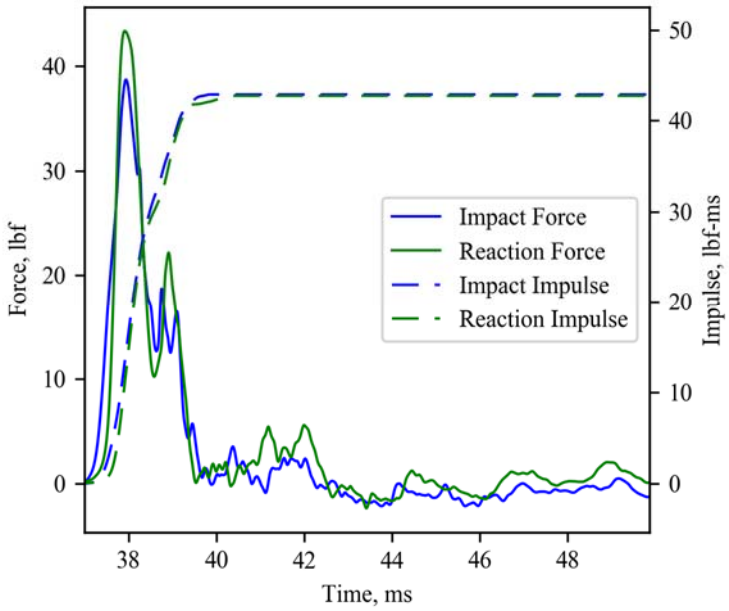
Force, lbf
Impulse, lbf-ms
Time, ms
Impact Force
Reaction Force
Impact Impulse
Reaction Impulse

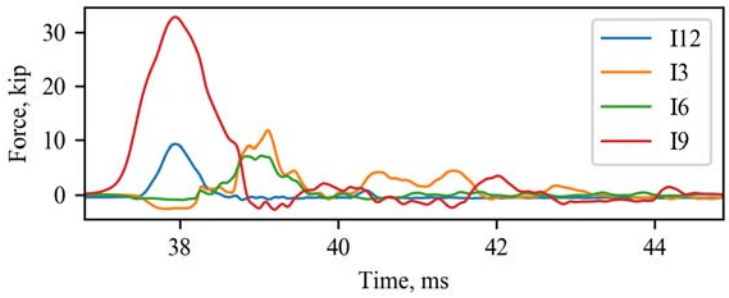
Force, kip
Time, ms
I12
I3
I6
I9

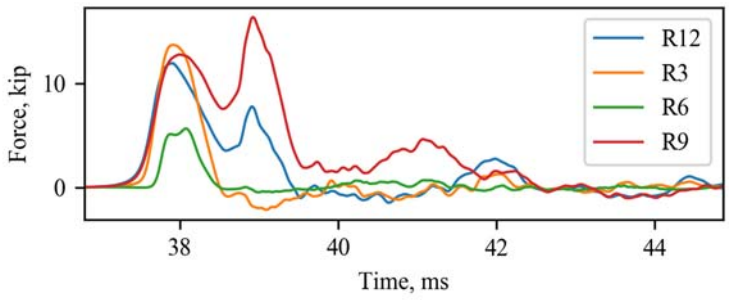
Force, kip
Time, ms
R12
R3
R6
R9

Test 1-6

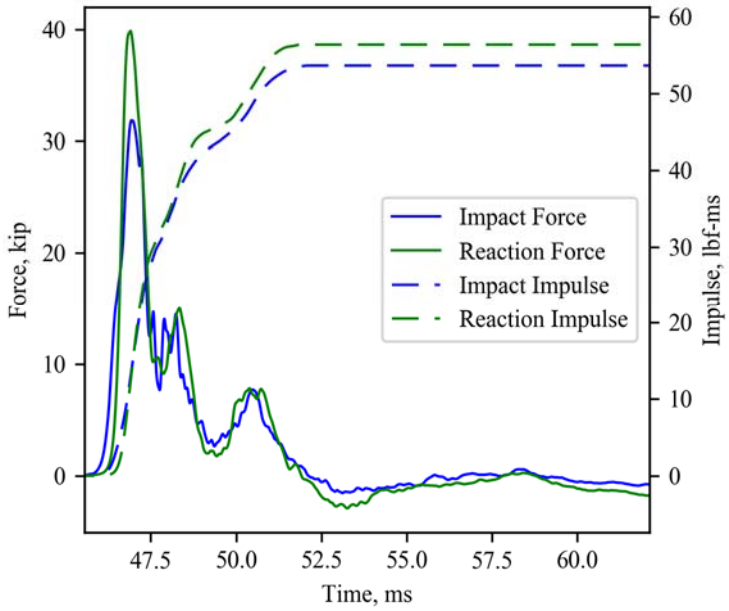
Force, kip
Impulse, lbf-ms
Time, ms
Impact Force
Reaction Force
Impact Impulse
Reaction Impulse

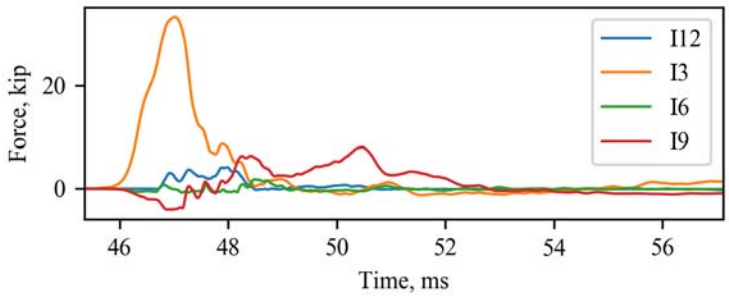
Force, kip
Time, ms
I12
I3
I6
I9

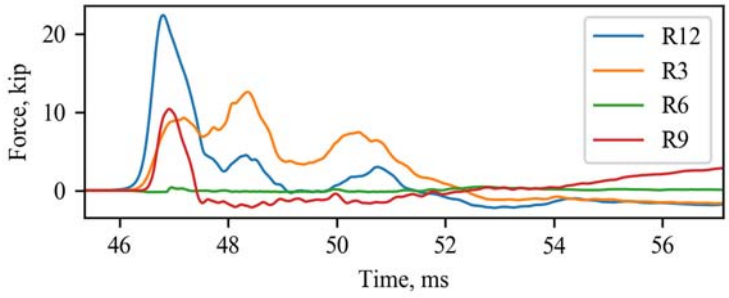
Force, kip
Time, ms
R12
R3
R6
R9

Test 1-7

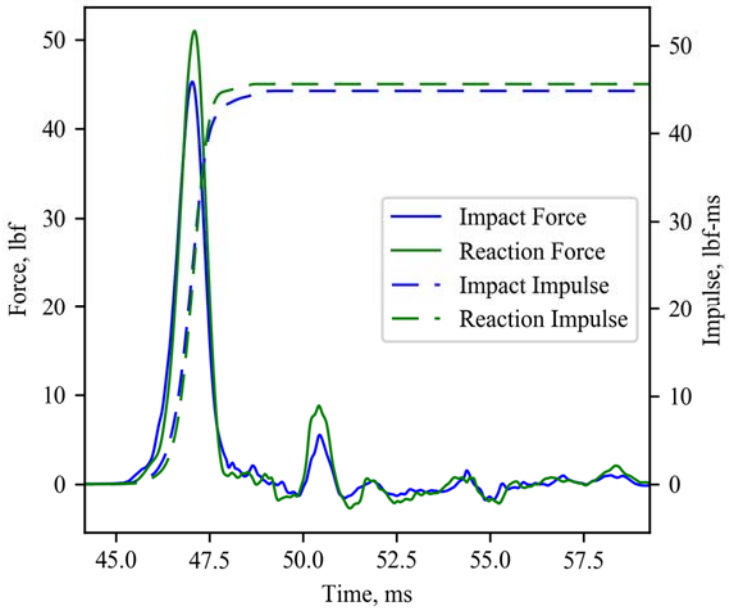
Force, lbf
Impulse, lbf-ms
Time, ms
Impact Force
Reaction Force
Impact Impulse
Reaction Impulse

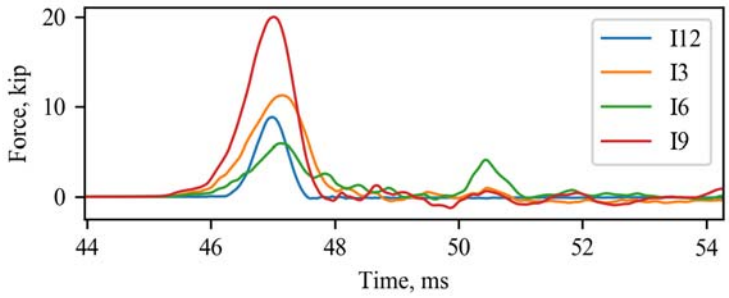
Force, kip
Time, ms
I12
I3
I6
I9

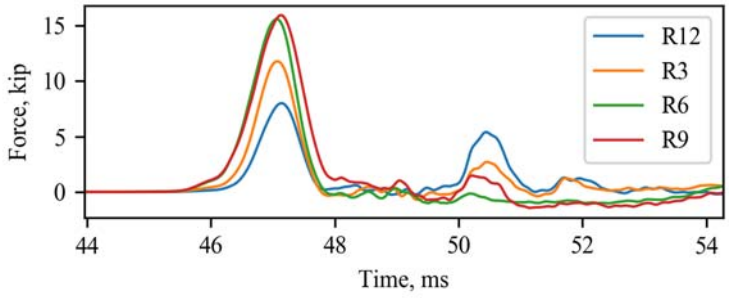
Force, kip
Time, ms
R12
R3
R6
R9

Test 1-8

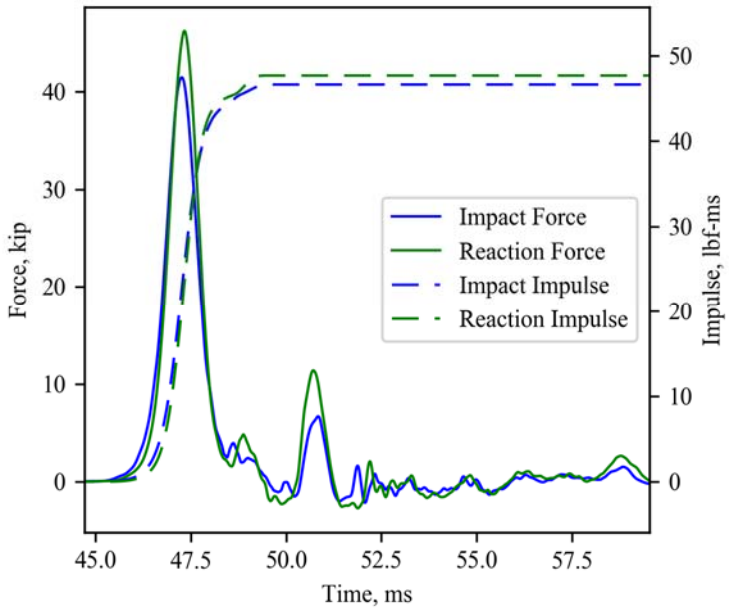
Force, kip
Impulse, lbf-ms
Time, ms
Impact Force
Reaction Force
Impact Impulse
Reaction Impulse

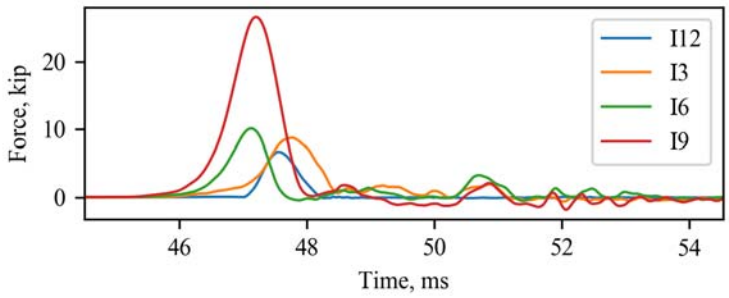
Force, kip
Time, ms
I12
I3
I6
I9

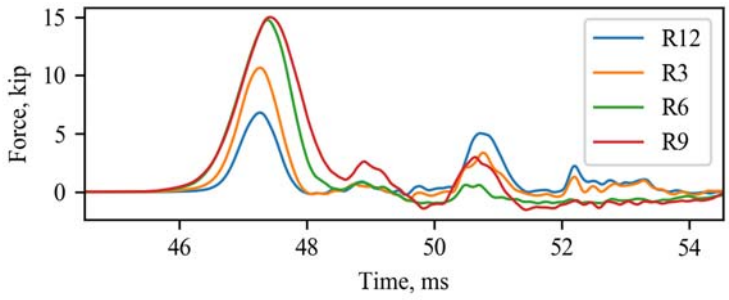
Force, kip
Time, ms
R12
R3
R6
R9

Test 1-9

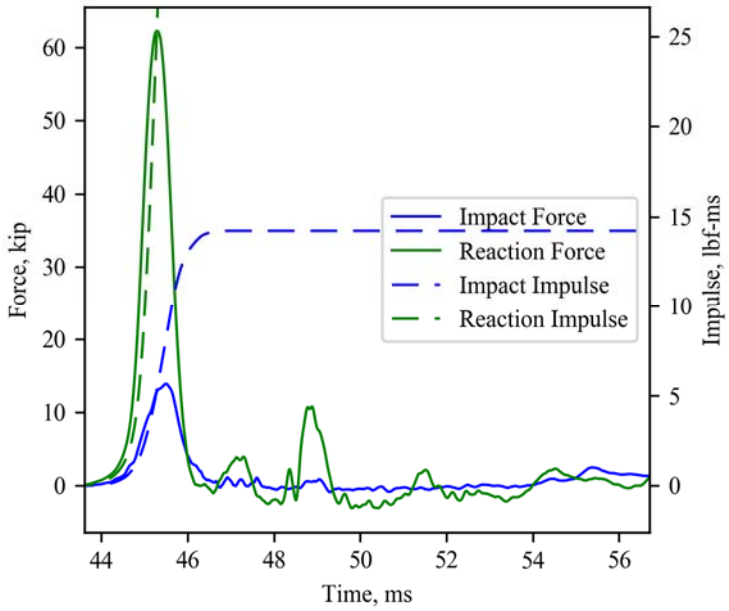
Force, kip
Impulse, lbf-ms
Time, ms
Impact Force
Reaction Force
Impact Impulse
Reaction Impulse

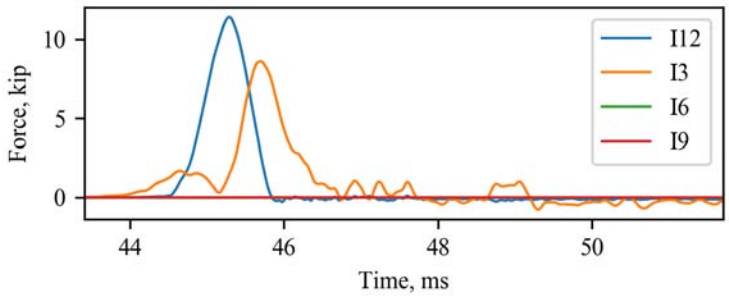
Force, kip
Time, ms
I12
I3
I6
I9

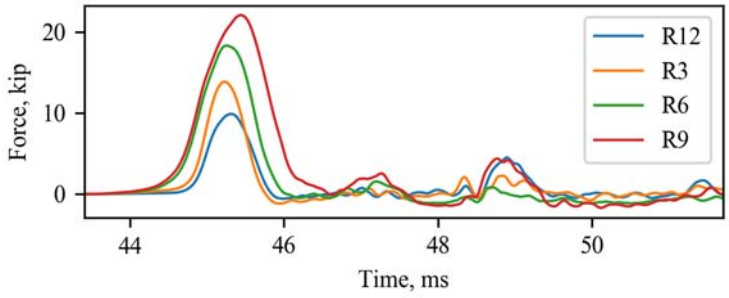
Force, kip
Time, ms
R12
R3
R6
R9

Test 1-10

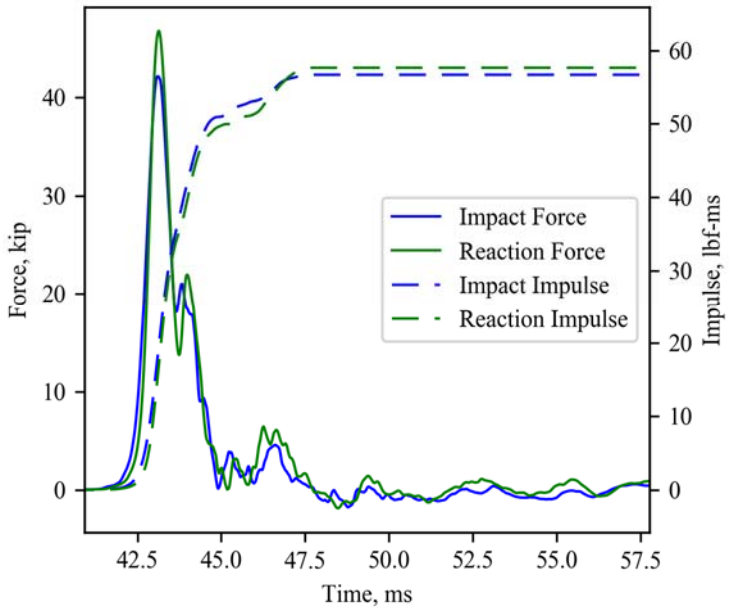
Force, kip
Impulse, lbf-ms
Time, ms
Impact Force
Reaction Force
Impact Impulse
Reaction Impulse

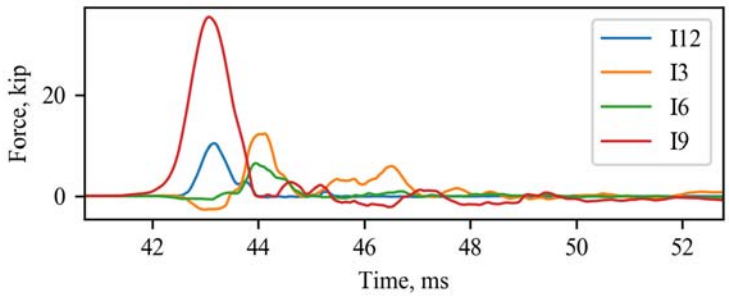
Force, kip
Time, ms
I12
I3
I6
I9

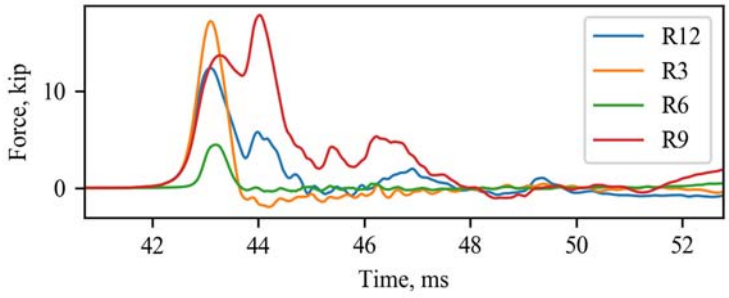
Force, kip
Time, ms
R12
R3
R6
R9

Test 1-11

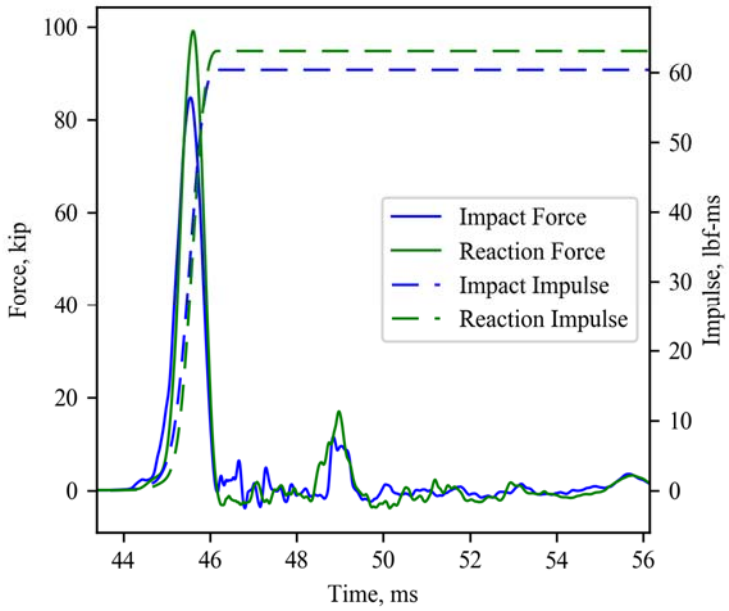
Force, kip
Impulse, lbf-ms
Time, ms
Impact Force
Reaction Force
Impact Impulse
Reaction Impulse

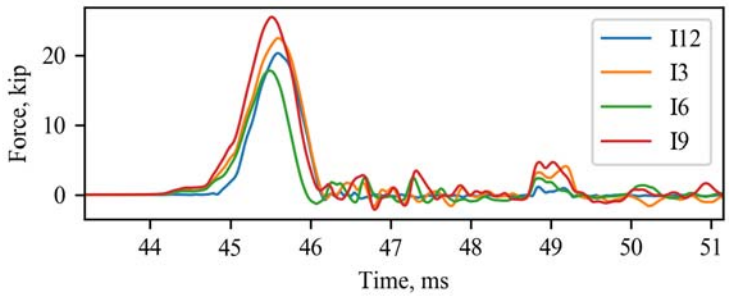
Force, kip
Time, ms
I12
I3
I6
I9

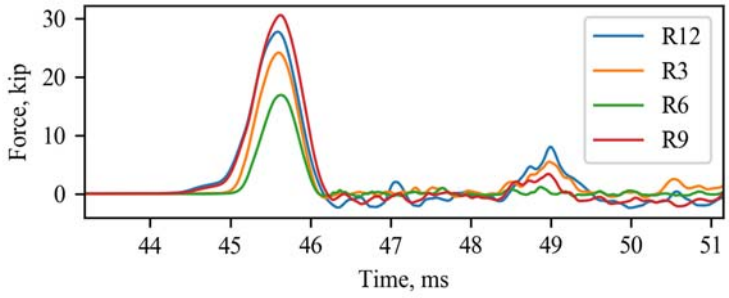
Force, kip
Time, ms
R12
R3
R6
R9

Test 1-12

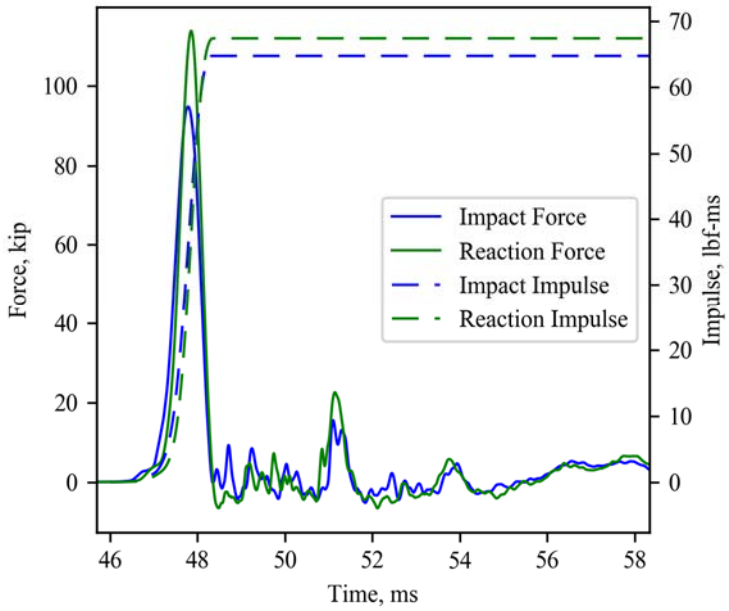
Force, kip
Impulse, lbf-ms
Time, ms
Impact Force
Reaction Force
Impact Impulse
Reaction Impulse

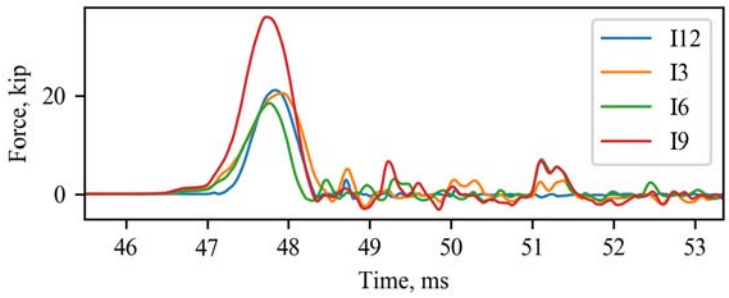
Force, kip
Time, ms
I12
I3
I6
I9

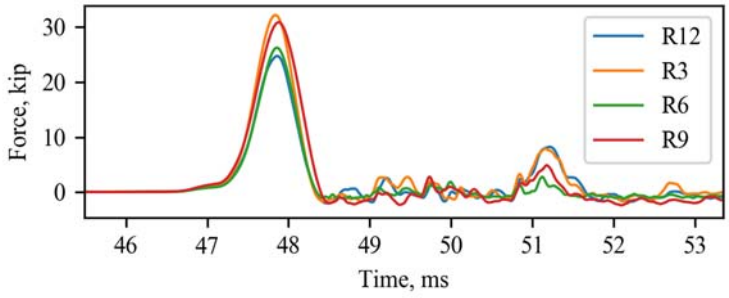
Force, kip
Time, ms
R12
R3
R6
R9

Test 1-13

No load cell data.

Test 1-14

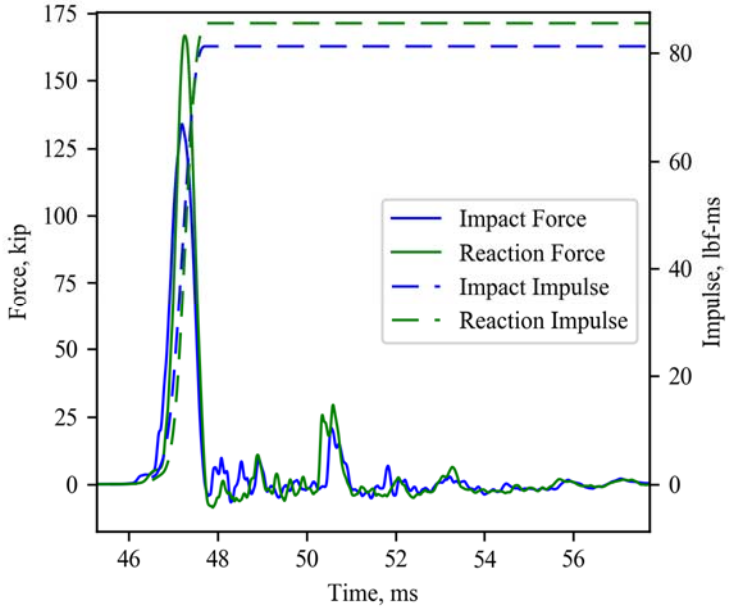

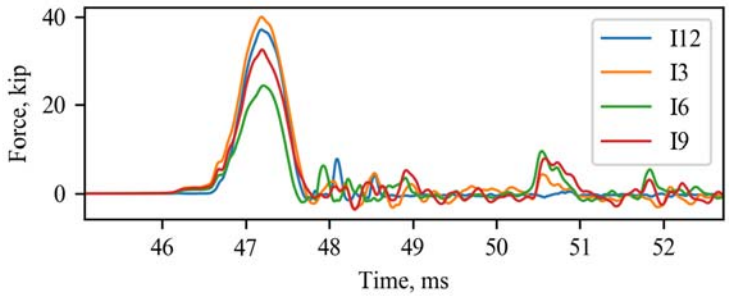

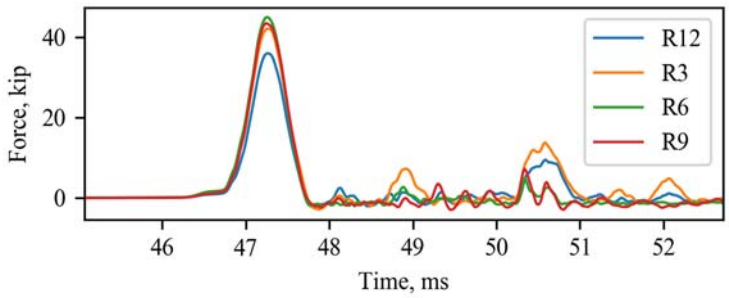

Test Hybrid-1

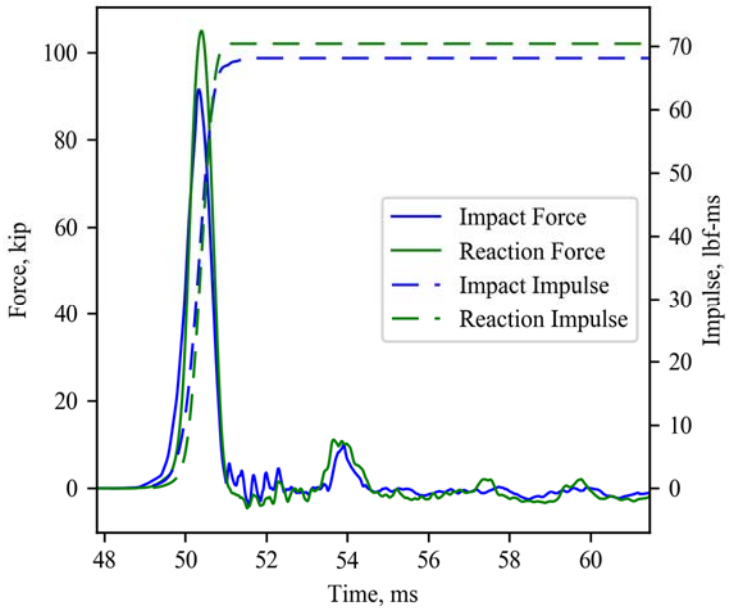

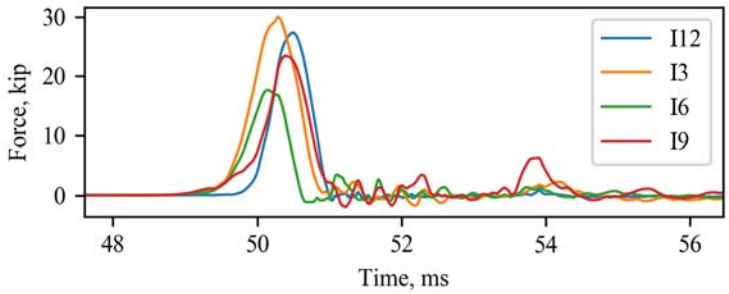

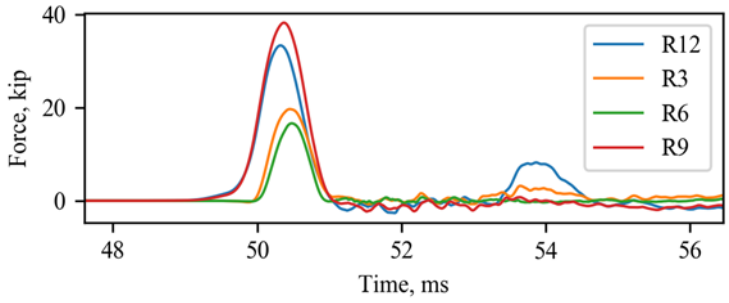

Test Hybrid-2

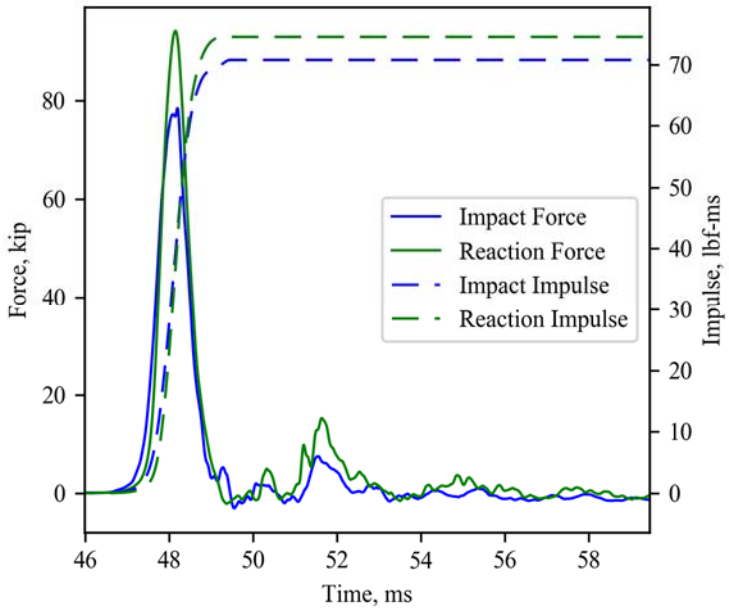

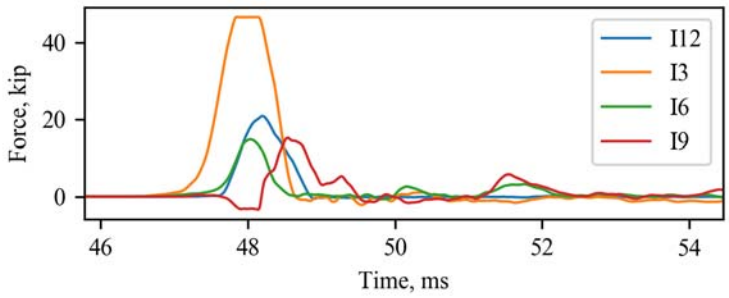

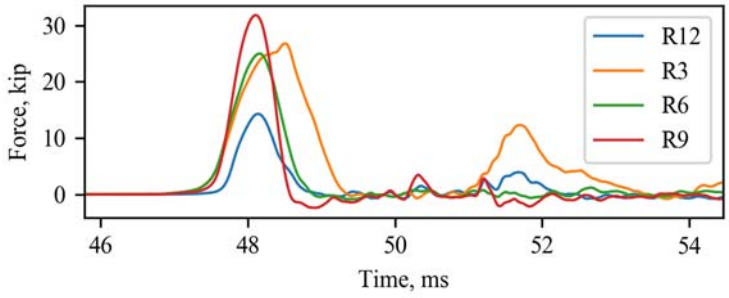

Test 2-1

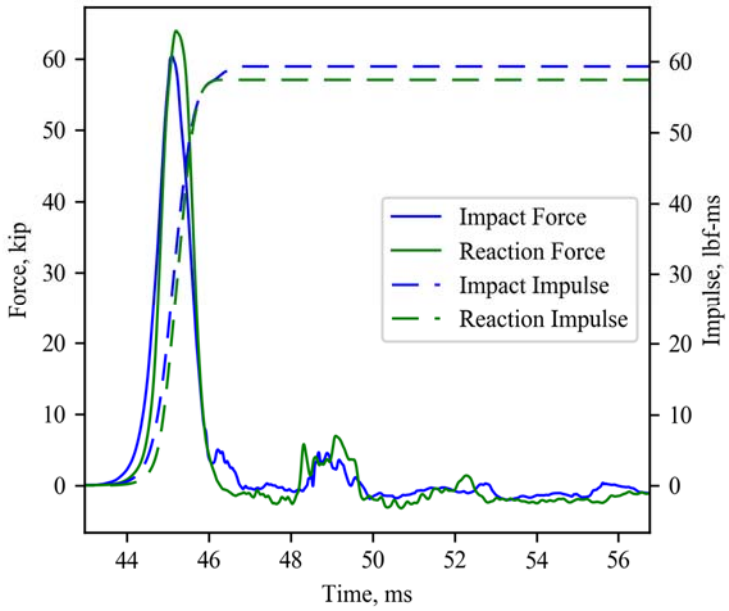
Force, kip
Impulse, lbf-ms
Time, ms
Impact Force
Reaction Force
Impact Impulse
Reaction Impulse

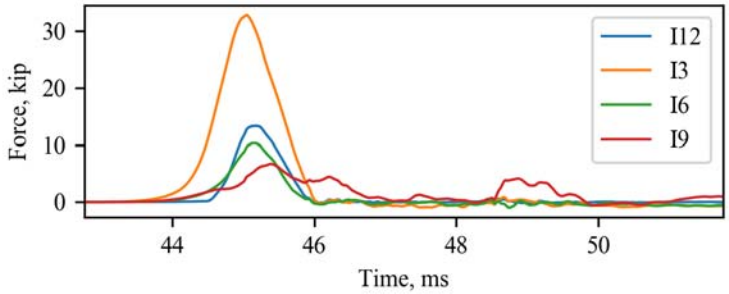
Force, kip
Time, ms
I12
I3
I6
I9

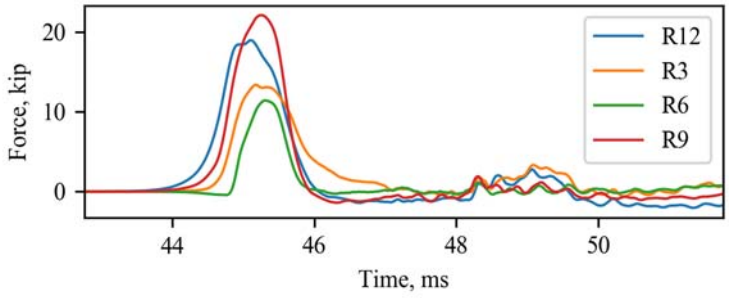
Force, kip
Time, ms
R12
R3
R6
R9

Test 2-2

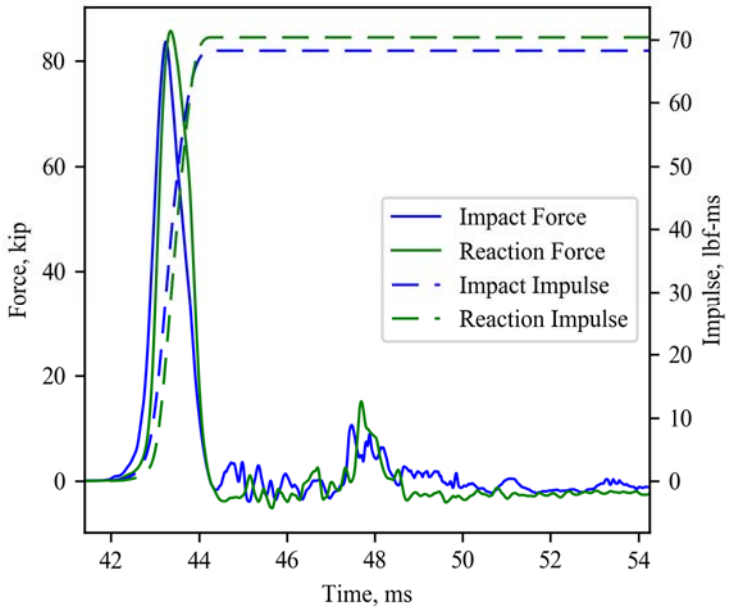
Force, kip
Impulse, lbf-ms
Time, ms
Impact Force
Reaction Force
Impact Impulse
Reaction Impulse

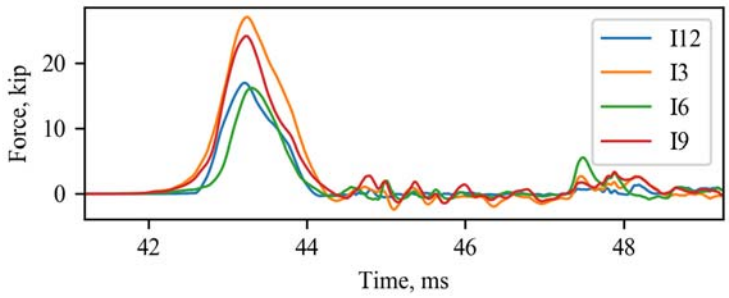
Force, kip
Time, ms
I12
I3
I6
I9

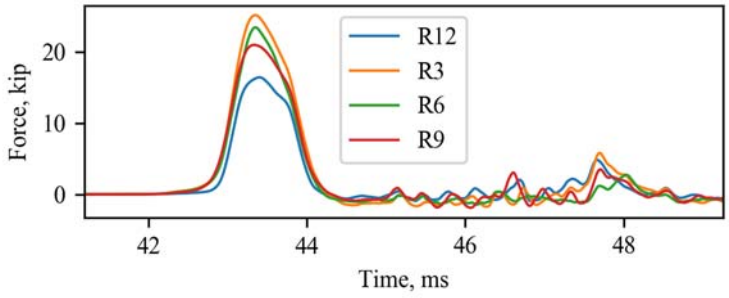
Force, kip
Time, ms
R12
R3
R6
R9

Test 2-3

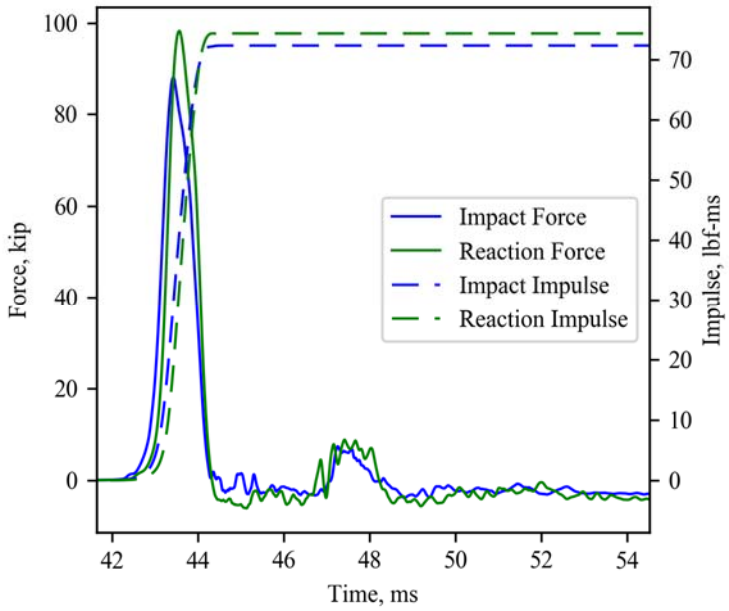
Force, kip
Impulse, lbf-ms
Time, ms
Impact Force
Reaction Force
Impact Impulse
Reaction Impulse

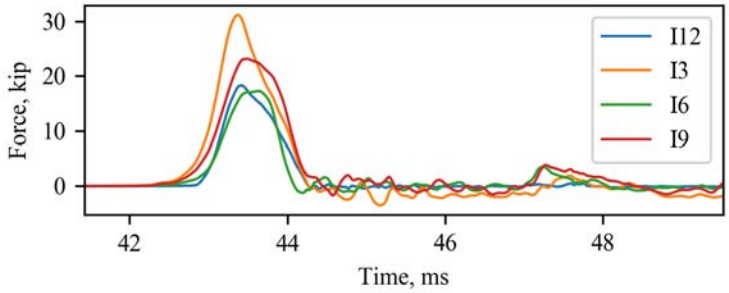
Force, kip
Time, ms
I12
I3
I6
I9

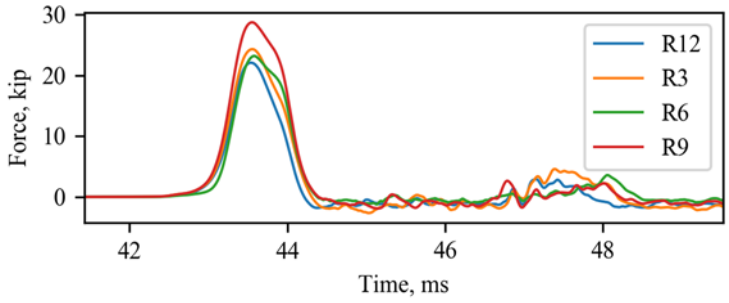
Force, kip
Time, ms
R12
R3
R6
R9

Test 2-4

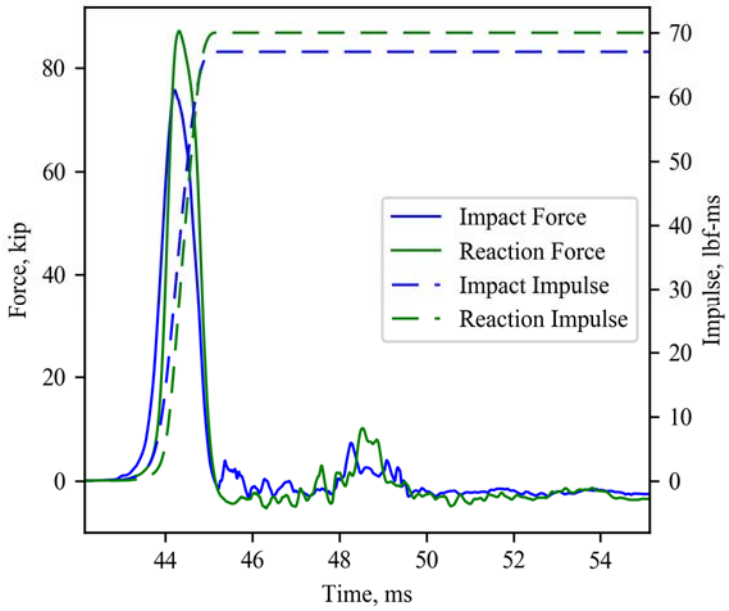
Force, kip
Impulse, lbf-ms
Time, ms
Impact Force
Reaction Force
Impact Impulse
Reaction Impulse

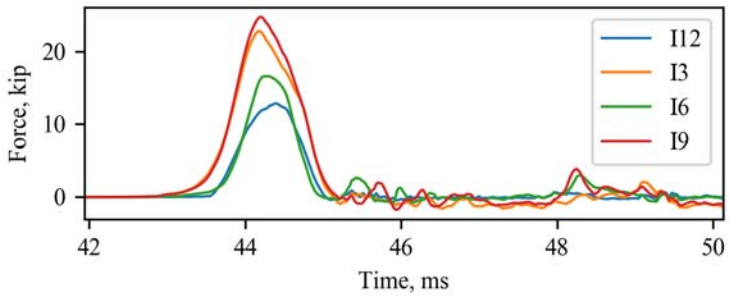
Force, kip
Time, ms
I12
I3
I6
I9

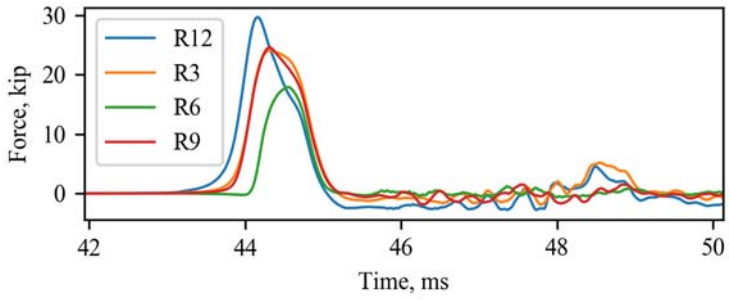
Force, kip
Time, ms
R12
R3
R6
R9

Test 2-5

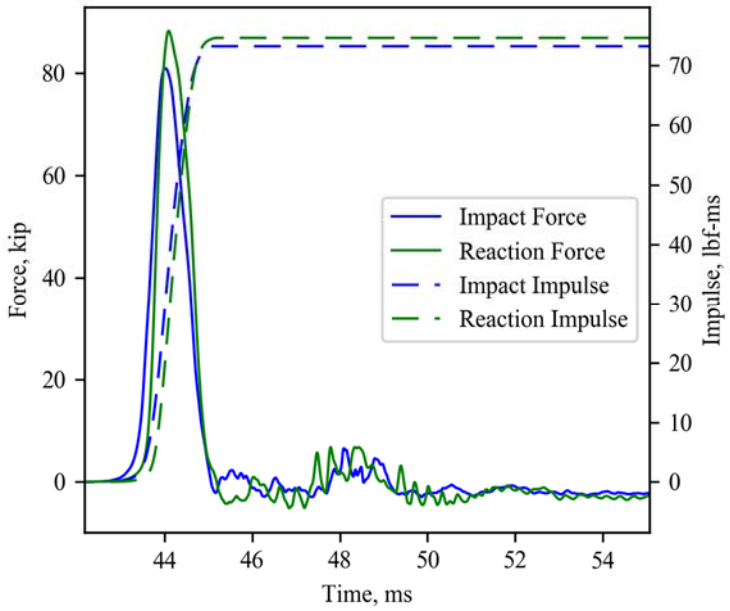
Force, kip
Impulse, lbf-ms
Time, ms
Impact Force
Reaction Force
Impact Impulse
Reaction Impulse

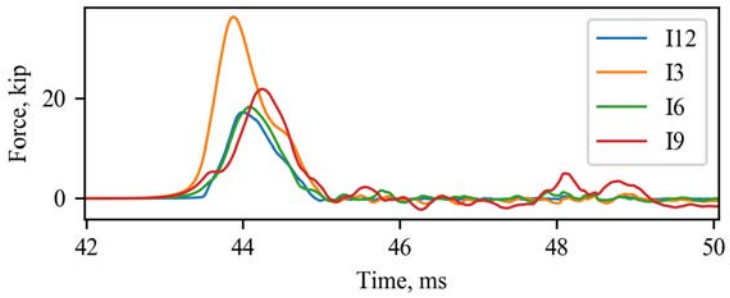
Force, kip
Time, ms
I12
I3
I6
I9

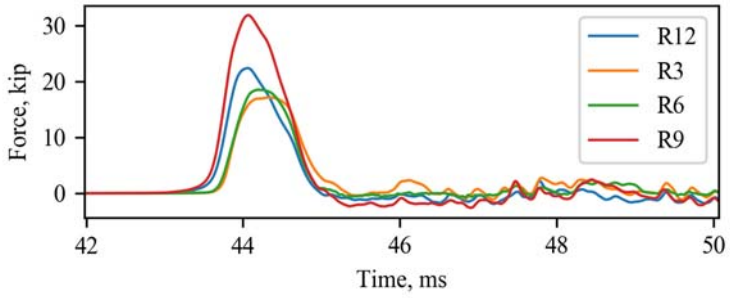
Force, kip
Time, ms
R12
R3
R6
R9

Test 2-6

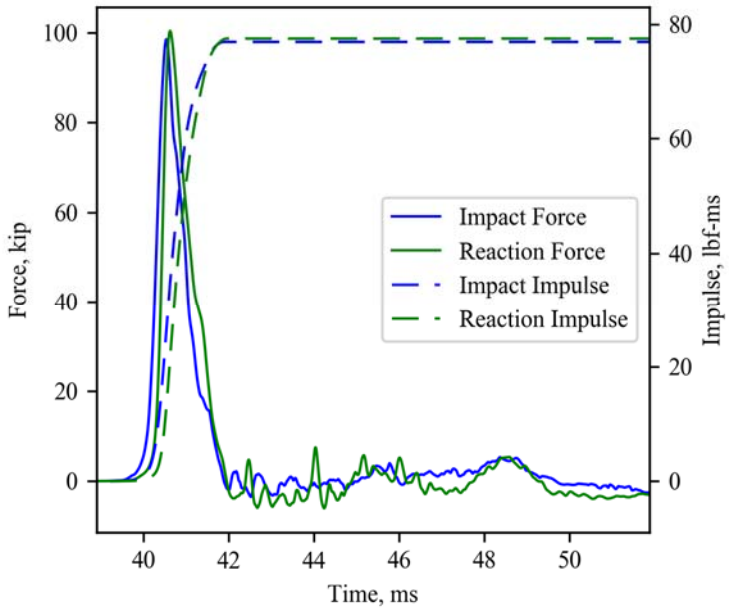
Force, kip
Impulse, lbf-ms
Time, ms
Impact Force
Reaction Force
Impact Impulse
Reaction Impulse

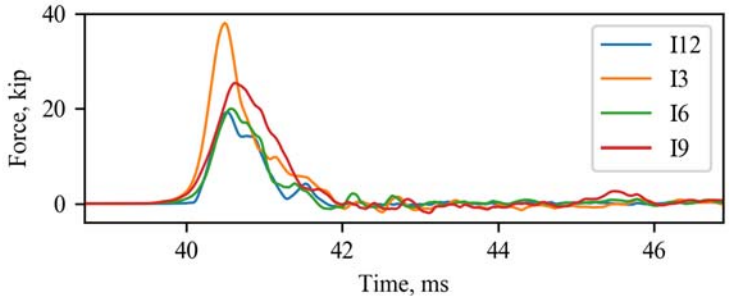
Force, kip
Time, ms
I12
I3
I6
I9

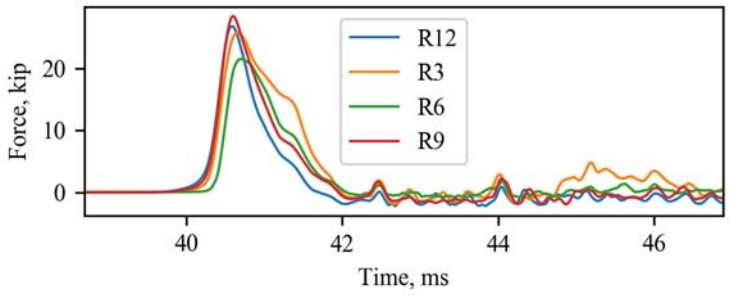
Force, kip
Time, ms
R12
R3
R6
R9

Test 2-7

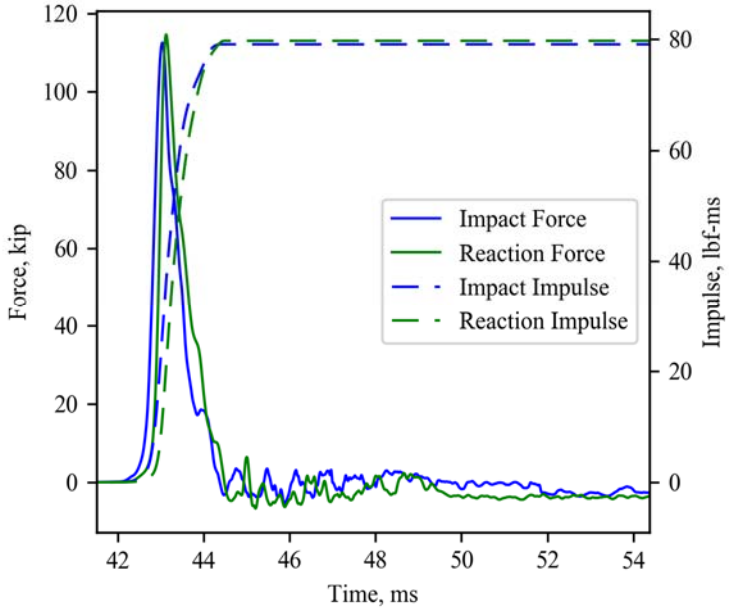
Force, kip
Impulse, lbf-ms
Time, ms
Impact Force
Reaction Force
Impact Impulse
Reaction Impulse

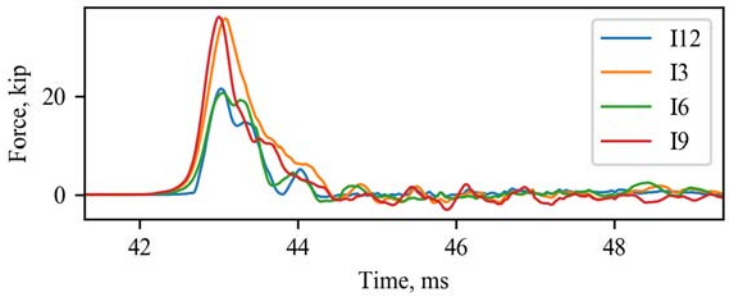
Force, kip
Time, ms
I12
I3
I6
I9

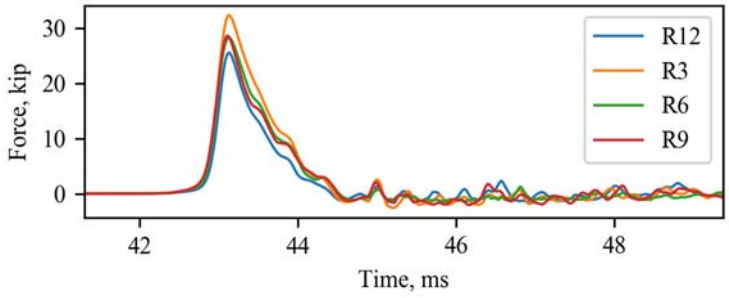
Force, kip
Time, ms
R12
R3
R6
R9

Test 2-8

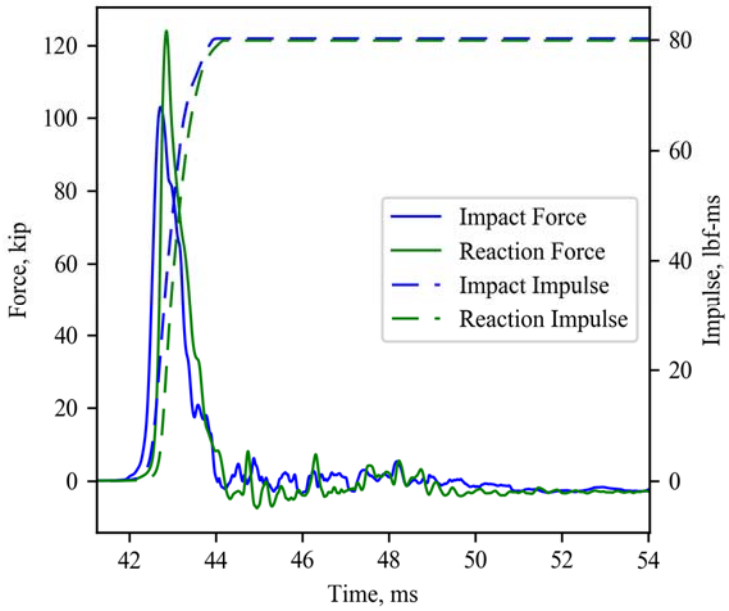
Force, kip
Impulse, lbf-ms
Time, ms
Impact Force
Reaction Force
Impact Impulse
Reaction Impulse

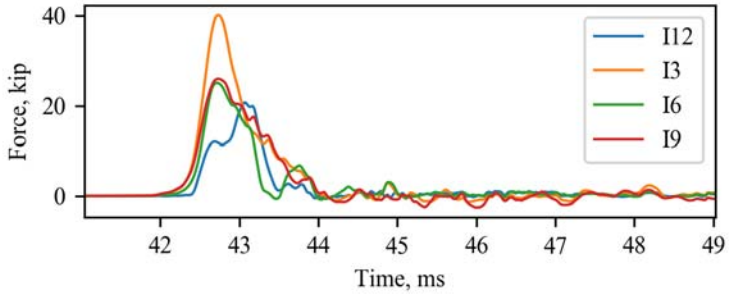
Force, kip
Time, ms
I12
I3
I6
I9

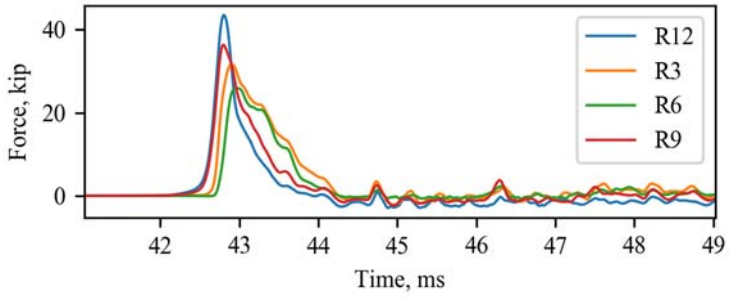
Force, kip
Time, ms
R12
R3
R6
R9

Test 2-9

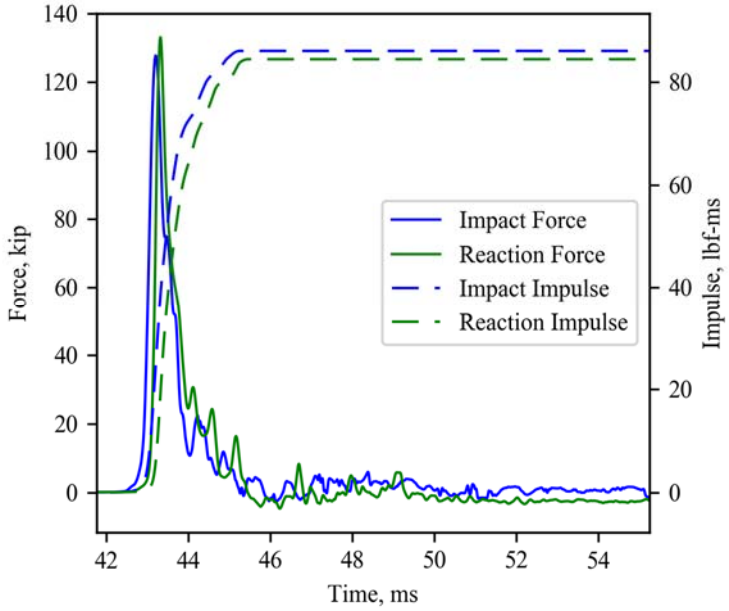
Force, kip
Impulse, lbf-ms
Time, ms
Impact Force
Reaction Force
Impact Impulse
Reaction Impulse

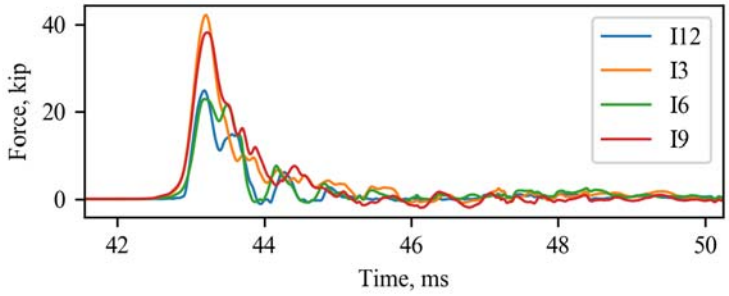
Force, kip
Time, ms
I12
I3
I6
I9

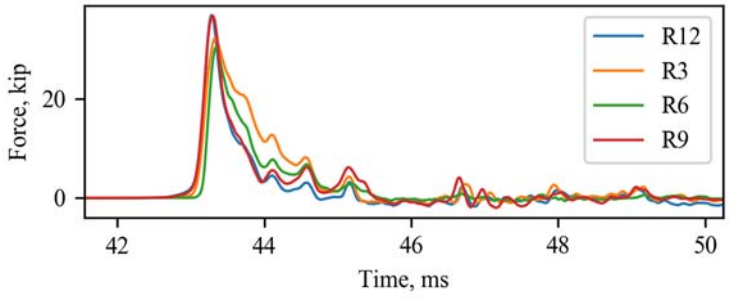
Force, kip
Time, ms
R12
R3
R6
R9

Special Test Case: Double Impulsive Hit

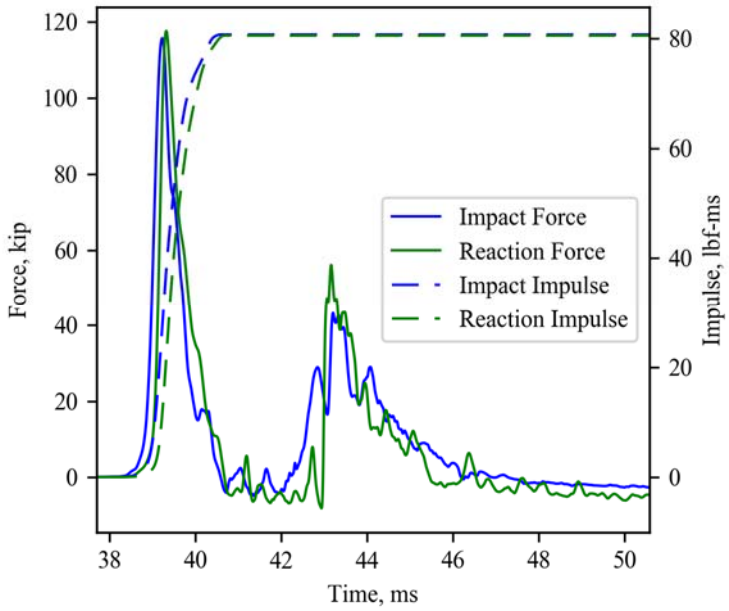

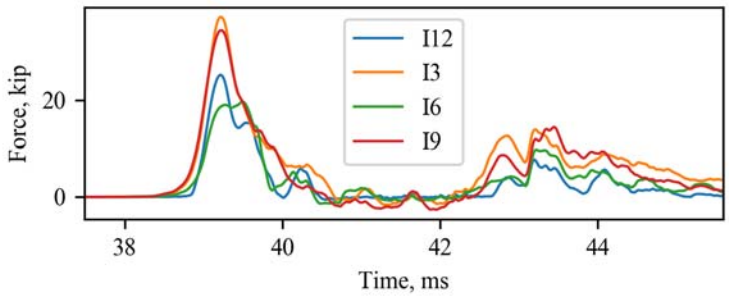

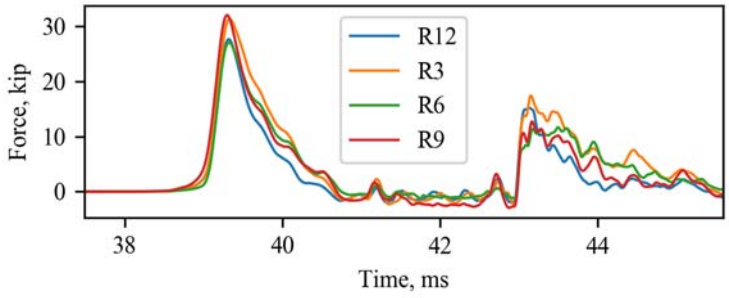

APPENDIX B: EXPERIMENTAL DESIGN DRAWINGS

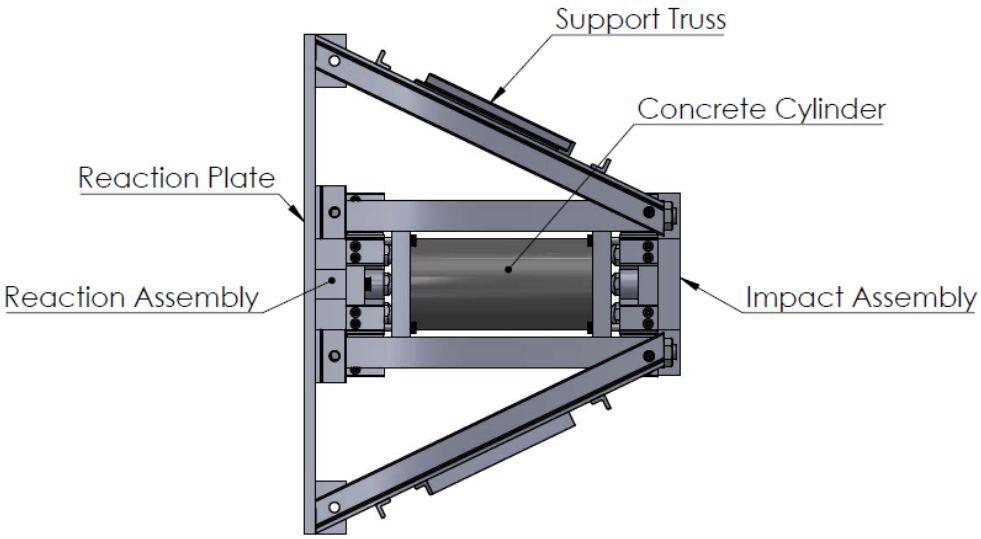

SIDE VIEW

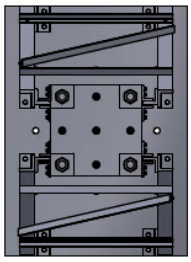

FRONT VIEW

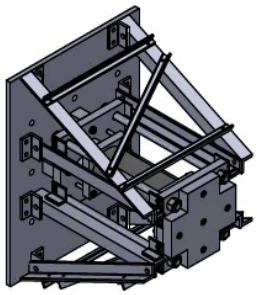

ISOMETRIC VIEW

PROJECT	COMPONENT	SHEET DESCRIPTION	
CONCRETE RESIDUAL CAPACITY	ENTIRE ASSEMBLY	ENTIRE ASSEMBLY	SHEET 1 OF 15

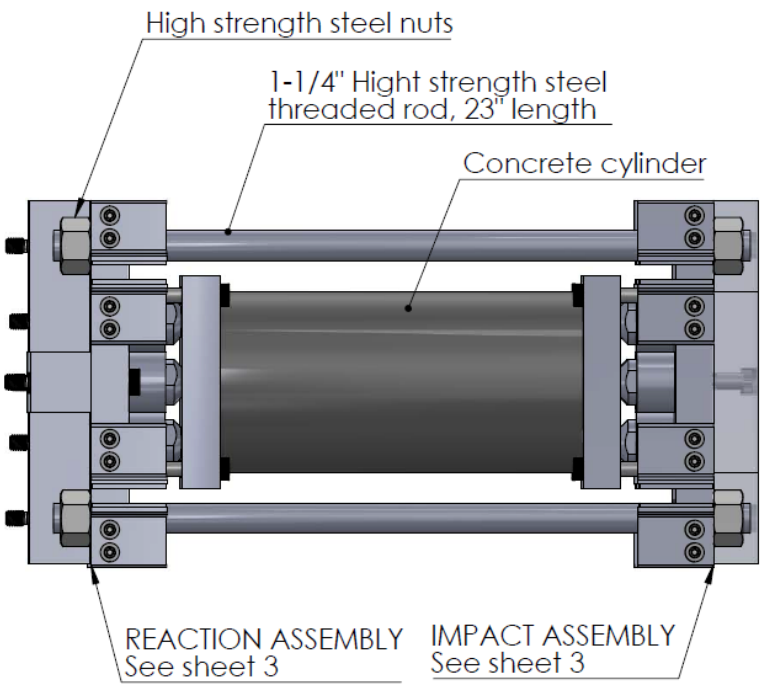

SIDE VIEW

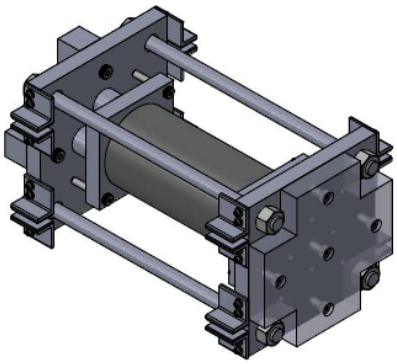

ISOMETRIC VIEW

PROJECT	COMPONENT	SHEET DESCRIPTION	
CONCRETE RESIDUAL CAPACITY	CONCRETE ASSEMBLY	CONCRETE ASSEMBLY	SHEET 2 OF 15

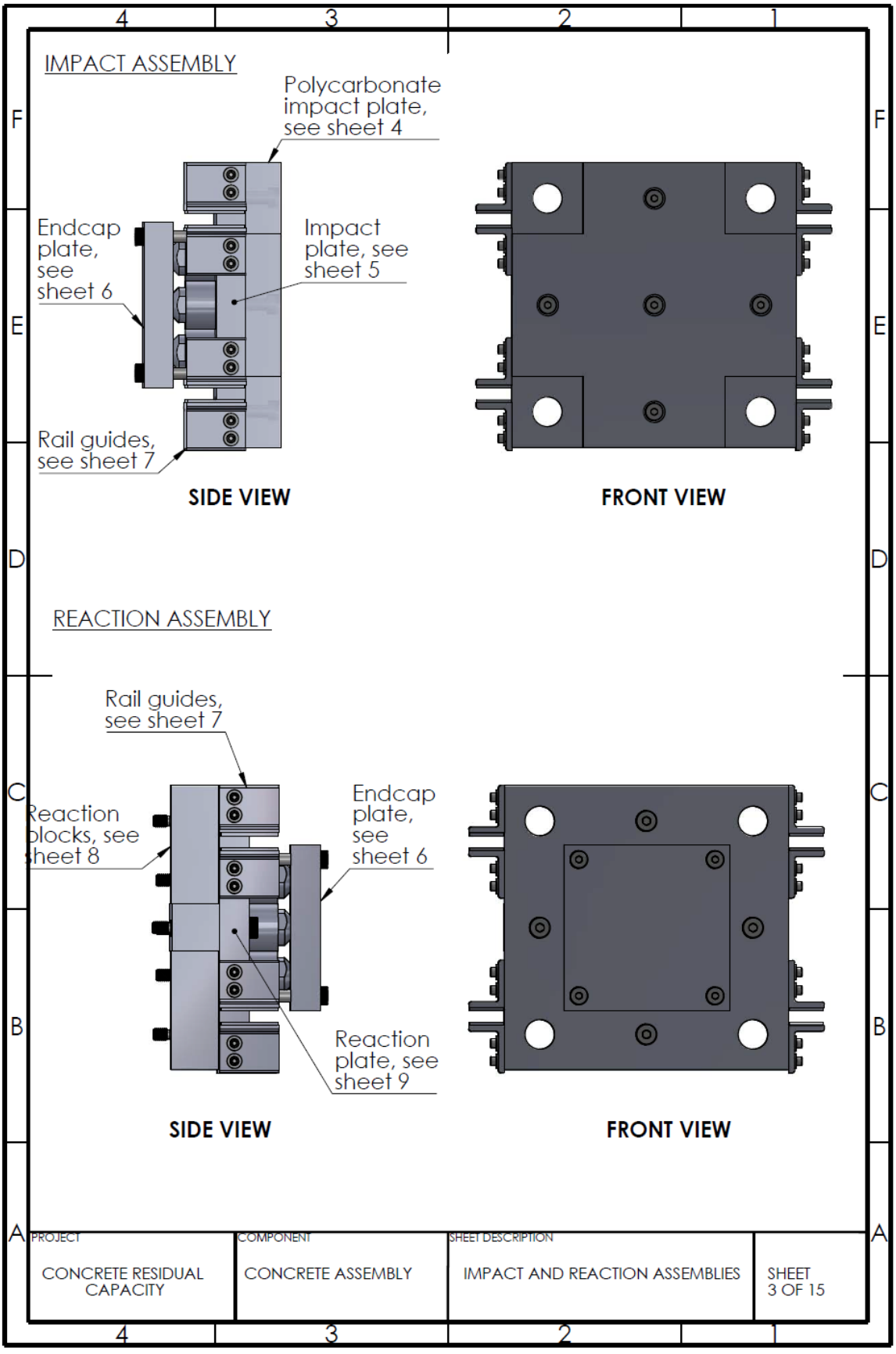
IMPACT ASSEMBLY
Polycarbonate impact plate, see sheet 4
Endcap plate, see sheet 6
Impact plate, see sheet 5
Rail guides, see sheet 7
SIDE VIEW
FRONT VIEW
REACTION ASSEMBLY
Rail guides, see sheet 7
Reaction blocks, see sheet 8
Endcap plate, see sheet 6
Reaction plate, see sheet 9
SIDE VIEW
FRONT VIEW
PROJECT
CONCRETE RESIDUAL CAPACITY
COMPONENT
CONCRETE ASSEMBLY
SHEET DESCRIPTION
IMPACT AND REACTION ASSEMBLIES
SHEET 3 OF 15

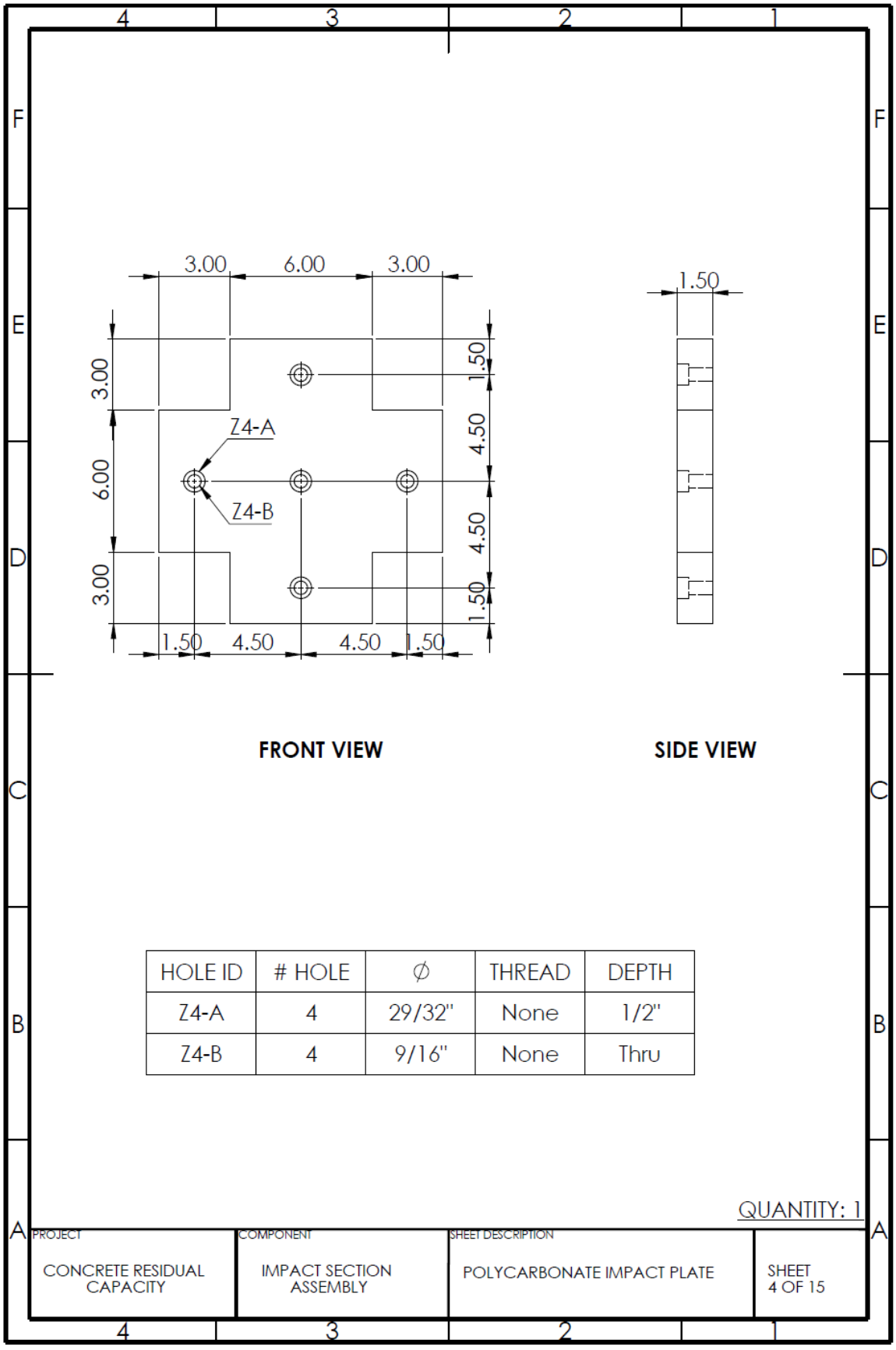

HOLE ID	# HOLE	∅	THREAD	DEPTH
Z4-A	4	29/32"	None	1/2"
Z4-B	4	9/16"	None	Thru

QUANTITY: 1

PROJECT	COMPONENT	SHEET DESCRIPTION	
CONCRETE RESIDUAL CAPACITY	IMPACT SECTION ASSEMBLY	POLYCARBONATE IMPACT PLATE	SHEET 4 OF 15

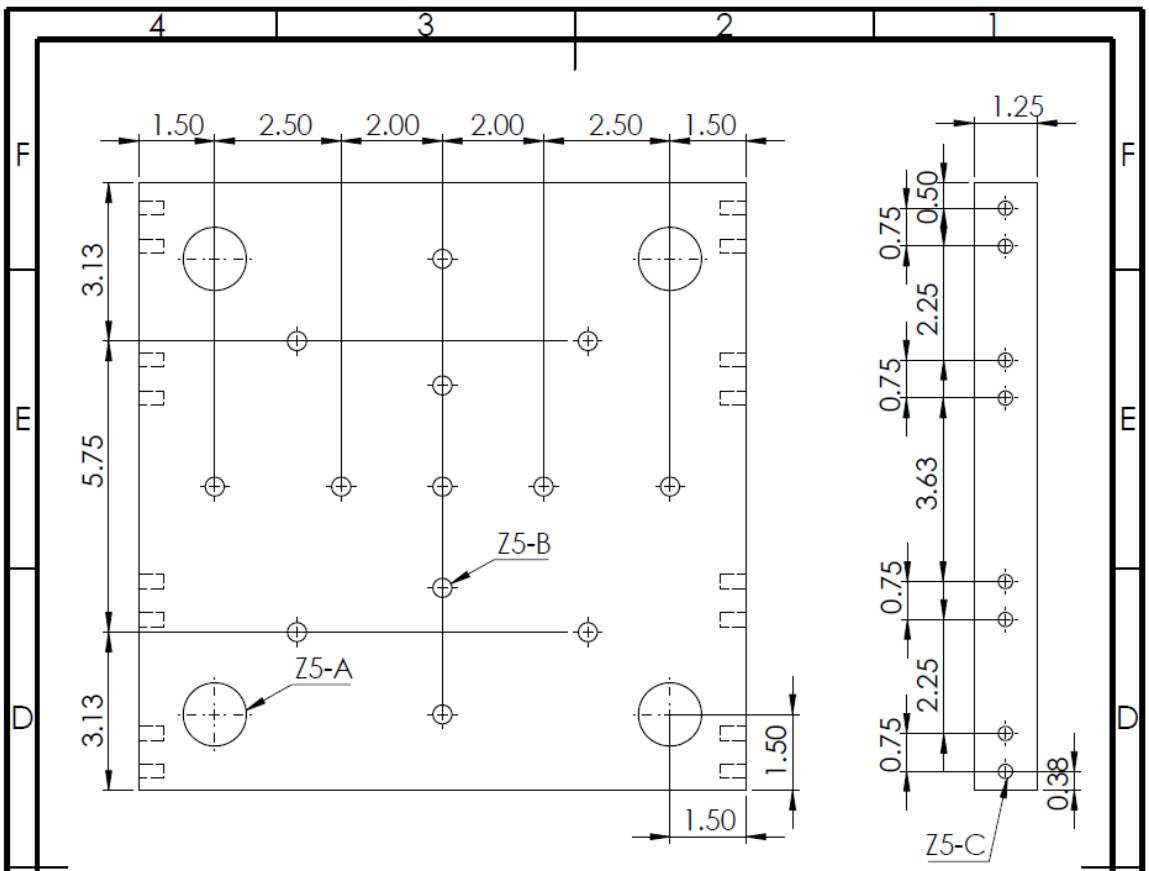

FRONT VIEW **SIDE VIEW**

HOLE ID	# HOLE	∅	THREAD	DEPTH
Z5-A	4	1-1/4"	None	Thru
Z5-B	13	3/8"	3/8"-16	Thru
Z5-C	16	1/4"	1/4"-20	1/2"

QUANTITY: 1

PROJECT	COMPONENT	SHEET DESCRIPTION	
CONCRETE RESIDUAL CAPACITY	IMPACT SECTION ASSEMBLY	IMPACT PLATE	SHEET 5 OF 15

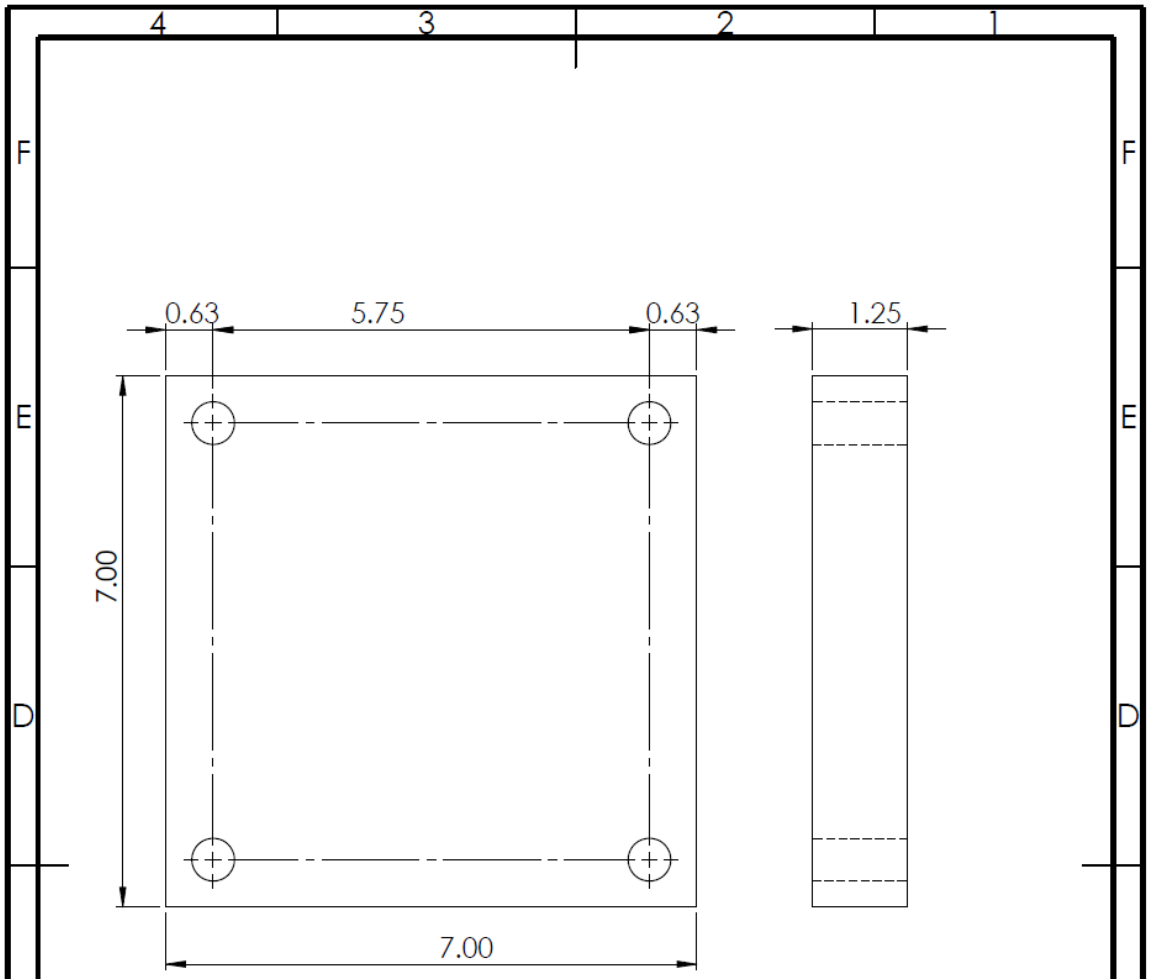

Hole ID	# Hole	∅	Thread	Depth
Z4-A	4	9/16"	None	Thru

QUANTITY: 2

PROJECT	COMPONENT	SHEET DESCRIPTION	
CONCRETE RESIDUAL CAPACITY	IMPACT SECTION ASSEMBLY	INNER ENDCAPS	SHEET 6 OF 15

RAIL GUIDE 1

QUANTITY: 8

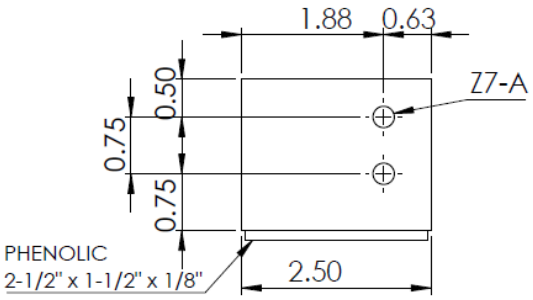

BACK VIEW

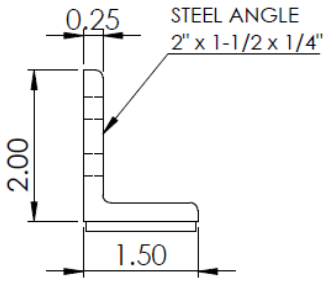

SIDE VIEW

RAIL GUIDE 2

QUANTITY: 8

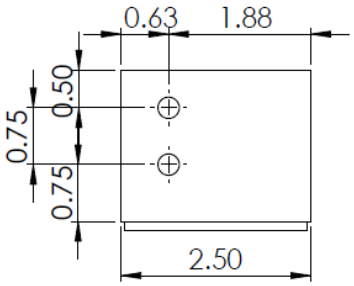

BACK VIEW

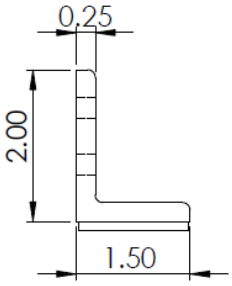

SIDE VIEW

HOLE ID	# HOLE	∅	THREAD	DEPTH
Z7-A	2 ea	9/32"	None	Thru

PROJECT	COMPONENT	SHEET DESCRIPTION	
CONCRETE RESIDUAL CAPACITY	IMPACT SECTION ASSEMBLY	RAIL GUIDES	SHEET 7 OF 15

REACTION BLOCK 1

QUANTITY: 2

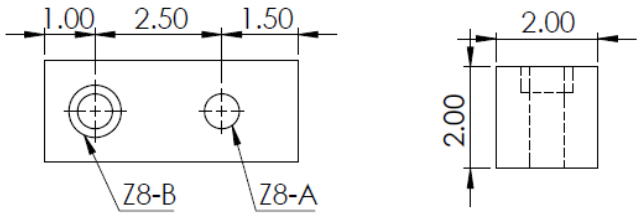

REACTION BLOCK 2

QUANTITY: 1

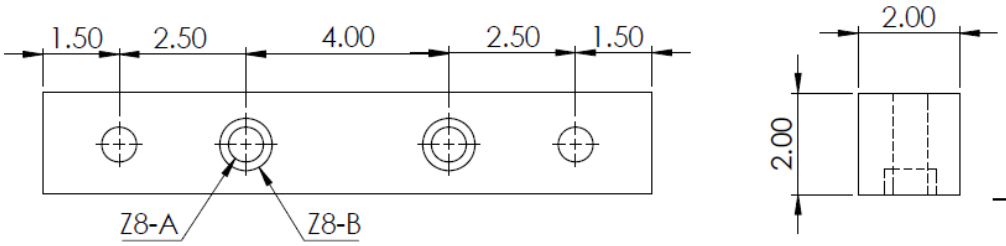

Hole ID	# Hole	∅	Thread	Depth
Z8-A	8 total	11/16"	None	Thru
Z8-B	4 total	33/32"	None	1/2"

PROJECT	COMPONENT	SHEET DESCRIPTION	
CONCRETE RESIDUAL CAPACITY	REACTION SECTION ASSEMBLY	REACTION BLOCKS	SHEET 8 OF 15

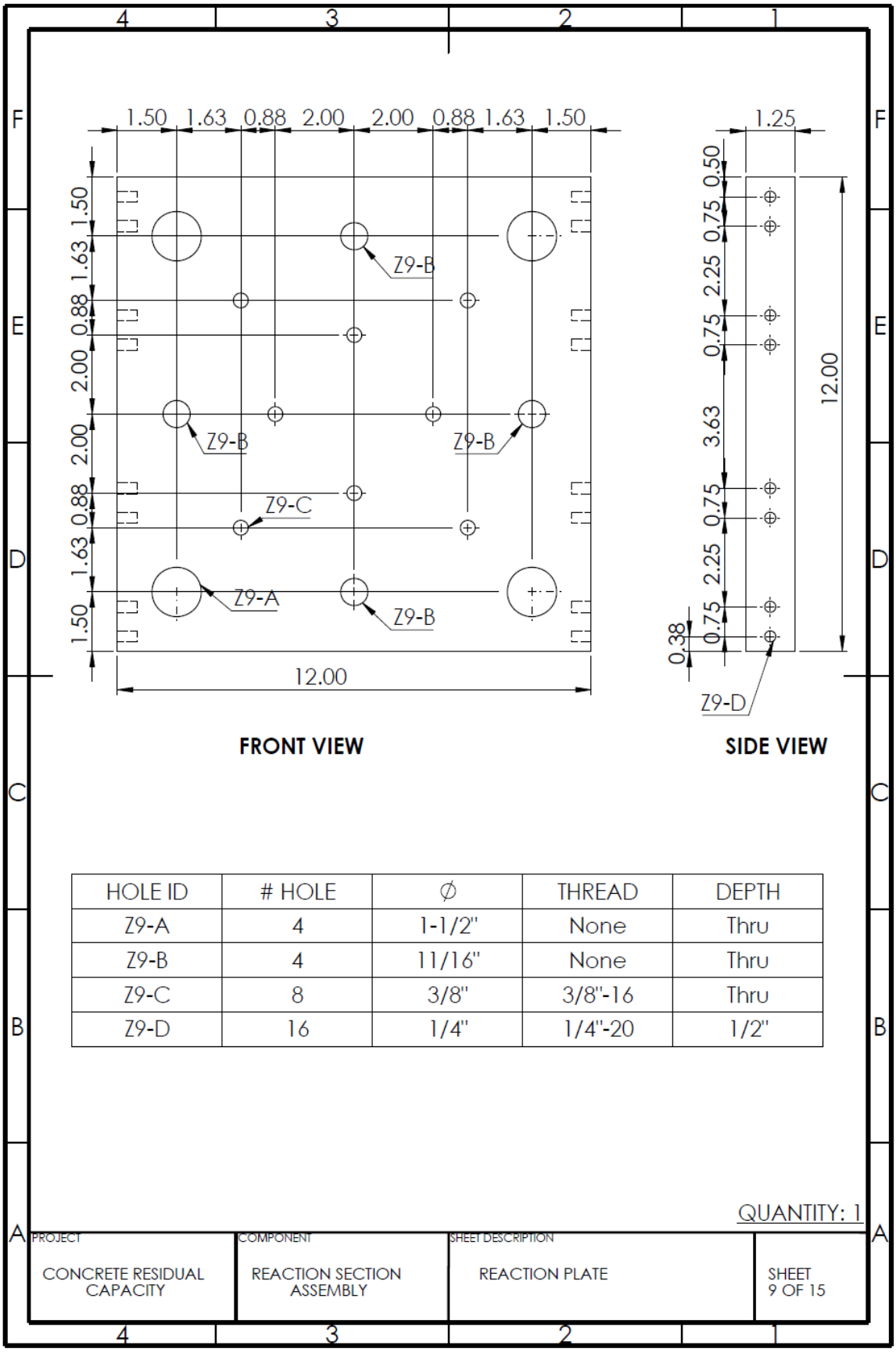

HOLE ID	# HOLE	∅	THREAD	DEPTH
Z9-A	4	1-1/2"	None	Thru
Z9-B	4	11/16"	None	Thru
Z9-C	8	3/8"	3/8"-16	Thru
Z9-D	16	1/4"	1/4"-20	1/2"

QUANTITY: 1

PROJECT	COMPONENT	SHEET DESCRIPTION	
CONCRETE RESIDUAL CAPACITY	REACTION SECTION ASSEMBLY	REACTION PLATE	SHEET 9 OF 15

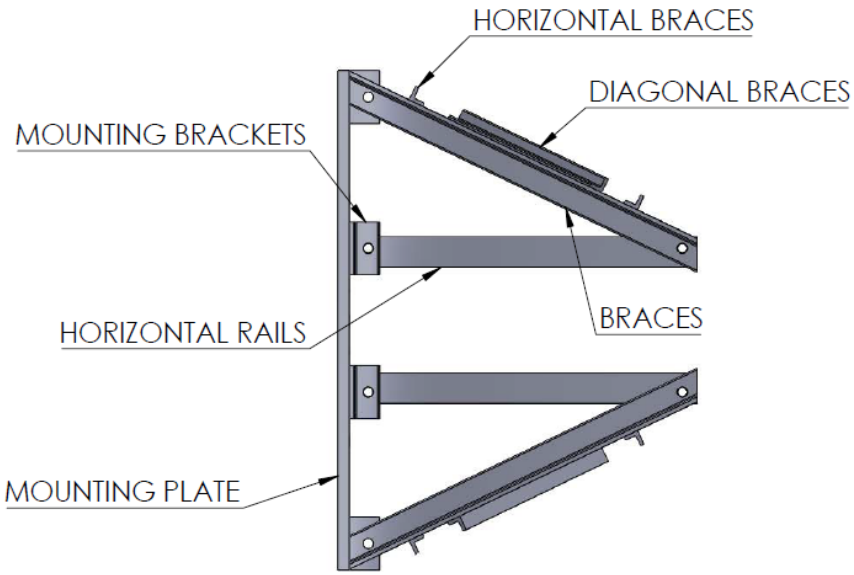

SIDE VIEW

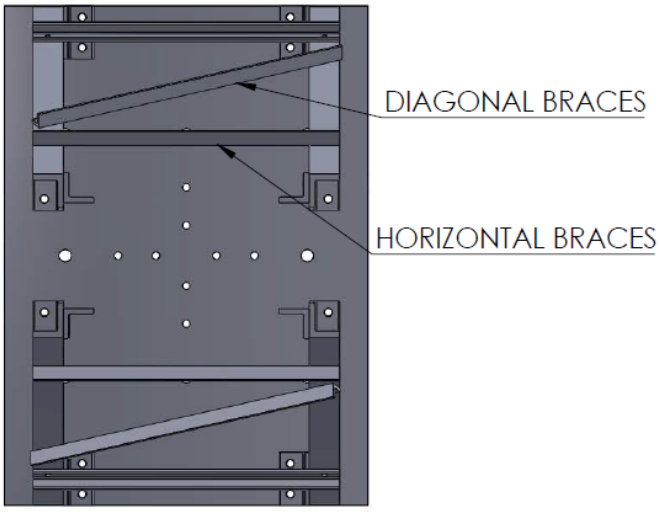

FRONT VIEW

PROJECT	COMPONENT	SHEET DESCRIPTION	
CONCRETE RESIDUAL CAPACITY	SUPPORT TRUSS ASSEMBLY	SUPPORT TRUSS ASSEMBLY	SHEET 10 OF 15

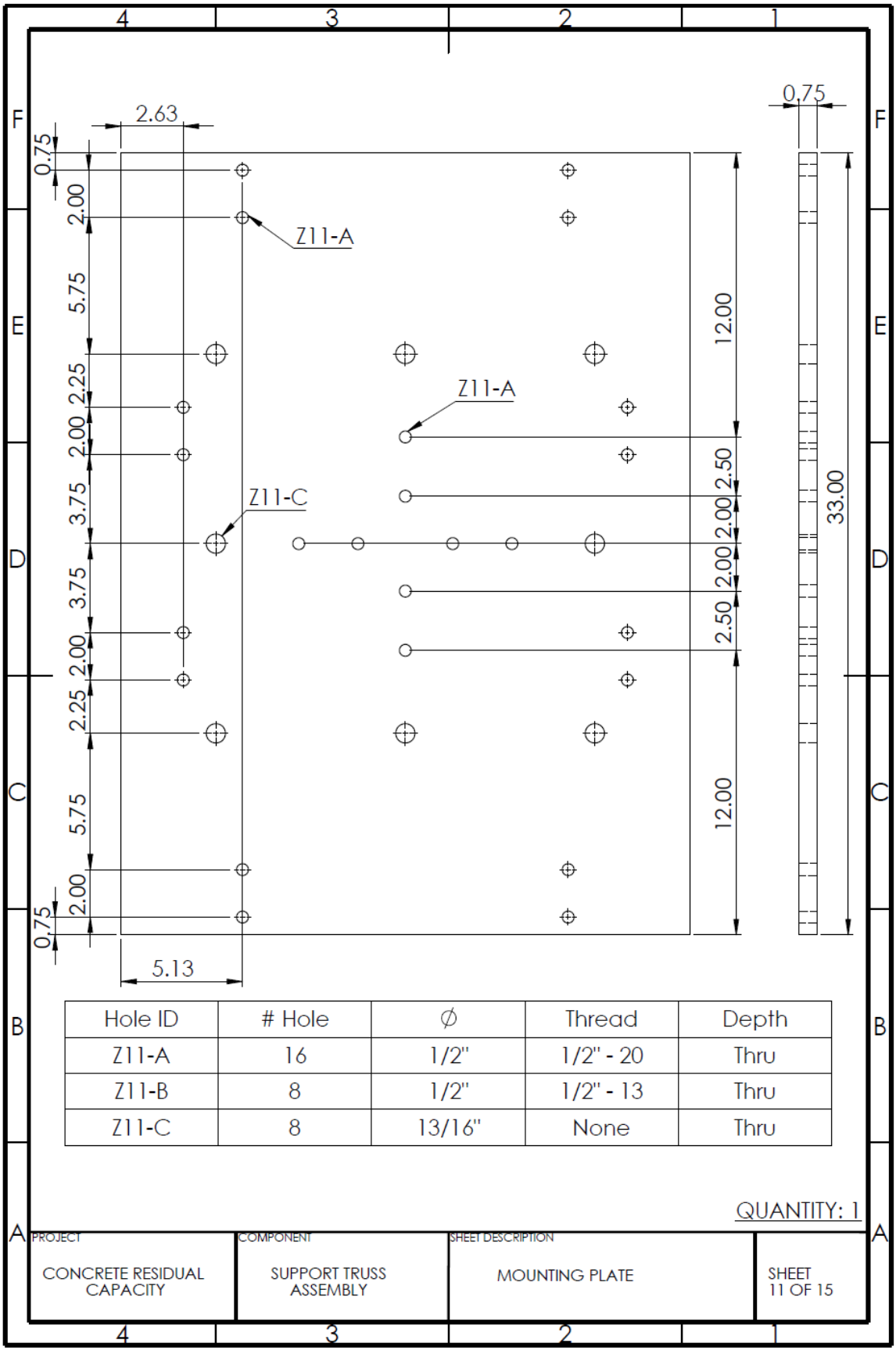

Hole ID	# Hole	∅	Thread	Depth
Z11-A	16	1/2"	1/2" - 20	Thru
Z11-B	8	1/2"	1/2" - 13	Thru
Z11-C	8	13/16"	None	Thru

QUANTITY: 1

PROJECT	COMPONENT	SHEET DESCRIPTION	
CONCRETE RESIDUAL CAPACITY	SUPPORT TRUSS ASSEMBLY	MOUNTING PLATE	SHEET 11 OF 15

BRACE 1

QUANTITY: 2

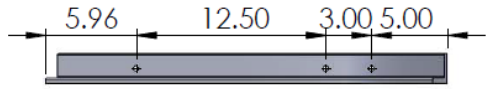

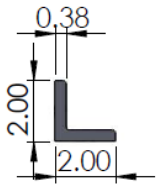

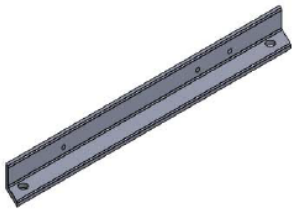

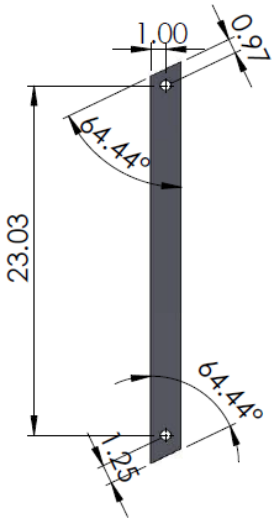

BRACE 2

QUANTITY: 2

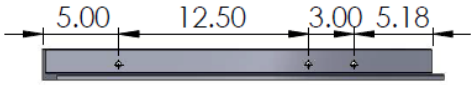

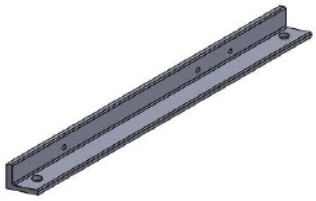

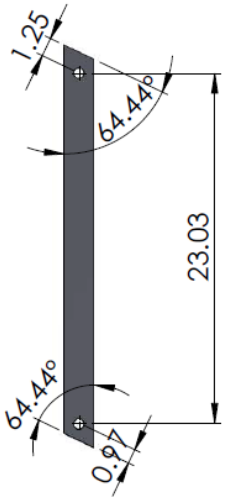

Hole ID	# Hole	∅	Thread	Depth
Z12-A	3 ea	11/32	None	Thru
Z12-B	1 ea	11/16	None	Thru

PROJECT	COMPONENT	SHEET DESCRIPTION	
CONCRETE RESIDUAL CAPACITY	SUPPORT TRUSS ASSEMBLY	BRACES	SHEET 12 OF 15

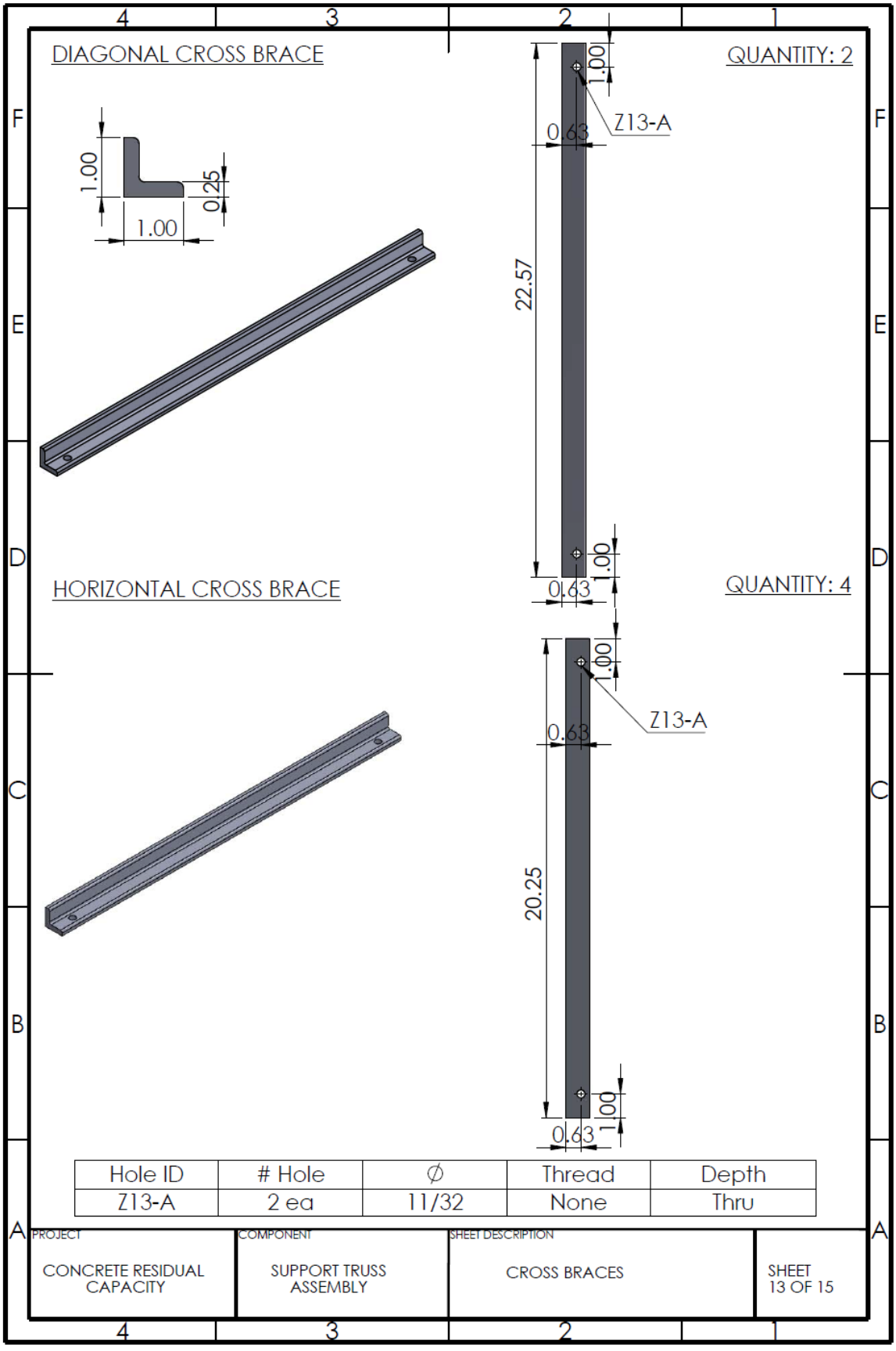
DIAGONAL CROSS BRACE
QUANTITY: 2
1.00
0.25
1.00
1.00
Z13-A
0.63
22.57
1.00
0.63
HORIZONTAL CROSS BRACE
QUANTITY: 4
1.00
Z13-A
0.63
20.25
1.00
0.63
Hole ID | # Hole | ∅ | Thread | Depth
Z13-A | 2 ea | 11/32 | None | Thru
PROJECT
CONCRETE RESIDUAL CAPACITY
COMPONENT
SUPPORT TRUSS ASSEMBLY
SHEET DESCRIPTION
CROSS BRACES
SHEET 13 OF 15

HORIZONTAL RAIL 1

QUANTITY: 2

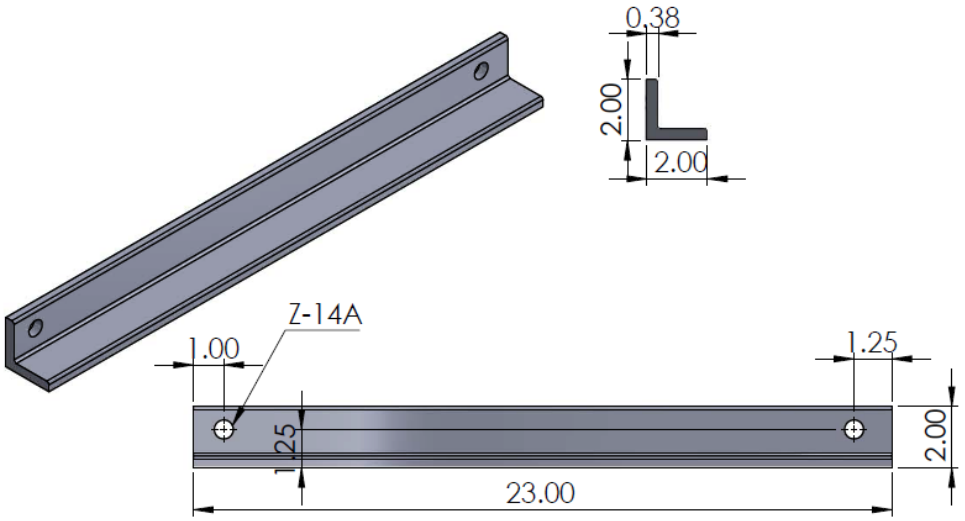

HORIZONTAL RAIL 2

QUANTITY: 2

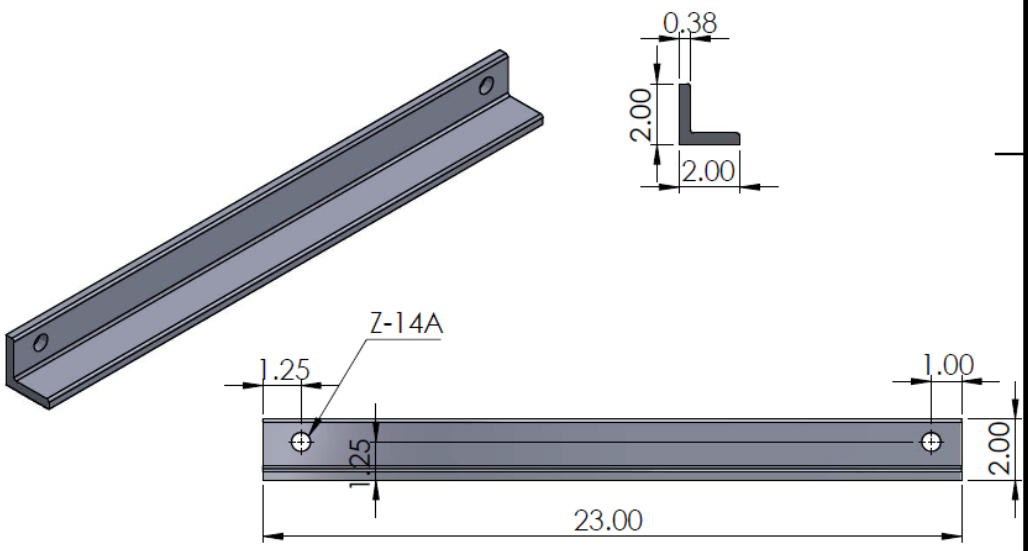

Hole ID	# Hole	∅	Thread	Depth
Z-14A	1 ea	5/8"	5/8"-18	Thru

PROJECT	COMPONENT	SHEET DESCRIPTION	
CONCRETE RESIDUAL CAPACITY	SUPPORT TRUSS ASSEMBLY	HORIZONTAL RAILS	SHEET 14 OF 15

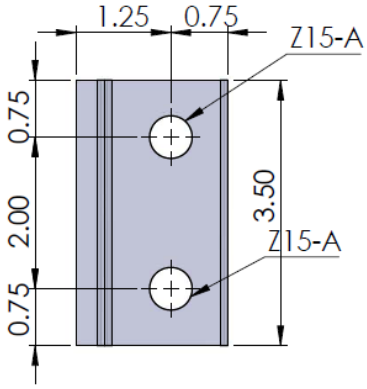

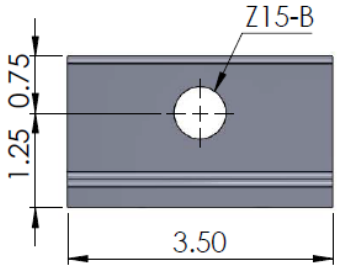

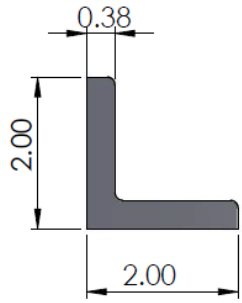

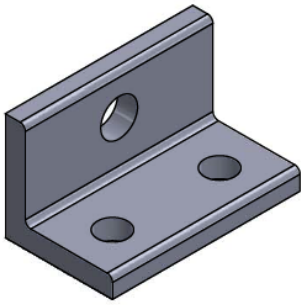

Hole ID	# Hole	∅	Thread	Depth
Z15-A	2 ea	9/16	None	Thru
Z15-B	1 ea	11/16	None	Thru

QUANTITY: 8

PROJECT	COMPONENT	SHEET DESCRIPTION	
CONCRETE RESIDUAL CAPACITY	SUPPORT TRUSS ASSEMBLY	MOUNTING BRACKETS	SHEET 15 OF 15

FLYER PLATE MASS – VERSION 1

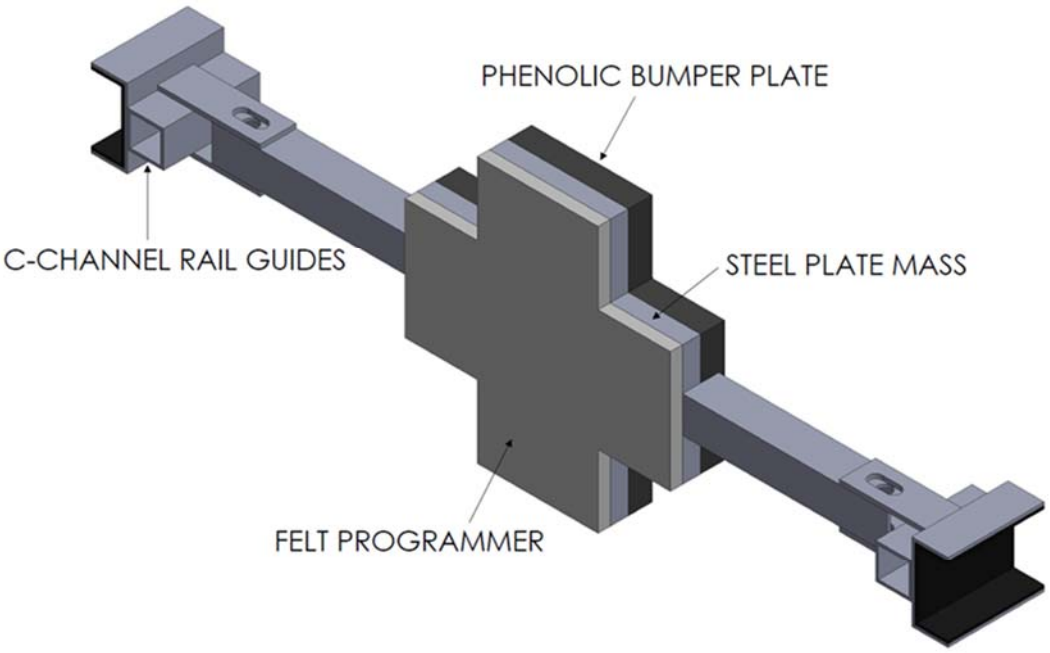

FLYER PLATE
Sheet 1 of 4

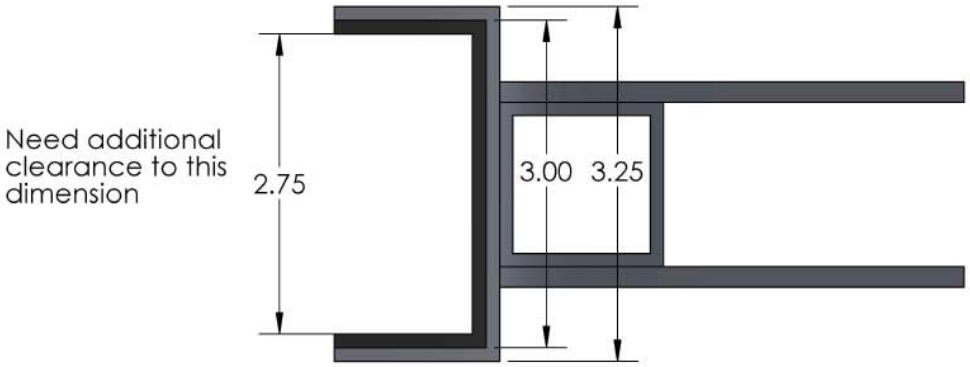

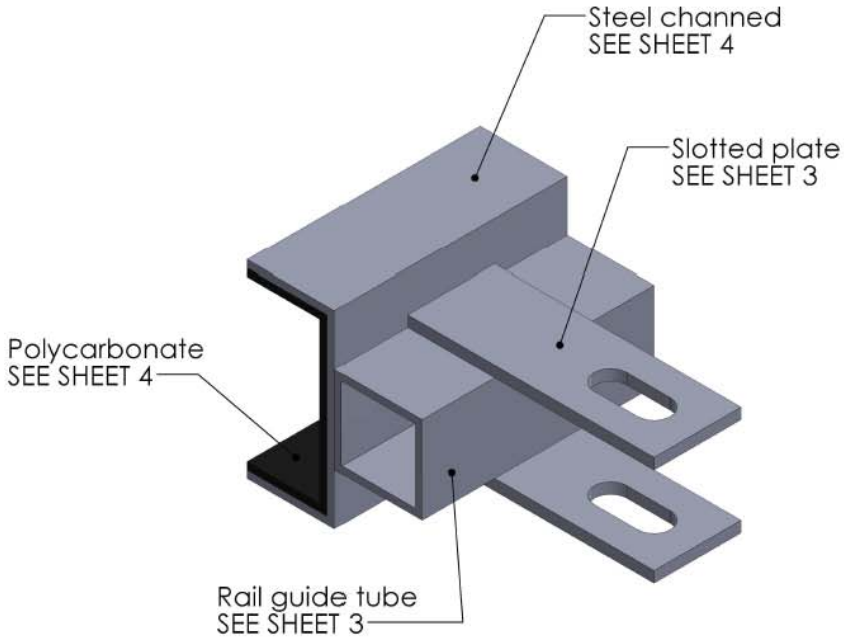

Weld all components to fasten

FLYER PLATE
Sheet 2 of 4

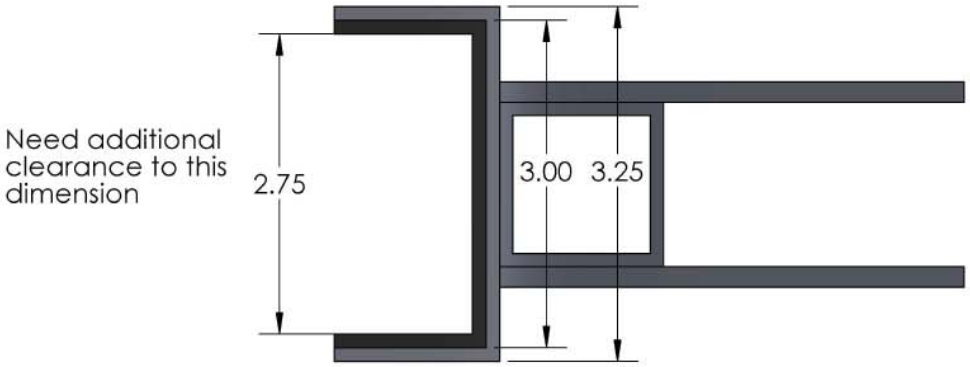

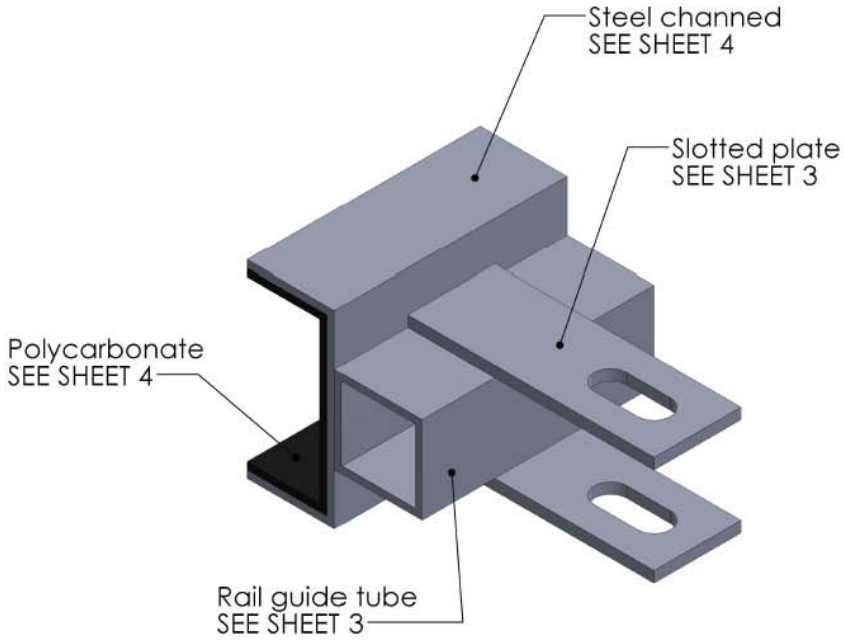

Weld all components to fasten

FLYER PLATE
Sheet 2 of 4

Slotted plate
Cut from 3/16" steel plate, .dxf drawings provided
Quantity: 4

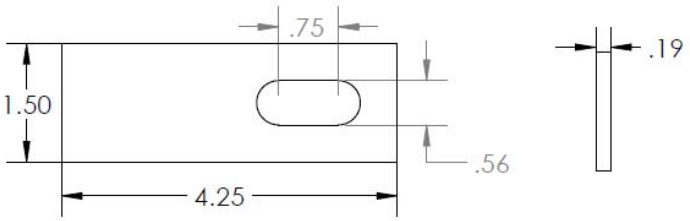

Front view Side view

Rail guide tube
Cut from 1.5" x 1.5" x 1/8" steel tube
Quantity: 2

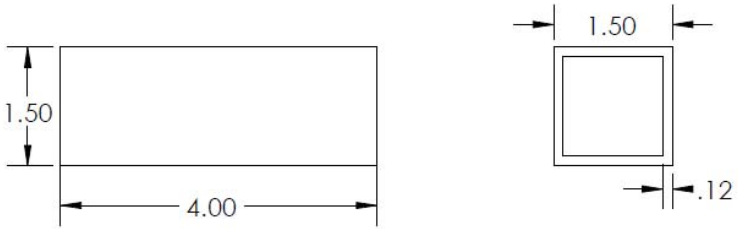

Front view Side view

FLYER PLATE
Sheet 3 of 4

Steel channel
Cut from 1/8" steel plate, .dxf drawings provided
Weld to assemble
Quantity: 2

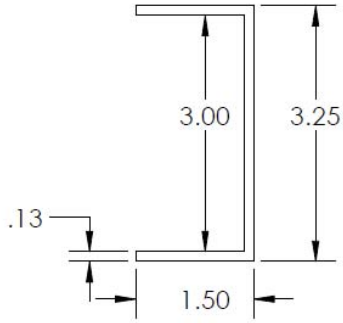

Phelonic channel
Cut from 1/8" phenolic plate, .dxf drawings provided
Glue to steel channel to assemble
Quantity: 2

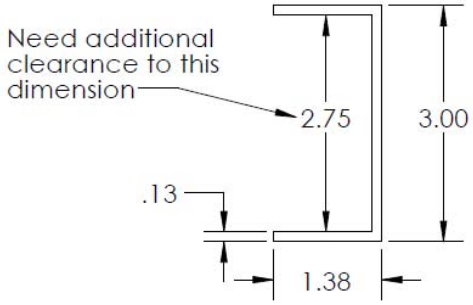

FLYER PLATE
Sheet 4 of 4

FLYER PLATE MASS – VERSION 2

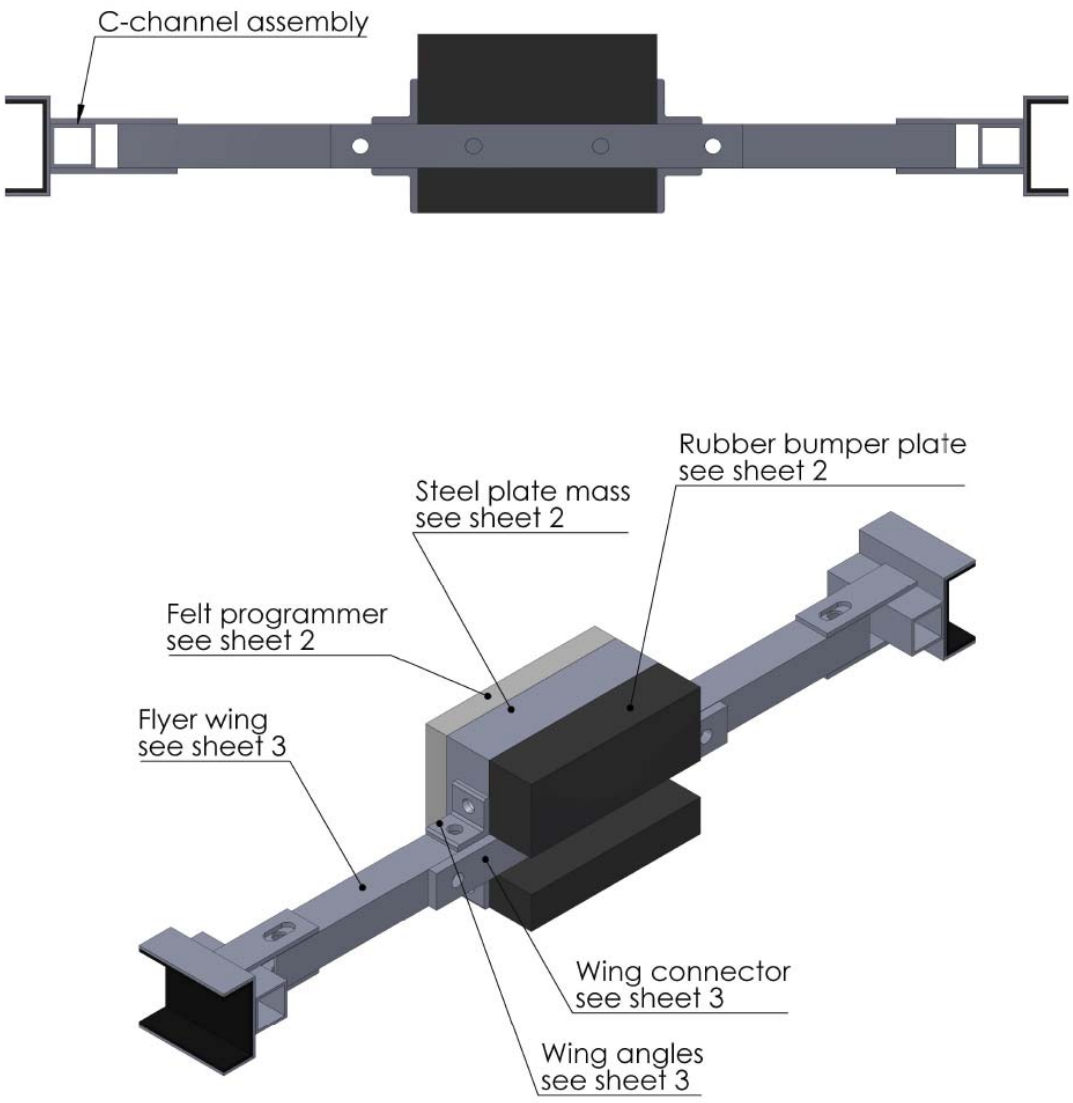

PROJECT	COMPONENT	SHEET DESCRIPTION	SHEET 1 OF 3
FLYER PLATE MOD1	ENTIRE ASSEMBLY	ENTIRE ASSEMBLY	

Rubber bumper plates

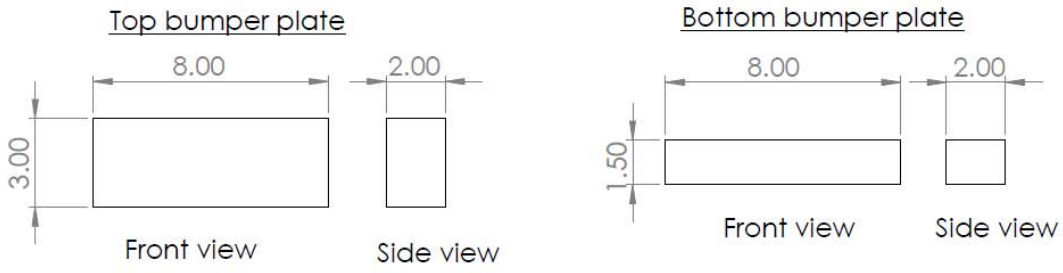

Felt programmer

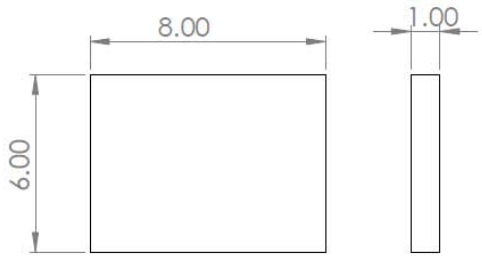

Steel plate mass

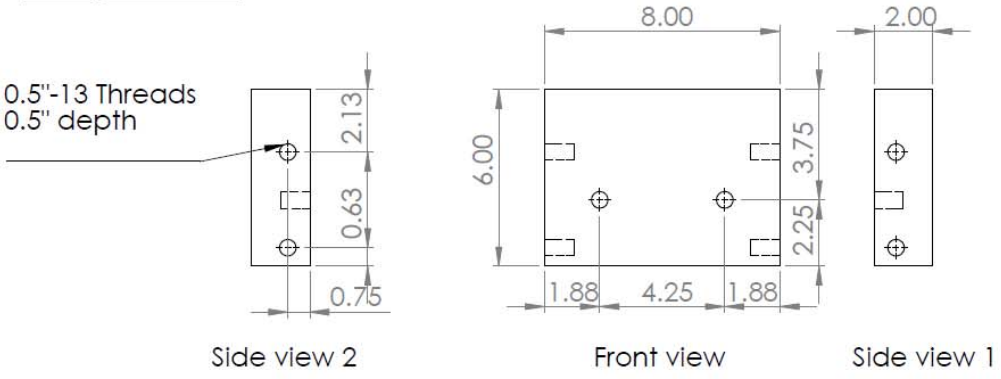

PROJECT	COMPONENT	SHEET DESCRIPTION	SHEET 2 OF 3
FLYER PLATE MOD1	ENTIRE ASSEMBLY	ENTIRE ASSEMBLY	

Flyer wing

Through holes for 1/2" bolts

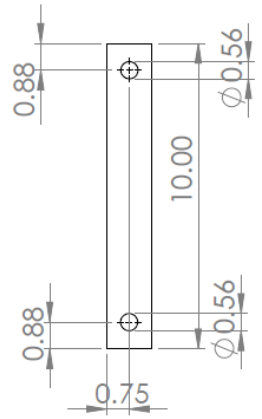

Top view

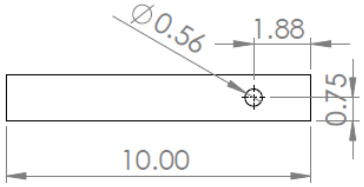

Side view

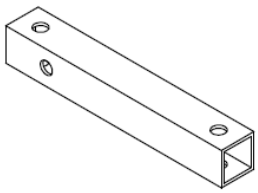

Isometric view

Wing connector

Through holes for 1/2" bolts

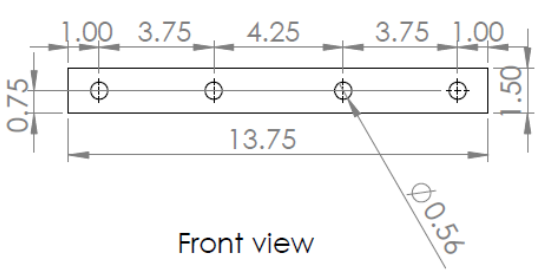

Front view

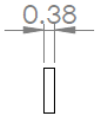

Side view

Wing angles

Through holes for 1/2" bolts

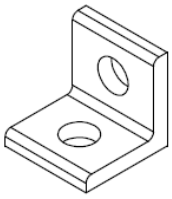

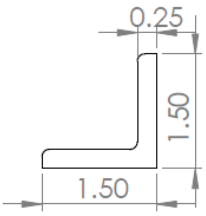

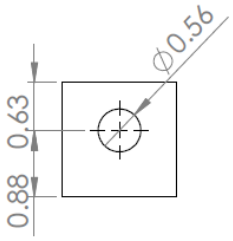

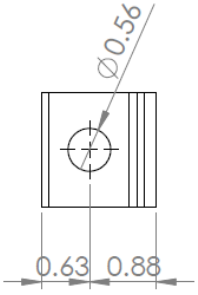

PROJECT	COMPONENT	SHEET DESCRIPTION	SHEET 3 OF 3
FLYER PLATE MOD1	ENTIRE ASSEMBLY	ENTIRE ASSEMBLY	

REFERENCES

1. Sanborn, M., *Experimental methods for understanding the behavior and residual capacity of bolts and steel bolted connections under impulsive loads*, in *School of Civil and Enviromental Engineering*. 2018, Georgia Institute of Technology. p. 363.
2. Mehta, P.K. and P.J. Monteiro, *CONCRETE Microstructure, Properties and Materials*. 2017.
3. International, A., *ASTM C39/C39M-18 Standard Test Method for Compressive Strength of Cylindrical Concrete Specimens*. 2018: West Conshohocken, PA.
4. Chen, W.-F., *Plasticity in reinforced concrete*. 1982, New York: New York : McGraw-Hill.
5. Richart, F.E., A. Brandtzæg, and R.L. Brown, *Failure of plain and spirally reinforced concrete in compression*. 1929, University of Illinois at Urbana Champaign, College of Engineering ….
6. Gu, X., X. Jin, and Y. Zhou, *Basic principles of concrete structures*. 2016: Springer.
7. Torrenti, J.-M., G. Pijaudier-Cabot, and J.-M. Reynouard, *Mechanical behavior of concrete*. 2013: John Wiley & Sons.
8. Terrien, M., *Emission acoustique et" comportement mecanique post-critique" d'un beton sollicite en traction.* BULL LIAISON LAB PONTS CHAUSS, 1980(105).
9. Visser, J. and J. Van Mier, *Deformation controlled hydraulic fracture experiments on concrete.* Dam fracture and Damage, 1994: p. 133-141.
10. Reichard, B., et al., *Coupled Hydraulic System for Tensile Testing in Compression-only Machines.* Experimental Mechanics, 2016. **56**(7): p. 1179-1190.
11. ASTM-International, *ASTM C496 / C496M-17 Standard Test Method for Splitting Tensile Strength of Cylindrical Concrete Specimens*. 2017.
12. Kupfer, H., H.K. Hilsdorf, and H. Rusch. *Behavior of concrete under biaxial stresses*. in *Journal Proceedings*. 1969.
13. Attard, M.M. and S. Setunge, *Stress-strain relationship of confined and unconfined concrete.* Materials Journal, 1996. **93**(5): p. 432-442.
14. Shawn S. Smith, K.J.W.K.H.G. and S. Stein, *Concrete Over the Top--Or, is there Life After Peak?* Materials Journal. **86**(5).
15. Zhang, Q.B. and J. Zhao, *A review of dynamic experimental techniques and mechanical behaviour of rock materials.* Rock mechanics and rock engineering, 2014. **47**(4): p. 1411-1478.
16. Fu, H., M. Erki, and M. Seckin, *Review of effects of loading rate on concrete in compression.* Journal of structural engineering, 1991. **117**(12): p. 3645-3659.
17. Beton, C.E.i.d., *CEB-FIP Model Code 1990*. Towbridge, Wiltshire, UK: Redwood Books.
18. Bischoff, P.H. and S. Perry, *Compressive behaviour of concrete at high strain rates.* Materials and structures, 1991. **24**(6): p. 425-450.

19. Malvar, L.J. and J.E. Crawford, *Dynamic increase factors for concrete*. 1998, Naval Facilities Engineering Service Center Port hueneme CA.
20. Malvar, L.J. and C.A. Ross, *Review of strain rate effects for concrete in tension.* Materials Journal, 1998. **95**(6): p. 735-739.
21. Ross, C.A., J.W. Tedesco, and S.T. Kuennen, *Effects of strain rate on concrete strength.* Materials Journal, 1995. **92**(1): p. 37-47.
22. Ross, C.A., et al., *Moisture and strain rate effects on concrete strength.* Materials Journal, 1996. **93**(3): p. 293-300.
23. Grote, D., S. Park, and M. Zhou, *Dynamic behavior of concrete at high strain rates and pressures: I. experimental characterization.* International Journal of Impact Engineering, 2001. **25**(9): p. 869-886.
24. Park, S., Q. Xia, and M. Zhou, *Dynamic behavior of concrete at high strain rates and pressures: II. Numerical simulation.* International journal of impact engineering, 2001. **25**(9): p. 887-910.
25. Rossi, P., *A physical phenomenon which can explain the mechanical behaviour of concrete under high strain rates.* Materials and Structures, 1991. **24**(6): p. 422-424.
26. Meyers, M.A., *Dynamic behavior of materials*. 1994: John wiley & sons.
27. Broek, D., *Elementary engineering fracture mechanics*. 2012: Springer Science & Business Media.
28. Freund, L., *The stress intensity factor due to normal impact loading of the faces of a crack.* International Journal of Engineering Science, 1974. **12**(2): p. 179-189.
29. Grady, D. and M. Kipp, *Dynamic rock fragmentation.* Fracture mechanics of rock, 1987. **10**: p. 429.
30. Roller, C., et al., *Residual load capacity of exposed and hardened concrete columns under explosion loads.* Engineering Structures, 2013. **55**: p. 66-72.
31. Bao, X. and B. Li, *Residual strength of blast damaged reinforced concrete columns.* International journal of impact engineering, 2010. **37**(3): p. 295-308.
32. Wu, K.-C., B. Li, and K.-C. Tsai, *Residual axial compression capacity of localized blast-damaged RC columns.* International Journal of Impact Engineering, 2011. **38**(1): p. 29-40.
33. Kaewunruen, S. and A.M. Remennikov, *Impact capacity of railway prestressed concrete sleepers.* Engineering Failure Analysis, 2009. **16**(5): p. 1520-1532.
34. Jayasooriya, R., et al., *Blast and residual capacity analysis of reinforced concrete framed buildings.* Engineering structures, 2011. **33**(12): p. 3483-3495.
35. Xiao, J. and H. Falkner, *On residual strength of high-performance concrete with and without polypropylene fibres at elevated temperatures.* Fire safety journal, 2006. **41**(2): p. 115-121.
36. Li, Y.-H. and J.-M. Franssen, *Test results and model for the residual compressive strength of concrete after a fire.* Journal of Structural Fire Engineering, 2011. **2**(1): p. 29-44.
37. Sain, T. and J.C. Kishen, *Residual fatigue strength assessment of concrete considering tension softening behavior.* International journal of fatigue, 2007. **29**(12): p. 2138-2148.
38. Isojeh, B., M. El-Zeghayar, and F.J. Vecchio, *Concrete damage under fatigue loading in uniaxial compression.* ACI Mater. J, 2017. **114**(2): p. 225-235.

39. Malek, A., et al., *Residual Capacity and Permeability-Based Damage Assessment of Concrete under Low-Cycle Fatigue.* Journal of Materials in Civil Engineering, 2018. **30**(6): p. 04018081.
40. Roth, M., Vankirk, G., Frank, A., *Application of Residual Strength Study to Improve Concrete Constitutive Models*. 2018, 13th World Congress on Computational Mechanics: New York City, New York.
41. Chinn, J. and R.M. Zimmerman, *Behavior of plain concrete under various high triaxial compression loading conditions*. 1965, University of Colorado at Boulder.
42. Zhang, B. and K. Wu, *Residual fatigue strength and stiffness of ordinary concrete under bending.* Cement and Concrete Research, 1997. **27**(1): p. 115-126.
43. Sanborn, M. and L. Stewart, *Method for evaluating impulsive shear and residual capacity behavior of bolted connections.* Engineering Structures, 2020. **220**: p. 110372.
44. Sandia National Laboratories, *CUBIT 15.3 Geometry and Mesh Generation Toolkit User Documentation* 2017.
45. Sanborn, M. and L. Stewart, *Behavior of Slip-Critical Bolted Connections Subjected to Impulsive Loads.* International Journal of Impact Engineering, 2020: p. 103501.
46. Stewart, L., et al., *Experimentally generated high-g shock loads using Hydraulic Blast Simulator.* International Journal of Impact Engineering, 2014. **69**: p. 86-94.
47. Freidenberg, A., et al., *Demonstration of tailored impact to achieve blast-like loading.* International Journal of Impact Engineering, 2014. **71**: p. 97-105.
48. Stewart, L.K., Gao, N., Pezzola, G., Sanborn, M., Sanborn, K., Nail, A., and G. and Loreto. *Georgia institute of technology laboratory for blast, shock and impact*. in *7th International Conference on Advances in Experimental Structural Engineering*. 2017.
49. Gram, M., et al., *Laboratory simulation of blast loading on building and bridge structures.* WIT Transactions on State-of-the-art in Science and Engineering, 2012. **60**.
50. Stewart, L., et al., *Methodology and validation for blast and shock testing of structures using high-speed hydraulic actuators.* Engineering Structures, 2014. **70**: p. 168-180.
51. Xcitex, I., *ProAnalyst User Guide.* 2014.
52. Vision Research, *PCC 2.6 User Manual.* 2014.
53. Sanborn, M., *BG-25 Standard Operating Procedure: MTS Single Channel Shock Impactor.* Georgia Institute of Technology, 2016.
54. Sinha, B., K.H. Gerstle, and L.G. Tulin. *Stress-strain relations for concrete under cyclic loading*. in *Journal Proceedings*. 1964.
55. Darwin, D. and D. Pecknold, *Inelastic model for cyclic biaxial loading of reinforced concrete*. 1974, University of Illinois Engineering Experiment Station. College of ….
56. Karsan, I.D. and J.O. Jirsa, *Behavior of concrete under compressive loadings.* Journal of the Structural Division, 1969.
57. Saenz, L.P., *discussion of" Equation for the Stress-Strain Curve of Concrete" by Desayi and Krishnan.* Journal of the American Concrete Institute, 1964. **61**: p. 1229-1235.

58. Malvar, L.J., et al., *A plasticity concrete material model for DYNA3D.* International journal of impact engineering, 1997. **19**(9-10): p. 847-873.
59. Holmquist, T.J. and G.R. Johnson, *A computational constitutive model for glass subjected to large strains, high strain rates and high pressures.* Journal of Applied Mechanics, 2011. **78**(5): p. 051003.
60. Johnson, G.R. and T.J. Holmquist. *An improved computational constitutive model for brittle materials*. in *AIP Conference Proceedings*. 1994. American Institute of Physics.
61. Sandia National Laboratories, *Sierra Solid Mechanics 4.48 User's Guide.* 2018.
62. Kitware, *ParaView 3.0 Users Manual.* 2007.